UNIVERSITY OF SOUTHAMPTON

FACULTY OF ENGINEERING, SCIENCE AND MATHEMATICS

School of Engineering Sciences

Abrasion-Corrosion of Downhole Drill Tool Components

by

Mandar Rajiv Thakare

Thesis submitted for the degree of Doctor of Philosophy

April 2008

UNIVERSITY OF SOUTHAMPTON

ABSTRACT

FACULTY OF ENGINEERING, SCIENCE & MATHEMATICS
SCHOOL OF ENGINEERING SCIENCES

Doctor of Philosophy

ABRASION-CORROSION OF DOWNHOLE DRILL TOOL COMPONENTS

By Mandar Rajiv Thakare

The present work is a Schlumberger funded PhD project entitled 'Abrasion-corrosion of downhole drill tool components'. The objective of this project was to replicate the wear-corrosion mechanisms of tungsten carbide (WC)-based hardmetals and coatings occurring in downhole environments (pH 9-11) under controlled laboratory conditions, to identify and establish a better understanding these mechanisms and the factors influencing them so as to minimise the material wastage during service.

The presence of hard and soft phases within WC-based hardmetals and coatings results in complex wear mechanisms. In addition, the presence of a corrosive environment downhole further complicates the contact conditions and can lead to accelerated surface degradation and even catastrophic failures. A Scanning Electron Microscope (SEM) investigation of worn drill-tool components revealed the presence of micro-scale (by abrasives similar size to the carbide grains i.e. less than 5 μm) and macro-scale abrasion (by abrasives orders of magnitude larger in size compared to the carbide grains). The wear-corrosion testing of candidate materials was investigated using a micro-macro dual approach comprising of micro-scale abrasion testing (University of Southampton) and the modified ASTM G65 tester (National Physical Laboratories, Teddington). To mimic exposure to alkaline drilling fluids for long durations, selected samples were exposed to pH 11 NaOH solution / drilling fluid for 168 h prior to wear testing. Screening of candidate materials on the basis of their wear-corrosion performance using micro-abrasion tester was performed and WC-10Co-4Cr coating along with sintered WC-5.7Co-0.3Cr were selected for in-depth analysis and the micro-macro dual test programme.

The WC-10Co-4Cr coating exposed to pH 11 and pH 7 distilled water (for comparison), revealed the presence of an intense localised corrosion in the form of 'corrosion trenches' due to the preferential dissolution of decarburised metallic tungsten (W), which occurred around the periphery of the carbide grains. These 'corrosion trenches' were found to be one-carbide deep and resulted in the carbide being held loose in the corrosion trenches. Alternatively, for the sintered WC-5.7Co-0.3Cr, exposure to pH 11 did not show any evidence of localised corrosion. However, exposure to pH 7 distilled water resulted in the preferential dissolution of the binder phase.

For the first time, a modified micro-abrasion tester capable of *in situ* electrochemical measurements was developed to monitor the corrosion kinetics during micro-scale wear-corrosion. Interestingly, the lowest wear occurred under pH 11 conditions. It was proposed that the presence of $Co(OH)_2$ based passive films, also detected by XPS analysis, appears to influence the rate of binder-phase removal by altering the stiffness of the abrasive-surface contact and lowering the friction between abrasives and the surface and in turn lowers the overall wear rates. This was also corroborated by the observed wear mechanism of preferential removal of the binder-phase leading to the undermining of carbides. Conversely, for the sintered WC-5.7Co-0.3Cr, despite the lack of surface passivation under similar test conditions, the wear rates were found to be independent of pH.

The influence of abrasive size on the wear-corrosion performance of sprayed WC-10Co-4Cr coating was investigated using the modified ASTM G65 test. It was revealed that in addition to the size of abrasives, the wear rates are dependent on the overall wear mechanisms. In general, severe damage to the coating was caused by delamination due to the propagation of sub-surface cracks resulting in the doubling of wear rates. The sub-surface cracking of the coating increases with an increase in the abrasive size. Alternatively, for the sintered WC-5.7Co-0.3Cr, an increase in the extent of cracking in the carbide grains increased with the abrasive size. An order of magnitude increase in wear resulted from the extensive carbide cracking and the subsequent removal of the carbide grains. The dual approach successfully replicated the wear in downhole conditions by examining the influence of contact conditions and abrasive size on the wear-corrosion of WC-based sintered hardmetals and sprayed coatings to inform a better design / selection of surfaces subjected to downhole environments.

CONTENTS

LIST OF FIGURES

LIST OF TABLES

DECLARATION OF AUTHORSHIP

I, Mandar R. Thakare declare that the thesis entitled 'Abrasion-corrosion of downhole drill tool components' and the work presented in the thesis are both my own, and have been generated by me as the result of my own original research. I confirm that:

- this work was done wholly or mainly while in candidature for a research degree at this University;

- where any part of this thesis has previously been submitted for a degree or any other qualification at this University or any other institution, this has been clearly stated;

- where I have consulted the published work of others, this is always clearly attributed;

- where I have quoted from the work of others, the source is always given. With the exception of such quotations, this thesis is entirely my own work;

- I have acknowledged all main sources of help;

- where the thesis is based on work done by myself jointly with others, I have made clear exactly what was done by others and what I have contributed myself;

- parts of this work have been published as

    1. Exposure effects of alkaline drilling fluid on the microscale abrasion–corrosion of WC-based hardmetals
    Wear, *Volume 263, Issues 1-6*, *10 September 2007*, *Pages 125-136*
    M.R. Thakare, J.A. Wharton, R.J.K. Wood and C. Menger

    2. Exposure effects of strong alkaline conditions on the microscale abrasion–corrosion of D-gun sprayed WC–10Co–4Cr coating
    Tribology International, *In Press, Corrected Proof*, *Available online 27 September 2007* (http://dx.doi.org/10.1016/j.triboint.2007.07.012)
    M.R. Thakare, J.A. Wharton, R.J.K. Wood and C. Menger

Signed: ……..

Date:…….

ACKNOWLEDGMENTS

I am indebted to my supervisor, Professor Robert Wood and advisor, Dr. Julian Wharton for their guidance and excellent supervision throughout this project. Guidance received from my industrial supervisor, Dr. Christian Menger is also greatly appreciated.

I wish to thank the technicians, Mr. Steve Pilcher for his assistance in fabricating / maintaining the micro-abrasion rig, Mr. Robert Barnes, Mr. Chris Williams and Mr. Dave Beckett for assisting in machining hardmetal samples. The help and advice of Drs. Terry Harvey, Ling Wang and Shuncai Wang throughout the experimentation is also gratefully acknowledged. I would like to express my appreciation for my colleagues in the Surface Engineering and Tribology (SET) group, in particular Rakesh, Lily, Sun Dan, Ramkumar, James, Mark, Prasanna, Fitri and Jenny for all the interesting discussions during coffee breaks, group activities and for making the SET group an exciting place for research.

I am most grateful to the School of Engineering Sciences and Schlumberger plc for providing financial support throughout this project. I am thankful to Drs. Allan Humphreys and Beth Nicholson from Schlumberger plc for their encouragement and some very useful discussions during visits to Schlumberger. I would also like to thank the management of National Physical Laboratories, Teddington for granting access to the ASTM G65 rig and in particular, Drs. Mark Gee and Andrew Gant for their advice on wear-testing. Others who provided help include Dr. Graham Beamson (NCES, Daresbury) for his guidance during XPS analysis and ing. Robbert Weemaes (MiPlaza, Philips Research) for the preparation of FIB sections. I also wish to acknowledge Dymet Alloys for supplying sintered WC samples and Praxair Surface Technologies Ltd. for supplying the WC-10Co-4Cr coating for testing.

Last, but by no means the least, I wish to thank my parents and Sheetal for their love, support and patience. The magnitude of their contribution can not be expressed in a few words, so it is to them that this thesis is dedicated.

1 Introduction

1.1 Tribology in downhole environment

Whenever surfaces move over each other, wear will occur in the form of damage to one or both surfaces, generally involving progressive loss of material [1]. In most cases, this wear is detrimental and leads to increased clearance between moving components, loss of precision and failure of component due to material loss. A national survey in 1997 indicated that the cost of wear to the UK industry was of the order of £650 million per year [2, 3]. Also, for companies which have these wear problems, the costs were typically about 0.25 percent of their turnover [3]. More often than not, these costs can be at least halved by appropriate design and/or material changes to reduce or eliminate wear [3]. This brings into focus the subject of *'tribology'*, which is defined as 'the science and technology of interacting surfaces in relative motion' and encompasses the study of friction, wear and lubrication. The word 'tribology' was derived from the Greek word *τριβοσ* (tribos) which means rubbing or attrition [4]. It was first coined in 1966 by a UK Government committee chaired by Dr. P. Jost, although friction, wear and lubrication have been studied for many years before then.

The process of wear resistance and protection against component failure is far more significant if components are subjected to harsh environments such as those encountered by downhole drill tool components. Typically, downhole operations expose these materials to harsh working conditions for long durations in various chemical environments such as aqueous solutions containing chlorides, H_2S and/or CO_2 at various pH levels (pH 9-11) as well as thermal environments at elevated temperatures up to 150°C [5-7]. The process of directional drilling allows the drill tool to travel in a horizontal direction allowing access to oil reserves not directly below the oil-well, see Figure 1.1. The steering mechanism for the drilling tool comprises of a series of 'stabiliser -pads' which push against the rock formations and steer the drill tool in the opposite direction, see Figure 1.2. The 'mud-motor' is a hydraulic motor driven by the drilling fluid (Bentonite mud) and provides the power to rotate the drill-bit, as well as, steer the tool in the desired direction. Collectively the stabiliser pads, mud motor and the drill-bit are known as bottom-hole assembly (BHA), see Figure 1.2a. Apart from providing hydraulic power to the BHA, the alkaline (pH 9 - 11) Bentonite mud based drilling fluid is also expected to lubricate the system and also transport rock cuttings / silica sand debris (SiO_2) to the surface as shown in Figure 1.2a.

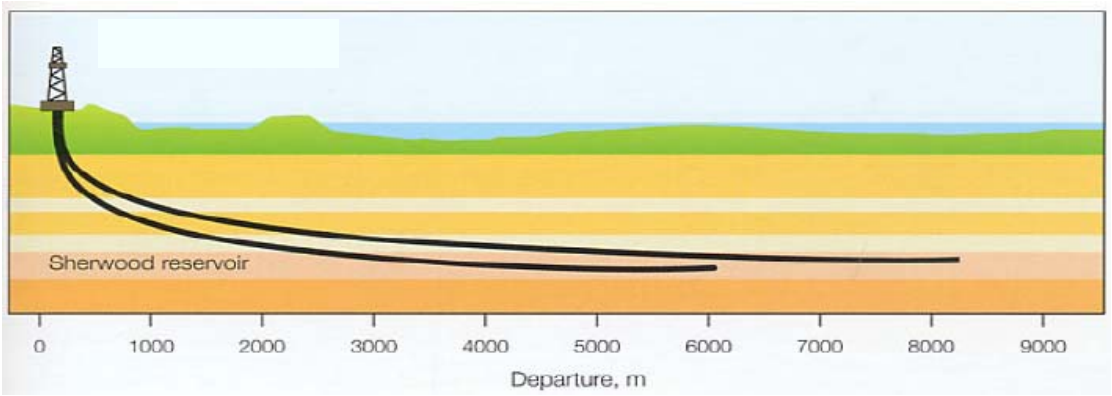

Figure 1.1: Directional drilling allows access to distant oil reserves.

.

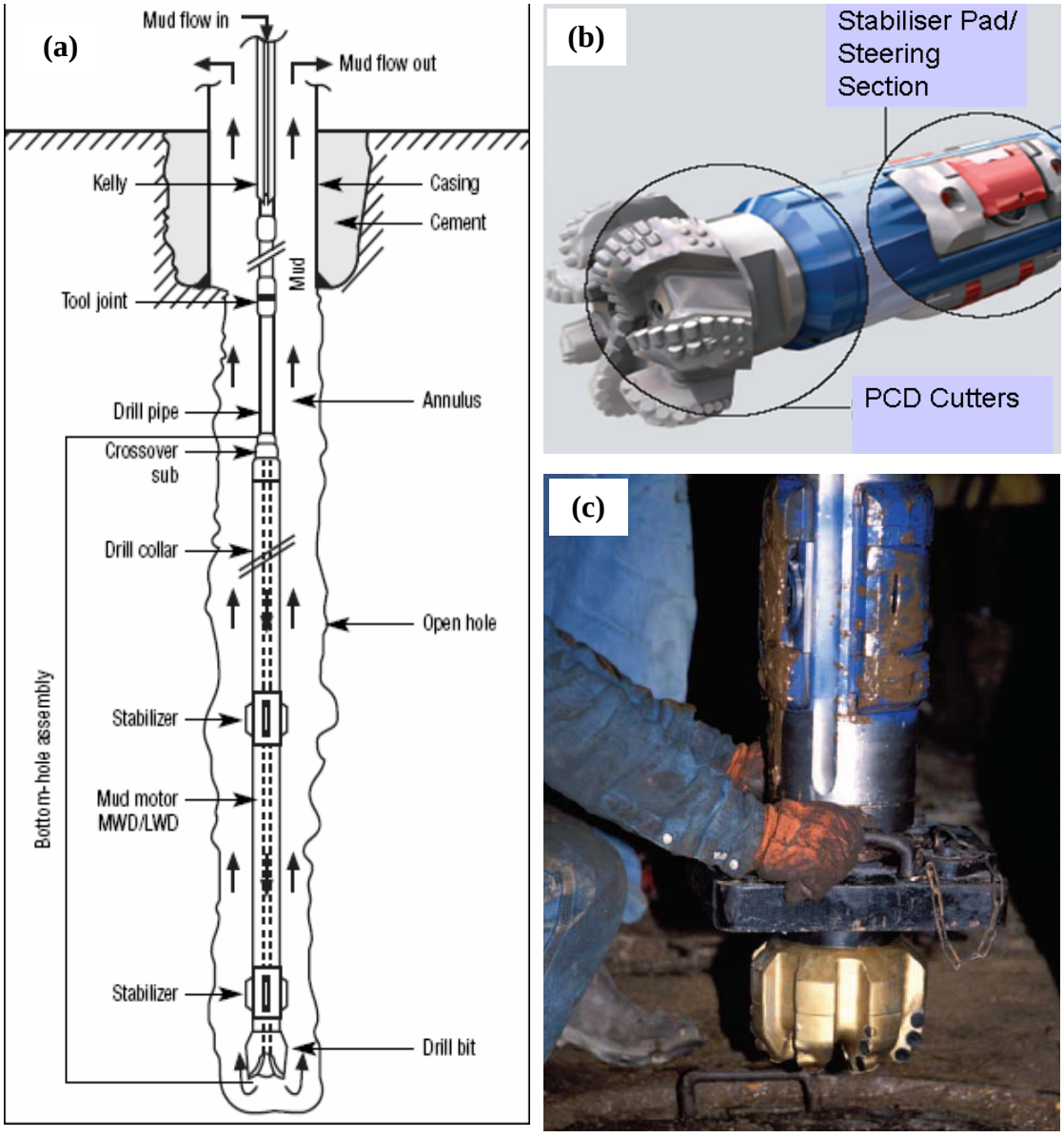

Figure 1.2: (a) Drill tool bottom hole assembly, (b) and (c) typical drill tools showing the polycrystalline diamond (PCD) cutters on the drill- bit and HVOF tungsten carbide coated stabiliser pads (Schlumberger plc).

The drilling mud carrying the rock cuttings (SiO_2) passes through a filtration process and is recirculated. However, the filtration process does not remove the fine rock cuttings (less than 500 μm) [6] which remain suspended in the drilling mud. Subsequently the suspended debris can become trapped between rolling and sliding contacts of the downhole components aggravating the process of wear. Due to the high cost involved in the maintenance and replacement of the drill tool parts, which are at times inaccessible, it is essential to extend the useful life of these components by developing a better understanding of the damage mechanisms and improving the material selection criteria. The wear in downhole components can be due to either components abrading against rock formations and / or abrasives trapped between moving parts. The focus of this project will be on the abrasion caused by abrasives trapped between two moving parts. Typically, different grades of tungsten carbides (bulk/sprayed) along with polycrystalline diamond inserts and functionally graded carbides have been used in the offshore industry to resist this harsh environment. The present work is part of a PhD project funded by Schlumberger Oilfield UK plc. entitled 'Abrasion-Corrosion of Downhole Drill Tool Components' and focuses on investigating the tribological performance of WC-based sintered hardmetals and sprayed coatings.

1.2 Objectives the project

The main objective of the work was to replicate wear-corrosion mechanisms of WC-based hardmetals and coatings, occurring in downhole conditions under controlled laboratory conditions for a better understanding of these mechanisms and the factors influencing them, such as:

- pH of the environment
- Effects of exposure to alkaline conditions
- Effect of increase in abrasive size

- It also aimed to provide Schlumberger with a better understanding of wear-corrosion interactions in downhole conditions for improved materials selection for downhole applications.

1.3 Scope of the project

A Schlumberger funded 3rd year student project at the University of Southampton in 2005 studied the feasibility of using silica sand and drilling fluid for the micro-scale abrasion of typical hard materials used for wear resistance in downhole conditions. The results from this feasibility study showed that the size distribution of suspended particles in the drilling fluid along with its non-Newtonian behaviour of resulted in very complex contact conditions due to possible adsorption of the drilling fluid on the rotating ball and hampered a consistent entrainment of abrasive particles (due to solidification of the drilling fluid at the ball-sample contact) during the micro-abrasion testing resulting in inconsistent results [8]. Concerns over degradation of the drilling fluid over a period of time along with the complex contact conditions created resulted in the feasibility study concluding that for better control of abrasives in the contact, laboratory test solutions such as pH 11 NaOH should be used during micro-abrasion.

As part of the current work, a preliminary study was undertaken to understand the wear-mechanisms present under downhole conditions. Worn drill tool components were analysed and categorised according to the wear mechanisms detected by surface analysis techniques such as optical microscopy, scanning electron microscopy (SEM) and 2-D, 3-D surface profilometry. SEM micrographs of the worn components revealed that abrasive wear can be classified as micro-scale (caused by abrasives similar in size as the carbide grains, i.e. less than 5 μm) and macro-scale wear (caused by abrasives larger than the carbide grains). Figure 1.3a shows worn a sintered WC-based thrust washer subjected to micro-scale abrasives, while Figure 1.3b shows a worn HVOF-WC-based coating on the stabiliser pad worn by macro-scale abrasives. Clearly, to investigate the influence of abrasive size on the wear-corrosion interactions of candidate materials, a ‘dual approach’ was necessary. As part of the dual approach, abrasive wear tests were conducted on the modified ASTM-G65 tester at National Physical Laboratories (NPL) on candidate materials using three different sizes of abrasives which are of the same size, 10 times and 100 times the size of typical carbide grains (4.5. μm, 17.5 μm and 180 μm), one of which was the same as abrasives used in the micro-scale abrasion (4.5 μm) tests conducted in the Surface Engineering and Tribology laboratory at the University of Southampton.

To mimic the prolonged exposure of downhole drill tool components to alkaline conditions, a novel method of ‘exposing’ samples to alkaline conditions for a duration of 1 week prior to abrasive wear testing was deployed. Static electrochemical techniques such as

potentiodynamic polarisation, advanced surface analysis techniques like SEM analysis and X-ray photoelectron spectroscopy (XPS), focussed ion-beam (FIB) sectioning of exposed samples were used to study the effects of static exposure.

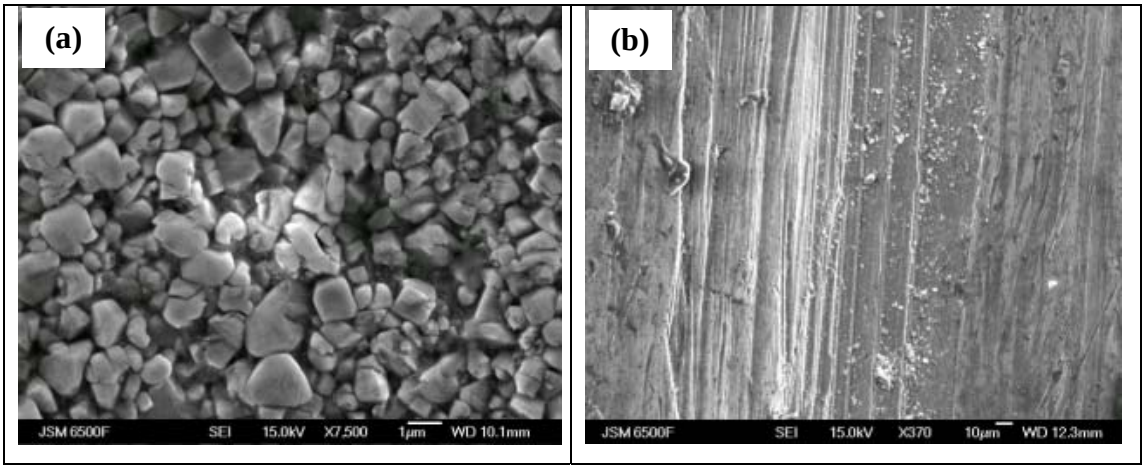

Figure 1.3: Wear observed on downhole components; (a) micro-scale abrasion of a WC-6Ni thrust washer and (b) macro-scale abrasion of WC-Ni coating on the stabiliser pad.

Also, to study the corrosion kinetics occurring during wear under alkaline conditions, a novel modification to the micro-abrasion tester was achieved to allow in situ electrochemical current-noise measurements. This allowed the systematic investigation of repassivation / depassivation rates, electrochemical and mechanical components of wear-corrosion interactions under neutral and alkaline pH conditions with respect to binder-phase composition and the microstructure of the hardmetal / coating. For the first time, the 'size effect' of abrasives was studied for WC-based sintered hardmetals and sprayed coatings by deploying a novel technique of using three different sizes of abrasives on the modified ASTM G65 rubber wheel test to investigate the effects of increase in abrasive size on the observed wear mechanisms. Comparison of results from the micro-abrasion tester and the modified ASTM G65 tester allowed the influence of contact conditions (applied load, contact area, load per particle) on the wear mechanisms, wear rates and wear-corrosion interactions to be investigated.

1.4 Thesis structure

The structure of this PhD thesis is as follows:

Chapter 2: Literature Review

Chapter 2 discusses the available published literature on the wear, corrosion and wear-corrosion interactions for WC-based sintered hardmetals and coatings. In addition, the literature on the use of standard wear tests, static corrosion tests and wear-corrosion tests has also been critically reviewed.

Chapter 3: Methodology and experimental procedures

Chapter 3 discusses the methodology for the test programmes discussed in subsequent chapters. Chapter 3 also provides a detailed description of the properties of the WC-based sintered hardmetals and coatings tested. This chapter also details the test procedures followed for abrasion and corrosion tests conducted on the samples.

Chapter 4: Initial Work

Chapter 4 discusses the preliminary tests done on the micro-abrasion tester using silica sand and distilled water. It briefly outlines the aims and conclusions from this preliminary research. The chapter also includes the preliminary exposure tests to evaluate the effect on surface composition of exposure to alkaline conditions on the wear rates of a selection of WC-based sintered hardmetals and coatings.

Chapter 5: Exposure to drilling fluid and micro-abrasion

Chapter 5 discusses the effects of exposing sintered and sprayed samples to an alkaline drilling fluid. The wear-corrosion interactions and the associated mechanisms will be discussed.

Chapter 6: Surface analysis and wear-corrosion interactions

Chapter 6 details the analysis of wear-corrosion interactions in WC-10Co-4Cr coating using anodic treatments and exposure in pH 11 NaOH solution by micro-abrasion for varying sliding distances. Advanced techniques such as XPS, SEM and FIB sectioning have been deployed to characterise the exposed surfaces of sprayed samples. For comparison, SEM analysis and XPS has also been performed on sintered samples.

Chapter 7: *In situ* electrochemical current noise measurements during micro-abrasion

Chapter 7 details the use of *in situ* electrochemical current noise measurements conducted during the micro-abrasion testing of WC-based sintered and sprayed samples using neutral and alkaline abrasive slurries. This chapter discusses the corrosion kinetics occurring during micro-abrasion tests. The use of *in situ* electrochemical measurements also enabled decoupling the electrochemical and mechanical components of wear-corrosion interactions.

Chapter 8: Effects of increase in abrasive size on wear mechanisms and wear-corrosion interactions

Chapter 8 details the work using a modified ASTM G65 tester at NPL as part of the dual approach. The influence of increase in abrasive size on the wear mechanisms was investigated for sintered and sprayed samples.

Chapter 9: Influence of contact conditions on the wear mechanisms and wear-corrosion interactions

Chapter 9 compares the wear-mechanisms observed during micro-scale abrasion and the modified ASTM G65 tests. The observed wear mechanisms, wear rates and wear-corrosion interactions are discussed in terms of the prevalent contact conditions.

Chapter 10: Conclusions and further work

Chapter 10 presents the conclusions, recommendations and further work from this PhD project.

2 Literature Review

2.1 Sintered and sprayed tungsten carbide based hardmetals

2.1.1 Microstructure and properties of sintered tungsten carbides

Cemented carbides are commercially one of the oldest and most successful powder metallurgy products. These composites are aggregates of particles of tungsten carbide bonded with a binder phase by liquid-phase sintering [9, 10]. During the sintering of WC-based hardmetals, treated powder of WC and binder is heated to approximately 1500 ^{o}C with an applied pressure of about 70-100 M Pa.[11].

The properties of the resulting sintered composites are derived from the constituents of large and brittle carbides and the softer and more ductile binder. WC composites have been used as bulk (sintered) materials or as high velocity oxy-fuel (HVOF) spray coatings depending on the application. HVOF WC coatings are commonly used on aircraft landing gear for wear resistant surfaces to replace hard chromium coatings. They are also widely used in the oil and gas industry for their superior wear resistance [12-14] and high hardness between 1200 and 1800 HV at room temperature. Co is the most commonly used binder with additions of Cr and Ni for added corrosion resistance [15]. The hardness range is achieved by changing the binder content or the carbide size or the binder composition; the effects of each will be discussed later. At a very basic level, tungsten carbides are expected to offer higher resistance to wear due to the fact that they are harder than the quartz abrasives found in rocks (hardness of quartz is in the range 750-1200 HV). Despite their high hardness, WC composites do suffer wear and corrosion depending on factors such as fracture toughness, carbide size, binder percent, abrasive size, wear mechanism and environment [16].

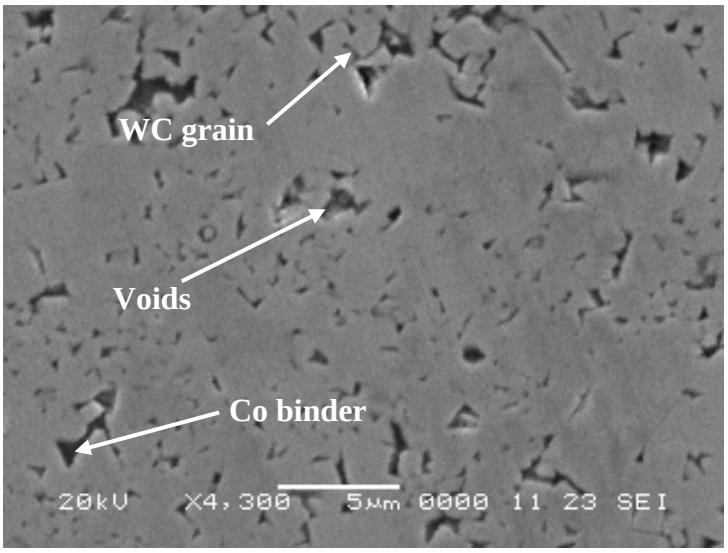

Figure 2.1: SEM micrograph showing the microstructure of a sintered WC-6Co sample polished to 1 μm diamond finish.

Figure 2.1 shows the SEM micrograph of a polished sample of a sintered hardmetal revealing the uniform skeletal structure. The size of the carbide grains in sintered hardmetals usually vary from 0.1 to 10 μm and the mass of the binder used ranges from 4-30 % [17]. During sintering, substantial amounts of WC dissolve in Co and re-precipitate during cooling, mainly along the periphery of existing WC grains and as finely dispersed particles in the binder which results in a strong bond between the carbide and the Co binder. This is due to the ability of Co to dissolve WC at high temperatures (up to 35%) [11]. The mechanical properties of the sintered WC composite depends on the binder content, binder mean free path and the carbide grain size [18, 19]. These parameters are interrelated and sometimes it is difficult to determine their individual effect on the mechanical properties of the hardmetal. An increase in the carbide content leads to an obvious increase in the hardness of the hardmetal, however, this is also accompanied by a corresponding decrease in the fracture toughness of the cemented carbide [20], see Figure 2.2.

Another parameter which strongly influences the hardness of WC-based hardmetals is the carbide grain size. Based on the carbide grain size, WC-based hardmetals can be classified as conventional (carbide size between 1-10 μm) and nano-structured (carbide size less than 1 μm). Jia *et al.* [21] compared the micro-structures of conventional and nano-structured carbide based hardmetals and found that the hardness of WC-Co composites increases with a decrease in the carbide size. This increase in the hardness with decrease in the carbide size is due to a corresponding decrease in the binder mean free path. Binder mean free path is the measure of the average distance of binder between the WC grains and a decrease in the

binder mean free path results in an increase in the ability of the hardmetal to resist plastic deformation due to the higher resistance offered by the carbide grains.

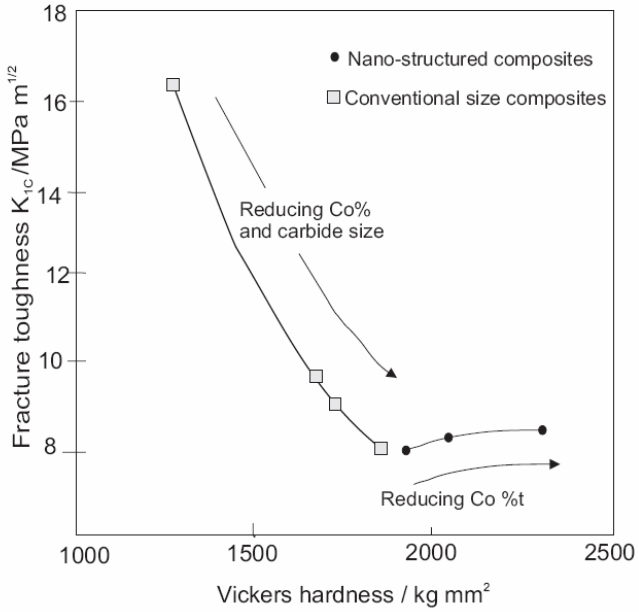

Figure 2.2: Effect of carbide size and binder volume on the fracture toughness and hardness of conventional and nanostructured sintered hardmetals [21].

The hardness of sintered hardmetal is also influenced by the contiguity of the WC grains [22]. Contiguity is defined as "the fraction of the total internal surface area of a phase that is shared by particles of the same phase" [23] and by definition is expected to be between 0 and 1. Contiguity of WC grains will tend to 1 when the binder content tends to 0 % and will tend to 0 when the binder content tends to 100%. Luyckx *et al.* [24] studied this relationship of contiguity of WC grains with the binder volume and concluded that the contiguity of the WC grains solely depends on the volume of binder present and is independent of the carbide grain size. As such, a higher contiguity between the WC grains would lead to an increase in the hardness along with a decrease in mean free path and binder volume [17].

The strength of individual carbide grains decrease with increase in grain size. It is observed during hardness, compressive and bend tests that plastic deformation of WC grains occurs in the form of slip bands [25]. Due to the higher thermal expansion coefficient of Co as compared to WC phase, residual stresses arise during cooling from the sintering temperature. While tensile residual stresses are observed on the binder phase, compressive residual stresses are observed in the WC grains [25]. Detailed discussion of the influence of fracture of carbide grains on the wear of sintered WC-based hardmetals is included in Section 2.2.4.

2.1.2 Microstructure and properties of sprayed tungsten carbide based coating

WC-based coatings are an extremely successful surface engineering product. They are typically used in cases where WC-based sintered compacts can not be used (e.g. complicated shape of the component). WC-based coating can be deposited on the surface of components subjected to wear to increase surface wear resistance. The High Velocity Oxy-fuel (HVOF) spray technique is commonly used for depositing wear resistant WC-based coatings and has the advantage of generating higher particle velocities and the relatively low temperatures involved which minimise degradation of both the coating and substrate [26]. To assess the response of these coatings to abrasive wear and corrosion, it is important to understand the interactions between the different phases present during the spraying process since varying the spray parameters can significantly alter the properties of the coating. The Detonation gun (D-gun) process shown schematically in Figure 2.3 is a modification of the conventional HVOF process in which the coating is deposited by means of a detonation caused in the detonation-gun barrel. The advantage of the D-gun process is that it produces a dense coating with minimum porosity (less than 1%) and high adhesion with the substrate [27]. A mixture of oxygen and acetylene, along with a pulse of pulverised WC, Co and Cr (in correct proportion) are introduced into a barrel and detonated using a spark. The resulting high-temperature, high-pressure detonation wave heats the powder particles to around 3000 °C and accelerates them at a velocity of about 750 m s^{-1} towards the substrate while maintaining relatively low substrate temperatures between 95-150 °C [28]. Although the mechanism of bonding of the particles to the substrate is not fully understood, it is thought to be largely due to mechanical interlocking of the solidifying and shrinking “splats” (lamellar structure) with the asperities on the surface being coated [28]. These splats are approximately 50 μm wide and 10 μm thick and can vary depending on factors like velocity of deposition and the rate of cooling.

The HVOF WC coating microstructure is extremely complex and consists of WC grains in an amorphous matrix consisting of Co with W and C in solution, see Figure 2.4. Compared to the uniform distribution of carbides and binder observed in sintered hardmetals, the coating shows a random distribution of carbides and binder rich areas also known as Co-lakes. During the spraying process, the WC particles partially melt and react with the binder to form metallic W and complex WC-M (where, M is the binder) compounds [27, 29].

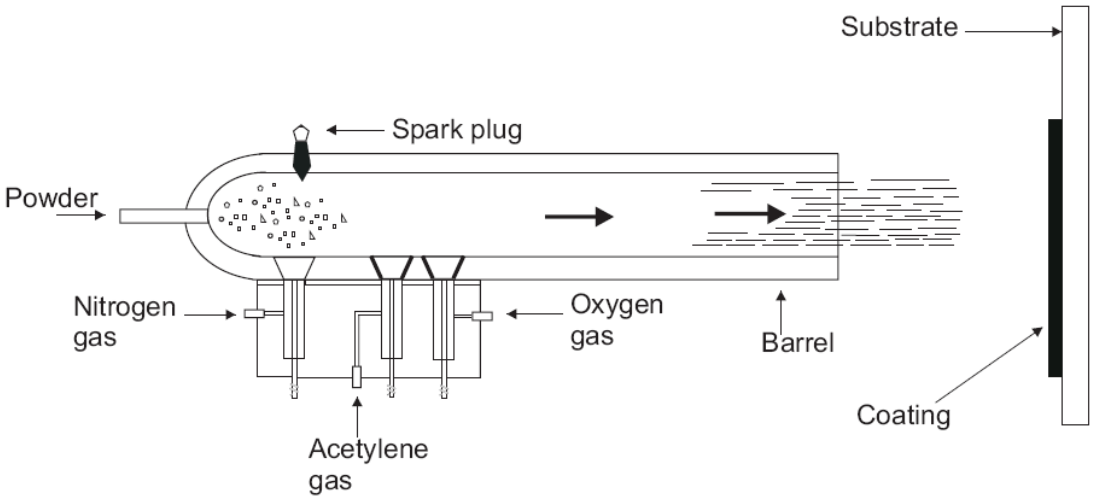

Figure 2.3: Schematic of the detonation gun process (Praxair Surface Technologies Ltd.).

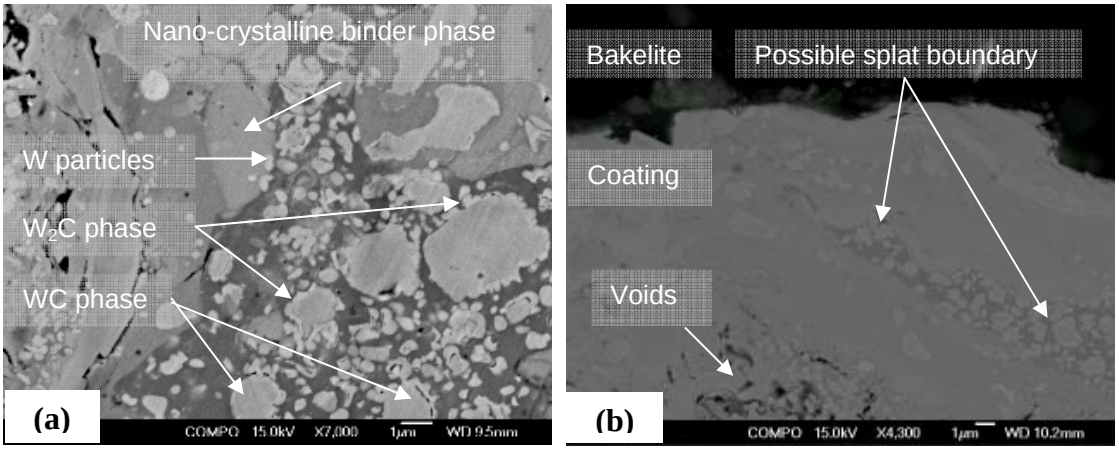

Figure 2.4: SEM-BSE image of a D-gun sprayed WC-10Co-4Cr coating (a) polished surface showing the distribution of carbide particles and soft binder phase and (b) Cross-section showing splat boundary and voids in the coating.

The formation of W or WC-M compounds is more likely to occur at the periphery of the carbide particles where the temperature is expected to be highest. Alongside the main WC hard phase, W_2C and more complex carbides are often observed in the carbide phase. The formation of amorphous matrix, W_2C and complex carbides result from dissolution of WC into the molten binder phase during spraying and subsequent oxidation and precipitation reactions [30]. The decomposition of WC is thought to proceed in three stages [31, 32].

$$2WC \rightarrow W_2C + C \qquad \textbf{2.1}$$

$$W_2C + \frac{1}{2}O_2 \rightarrow W_2(C,O) \qquad \textbf{2.2}$$

$$W_2(C,O) \rightarrow 2W + C\,O \qquad \textbf{2.3}$$

The decarburised W_2C phase is precipitated along the WC grain boundary along with a ring of metallic W between the WC grain and W_2C phase [29]. Higher degree of oxidation is observed along the coating splat boundary which results in the formation of nano-scale W precipitates resulting in a nano-crystalline structure [29] as shown schematically in Figure 2.5. This is due the higher temperatures and higher cooling rates observed along the splat boundaries during the spray process. Hence unlike the sintered WC hardmetals, the composition of the sprayed WC-based coating does not correspond to the nominal powder composition used for the spraying process and the response to wear and corrosion can be very different from that observed in sintered WC-based materials. Although the parameters governing the wear performance of WC-based sprayed coatings should ideally be similar to sintered hardmetals, this is not the case since the ductile binder in the sintered material has been replaced by a relatively brittle, inhomogeneous binder phase in the HVOF-sprayed coating [30].

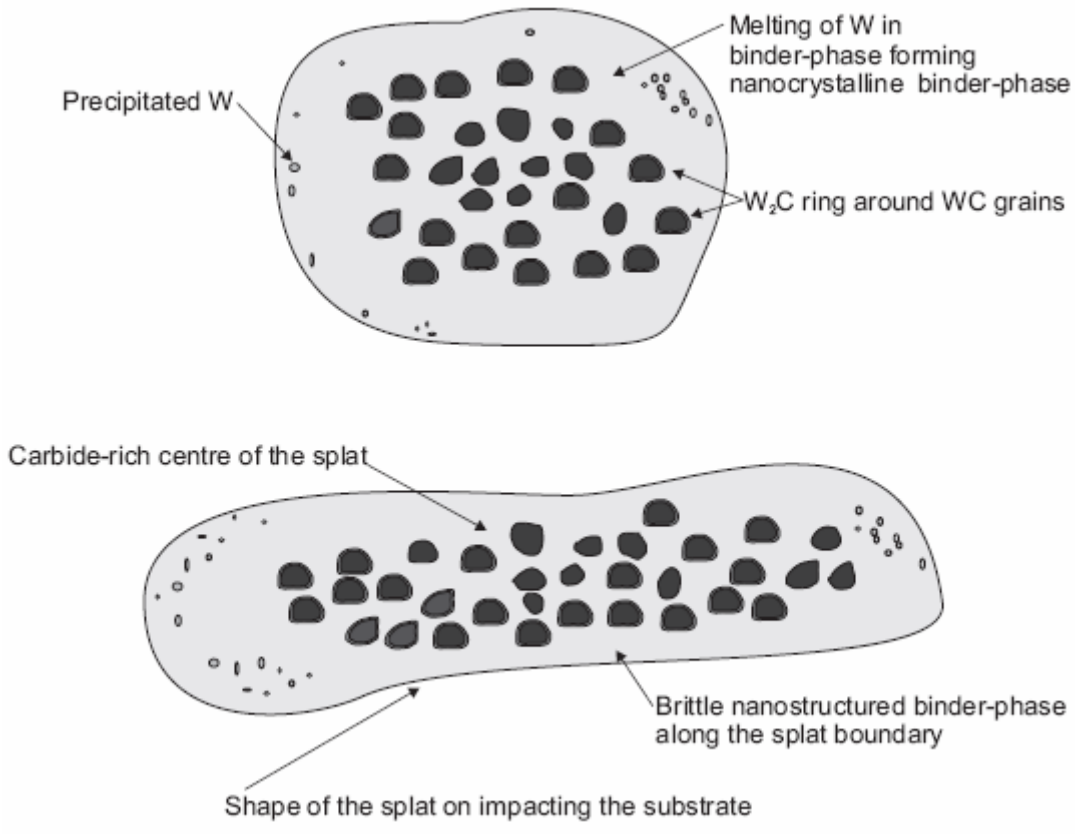

Figure 2.5: Schematic of a molten droplet and a solidified splat structure of the WC-Co coating (Adapted from [30]) .

Stewart *et al.* [30] compared the X-ray diffraction (XRD) patterns of nanostructured and conventional powders with the coatings and observed that the nanostructured coatings

showed a higher degree of decomposition of WC grains during spraying. A higher degree of decomposition of WC grains leads to lowering of carbon content in the WC grain (decarburisation) and formation of higher amounts of amorphous W-C-M compounds in the binder. This occurred due to the larger surface area exposed to react in the nanostructured WC particles.

Residual stresses are formed in the coating and the substrate in contact with the coating due to the high temperatures reached during the spraying process and subsequent cooling of the coating [33, 34]. The process of stress formation in the coating is complex and may result in the formation of either tensile or compressive residual stresses in the coating and substrate [35]. Tensile stresses can be formed in the coating due to temperature effects caused by quenching of the splats [36]. The presence of tensile residual stresses in the coating can be detrimental as they aid in propagation of cracks in the coating and also limit the thickness of the coating [35]. Compressive stresses in WC–Co coatings/ substrate are produced by a 'peening' action of WC particles during the spraying process which can potentially lead to an increase in the fatigue strength of the component [34, 35]. Another property which strongly influenced by the microstructure of the WC-based coatings is its fracture toughness. Lopez-Cantera and Mellor [37] investigated the indentation fracture toughness of WC-10Co-4Cr coatings and found that crack propagation parallel to the substrate is more than the crack propagation transverse to the substrate. They observed that crack propagation preferentially occurred in the nano-crystalline zone between the splat boundary and the carbide rich centre of the coating splat. This was due to the fact that W_2C and other W-C-M phases created during the spraying process are more brittle than WC [38]. Detailed discussion on the influence of the properties of the WC-based sprayed coatings on their wear performance is included in section 2.2.4.

2.2 Wear and wear testing

2.2.1 Wear

Wear can be defined as the progressive loss of substance from the operating surface of a body occurring as a result of relative motion at the surface [39]. In most cases, this wear is detrimental and leads to increased clearance between moving components, loss of precision and failure of component due to material loss. Wear can be caused by adhesion, abrasion, delamination, corrosion as well as by melting and a variety of other phenomena [40]. More

often, wear occurs with a combination of the above mentioned phenomena and hence the process of quantifying and understanding wear is complicated.

For wear to occur, the surface has to be deformed plastically for ductile materials or stress fields interact with above critical size defects / cracks to cause brittle failure. Plastic deformation of material can occur if it is suffers stress beyond its elastic limit. When two nominally plane surfaces are brought gently together, contact will initially occur only at a few points. As the load applied is increased, the surfaces move closer and a larger number of *asperities* on the two surfaces come into contact. These asperities are responsible for supporting the normal load on the surface and for generating any frictional forces which acts between them. The deformation caused to these asperities and to the surface can either elastic or plastic. Hertz (1881) studied an idealised case of single asperity (sphere) in contact with a flat surface (Figure 2.6) under a normal load w, generating a contact area of radius a which is given by the following equation [1].

$$a = \left(\frac{3wr}{4E'} \right)^{1/3} \qquad \textbf{2.4}$$

Where, r is the radius of the sphere and E' is an elastic modulus which depends on Young's moduli E'_1 and E'_2, and on the Poisson's ratios, ν_1 and ν_2, for the materials of the sphere and of the plane such that,

$$\frac{1}{E'} = \left(\frac{(1-\nu_1^2)}{E'_1} \right) + \left(\frac{1-\nu_2^2}{E'_2} \right) \qquad \textbf{2.5}$$

The area between the sphere and the plane is given by,

$$\pi a^2 = 0.83\pi \left(\frac{wr}{E'} \right)^{2/3} \qquad \textbf{2.6}$$

Since the deformation is purely elastic in this case, the area of contact is proportional to $w^{2/3}$. The normal stress distribution is as shown in Figure 2.6. The stress is not uniform over the circular area of contact, but is highest (3/2 times the mean pressure P_{mean}, which is given by $w/\pi a^2$) at the centre and reduces to zero at the edge.

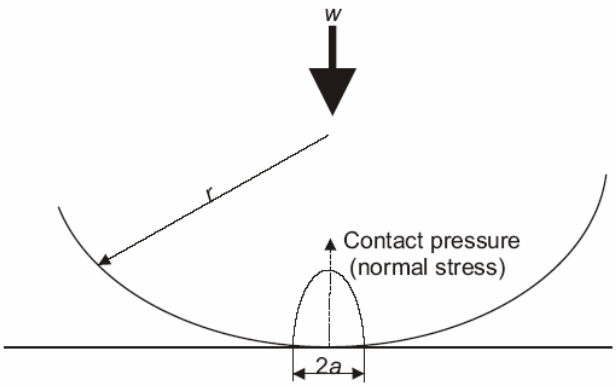

Figure 2.6: Distribution of normal stress (contact pressure) under a sphere elastically loaded against a plane [1].

If the normal load between the sphere and plane is increased, one or the other components start to deform plastically. Hertz analysis of the elastic stress field due to spherical indenter on a flat surface shows that the maximum shear stress beneath the indenter will occur at a depth of $0.47a$ for materials with ν of approximately 0.3. Plastic flow is assumed to first occur at this point when the Tresca yield criterion (peak pressure = $1.67Y$) is satisfied (where Y is uniaxial yield stress of the material). As the normal load is further increased, the zone of plastic deformation extends from beneath the indenter until it eventually reaches the surface. The mean pressure at this stage rises to about $3Y$ and remains nearly at the same value for the subsequent increase in load. Similar theory is used in case of a multiple asperity contact considering that for a perfectly plastic behaviour of the asperities area of contact is directly proportional to the applied load. Since the asperities are not of same radius and height, the surface irregularities are statistically distributed. Greenwood and Williamson [41] proposed the first statistical theories for contact of rough surfaces. This theory was derived for purely elastic contact, but it allows the onset of plastic flow at asperities to be predicted. It is found that the proportion of asperity contacts at which plastic flow occurs depends on the value of a plasticity index, ψ, given by

$$\psi = \frac{E'}{H}\left(\frac{\sigma^*}{r}\right)^{1/2} \qquad \textbf{2.7}$$

Where E' is defined by Equation 2.5, H is the indentation hardness of the surface (a measure of the plastic flow stress of the asperities), σ^* is the standard deviation of asperity heights and r is the radius of spherical asperity tips. A plasticity index of more than 1 would result in most asperities deforming and yielding plastically and ψ less than 0.6 would result in plastic flow at the asperities being caused only by extremely high normal pressures. Plasticity index depends on the ratio E'/H which is a material property and influences wear resistance of that material. Materials with a high H/E' ratio possess a long elastic strain to failure and thus can

tolerate substrate deformation. The ratio *H/E´* is a measure of the ability to absorb energy elastically and infers high resilience and toughness [42].

Oberle [43] defined "Modell" factor as the ratio of hardness (Brinell) to the elastic modulus of a material. He found that, in general wear decreases with an increase in the Modell value.

$$WR \propto \frac{1}{Modell} \qquad \textbf{2.8}$$

Modell factors for some of the materials tested by Oberle [43] are given in Table 2-1. Sintered WC is seen to have a relatively high Modell factor, hence it is considered for wear resistant application.

Table 2-1: Modell factors defined by Oberle [43]

Material	E x 10^8	Bhn	Modell Factor (H/E)
Grey Iron (hard)	15	500	33
Sintered WC-6Co composite	81	1650	20.3
Steel	29	600	21
Titanium	17.5	300	17
Chromium	36	125	3.5
Aluminium alloy	10	20	2
Lead	2	4	2
Tin	6	4	0.7

Abrasive wear is the damage occurring to a component surface due to the relative motion of hard particles trapped in the contact or harder asperities of the counterface material. The amount of material removed can be of great importance both when the removal is intentional, as in many finishing operations, and when it is unintentional, as in abrasive wear [44].

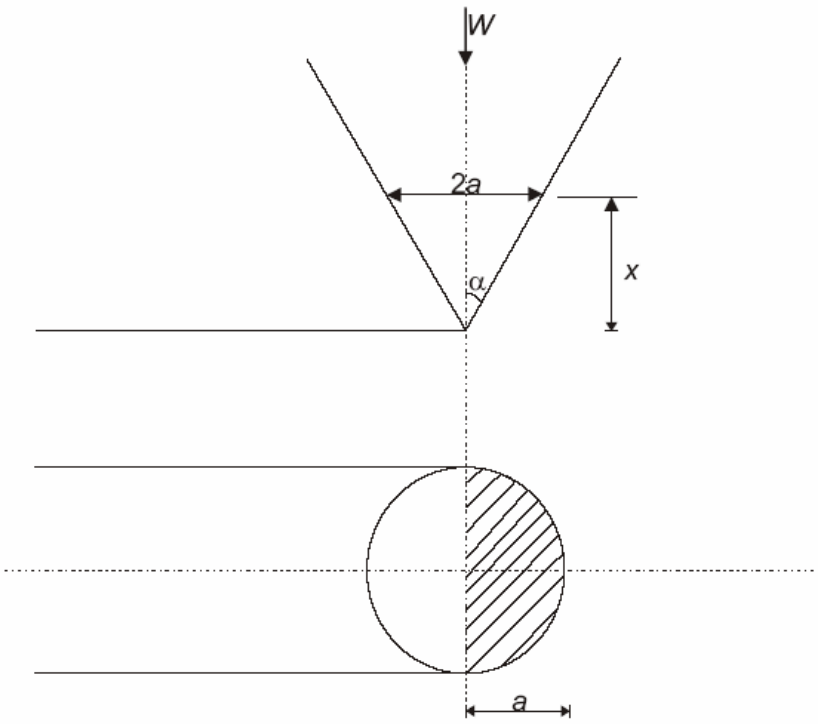

Figure 2.7: Geometry of contact between an idealised conical abrasive particle and a surface.

A simple model of abrasive wear involves the removal of material by plastic deformation. Figure 2.7 shows a conical abrasive particle of semiangle α, being dragged across the surface of a ductile material which flows under an indentation pressure P. It forms a groove in the material and wear is assumed to occur by the removal of some proportion of the material which is displaced by the particle from the groove. The normal load w carried by the particle is supported by the plastic flow underneath the particle, which causes a pressure P to act over the area of contact between the particle and the surface. Since the cone is moving, it is in contact only over its front surface,

$$w = P\frac{\pi a^2}{2} = \frac{1}{2}P\pi x^2 \tan^2\alpha \qquad \textbf{2.9}$$

The volume of material displaced from the groove by sliding the cone by a distance l along the surface is $l\ a\ x$ or $l\ x^2\tan\alpha$. The quantities a and x are defined in Figure 2.7. If a fraction η^* of the material displaced from the groove is actually removed as wear debris, then the volume of wear debris produced by this one particle per unit sliding distance, q, will be given by

$$q = \frac{2\eta^* \ w}{\pi P \tan\alpha} \qquad \textbf{2.10}$$

Summing over many abrasive particles, and assuming that $P = H$, the indentation hardness of the material, it can be shown that the total volume removed per unit sliding distance Q is given by,

$$Q = \frac{V}{L} = \frac{KW}{H} \qquad \textbf{2.11}$$

Where W is the total applied normal load and K is a constant known as dimensionless wear coefficient. This equation is exactly same as the Archard's [45] equation, which was originally derived for sliding wear of metals. Archard's wear equation states that the wear rate Q in any contact is directly proportional to the load applied W and inversely proportional to the surface hardness of the wearing material H. Since the knowledge of the dimensionless wear coefficient and the hardness of the top layer of the surface may not be known with certainty, a more useful term is defined by taking the ratio K/H, which is known as the *specific wear rate (κ, SWR)* with the units of $m^3N^{-1}m^{-1}$ and represents wear volume (m^3) per unit sliding distance (m) per unit normal load (N). The modified Archard's wear equation is given by

$$\kappa = \frac{V}{WL} = \frac{K}{H} \qquad \textbf{2.12}$$

Where, V is the wear volume in m^3, W is the applied load in N, L is the sliding distance, K is the dimensionless wear coefficient and H is the hardness of the material.

It has been shown experimentally that the loss of material is proportional to the sliding distance except for short tests where the non-linear running-in periods are significant. However, proportionality between wear rates and normal loads is found less often. Abrupt transitions from low to high wear rates and sometimes back again are often found with increase in load. This is due to the transition between wear mechanisms observed with change in applied loads. Also, no mention has been made of the velocity of sliding or the apparent area of contact in the Equation 2.12, suggesting that the wear rate Q should be independent of these factors.

For the brittle materials, abrasive wear occurs by brittle fracture. If a brittle material is indented at sufficiently high loads by a blunt abrasive particle and the contact stresses remain elastic, then a Hertzian cone crack is formed, see Figure 2.8a. Multiple indentation by blunt abrasives result in the intersection of these incomplete conical cracks which can lead to material removal. However, if the abrasive is sharp and angular, it will result in local plastic deformation at the point of contact resulting in the development of cracks which can lead to immediate wear as shown in Figure 2.8b. These are entirely different from the Hertzian cone

cracks developed due to elastic stress fields under a blunt indenter. The intense high local stresses caused by the sharp indentation are relieved by local plastic flow resulting in a median vent crack at a critical value of applied load. Relaxation of the applied load causes the formation and growth of lateral vent cracks which are driven by residual elastic stresses developed by the relaxation of deformed material around the contact. These lateral cracks curve towards the surface causing wear. Lateral cracks develop only when the applied load exceeds a critical value which depends on the ratio of fracture toughness (plane stain fracture toughness for thick specimen, K_{Ic}) to hardness (H) of the brittle material. Hence, having very high hardness may result in lowering of the load required to initiate lateral cracks. The small scale of carbides may modify the cracks system seen in brittle carbide grains.

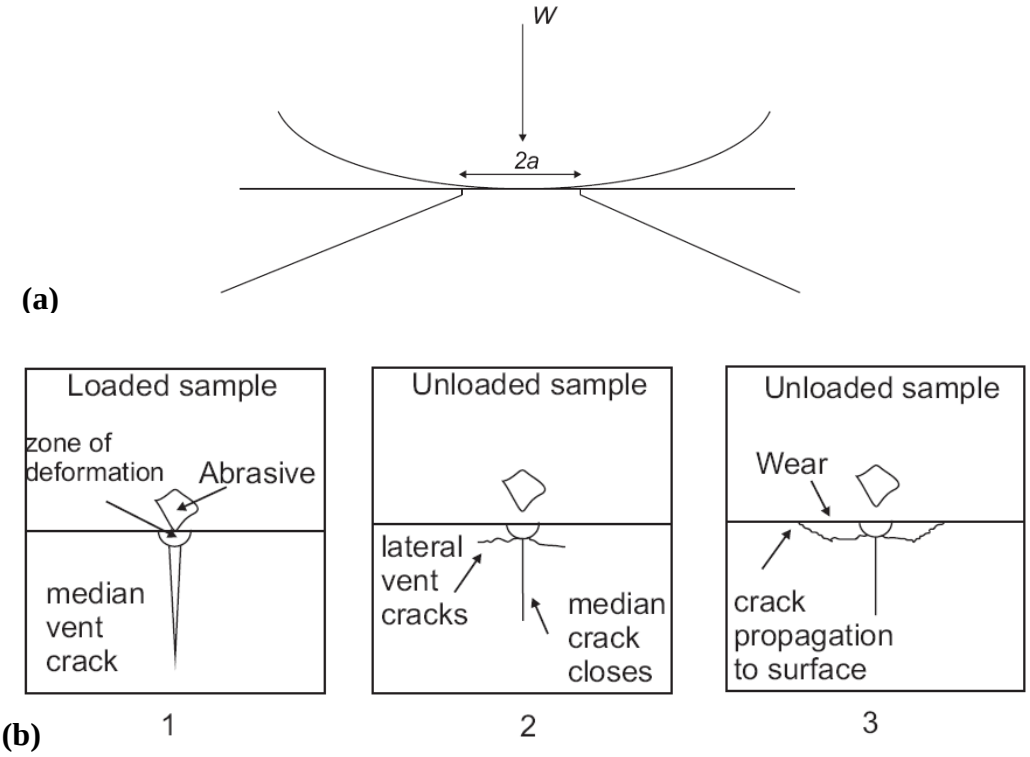

Figure 2.8: (a) Hertzian cone crack formation in a brittle material with a blunt abrasive and (b) crack formation in a brittle material due to point indentation.

2.2.2 Classification of abrasive wear

Abrasive wear is one of the most prevalent causes of wear. The hard particles present in the contact could be due to the outside environment or due to other processes occurring

simultaneously like corrosion. As discussed in the previous section, the mechanism for abrasive wear can involve both plastic flow and brittle fracture and often both occur together. Abrasive wear can be classified as two-body (grooving) and three-body (rolling) abrasive wear as illustrated in Figure 2.9 [1]. The origin of these terms comes from system analysis [46] of wear. Two-body abrasive wear is caused when hard particles are embedded in the counterface and cause a grooving type of wear scar on the surface of the 1st body. In three-body wear, the hard particles roll between the two surfaces and produce a wear scar that does not appear directional and is less severe [47] as compared to the two-body wear. An example of two-body wear is a drill bit cutting through rocks and grit particles entrained between sliding surfaces can be considered as an example of three-body wear.

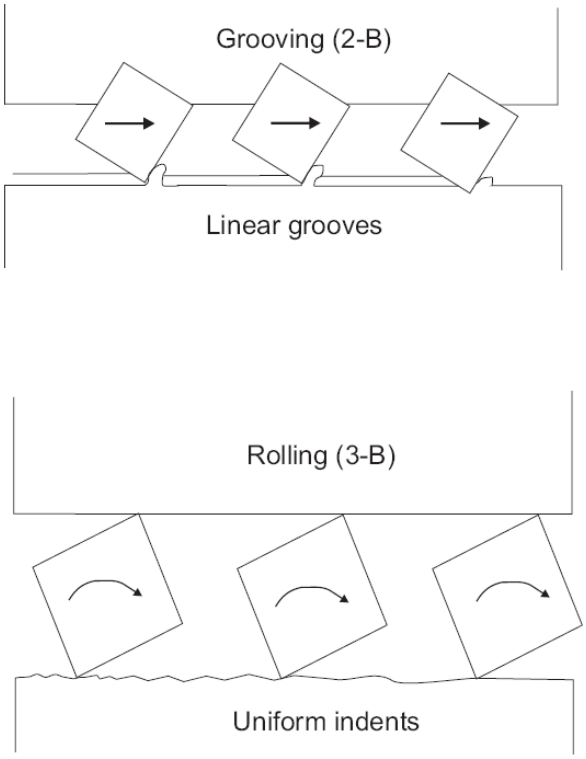

Figure 2.9: Two-body and three-body abrasion [1].

Abrasive wear can easily be classified as either two-body or three-body depending on the type of wear scar obtained. There have been many attempts [48-51]at providing a model to understand the transition between two-body and three body wear. Gates [51] questioned the use of 2-body and 3-body to define grooving and rolling abrasion respectively. The critical issue with using the term three-body was that it leads to the presumption that the wear process consisted of three bodies, while three-body wear could easily occur even in the absence of the 'third body'. In their paper on transitions between two-body and three-body abrasive wear, Trezona *et al.* [52] stated that the current use of the terms two-body and three-

body is mechanistic, describing the behaviour of particles in a wear contact, rather than the situation, as in case of system analysis. They redefined the terms as follows:

Grooving abrasive wear (2-body):

> "An abrasive wear process in which effectively the same region of the abrasive particle or asperity is in contact with the wearing surface throughout the process. Wear surfaces produced by grooving abrasion are characterised by grooves parallel to the direction of sliding".

Rolling abrasive wear (3-body):

> "An abrasive wear process in which the region of the abrasive particle in contact with the wearing surface is continually changing. Wear surfaces produced by rolling abrasion are characterised by a heavily deformed, multiply indented appearance and little or no directionality."

Figure 2.10 shows the typical surface features observed during rolling and grooving abrasive wear.

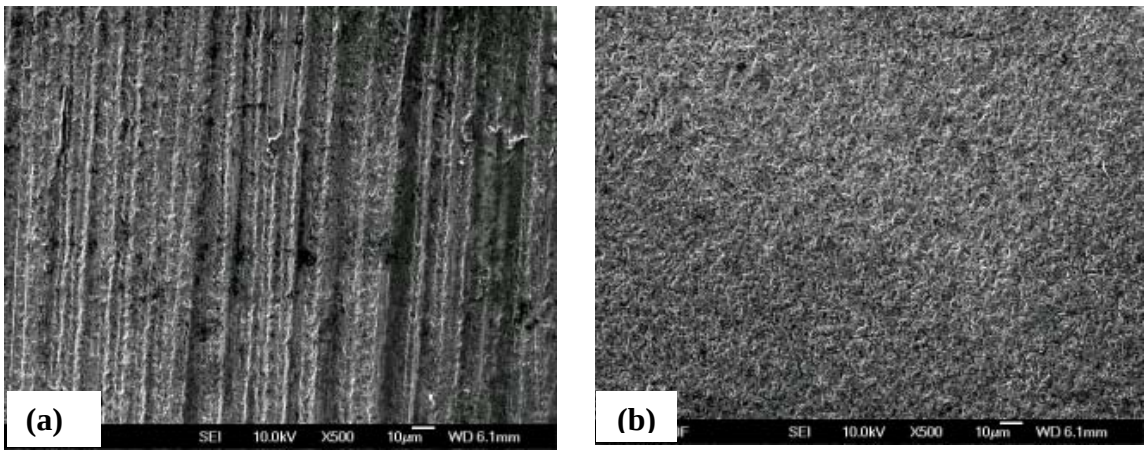

Figure 2.10: Micro-abrasion wear scar on a SS316 stainless steel showing (a) unidirectional grooving abrasive wear features and (b) uniformly indented surface typical of rolling abrasive wear.

2.2.3 Wear models and parameters influencing abrasive wear

Wear models have been used to predict the mechanism of wear under a given condition of load, abrasive particle size/concentration and other related factors. Models have also been developed which predict wear rate for specific wear mechanisms occurring [53]. One of the first attempts to predict the wear modes in sliding contact has been conducted by Williams *et al.* [48]. The Williams model, considers the ratio of largest abrasive particle size (*D)* and minimum lubricant film thickness (h^*) to predict the transition between rolling (3-B) to grooving (2-B) abrasion. This model predicts that the transition between rolling to grooving depends on the equilibrium condition of a particle in a contact, which depends on the D/h^* ratio, the hardness of the two surfaces in contact and the angle of the particle (β) (Figure 2.11). Since, in this case the experiments were performed on lubricated bearings it is

considered that the substantial part of the normal load on the bearing is carried by the hydrodynamic pressure in the fluid, irrespective of any abrasives. The particles roll or tumble through the gap associated with occasional indentation producing a characteristic pitted surface which shows little directionality. For this low wear regime to occur, the D/h^* ratio is roughly equal to 2.

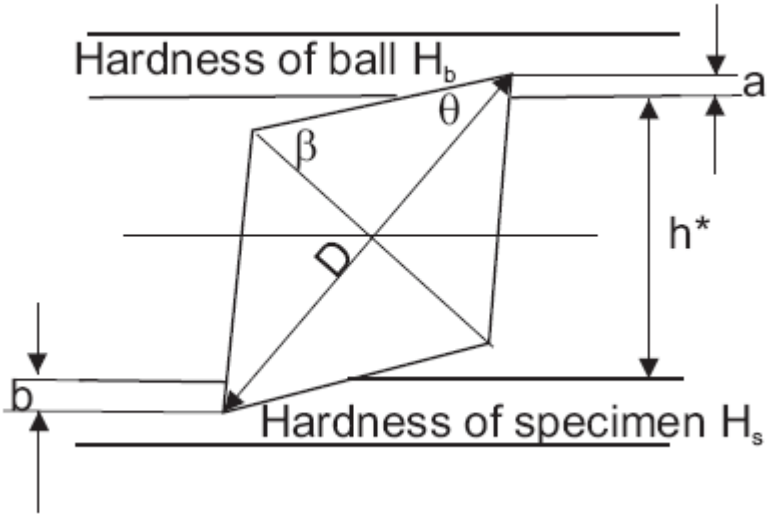

Figure 2.11: Idealised two-dimensional model by Williams *et al.* [48].

At a critical stage the mode of surface damage changes to a mechanism characterised by grooving of either or both the solids. In this case, the hardness of the two solids is of some significance. If the hardness is similar, there will be evidence of grooving on both the surfaces while if there is a significant difference in the hardness of the two solids, hard particles are likely to get embedded in the softer surface thereby causing considerable damage to the harder surface.

This model was further developed and applied in micro-abrasion test by Adachi and Hutchings [49]. It has been reported previously that the dominant wear modes in micro-abrasion tests are influenced by applied load, volume fraction of abrasives in the slurry, abrasive material [52], material of both ball and specimen [54] and the surface condition of the ball [47]. Considering the various factors involved in predicting the transition, Adachi and Hutchings derived a critical condition for transition from rolling to grooving motion at a certain value of (D/h^*). This was expressed in terms of a dimensionless expression group $(W/Av H')$. This dimensionless group contains all quantities which can be measured experimentally and is termed as the *'severity of contact'*. Thus, the condition of transition from rolling to grooving can be written as:

$$S = \frac{W}{H'Av} \leq \phi \left(\frac{H_s}{H_b} \right)^{\zeta} \qquad \textbf{2.13}$$

Where W is the applied load, A is the interaction area considering a Hertzian point contact and including a particle size term, v is volume fraction of abrasive in the slurry, H_s and H_b the hardness of the specimen and ball respectively and α, β are constants. The severity of contact attempts to calculate the load acting on each particle in the contact. Based on static analysis, they plotted a '*wear mode map*' as a function of severity of contact S and the hardness ratio between the specimen and the ball (H_s/H_b). They predicted that the transition from rolling to grooving would occur at a critical value of S defined by the Equation 2.13 with $\phi = 0.0076$ and $\zeta = -0.49$. Among the different models discussed, the Adachi-Hutchings model has proven to be the most successful in predicting the nature of wear (rolling or grooving). However, there are certain limitations of this model as it ignores the abrasive particle hardness and can not be applied to contact geometries other than the ball on flat surface. It is also a static analysis and does not include entrainment terms or sliding velocity or particle fragmentation within the contact. It also ignores the surface energy effects of ball, abrasives and the sample.

As discussed earlier, the Williams model considers the case of a lubricated bearing with the hydrodynamic pressure in the fluid carrying the load. Shipway [55] in his model considers a situation in which the load is carried by the abrasive particles, which may be the case in some contacts. He considers the effect of the turning moment along with the D/h^* ratio, as a critical condition for transition from rolling to grooving abrasion which depends on the dimensions of the particle and the applied load. This work concluded that particle sliding will tend to be promoted by high loads, a large hardness difference between the two surfaces and by particles with high aspect ratios. However, the success of this model is largely dependent on the assumption that the shape of all the abrasives entrained is exactly the same (parallelogram) and it ignores the forces acting in the z axis (perpendicular to the plane of motion). As these papers show, the present level of understanding on particle behaviour in the contact is very limited and as seen from the models discussed the dependence on parameters such as the particle shape and angle which are difficult to measure and control, the ability to predict abrasion is also limited. In general, abrasive wear is influenced by more easily measurable parameters such as load, sliding distances, sliding velocities, hardness of the materials used as well parameters associated with hard particles such as their hardness, abrasivity, size and shape. Not many models look at changing geometry, size and surface roughness with time or sliding distance.

Previous work has studied the influence of abrasive properties on wear rates. A particle is usually defined as abrasive when it can cause rapid or efficient abrasive wear [56]. It has also been experimentally observed that plastic scratching will occur if the ratio of the hardness of abrasive to that of the sample (H_a/H_s) is greater than 1.2 (Figure 2.12) [57]. This is due to the fact that for a spherical particle pressed against a flat surface, the maximum contact pressure is about 0.8 times the indentation hardness of the particle material. The observation that a certain minimum ratio of hardness is needed for one material to be able to scratch another provides the basis of scale of hardness devised by the Austrian mineralogist Mohr in 1824. He assigned integer hardness numbers to a sequence of ten minerals, each of which would scratch all those below it in the scale. The scale is as shown in the Table.2-2. Silica (quartz) is the most commonly occurring natural abrasive contaminant, constituting about 60% of Earth's crust and has a hardness of about 750-1200 kgf mm^{-2} (i.e. 750-1200 HV). Considering the fact that most steels will have hardness lower than 1.2 times the hardness of silica, most steels and non-ferrous metals will be vulnerable to abrasive wear. One of the basic approaches to improve abrasive wear resistance is to consider the use of materials which have higher hardness than silica abrasives. Hence WC-based hardmetals which have a hardness of 1500 HV are commonly used for wear resistant applications.

Table 2-2: Mohs scale of hardness [1]

Mohs Number	**Mineral**	**Indentation Hardness (kg mm^{-2})**
1	Talc	40-60
2	Gypsum	70-80
3	Calcite	90-120
4	Fluorite	180-190
5	Apatite	300-600
6	Orthoclase	500-650
7	Quartz	750-1200
8	Topaz	900-1400
9	Corundum	1800-2000
10	Diamond	6000-10000

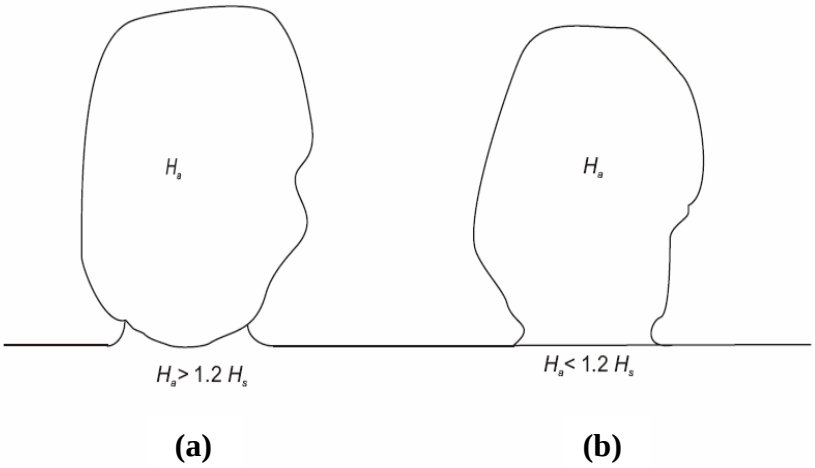

Figure 2.12: Contact between a grit particle under normal load and a plane surface; (a) if H_a is greater than ~1.2H_s, the particle will indent the surface and (b) if H_a is less than H_b, plastic flow will occur in the particle, which will be blunted [1].

Another factor influencing wear rate is the angularity of the abrasive particles used [58-60]. Qualitative descriptions of particle visual appearance, such as "rounded", "semi-angular" or "angular", have been used to classify and differentiate between various groups of abrasive particles. One of the simplest descriptions of shape is based on measurements of perimeter and area of a two-dimensional projection of the particle, usually generated by optical microscopy. *Roundness factor F* can be defined as the ratio between the actual area of the projection, Γ and the area of a circle with the same perimeter Λ as the projection as shown in Figure 2.13.

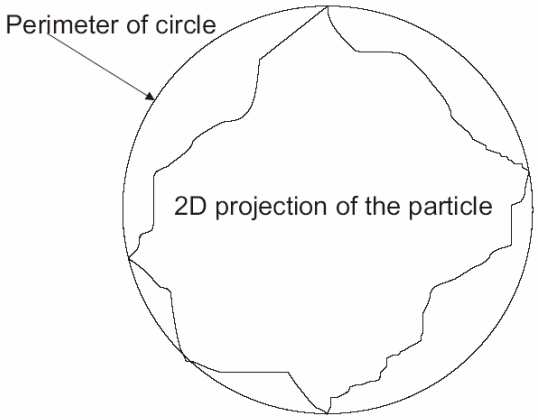

Figure 2.13: Projection of particle for calculating Roundness factor F.

Roundness factor can be given by the following equation [1]

$$F = \frac{4\pi\Gamma}{\Lambda^2} \qquad \textbf{2.14}$$

Stachowiak and Batchelor [56] found that the abrasivity of abradants reduces as they become more rounded. Hence a higher roundness factor is likely to result in lowering of the abrasivity of the abrasive particles.

Abrasive particles responsible for most abrasive wear are between 5 and 500 μm in size, although the process of gouging wear may involve particles of much larger size [1]. Misra and Finnie [61] compared and contrasted the different theories explaining the effect of abradants size on the wear rates obtained.

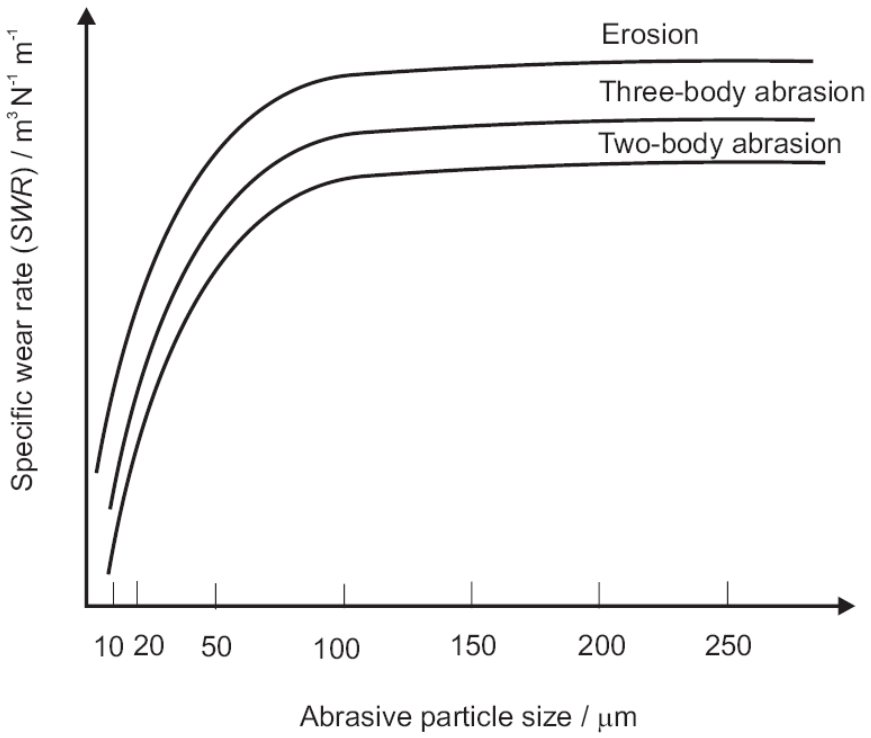

Figure 2.14: Typical wear rate trends observed with change in abrasive size for ductile materials [56, 61].

The general trend of *SWR* observed with increasing abrasive size for ductile materials is shown in Figure 2.14. Comparing the results obtained from erosion, grooving and rolling mode of abrasion, they observed that wear rates for SiC particles smaller than about 100 μm dropped markedly with decreasing particle size. Above 100 μm particle size, there was a steady increase in wear rates till about 250 μm. Stachowiak and Batchelor [56] found similar results when they studied the effect of increasing abrasive size on the wear rates for ductile materials such as AISI 1096 steel and Ni. One of the earliest explanations for the size effect

is the hard ("*debris"*) layer model, first proposed by Kramer and Demer [62] which suggests that a surface layer of 50-100 μm thickness becomes work hardened. Thus, increased abrasion resistance is offered to small particles or abradants due to the debris layer compared to larger particles which also deform the material below the debris layer and can abrade material due to plastic deformation. Moore and Douthwaite [63] suggested the theory of strain distribution near the surface creating a hardened layer of around 10 μm at the surface. Because of this hardness gradient, small particles will not be able to cause as much damage as the large particles which will be large enough to penetrate the hard layer and deform the material plastically. However, the models discussed in the literature can only be applied for ductile materials and not for composite materials with hard brittle phase embedded in a soft ductile binder.

Stachowiak *et al.* [64] found that smaller particles with more angular features could cause more wear than larger particles which were more rounded and hence it is difficult to rank the parameters of abrasive size and shape with respect to their effect on the wear rates obtained. Another property of the abrasive which is likely to affect abrasion rates is the crush strength of the abrasives. If the abrasives are very brittle they are likely to break up into fine particles and thus minimise wear [65]. If the abrasive is very tough, it may not fracture into smaller, sharper fragments and lead to rounding off of its sharp edges over the period of time thus become less efficient. Clearly, work needs to be done in comparing the wear rates obtained by different size of the same abrasive, keeping the other parameters such as applied load and abrasive concentration constant.

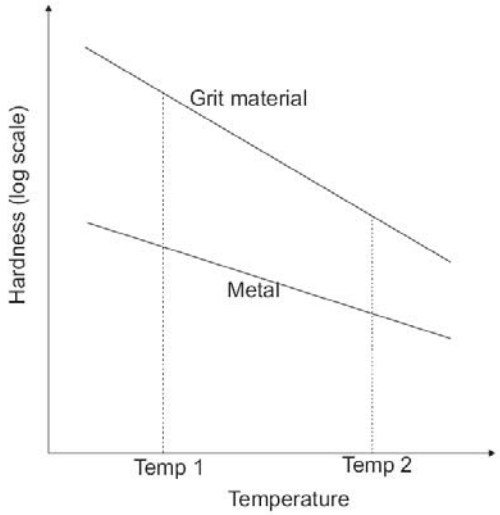

Figure 2.15: Temperature effects on abrasion under uniformly hot conditions [56].

The effects of temperature on abrasive wear can be due to the influence of ambient temperature or due to temperature rise induced by plastic deformation of worn material [56].

Due to experimental difficulties the effects of ambient temperatures have not been extensively studied. However, it is known that with an increase in the temperature, the hardness of both worn material and the abrasive grit is expected to decline, see Figure 2.15. The temperature increase due to localised hearing caused by friction during plastic deformation (during abrasion) is associated with high grit speed [66]. In such cases, if the abrasive particles remain relatively cool during the process of abrasion it would also maintain its hardness while the worn metal would soften, causing an increase in wear. Thus at higher grit speed, a relatively softer abrasive will abrade harder materials significantly. This effect was observed by Wing [66] in his study of abrasion of steel by relatively soft coal. Another effect of an increase in the temperature is the increase in the rates of corrosion reactions at the surface of the sample which can influence the wear-corrosion synergy. The effects of wear-corrosion synergy on the abrasive wear process will be discussed later in this chapter.

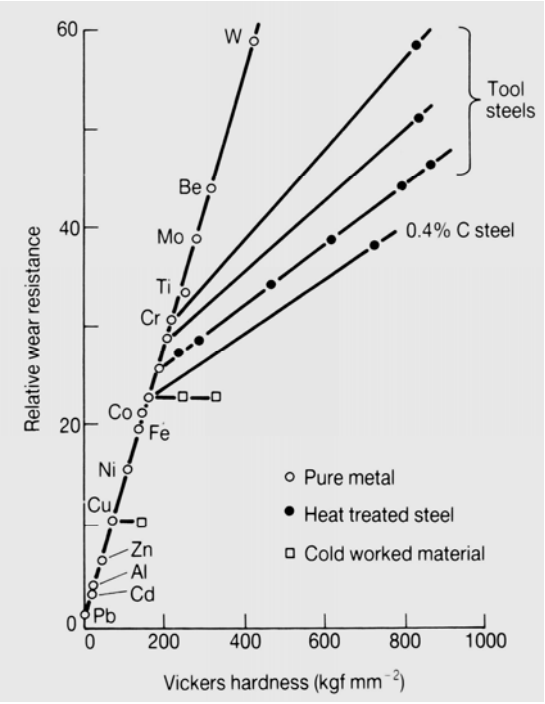

Figure 2.16: Relative wear resistance (proportional to 1/wear rate) for pure metals and heat treated steels under conditions of grooving abrasion [1].

Figure 2.16 compares the abrasive wear resistance (grooving) of some pure metals with heat treated and cold worked steels. Tungsten metal shows high wear resistance, similar to that of tool steels. Among the commonly used metallic binders for WC-based hardmetals, the abrasive wear resistance of Cr was found to be highest followed by Co and Ni.

2.2.4 Wear of WC-based sintered hardmetals and coatings

The abrasive wear of sintered WC occurs by a combination of plastic grooving, binder phase extrusion and fracture of WC grains [67]. Axén and Jacobson [68] introduced a model for the upper and lower limits of the wear resistance of composites. They introduced the concept of equal wear (EW) of the phases and equal pressure (EP) on the phases. EW mode of wear implies that the hard and soft phases in the composite are worn in the same rate and hence in this mode, the hard phase offer maximum protection to the softer phase and result in minimum wear. In EP mode of wear, equal pressure is exerted on the hard as well as the soft phases and as a result, preferential removal of the softer phase occurs since it has a lower wear rate. In the EP mode, the reinforcement phase particles provide minimum protection and are only able to take load in proportion to the area they cover. In this mode of equal pressure of the phases, the wear rate is substantially higher than in the EW mode of wear. The two modes of wear are shown schematically in Figure 2.17. However, as observed by Larsen-Basse [13], in real environments, combinations of wear mechanisms are observed.

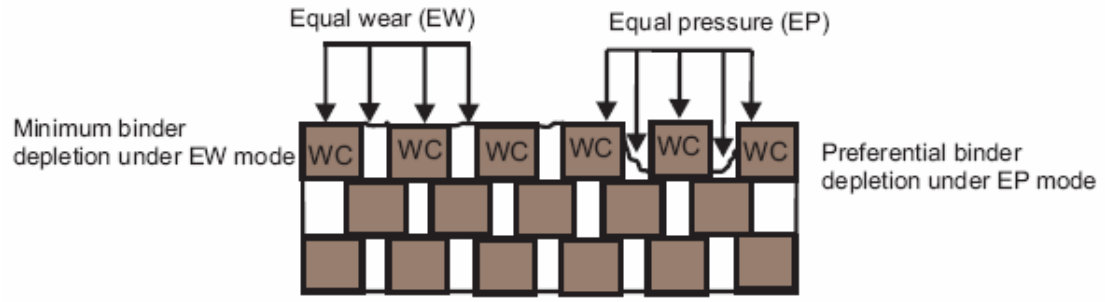

Figure 2.17: Schematic showing the Axén and Jacobson's model of wear of WC-based hardmetals.

Bailey *et al* [69] studied the wear exhibited by WC-Co composites and found that wear occurred by a combination of binder extrusion and nucleation of cracks in the skeletal carbide structure due to direct impingement of abrasives. Similarly, Larsen-Basse *et al* [70] found that wear occurred by a combination of binder depletion and by gross fracture of the carbide skeleton. Clearly, wear of WC-based hardmetals closely follows the equal pressure (EP) mode predicted by Axén and Jacobson. During abrasive wear by micro-scale abrasives (abrasives similar in size as the carbide grains), removal of the binder-phase occurs by 2-B grooving or 3-B indentation of the binder-phase as observed during micro-abrasion of sintered WC-Co [71, 72]. The preferential removal of the binder using micro-scale abrasives is shown schematically in Figure 2.18a.

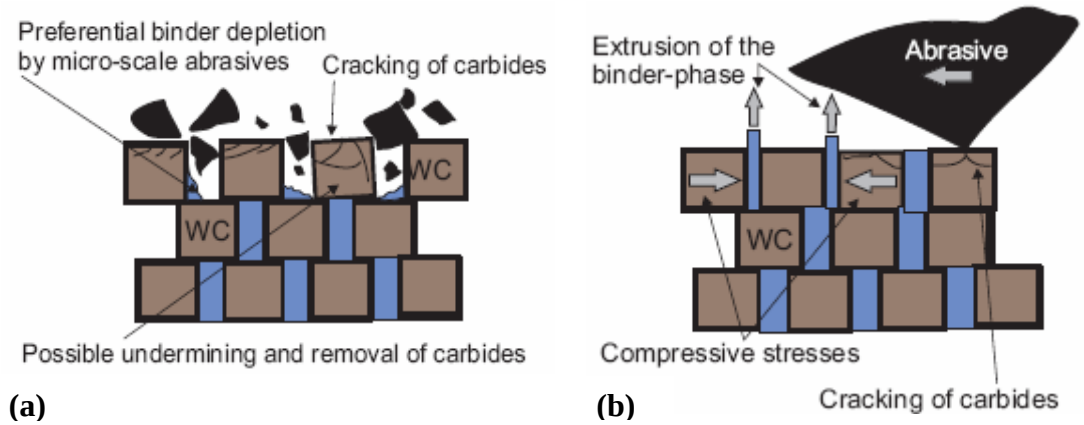

Figure 2.18: Preferential removal of the binder-phase from the surface of sintered WC-based hardmetals using; (a) abrasives smaller than the carbides and (b) abrasives larger than the carbides.

Preferential removal of the binder-phase by an extrusion mechanism was observed by Larsen-Basse [13] during a survey of wear mechanisms observed during rock drilling. The same author studied the extrusion of the binder-phase in sliding wear of WC-Co composites [73] and proposed an empirical relationship for the amount of binder extruded during wear by hard particles. The binder-phase was found to be 'squeezed' out by compressive stresses induced due to deformation as shown in Figure 2.18. The amount of binder-phase extruded was found to be directly proportional to the induced strain and the carbide size and inversely proportional to the binder mean free path.

In a further study comparing the similarities in the mechanisms of wear of WC-Co tools in rock and metal cutting, Blombery *et al.* [74, 75] observed that the influence of binder removal on the wear of WC-Co is more damaging than the simple depletion of the binder leading to the pull-out of carbide grains. Comparing a sequence of SEM micrographs of abrasion of WC-Co samples with sandstone they found that removal of small amounts of binder from between the carbide grains at the surface results in a lowering of activation energy for propagation of intergranular surface cracks which accelerates the wear. Similar observation was made by Gee *et al.* [76] when they compared wear scars on WC-Co hardmetals from different tests. They proposed that formation of lateral cracks on the surface of WC grains was a mechanism of relieving the plastic strain accumulated due to depletion and extrusion of the binder around them. This was further confirmed by Klassen and Kubarsepp [77] by the study of XRD patterns of worn and unworn carbide surfaces to detect strain. They suggested that the failure of carbide grains during abrasive and erosive wear is preceded by plastic strain of the carbide phase. Gee *et al.* [78] studied the stepwise erosive wear of WC-based hardmetals and proposed that the removal of material from the surface occurs by the following steps:

- Removal of binder from the surface by plastic deformation or grooving
- Accumulation of plastic strain in WC grains
- Fracture and fragmentation of individual WC grains
- Cracking between WC grains
- Breaking away of unsupported WC grains

Abrasive wear resistance of WC-based hardmetals is found to increase with an increase in the hardness [67, 76, 79]. Jia *et al.*[80, 81] also studied the sliding wear and abrasion resistance of nanostructured WC-based hardmetals and found that the higher wear resistance offered by the nanostructured WC-based hardmetals was due to its high hardness (i.e. its ability to resist penetration of abrasives) and due to small WC grain size which lowered its tendency to fracture. The same authors.[21] compared the hardness and fracture toughness of WC-based hardmetals and found that for conventional grades of hardmetals, the hardness was inversely proportional to the fracture toughness (see Figure 2.2). Despite higher hardness, the fracture toughness of nanostructured hardmetals was comparable to the conventional hardmetals with high hardness. However, the wear resistance of WC-based hardmetals was found to be directly proportional to their fracture toughness during sliding wear [82] and erosive wear [83].

Attempts have been made to study the 'scaling effect' of abrasives on the erosive wear of WC-Co hardmetals by Anand and Conrad [84] by varying the size of Al_2O_3 abradant during single impact erosion tests. They proposed that the erosive wear mechanisms for cemented carbides depend on the size of the damage (as estimated from SEM micrographs) in relation to the microstructure. For "small" impact areas (less than 10 WC grains) the erosion mode was found to be the brittle type, and resulted in the cracking of carbides. For impacts areas involving more than 100 WC grains, the erosion was found to be ductile type and resulted in the gross plastic deformation of the surface. Impact tests using large abrasives also resulted in their extensive fragmentation. However, this work does not look at the influence of abrasives which are of the same size as the carbide grains. The single particle impact relied on the formation of a crater on the surface and was not able to investigate the effect of abrasives smaller than 50 μm (limiting particle size for producing an impact crater). However, as shown by the stepwise erosion of WC-Co by Gee *et al.* [78], the damage of sintered hardmetals occurs progressively and may not be replicated by the single particle impacts.

Although the parameters governing the wear performance of WC-based sprayed coatings should ideally be similar to sintered hardmetals, this is not the case since the ductile binder in

the sintered material has been replaced by a relatively brittle, inhomogeneous binder phase in the HVOF-sprayed coating [30]. As observed for sintered hardmetals, the abrasive wear of WC-based coatings using abrasives similar in size to the carbide grains occurs by the preferential removal of the binder phase by rolling and grooving mode of abrasion [71, 85, 86]. Removal of the binder-phase around the carbides leads to the pull-out of carbides as they are undermined. The preferential removal of the binder-phase is easier in WC-based coatings due to the presence of distinct binder-rich regions and the uneven distribution of the carbide-phase. No evidence of sub-surface damage is reported in the literature during the micro-scale abrasion of WC-Co based coating (abrasives similar in size as the carbides) [71].

Abrasive wear using abrasives larger than the carbide grains result in the damage of the coating by the combination of plastic grooving and sub-surface cracking of the coating. As shown in the Figure 2.19, abrasive wear by an abrasive particle larger than the carbide grains results in ploughing of the binder-phase and fragmentation of carbides present within the grooves [87]. The indentation-induced sub-surface cracking develops in the coating by the formation of lateral cracks and median cracks underneath the plastic zone [88-91]. The sub-surface cracks in the coating propagate through the tungsten-rich binder phase present along the splat boundary and lead to the delamination of discrete sections of the coating as shown in Figure 2.19.

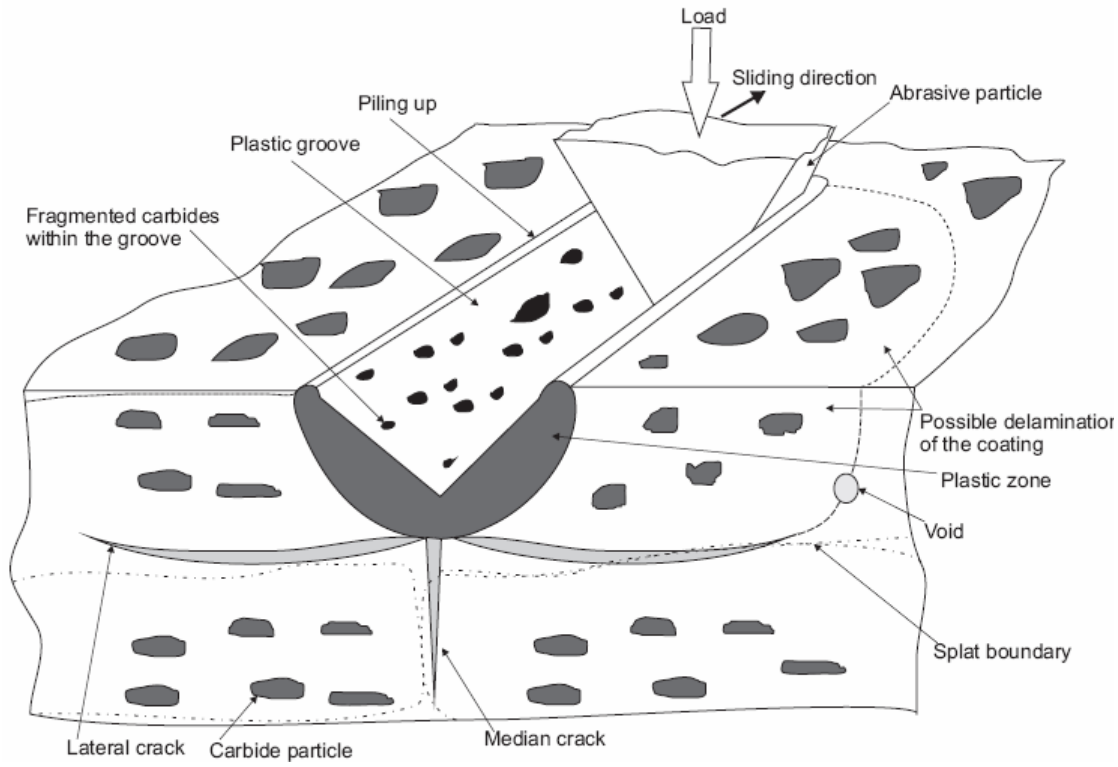

Figure 2.19: Schematic view of brittle fracture of the WC-Co coating during abrasive wear (adapted from [89]).

Similar wear mechanism has been observed during the erosion of WC-based sprayed coatings [92]. Wood *et al.* [27] investigated the erosion performance of WC-10Co-4Cr coating and proposed two mechanisms depending on the angle of impact and energy of the erodent. At low impact angle and particle energy, micro-cutting and ploughing of the binder-phase resulted in the embedded carbide particles being exposed. Subsequent erosion led to the gouging of the carbides as they were undermined. At high impact angle and higher kinetic energies, development and propagation of sub-surface cracks lead to the removal of large sections of the coating. Clearly, wear of WC-based coatings due sub-surface cracking and delamination is strongly dependent on its fracture toughness [92, 93]. As discussed in Section 2.1.2, lowering of fracture toughness occurs by the dissolution of metallic W in the binder-phase. Hence, unlike the sintered hardmetals, use of nanostructured carbide particles does not result in the improvement in wear resistance for WC-based coatings [94, 95].

2.2.5 Wear testing

There are many types of wear tests and the choice of these tests is governed by the type of wear and the situation in which wear occurs. Some are aimed at evaluating a material's response to a specific type of wear, such as solid–particle erosion, sliding wear or two-body abrasive wear while others are designed to simulate a particular field application in order to screen materials, surface treatments, or lubricants for that type of service. Some of them which are termed as *standard wear tests* are intended to be used for fundamental research of wear. Standard wear test methods have been used for all of these reasons, but like any type of wear test, standard test methods have both strengths and limitations [96]. At times, to get the desired test set up for a particular situation, a standard test needs to be modified. In this project, the basic requirement for selection of a test was the ability to replicate the wear-corrosion mechanisms observed in downhole components. Classification of abrasives as macro-scale and micro-scale as discussed earlier, was used to identify wear tests for micro-scale and macro-scale testing of hardmetals. The ASTM G65 can be used for abrasion with a wide range of abrasive sizes between 20 μm and 600 μm and hence can be effectively used to study the macro-scale abrasion of WC-based hardmetals i.e. with abrasives which are 20-200 times larger than the carbide grains. The micro-scale abrasion test, as the name implies, uses micro-scale (less than 10 μm in size) abrasives and can be effectively used to study the micro-scale abrasion occurring at the carbide scale of composite materials which are strongly influenced by microstructural details / changes.

2.2.5.1 ASTM G65 test

The test set-up of the ASTM G65 test is shown in Figure 2.20. The test uses a rubber rimmed wheel (low-stress) or steel wheel (high stress) as the counterface material depending on the field conditions being replicated, while the abrasives are fed between the wheel and the sample from a hopper by a nozzle. The sample is pressed against the wheel by a dead weight loaded lever. The test is run for a set period and the wear is measured by calculating the volume of material lost through weight loss and density measurements. Generally, Ottawa sand (AFS 50-70 test sand) of 200 μm in size is used as abrasives for this test.

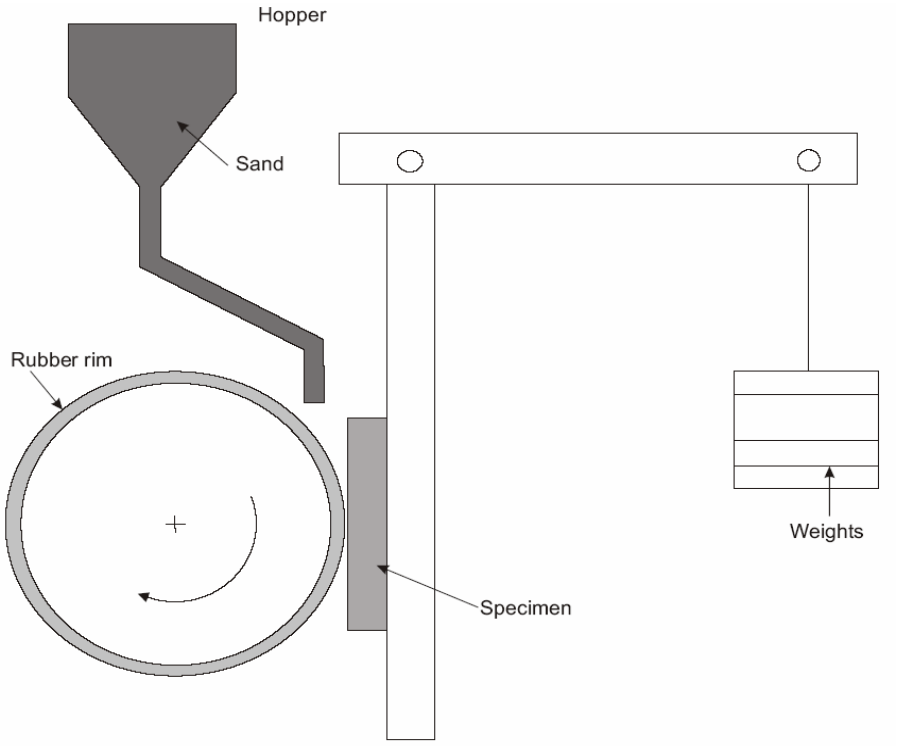

Figure 2.20: ASTM G65 test system.

The abrasive flow rate used is 300-400 g min^{-1} with a test load of either 20 N or 120 N. The speed of rotation for the wheel is usually 228 rpm (0.86 m s^{-1}) [3]. A useful modification to this test involves placing the specimen on top of the wheel and feeding the abrasive, under controlled conditions, to the rising upper side of the wheel [97]. This modification allows the test to be used with liquid slurries and gives more consistent results by controlling the amount of abrasives entrained throughout the test. This test is generally used to evaluate materials by rolling abrasion. Examination of worn samples along with the mass loss measurement provides an understanding of the wear mechanism.

2.2.5.2 Micro-abrasion test

The micro-abrasion test was developed by Rutherford and Hutchings [98] and it produces an imposed spherical capped wear scar on the sample. A ball, clamped between coaxial shafts is rotated while in contact with a stationary sample with a continuous feed of abrasive slurry being drawn into the contact. The arm holding the sample is pivoted and a load can be applied as shown in the Figure 2.21. The resulting wear scar has a spherical cap geometry and the diameter of the cap is measured to calculate the wear volume. The wear volume may

be calculated from the crater dimensions (i.e., surface chordial diameter *b* or depth *h*) (see Equation 2.15 and Equation 2.16).

2.15

$$V = \frac{\pi b^4}{64R'} \qquad \text{for b} << \text{R}'$$

2.16

$$V = \pi h^2 R' \qquad \text{for h} << \text{R}'$$

Where, V is the wear volume and R' is the radius of the ball being used. *SWR* is calculated using Archard's equation, see Equation 2.12

The micro-abrasion tester is well researched and is known to produce repeatable and reproducible results. Factors which affect the wear rate and wear mechanism (i.e. rolling or grooving) are the applied load [99], abrasive slurry concentration [52] and the hardness and condition of the counterface [99]. Generally, an increase in load and a decrease in the abrasive slurry concentration results in grooving abrasion. It has also been observed that a rougher or softer (high H_s/H_b ratio) counterface (pitted ball) is also likely to result in grooving abrasion due to embedding of abrasives in the ball [47]. Although this test is capable of producing both rolling and grooving abrasion, rolling abrasive wear is the preferred due to its repeatability. This is due to the fact that test conditions used to produce grooving abrasion are also likely to hamper consistent particle entrainment, often resulting in ridging [100] and non-circular wear scars. The major disadvantage of this apparatus is its inability to entrain abrasives larger 10 μm in size, however it has been demonstrated that by increasing the size of the ball and using the 'floating ball' apparatus, larger abrasives (up to 600 μm) can be used for the test [64].

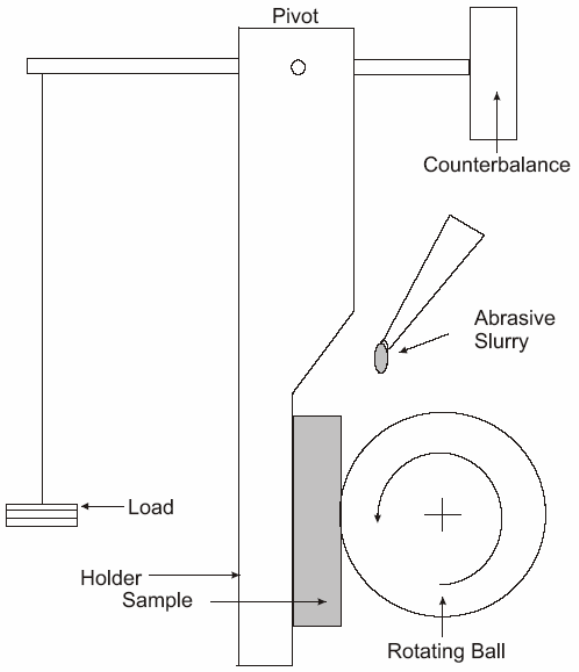

Figure 2.21: Schematic diagram of the micro-abrasion test rig.

2.3 Aqueous corrosion and corrosion testing

2.3.1 Introduction to aqueous corrosion

Most metals are naturally found in chemically combined states known as ores which are oxides, sulphides, carbonates and other compounds of the metal. In order to obtain metal from its ore, it is heated in furnaces and a large amount of energy is supplied to it. Hence most metals in uncombined conditions are at a higher energy state and display a thermodynamic tendency to transform into low energy state by combining with components of the environment leading to corrosion. The process of degradation of a metal by an electrochemical reaction with its environment is known as corrosion [101]. This definition suggests that corrosion is an electrochemical reaction in which electron transfer occurs between its participants and that one of the participants is the corroding metal. It also suggests that, for corrosion to occur, a metal must react with its environment (which describes all species adjacent to the corroding metal at the time of corrosion). This reaction of metal with its environment comprises of two half-reactions, namely the anodic and cathodic reactions. In simple terms, the anodic reaction produces electrons and the cathodic reaction consumes electrons. The part of the metal/electrolyte interface which behaves as the anode corrodes by the loss of electrons from electrically neutral metal atoms, forming discrete ions (Equation 2.17). These ions react with other species at the interface to form corrosion products, the nature of which determines the rate of corrosion. Oxidation of a metal occurs according to the following anodic reaction.

$$\mathrm{M} \rightarrow \mathrm{M}^{z+} + ze^{-} \qquad \textbf{2.17}$$

In which z represents the number of electrons taken from each atom and is governed by the valency of the metal. Commonly, *z* is equal to 1, 2 or 3.

The corresponding cathodic (reduction) reaction consumes electrons generated at the anode. There are different possible electron consuming reactions, one of them being the reverse of Equation 2.17, commonly known as the replating reaction.

$$\mathrm{M}^{z+} + ze^{-} \rightarrow \mathrm{M} \qquad \textbf{2.18}$$

Two other reactions may also occur at the cathode:

A process in which hydrogen gas is formed:

$$2\,\mathrm{H}^{+} + 2e^{-} \rightarrow \mathrm{H}_2 \qquad \textbf{2.19}$$

and a process that consumes dissolved oxygen and generates hydroxyl ions

$$2\mathrm{H}_2\mathrm{O} + \mathrm{O}_2 + 4e^{-} \rightarrow 4\mathrm{OH}^{-} \qquad \textbf{2.20}$$

The reaction represented by Equation 2.19 is more likely to occur in solutions with high concentration of [H^+] ions (solutions with low pH, i.e. acidic solutions). The second reduction reaction is dependent on the concentration of dissolved oxygen in the solution and is likely to occur in aerated solutions. The anode, the cathode, the electrolyte and electrical contact between them constitute the basic wet corrosion cell. The removal of one of these four components of the simple wet corrosion cell will stop the corrosion reaction. It is also possible that the formation of both anode and cathode may occur on the same surface, see Figure 2.22. The formation of anodes and cathodes on the same surface may occur due to the differences in the constituent phases of the sample (e.g. two phase materials like WC-Co) from variation in the surface deposits or coatings on the surface or from variation in the concentration or composition of the electrolyte present.

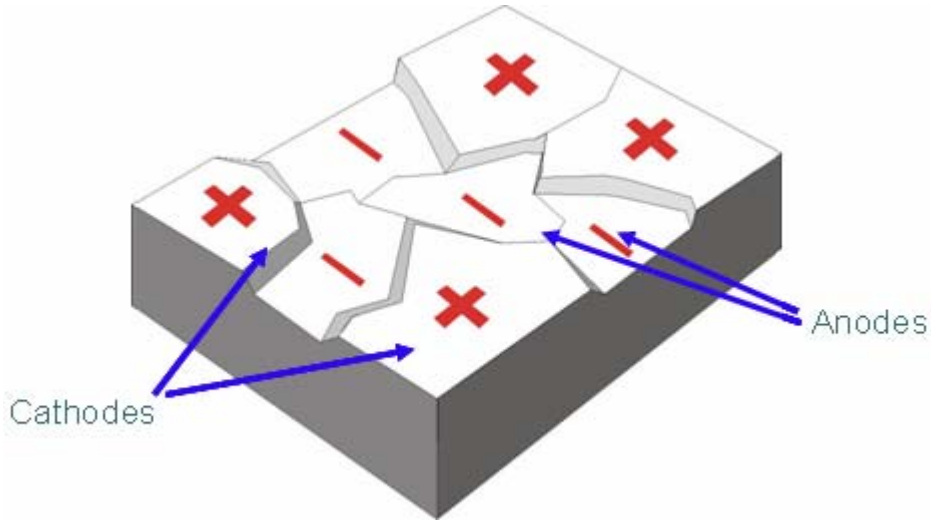

Figure 2.22: Schematic diagram showing the formation of anodes and cathodes on the sample surface.

2.3.2 Pourbaix Diagrams

Marcel Pourbaix [102] plotted potential (measured against the standard hydrogen electrode) versus the pH for metals to demonstrate the effect of change in the pH value and potential on their stability. These diagrams are known as Pourbaix diagrams or *E/pH* diagrams and consider the possible equilibrium reactions of metals with H_2O. However, these diagrams are purely thermodynamic in nature and do not take into account corrosion kinetics occurring. The boundary lines on the diagram are determined by the thermodynamic potentials calculated from using the Nernst equation. An example of a Pourbaix diagram for tungsten (W) is shown in Figure 2.23. *E*/*pH* diagrams can be used to distinguish a corroding condition from a non-corroding condition by means of a threshold potential calculated for a molar concentration of 10^{-6} M [101], i.e. a metal is deemed to be in a corroding condition when the concentration of its ions in solution is $\geq 10^{-6}$ M. When the concentration of ions is less than this value, the metal is considered to be immune to corrosion. The third case considered in the Pourbaix diagrams is when corrosion forms an insoluble product on the metal surface which acts as a protective film and prevents a direct contact between the electrolyte and the metal surface, thereby reducing corrosion rate.

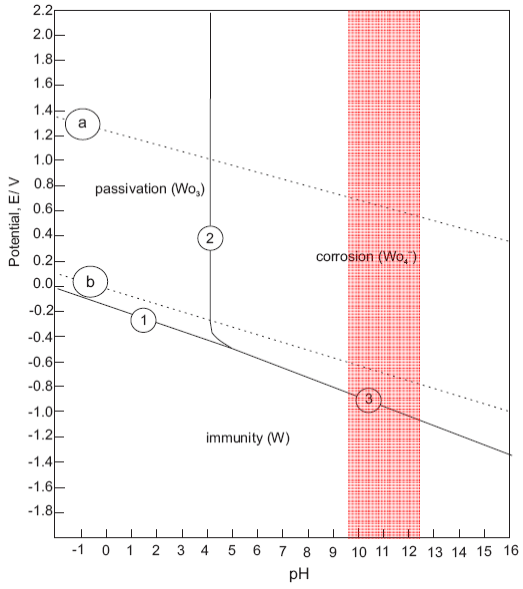

Figure 2.23: Theoretical conditions of corrosion, immunity and passivation for W according to Pourbaix. Highlighted region shows the stability of W between pH 10 and 12.

When W corrodes in water, up to five species can be present over the complete range of potential and pH: W, WO_2, W_2O_5, WO_3 and WO_4^{2-}

The reactions which describe the corrosion and passivation of W are given below.

$$W + 2H_2O \rightarrow WO_2 + 4H^+ + 4e^- \text{ (passivation)} \qquad \textbf{2.21}$$

$$WO_3 + H_2O \rightarrow WO_4^{2-} + 2H^+ \text{ (corrosion)} \quad \textbf{2.22}$$

$$W + 4H_2O \rightarrow WO_4^{2-} + 8H^+ + 6e^- \text{ (corrosion)} \quad \textbf{2.23}$$

The reactions involving the generation of electrons will be influenced by the variation of potential, whereas those in which hydrogen ions are formed will be controlled by pH. The reactions which generate both hydrogen ions and electrons are controlled by both potential and pH. The two dotted lines a and b represent the oxidation of water to liberate oxygen and reduction of hydrogen ions to liberate hydrogen gas respectively. The region between the lines a and b is the region where water is in a stable condition.

Figure 2.24a and Figure 2.24b show the Pourbaix diagrams for Co and Cr. Passivation of Co occurs by the formation of two insoluble oxides CoO_2 and Co_3O_4 and two insoluble hydroxides $Co(OH)_3$ and $Co(OH)_2$. Cr is known for its tendency to develop a passive film of Cr_2O_3 and $Cr(OH)_3$. It can be seen from the highlighted regions on the Pourbaix diagrams for W, Co and Cr, that although Co and Cr are passive under typical downhole conditions (between pH of 10 and 12), W is likely to suffer from corrosion. However, Pourbaix diagrams only consider equilibrium conditions of different metals with H_2O and care must be taken to relate these to tribocorrosion conditions.

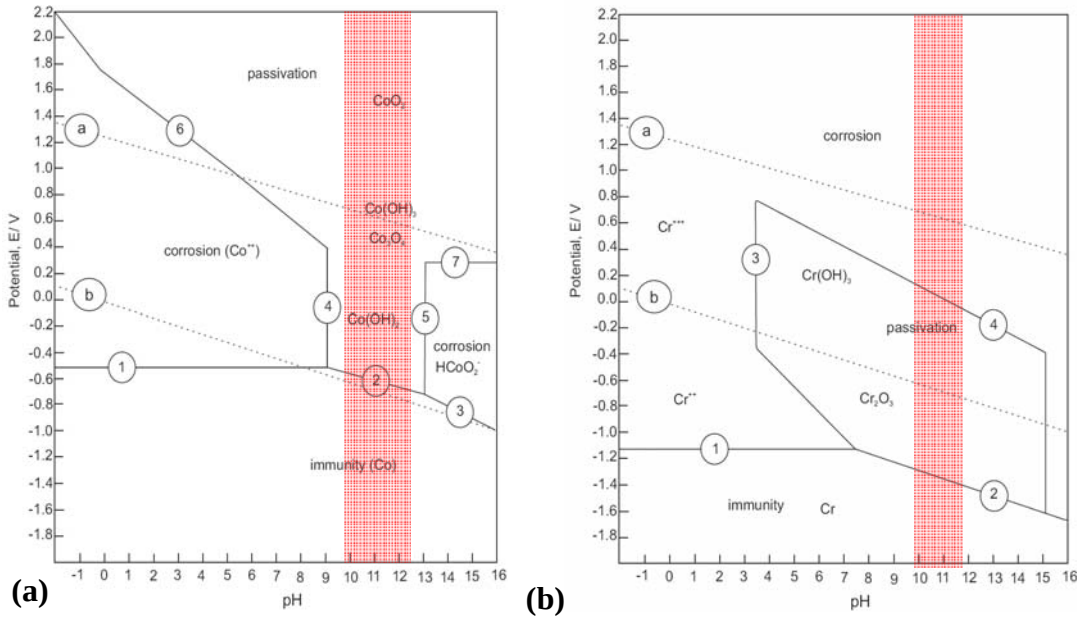

Figure 2.24: Theoretical conditions of corrosion, immunity and passivation of Co and Cr according to Pourbaix. Highlighted regions show the stability of Co and Cr between pH 10 and 12.

2.3.3 Corrosion of WC-based sintered and sprayed hardmetals

As discussed earlier in the chapter, WC-based hardmetals derive their superior hardness and abrasive wear resistance from presence of hard WC grains embedded in a ductile metallic binder-phase [10]. Corrosion of the binder-phase or the binder-carbide interface results in the weakening of the skeletal carbide structure and results in accelerated wear of the hardmetal. Kalish [103] investigated the corrosion performance of WC-bases sintered hardmetals and observed that the corrosion rates for WC-based hardmetals are much higher in acidic conditions than in alkaline conditions. This was due to the fact that the binders Co and Ni have a lower corrosion resistance at lower pH values i.e. in acidic environments as compared to the hard WC particles, see Pourbaix diagrams for Co and Ni. The removal of the binder phase is likely to be enhanced if the environment is corrosive which could also lead to accelerated loss of material. Tomlinson *et al.* [104] studied sintered tungsten carbides with Co and Ni binders in acidic conditions and reported that the electrochemical performance of WC based hardmetals reflected the performance of the binder and was representative of the high dissolution rate of pure Co as opposed to a lower dissolution rate of Ni. In the presence of corrosive environment, micro-galvanic cells are likely to be formed between the hard carbide phase and the soft binder. Carbides are likely to be cathodic to the binder in such micro-galvanic cells resulting in an increase in the binder loss during corrosion as proposed by Hocstrasser(-Kurz) [105]. The galvanic coupling between Co and WC results in the anodic dissolution of Co, given by the following reaction.

$$Co \rightarrow Co^{2+} + 2e^{-} \qquad \textbf{2.24}$$

The corresponding cathodic reaction of reduction of oxygen (in alkaline solutions, see Equation 2.19) or hydrogen (in acidic and neutral conditions, see Equation 2.20) occurs on the WC phase. The anodic reaction leads to an increase in local conductivity which increases the overall reaction rate. An increase in the rate of either of the cathodic reactions (Equations 2.19 or 2.20) causes an increase in the local pH. The stability of W [102] and WC [106] is known to decrease in alkaline conditions, thereby an increase in the local pH leads to the corrosion of W. The corrosion of W is a two step process.

$$W \rightarrow WO_3 \qquad \textbf{2.25}$$

$$WO_3 + 2H_2O \rightarrow WO_4^{2-} + 2H^{+} \qquad \textbf{2.26}$$

A consequence of the reaction in Equation 2.26 is the decrease in the local pH which can accelerate the dissolution of Co[106]. The galvanic coupling of WC and Co is expected to result in the preferential dissolution of Co in acidic conditions due to the low solubility of WO_3 and in preferential dissolution of W in alkaline and neutral conditions due to the low

dissolution rate/ passivation of Co. A similar observation was made by Anderson *et al* [107] when they studied the dissolution of WC-Co powders in acidic, neutral and alkaline conditions. They found that while the rate of dissolution of W is likely to remain constant at pH values between 4 and 13, dissolution of Co is likely to accelerate in acidic conditions and drastically reduce in alkaline conditions. Similarly, Imasato *et al.*[108] observed that the amount of metallic W dissolving increased with pH during the immersion tests of sintered hardmetals with Ni-Cr binders in neutral and alkaline solutions. They also observed that the corrosion current density decreased with an increase in Cr_3C_2 content in the binder-phase. However, presence of Cr_3C_2 is known to adversely affect the wear resistance of the sintered hardmetal [106].

The corrosion performance of the sprayed WC-based coatings is very different from their sintered counterparts due to the complex microstructure of the coating. Unlike the skeletal carbide structure observed in sintered hardmetals, WC grains in the coatings are randomly distributed in the metallic binder. Hence corrosion of the binder-phase has a stronger influence on the wear performance of the coating. However, the use of a corrosion resistant binder improves the corrosion as well as wear performance of the coating [109-112]. The influence of binder composition on the corrosion performance of WC-based coatings and have been studied previously [113, 114]. Cho *et al.*[114] studied the corrosion behaviour of WC-based coatings with different binder-compositions in strong H_2SO_4 solutions. Prolonged exposure to acidic conditions revealed micro-galvanic coupling between WC particles and the binder-phase leading to the preferential dissolution of the binder-phase. It was also found that the presence of Cr in the binder-phase led to a slight decrease in the corrosion rate of the binder-phase. They also noted that the presence of micro-cracks and defects on the surface led to accelerated corrosion attack penetrating the surface. Bolelli *et al.* [115] also observed that the HVOF WC-based coating with CoCr binder possesses superior corrosion resistance than ordinary thick chromeium plating. However, it was also observed that presence of microstructural defects such as oxide inclusions and splat boundaries on the coating surface results in crevice corrosion.

Perry *et al.* [116] studied the effects of prolonged exposure of WC-Co-Cr coating in artificial seawater (3.5% NaCl solutions). SEM micrographs of exposed coating revealed that corrosion occurred at the binder-carbide interface. They concluded that the interface between binder and carbide provided a site for micro-galvanic and or crevice corrosion. It was also concluded that as the matrix corrodes at the binder-carbide interface, the carbide particles then fall out and leave behind small pits. This was also observed during the anodic polarisation of the WC-Co-Cr samples in artificial seawater. These corrosion features

observed at the binder-carbide interface were confirmed by Souza and Neville [113] by comparing the corrosion performance of WC-Co-Cr coating and WC-CrNi coating. Souza and Neville [117, 118] further studied the corrosion characteristics of HVOF WC-10Co-4Cr in order to understand the effects of corrosion on the erosion-corrosion behaviour of sprayed WC-based coatings. They compared the electrochemical behaviour of UNS S31603 stainless steel with a HVOF WC-10Co-4Cr coating and found that unlike the continuous passive film of Cr_2O_3 present on stainless steels, only the CoCr matrix in the HVOF coating passivates and develops a Cr_2O_3 film in a 3.5% NaCl solution. They observed corrosion of small WC grains (< 1 μm) on coating samples subjected to an accelerated corrosion test and worn coating on a sleeve operating in a solid-free environment. It was concluded that the corrosion feature observed at the binder-carbide interface results from the corrosion of the binder-phase as well as WC grains, see Figure 2.25. Similarly, Takeda *et al.* [119] observed a Cr_2O_3 passive film on a WC-10Co-4Cr coating after immersion in Na_2SO_4 solution and concluded that this film does not cover the entire surface and was present in the form of islands. This passive film is likely to be weakest at the binder-carbide interface and hence in presence of a corrosive electrolyte, corrosion in HVOF WC-10Co-4Cr is likely to be initiated at this interface [118]

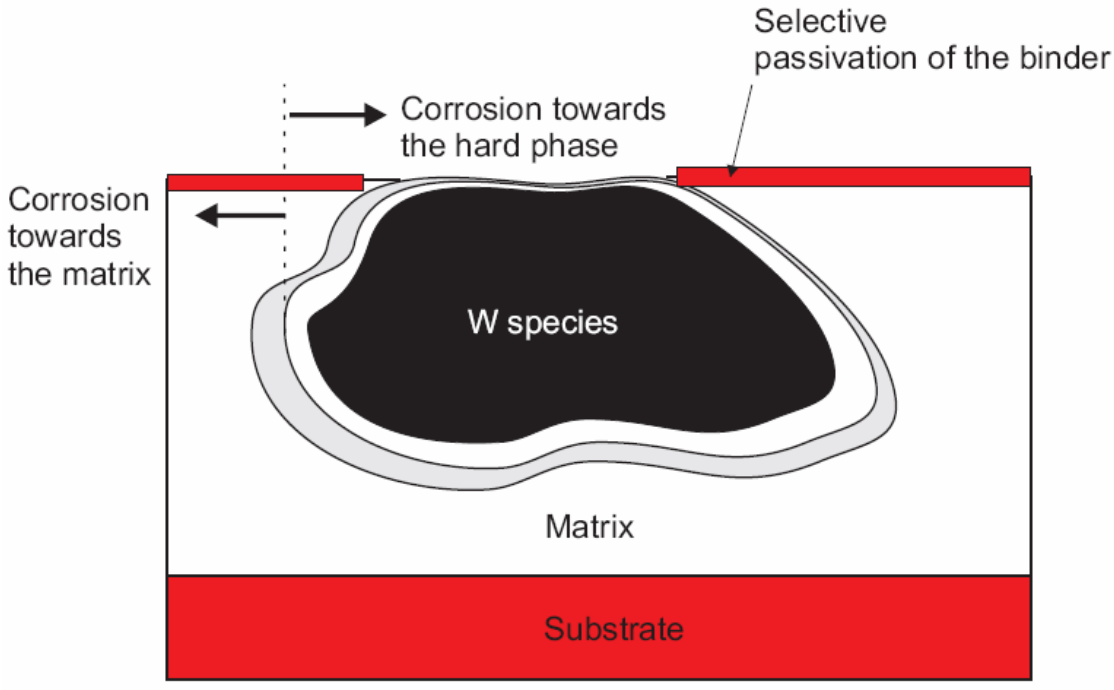

Figure 2.25: Corrosion at the binder-carbide observed by Souza *et al.* [117].

In summary, the corrosion reactions likely to occur at the surface of the coating are complex in nature and are influenced by the pH of the environment and the formation of micro-

galvanic coupling between the Co/Cr rich binder phase and WC phase (WC, W and W_2C) [29].

2.3.4 Corrosion testing

2.3.4.1 Potentiodynamic Polarisation

Immersing a sample in a solution results in the sample obtaining an equilibrium potential known as the open circuit potential (*OCP*) which is often referred to as the corrosion potential (E_{corr}). At E_{corr} both anodic and cathodic reactions occur, typically at random sites on the sample. When a metal is not in equilibrium with the solution of its ions, the potential of that metal differs from its corrosion potential by an amount known as polarisation [101]. The polarisation represents extra energy needed to force the electrode reaction at a required rate. The polarisation causes a flow of current (I) and by monitoring this flow; it is possible to monitor the corrosion kinetics. It is usual practice to consider the value of current density (i) instead of current to measure the corrosion current. This is because the value of current will change according to the surface area and hence it will not be possible to compare the corrosion rates of two metals with dissimilar surface area. Current density is often reported in terms of $\mu A\ cm^{-2}$.

Potentiodynamic polarisation tests are typically conducted using a three-electrode cell, see Figure 2.26. It consists of a working electrode (the sample being investigated), held in a specially designed Teflon specimen holder so as to expose a known surface area of usually 1 cm^2. The second electrode used is the counter (auxiliary) electrode which is present to carry the current created in the circuit and is made of carbon (graphite). This electrode is not essential in the measurement of potential of the sample in the solution. The third electrode in the circuit is the reference electrode (Ag/AgCl reference electrode, in this case) which provides a stable datum against which potential of the working electrode can be measured. No current passes through this reference electrode. Reference electrodes used for the potentiodynamic polarisation tests are relative to a standard hydrogen electrode which is a type of reference electrode. Some of the commonly used reference electrodes for laboratory scale measurements are standard calomel electrode (SCE), Ag/AgCl reference electrode (SSC) and the standard hydrogen electrode (SHE). Details of the potentials of the standard reference electrodes measured against a SHE is given in *Appendix 1*. The potential of a standard hydrogen electrode is defined as 0.00 V by international convention [120].

The three electrodes are connected to a current measuring device and a potential measuring device as shown in Figure 2.26. A source of potential is used to ‘drive’ the cell reaction (with

a sweep rate of 0.1 mV s^{-1}) [121]. A potentiodynamic polarisation plot (*E vs.* log *i*) is plotted using a Gamry Instruments PC4/750 potentiostat and CMS100 software. The assembly of the three electrodes is placed in a beaker containing the electrolyte. This assembly is placed in a Faraday cage to avoid interference from other electrical equipment in the laboratory. On the y-axis is the applied potential (measured versus a Ag/AgCl reference electrode in volts) and on the x-axis is the log of current density (measured in A cm^{-2} or μA cm^{-2}), see Figure 2.27. The value of the current density (i_{corr}) at the intersection of the straight lines drawn from the linear Tafel regions (from 50 mV to no more than 300 mV) on the anodic and the cathodic side of the polarisation curve is a measure of the dissolution rate for the material. This method is known as the Tafel extrapolation method. Details of this method can be found elsewhere [101].

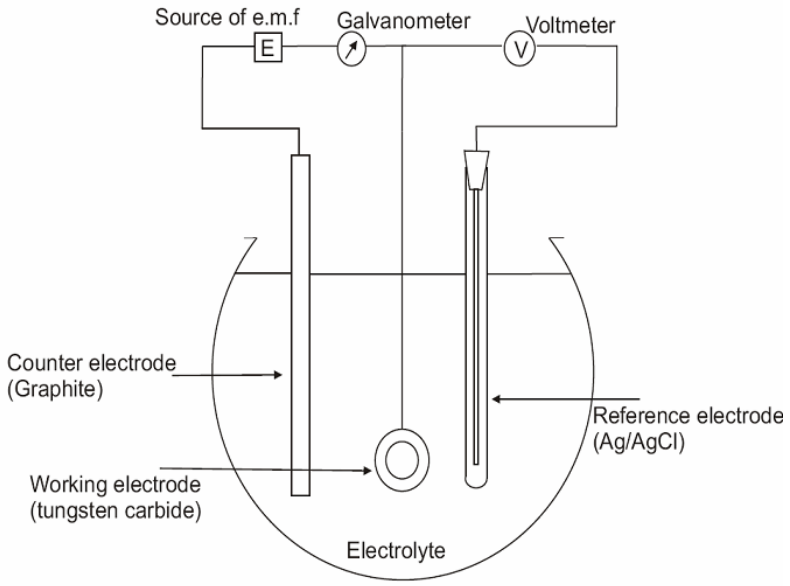

Figure 2.26: Schematic diagram of the three electrode cell showing the arrangement of working, counter and reference electrodes.

Corrosion rate can be readily estimated from the knowledge of the corrosion current density (i_{corr}) and the application of Faraday's laws of electrolysis. The mass loss of the metal (Δw) at a constant current (I) is given by

$$\frac{\Delta w}{M} = \frac{It}{zF} \qquad \textbf{2.27}$$

Where M is the molar mass of the metal in g mol^{-1}, t is the time in s, z is the number of electrons and F is the Faraday's constant (96485 A s mol^{-1}).

Dividing by area (A) and rearranging

$$\frac{\Delta w}{At} = \frac{IM}{AzF} \qquad \textbf{2.28}$$

Assuming 100% current efficiency for the anodic dissolution and inserting $i_{corr} = I/A$

$$\frac{\Delta w}{At} = \frac{i_{corr} M}{zF} \qquad \textbf{2.29}$$

The average mass loss per unit area per unit time is often given by [g m^{-2} day^{-1}]. The average penetration rate ($\Delta x/t$) may be calculated from the knowledge of the metal density (ρ), again assuming uniform corrosion

$$\frac{\Delta x}{t} = \frac{i_{corr} M}{\rho z F} \qquad \textbf{2.30}$$

where, ρ is the density in g cm^{-3}. Commonly used units of corrosion rate are cm s^{-1}. Potential vs. log *i* are valuable plots to reveal the dissolution and reduction rates and the presence of surface films or corrosion products on a corroding sample. Figure 2.27 shows a schematic of a classical passivation curve with well-defined active and passive regions. A sharp decrease in the current density with an increase in potential indicates a decrease in the surface reactivity. Typically, a passive behaviour is displayed when there is no increase in the current density with an increase in the potential and suggests the presence of a insoluble oxide film which acts as a barrier preventing any further reaction between the sample surface and the electrolyte.

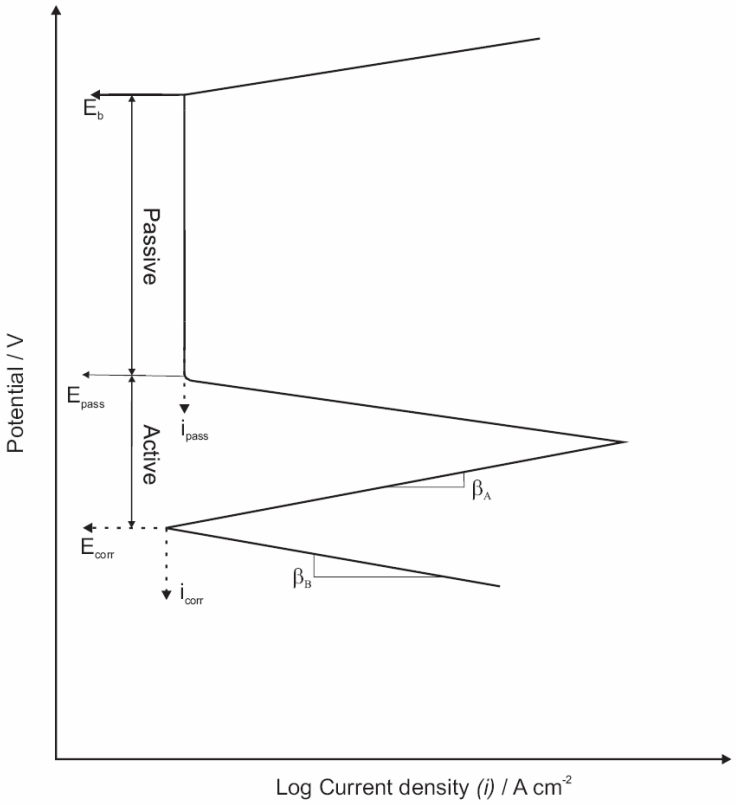

Figure 2.27: Schematic E/log *i* plot showing the values of E_{corr} , i_{corr} and typical passive behaviour.

2.3.4.2 Electrochemical current noise measurement

Fluctuations of the corrosion potential and corrosion current spontaneously generated by corrosion reactions are known as electrochemical noise [122]. Electrochemical current noise (ECN), measured under potentiostatic conditions can be used to study corrosion. Electrochemical current noise can be measured either as galvanic coupling current between two nominally identical working electrodes using a zero resistance ammeter (ZRA) or from a single working electrode held at a fixed potential [123]. Although the use of just a single working electrode does not allow simultaneous monitoring of potential and current noise, it is extensively used due to the relative ease of incorporating the three-electrode cell for *in situ* observation of ECN. The advantages offered by the ECN are that its utilisation does not lead to artificial disturbance of the system under investigation and it is sensitive to localised corrosion processes [124]. Hence, ECN measurement has been successfully used for *in situ* measurement of corrosion process occurring on the sample surface during wear-corrosion [124-126]. Bethune and Waterhouse [127] demonstrated the use of electrochemical current noise during the study of fretting corrosion by incorporating a three-electrode in a fretting-wear apparatus. The fretting wear sample acted as the working electrode. Potentiostatic control was imposed on the contacting surface to maintain a constant potential with respect to the reference electrode under stationary conditions (in the absence of fretting). To maintain a constant potential required the passage of a current through the cell between the working and counter electrodes. On disturbing the equilibrium (by the fretting action), the current flowing in the cell was adjusted by the potentiostat to maintain a constant potential. The adjustment of current was recorded with respect to time. The fluctuation in the current to maintain a constant potential was representative of the electrochemical effects of the fretting wear occurring at the surface (stripping of the passive film) of the copper working electrode.

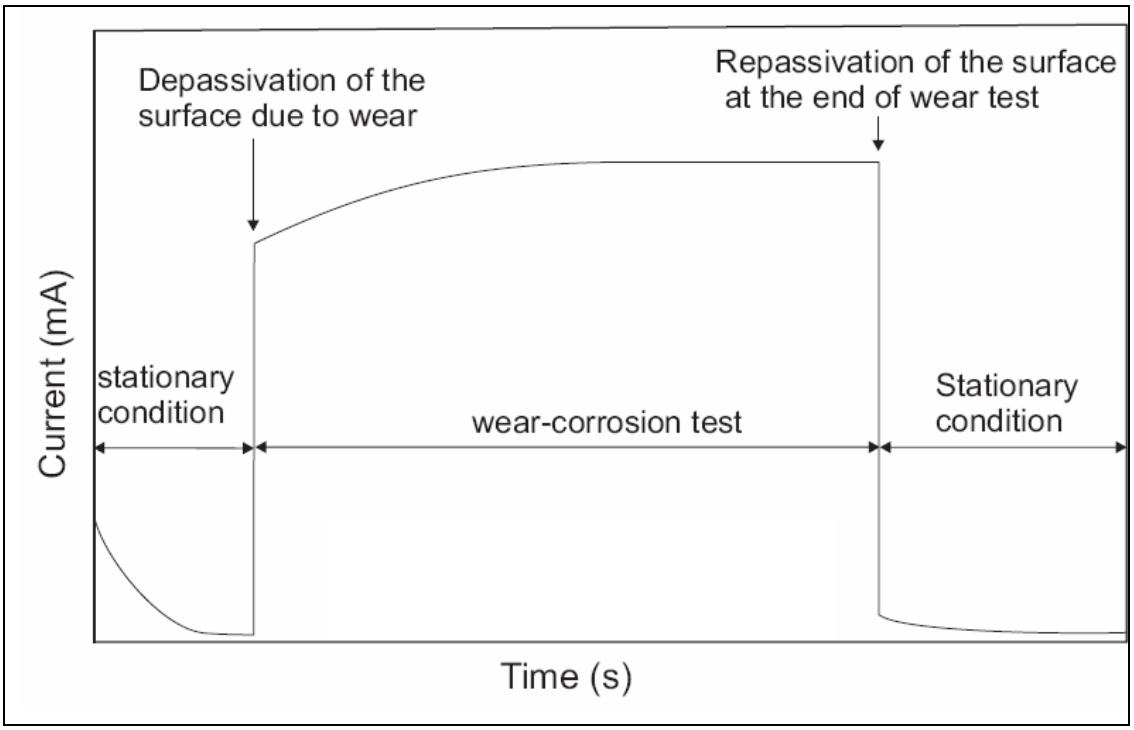

Figure 2.28: Evolution of the current with time during a typical wear-corrosion test.

A similar technique was employed by Mischler *et al.* [128] to study the role of passive oxide films on the degradation of carbon steel in a tribocorrosion system using a ball-on-plate reciprocating rig incorporating a three-electrode cell. Sliding wear tests were conducted by holding the samples (carbon steel disc) at a passive potential. A schematic of the recorded current-time is shown in the Figure 2.28. The area under the current-time curve can be converted to a mass loss using Faraday's law using Equation 2.27. Landolt *et al.* [129] reviewed the use of ECN in tribocorrosion systems and noted that the use of ECN provided an excellent tool to decouple electrochemical and mechanical effects in a tribo-corrosion system. ECN also provides a tool to monitor depassivation and repassivation kinetics in a tribocorrosion contact [125, 130]. ECN has been effectively used to study sliding wear [125] and erosive wear [124] on contacts fully immersed in the electrolyte. However, these tests are under simple contact conditions (fretting, sliding). Their use in three-body abrasion tests on partly immersed contacts needs to be fully explored.

2.4 Wear-corrosion interactions

Wear resistant materials functioning in corrosive environments and subjected to abrasive wear often fail prematurely due to the synergistic effects of coupling wear (mechanical process) and corrosion (electrochemical process). Wear-corrosion interaction can lead to either increase in the overall mass loss or a decrease in the overall mass loss. The change in the mass loss due to the synergistic effects of coupling wear and corrosion is often referred to as synergy (*S*). Positive synergy results in accelerated material loss due to the combined action of wear and corrosion and is an undesirable material property. On the other hand, negative synergy results in a decrease in the overall loss of material due to improvement in either wear or corrosion resistance and is a desirable material property.

According to the ASTM standard guide for determining synergism between wear and corrosion [131], the total wear during the process of abrasive wear-corrosion is defined by the following equations:

Total Wear (AC) = Pure Abrasion (PA) + Pure Corrosion (PC) + Synergy (S) **2.31**

Where,

$$S = \Delta PC_A + \Delta PA_C \quad \textbf{2.32}$$

ΔPC_A = Change in corrosion due to abrasion.

ΔPA_C = Change in abrasion due to corrosion

Attempts have been made to calculate 'pure corrosion (PC)' either under static conditions [132] or using wear tests without any abrasives [133]. The use of wear tests without abrasives for PC calculations is likely to result in mild sliding wear due to the contact between the sample and the asperities on the counterface material resulting in overestimation of PC. On the other hand, PC calculated under static condition may not be related to the actual corrosion occurring in the tribo-corrosion contact. Attempts have been made to calculate the value of PC using *in situ* electrochemical measurements as discussed in the previous section (Section 2.3.4.2) during erosion-corrosion [117, 118] and during abrasion-corrosion by modifying a micro-abrasion tester [133, 134]. Figure 2.29 shows the

electrochemical data (change in current) observed before (*PC*), during (ΔPC_A) and after (*PC*) the abrasion test.

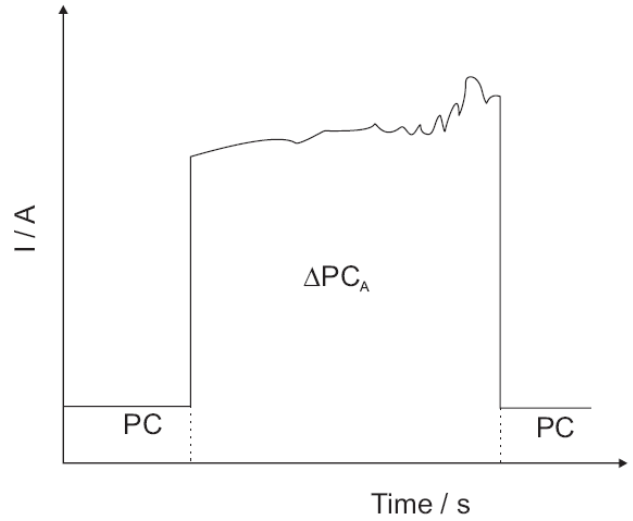

Figure 2.29: Schematic of the current (*I*) vs. time plot used for $PC_{\text{in situ}}$ calculations.

Accurate estimation of the 'pure abrasion (*PA*)'contribution is another cause of possible errors in the estimation of wear-corrosion interactions. In conventional wear tests, results obtained under neutral conditions (pH 7) have been considered as *PA,* assuming pH 7 to be a 'corrosion free' environment [135]. A potentially more accurate method for calculating *PA* is the application of cathodic protection (CP) to the wear test sample [133]. However, this can only be done by modifying conventional wear tests to incorporate an electrochemical cell. However, applying a low negative potential can lead to the evolution of hydrogen and lead to hydrogen embrittlement. Based on their model for corrosion of sintered WC-Co, Hochstrasser *et al*. [106] also proposed that corrosion of WC is likely to occur under cathodic potentials. Hence, the use of CP for calculating wear-corrosion interactions is debatable. It is also possible to estimate the *PA* contribution if there is a trend observed between corrosion due to wear (area under the *It* curve, ΔPC_A) and pH. Extrapolating the trend of ΔPC_A *vs.* pH to zero current and running the abrasion tests at that pH is expected to give pure abrasion (*PA*).

Mischler *et al.* [136] observed that the calculation of *PA* and *PC* led to erroneous estimation of wear-corrosion interactions and proposed an alternate method to quantify the wear-corrosion interactions. They proposed that the total loss of material during wear-corrosion is the sum of the material losses due to mechanical effects and electrochemical effects, see Equation 2.33. However, this equation can only be used in tribo-corrosion rigs which are capable of *in situ* electrochemical measurements as shown in Figure 2.28 and Figure 2.29.

$$V_{Mech} = V_{Total} - V_{Elec} \quad \textbf{2.33}$$

V_{Total} is the total volume loss due to mechanical and electrochemical effects and is measured from the volume of the wear scar. V_{Elec} is the volume loss due to electrochemical effects measured from the current-time (It) curve obtained during wear-corrosion test and V_{Mech} is the volume loss due to mechanical effect.

Table 2-3:Overview of the processes that could lead to positive or negative wear-corrosion interaction [137].

Mechanism	Positive interaction	Negative interaction
Passive film state	Depassivation (removal) of the passive film exposes fresh surface for further corrosion attack and accelerates material removal [138].	Oxide layer could reduce the friction between abrasives and bulk material. Presence of denser oxide film can reduce corrosion as well as abrasion [139].
Dissolution of active species in multiphase surfaces	Could lead to loss of bond integrity between the hard and binder phase. Preferential corrosion of binder undermines the hard phase and facilitates its easy removal by abrasive wear.	Corrosion of the interface can increase the compliance of the surface to abrasive particles.
Plastic deformation/strain	Plastically deformed and stressed surfaces enhance corrosion due to stress corrosion cracking. Corrosion can lead to premature detachment of plastically deformed or strain hardened splats.	Strain hardness would result in increased hardness and lead to a lower wear. Change in microstructure, grain orientation could lead to lower corrosion rate.
Surface roughness	Could lead to easier removal of oxide film by asperity peaks.	Surface roughness influences the contact mechanics of angular particles and the surface. Increase in R_a could reduce contact stresses and stress distribution [140].

Batchelor *et al.*[138] studied the effects of passive film on the abrasive wear of mild steel zinc and magnesium and found that the regular removal of passive film by abrasion and its regrowth results in a greater material loss than undisturbed corrosion. However, they also

noted that the synergistic effect largely depended on the physical nature of the passive film formed which could offer additional protection against mechanical wear, see Figure 2.30. Table 2-3 tabulates the mechanisms resulting from a conjoint action of wear and corrosion which could result in either positive or negative wear-corrosion interactions.

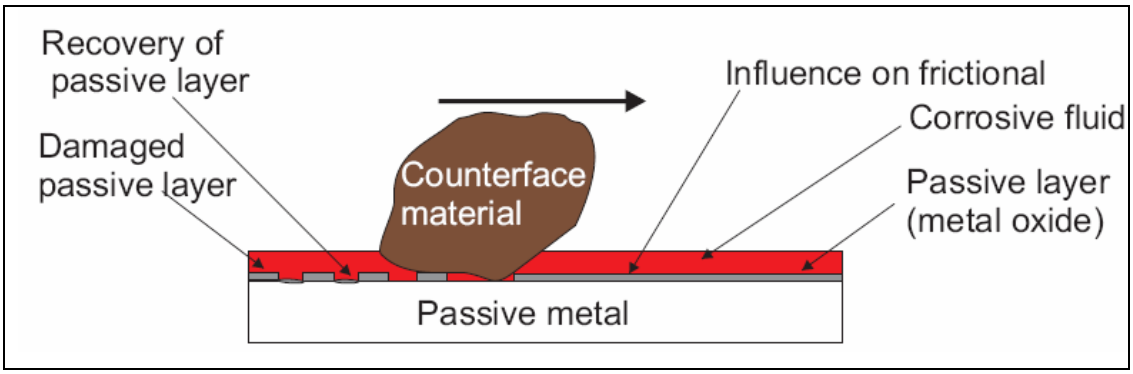

Figure 2.30: Abrasive wear of passive metal in a corrosive environment [141].

Ponthiaux *et al.* [142] suggested that the galvanic activity between the worn area and the surrounding unworn areas in a tribo-corrosion contact needs to be fully understood. Garcia *et al.* [143] studied the wear-corrosion of AISI 316 stainless steel immersed in 0.5 M H_2SO_4 solution and suggested the concept of 'active wear track area'. They defined the active wear track area as the part of the surface area that looses its passive film due to a mechanical loading and also suffers from corrosion. They presented a model for current (I) flowing through an electrode of total area (A) by considering two components for reciprocating wearing contacts. The first component is the product of the active wear track area, (A_a) and the repassivation current density ($i_a(t)$) and the second component is the product of passive area, (A-A_a) and the passive current density ($i_p(t)$).

$$I = fA_a \int_0^{1/f} i_a(t)dt + f(A - A_a) \int_0^{1/f} i_p(t)dt \qquad \textbf{2.34}$$

Where, f is the sliding frequency which is also equal to the depassivation frequency. Wear is also expected to enhance the effects of corrosion by creating a galvanic coupling between the worn area and the unworn surface. Goldberg *et al.* [130] suggested an equation by which the transient current and repassivation current by single scratch test could be modelled and predicted when an oxide film on a passive surface was removed.

$$I(t) = I_{peak} \exp\left[\frac{-(t - t_0)}{\tau}\right] + I_\infty \qquad \textbf{2.35}$$

Where, I_{peak} is the peak current ($I_{peak} = I_{max} - I_\infty$), τ is the time constant for repassivation, t_0 is the time to produce the scratch and I_∞ is the baseline current at $t = \infty$. If the sample had Tafel behaviour, the following equation can be used.

$$I_{peak} = i_{crit} A_0 \exp\left[\frac{\eta f}{\beta_a}\right] + \frac{\delta \rho Z F A_0}{M_w \tau} \quad \textbf{2.36}$$

Where, i_{crit} is the critical current density for passivation A_0 is the initial scratched area, ηf is the film overpotential (the difference between passivation and potentiostatically held potential), β_a is the Tafel slope, δ is the thickness of the repassivated oxide film, ρ is the oxide film density and M_w is the oxide film molecular weight. The equation suggests that an increase in the contact area will result in an increase in the ion release to the environments.

Mischler *et al*. [128] presented a model to describe the corrosive behaviour of passive metals sliding against a hard insulating body. They derived a relationship between anodic corrosion current under the influence of wear ($I_{a,w}$) and experimental parameters such as load (W), sliding frequency (f), wear track length (l) and the hardness of the metal (H).

$$I_{a,w} = K_w l f \left[\frac{W}{H}\right]^{\frac{1}{2}} \int_0^{1/f} i \, \mathrm{d}\tau \quad \textbf{2.37}$$

Where K_w is a proportionality constant. However, the wear component of material loss was not modelled using this equation.

Jiang *et al*. [144] developed a complex model to predict the transition between wear induced corrosion and corrosion induced wear. They predicted that under conditions of low load and high frequency of interaction between the metal and the counterface the dissolution rate (corrosion) at the sample surface is expected to increase and result in a wear-induced corrosion. On the other hand, under conditions of high load and low frequency of interaction between the metal and the counterface, especially for metals with high passivation capabilities, there would be an increase in material loss due to corrosion-induced wear.

2.4.1 Wear-corrosion interactions in WC-based sintered hardmetal and sprayed coatings

The degradation of hardmetals due to the combined effects of wear and corrosion is complex and it is often difficult to differentiate between them. Human *et al.* [145] investigated the combined mechanical and corrosion performance of scraper blades made from WC-based hardmetals with Ni-Cr and Co binders used for coal-ash handling, and found that the blades with WC-Ni-Cr showed very little binder depletion and maintained relatively sharp edges compared to WC-Co blades which showed signs of severe wear. Other researchers have observed that even in wear dominated conditions, improving the binder corrosion resistance

significantly improved the overall performance [146-148]. Gant *et al.* [135] suggested that the preferential removal of the binder-phase was accelerated in strong acidic conditions leading to an increase in the overall wear rates. However, according to Wenzel and Allen [149] wear-corrosion performance of WC-based hardmetals is not always representative of their corrosion performance. They studied the erosion-corrosion performances of WC-based hardmetals with Co, Ni and Ni-Cr binders and concluded that despite a better corrosion resistance offered by Ni-based grades due to the passive behaviour of the Ni binder, under conditions were the passive film is continuously removed as in the case of slurry erosion or abrasion, binders which offer better hardness and deformation characteristics performed better.

The wear-corrosion synergy performance of WC-based coatings have been studied previously [71, 109, 110, 116-118, 150]. As discussed in the Section 2.3.3, the uneven distribution of the binder-phase and the hard-phase within the coating making the coatings vulnerable to wear-corrosion attack. However, increasing the content of the more corrosion resistant binder improves the wear and corrosion performance of the coating [109-112]. As found by Souza and Neville [117, 118], corrosion of the WC-Co-Cr coating initiates at the binder-carbide interface and results in the accelerated removal of the carbide particles by subsequent erosive wear. A similar observation was made by Stack and El Badia [151] during the erosion-corrosion study of WC/Co-Cr coating. They found that preferential corrosion at the binder-carbide interface led to an increase in the mass loss during erosion-corrosion test. However, they also observed that under conditions when the Co-Cr binder was likely to passivate, there was a mild decrease in the mass loss during erosion-corrosion. It was proposed that this was probably due to the additional protection offered by the passivation of the binder-phase. Valentinelli *et al.* [150] noted that the wear-corrosion performance was strongly influenced by the passivation of the binder-phase and suggested the selection of the binder-composition in consultation with the Pourbaix diagrams (potential *vs.* pH) to ensure better performance.

As discussed in section 2.3.3, Kalish [103] observed that the corrosion rates for WC-based hardmetals are much higher in acidic conditions than in alkaline conditions due to the lower corrosion resistance of Co and Ni binders as compared to the hard WC particles in acidic environments. This has led to recent studies of wear-corrosion performance of WC-based hardmetals focussing on evaluating the performance of WC-based hardmetals in acidic conditions [71, 148]. Although the corrosion resistance of WC-based hardmetals is higher in alkaline conditions, the wear rates in alkaline conditions are clearly not insignificant [72, 135] (see Table 2-4) and hence cannot be ignored. Although Co and Ni show a strong

tendency to form insoluble oxide films at higher pH values which is likely to increase the corrosion resistance, the corrosion resistance of metallic W precipitated along the periphery of the carbide grain is expected to be poor [152]. Clearly, the nature of the wear-corrosion interactions occurring in WC-based sintered hardmetals and sprayed coatings is very complex and needs to be investigated using *in situ* electrochemical techniques and advanced surface analysis tools. The influences of environmental pH and abrasive size on the complex wear-corrosion interactions needs further investigation and are the focus of this thesis.

Table 2-4: *SWR* observed for sintered and sprayed WC samples under varying pH using SiC abrasives (three-body rolling)

Material	Binder	Carbide size (μm)	Test	pH	SWR ($x10^{-13}$) $m^3N^{-1}m^{-1}$	Ref
Sintered WC-6Co	Co	1.3	Micro-abrasion	1.1	5.34	[72]
Sintered WC-6Co	Co	1.3	Micro-abrasion	6.3	2.67	[72]
Sintered WC-6Co	Co	1.3	Micro-abrasion	13	2.54	[72]
HVOF WC-12Co	Co	1-5	Micro-abrasion	1.08	13	[71]
HVOF WC-12Co	Co	1-5	Micro-abrasion	7	9	[71]

2.5 Conclusions from the literature review

- The literature shows that abrasive wear is a complex process and although attempts have been made at modelling the abrasive particle motion in a contact, a full understanding is not yet achieved.
- Presence of corrosive slurry results in further complicating the process of abrasive wear. Models have also been developed for simple sliding between two surfaces in the presence of a corrosive slurry. However, the process of modelling abrasive wear with suspended abrasive particles has not been achieved. The presence of hard and soft phases in WC-based hardmetals results in complex processes such as formation of micro-galvanic coupling between the different phases, selective passivation and preferential wear of soft phase occurring on the wear scar. Simple "active area" models developed for single-phase materials cannot be used to explain the abrasive wear-corrosion process of WC-Co hardmetals.
- The corrosion performance of WC-based hardmetals is largely derived from the Pourbaix diagrams. The current understanding of wear-corrosion interactions in WC-based hardmetals is derived from the comparison of wear rates under neutral and acidic conditions. However, it does not provide any understanding of the corrosion kinetics during wear. Decoupling of electrochemical and mechanical effects of wear-corrosion interactions and understanding wear-corrosion interactions between phases needs to be developed, particularly in alkaline conditions.
- *In situ* electrochemical techniques have been effectively utilised to study the nature of passivation under simple contact conditions. However, the literature shows a lack of availability of robust wear-corrosion testing techniques which could be used to study abrasive wear of WC-based hardmetals. There is a need to develop novel techniques for testing the wear-corrosion performance of WC-based hardmetals. The use of *in situ* ECN techniques during abrasive wear needs to be explored.
- Although, there is some understanding of the influence of size effect on the wear of single-phase metals, very little can be said about the effect of change in abrasive size on the wear-corrosion of WC-based hardmetals and coatings. More work is needed for a fuller understanding of the size effect of abrasives on the wear-corrosion of WC-based sintered and sprayed hardmetals.

3 Methodology and experimental procedures

3.1 Methodology

As discussed in Chapter 1, microscopic observation of drill tool components worn in downhole conditions revealed that abrasive wear occurs by a range of abrasive sizes. To replicate the different possible wear-corrosion interactions occurring in downhole conditions, it was important to incorporate different exposure times to alkaline environment (pH 11) and vary the abrasive size during the wear-corrosion testing of candidate downhole materials (WC-based hardmetals and coatings). The tests conducted within this thesis can be classified as:

1. Electrochemical testing
    a. Exposure to pH 11 (drilling fluid or NaOH solution) conditions for 168 h (prior to wear testing)
    b. Static potentiodynamic polarisation tests after 0 h and 168 h exposure to pH 11 (drilling fluid or NaOH solution).
2. Micro-scale wear-corrosion testing (4.5 μm SiC abrasives)
    a. Wear testing using pH 11 slurries (NaOH solution+ SiC)
    b. Wear tests using pH 7 slurries (distilled water + SiC)
    c. Wear testing with *in situ* electrochemical testing using pH 7, pH 9, pH 11 and pH 13 slurries (distilled water / NaOH + background electrolyte + SiC)
3. Macro-scale wear-corrosion testing (4.5 μm, 17.5 μm and 180 μm SiC abrasives)
    a. Wear testing using pH 11 slurries (NaOH solution + SiC)
    b. Wear testing using pH 7 slurries (distilled water + SiC)

A brief overview and rationale of the tests conducted is shown in Figure 3.1. To mimic the effects of prolonged exposure of downhole drill tools to alkaline conditions due to long hours of operation and possible idle times, the test samples were exposed to alkaline conditions of pH 11 (NaOH solution or drilling fluid) for a duration of 168 h (1 week) prior to wear testing was deployed. Static potentiodynamic polarisation tests were also conducted on duplicate samples 0 hour and 168 hours after exposed to alkaline conditions. Comparison of the potentiodynamic polarisation curves 0 h after and 168 h after exposure to alkaline conditions provided valuable understanding of the degradation of WC-based materials under static conditions in alkaline environments. The advanced techniques of Scanning Electron Microscope (SEM), X-ray photoelectron spectroscopy (XPS), and Focussed ion beam (FIB)

sectioning of samples was employed to further understand of the effects of exposure to alkaline conditions on surface and sub-surface microstructure and composition.

To study the wear-corrosion interaction at a micro-scale (of the size of the carbides, 2-4 μm), a micro-scale abrasion test rig was used (Figure 2.21, Chapter 2). The micro-abrasion tester can effectively entrain abrasives of 4.5 μm in size and is known to give highly repeatable and reproducible results [153]. It has been extensively used to study micro-scale wear of different materials such as steels, hardfacings, hardmetals and thin coatings. Micro-abrasion tests were conducted using either distilled water based neutral slurries of pH 7 or NaOH based slurries of pH 11. Load and slurry concentration was selected so as to result in rolling abrasive wear mode as it is more stable and repeatable. Due to the small sample size and the geometry of the micro-abrasion arm, it is possible to modify the test rig to incorporate an electrochemical cell in the rig. A novel modification to the micro-abrasion tester allowed *in situ* electrochemical measurements and conducted pure abrasion tests by applying a negative potential to cathodically protect (*CP*) the sample. As discussed in the Chapter 2, CP is also known to have disadvantages such as, the application of a large negative potential can lead to the hydrogen embrittlement of the working electrode. As explained in detail at a later stage within this thesis, this modification also allows decoupling of mechanical and electrochemical components of wear-corrosion interaction. The *in situ* electrochemical test was used to study the influence of pH on the wear-corrosion of WC-based sintered and sprayed samples by conducting wear tests at pH 7, 9, 11 and 13.

A disadvantage of the micro-scale abrasion tester is that it cannot entrain abrasives larger than 10 μm in size. Hence, it was necessary to consider another test for macro-scale abrasion of WC-based samples. The ASTM G65 rubber wheel test (Figure 2.20, Chapter 2) is a standard wear test used for quantifying the wear resistance of WC-based hardmetals and other hard materials. The test can be used to study abrasion under dry conditions as well as under wet conditions. It has been effectively used to study the influence of pH on wear performance and degradation mechanisms by altering the pH of the slurries [79]. Typically, silica sand is used as abradants in the ASTM G65 test. A modified ASTM G65 test rig at NPL was used for this test programme. The modified rig (shown in Figure 3.8) allows a more controlled flow of abrasives by using a slotted drum mechanism. For the first time, SiC abrasives of 4.5, 17.5 and 180 μm sizes were employed to study the 'size effect' of abrasives during wear-corrosion. SiC abrasives were used instead of sand abrasives as they offer a more controlled size distribution of abrasives and to keep the conditions similar to the ones used for micro-abrasion testing. The slurry concentrations (solids to liquid ratio) were kept

constant for all abrasive sizes and were similar to that used for micro-abrasion test (130 g of abrasives per 200 ml of solution). Due to the location of the sample on the rig and its size, it is not possible to incorporate an electrochemical cell in the rig. As in the case of conventional micro-abrasion tests, abrasive wear tests were conducted using pH 7 and pH 11 slurries. Relatively mild test conditions (low load and rubber wheel instead of steel wheel) were employed to allow the influence of pH on wear to be measurable. The use of higher loads and a steel wheel results in high-stress wear making it difficult to observe the difference in the wear rates due to change in pH.

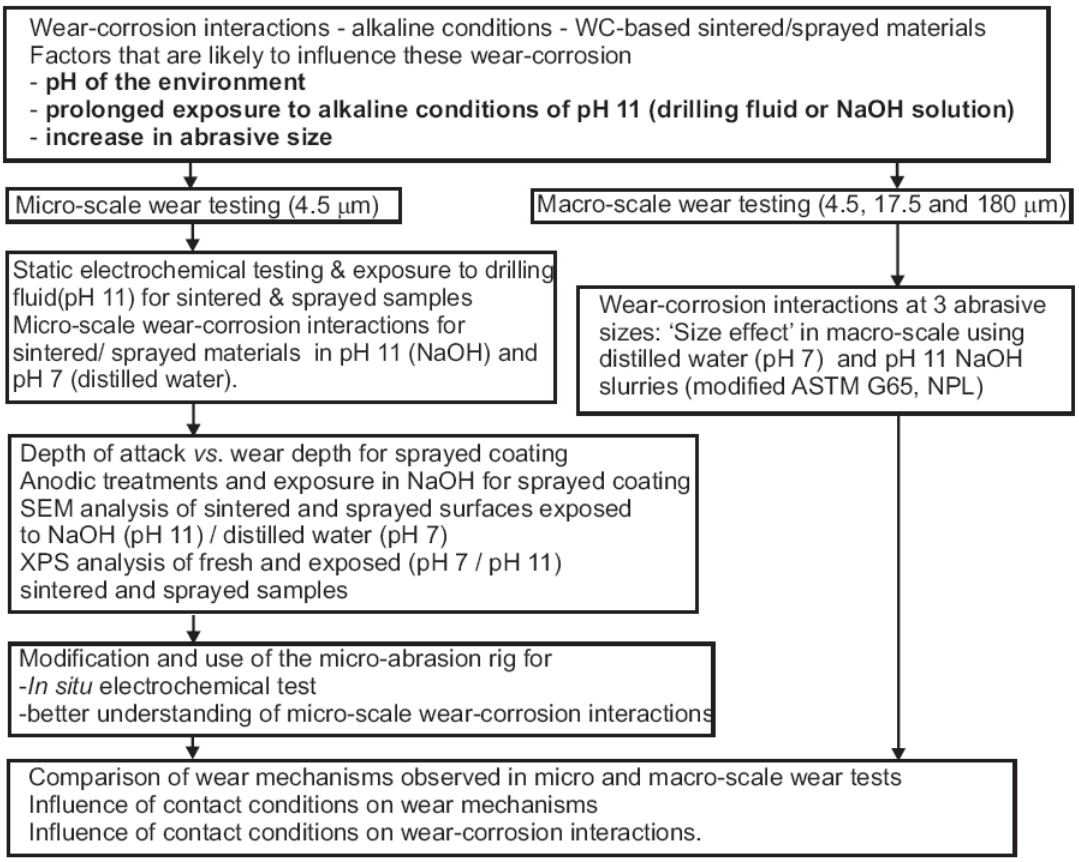

Figure 3.1: Flow diagram of the full experimental programme.

3.2 Test materials and microstructure analysis

Details of the properties, composition and designations of the sintered and sprayed samples tested are given in Table 3-1. The test samples were ground using resin bonded grinding wheel and polished using 6 μm and 1 μm diamond paste (R_a between 0.09-0.12 μm). The hardness of the sintered samples was measured using a Vickers macrohardness tester (using a 30 N load) and the coatings were measured with a Vickers micro-hardness tester (2.94 N load). Each hardness measurement was repeated six times on different locations and the average hardness calculated.

In both the sets of sintered hardmetals (supplied by Boart Longyear and Dymet Alloys), samples with Co binders have the highest hardness. The sintered hardmetal WC-5.7Co-0.3Cr has a higher hardness compared to S6 (WC-6Co), despite having similar composition, due to a smaller carbide grain size. The D-gun sprayed WC-10Co-4Cr and HVOF sprayed WC-10Co-4Cr coatings have similar hardness values possibly due to their similar composition.

The microstructure of the samples was observed using a Jeol 6500M Field Emission Gun-Scanning Electron Microscope (FEG-SEM).

3.2.1 Sintered WC-based hardmetals

Figure 3.2 shows a SEM micrograph of a polished surface of sintered WC-5.7Co-0.3Cr sample. The SEM micrograph reveals the skeletal carbide structure, typical of sintered hardmetals. The size of the carbides was 2-3 μm.

3.2.2 Sprayed WC-based hardmetals

Figure 3.3a shows the SEM- backscattered electron image (BEI) image of a polished WC-10Co-4Cr surface. The darker regions in the BEI image represent the heavier elements, such as W, in the composition and the lighter regions represent the lighter elements, such as Co, Cr or Ni, in the composition. The micrograph shows an inhomogeneous distribution of carbide rich and binder rich areas along with the presence of some voids and cracks formed on the surface during the cooling of the coating.

Table 3-1: Mechanical properties and designations of the WC hardmetals and coatings

Designation	Supplier	Hardness Hv	Binder	Composition	Carbide size (μm)	Coating Thickness (μm)	Coating type	Density* g cm^{-3}
S6	Boart Longyear	1550 ± 52	Co	WC-6Co	3-4			15.29
S11	Boart Longyear	1370 ± 46	Co	WC-11Co	3-4			14.94
V12	Boart Longyear	1200 ± 42	Ni	WC-12 Ni	3-4			14.88
P6	Boart Longyear	1100 ± 48	Co-Ni-Cr	WC-6 Co-Ni-Cr	3-4			14.66
WC-5.7Co-0.3Cr	Dymet Alloys	1773 ± 45	Co-Cr	WC-5.7Co-0.3Cr	2.3	-	-	15.28
WC-6Ni	Dymet Alloys	1578 ± 46	Ni	WC-6Ni	2.0	-	-	15.29
WC-10Co-4Cr	Praxair Surface Tech. Ltd.	1114 ± 100	Co-Cr	WC-10Co-4Cr	2-4	250-300	Detonation gun	14.68
G-WC-10Co-4Cr	Greenhey Coatings Ltd.	1065 ± 131	Co-Cr	WC-10Co-4Cr	2-4	250	HVOF	14.68

* *Densities of samples calculated from material composition.*

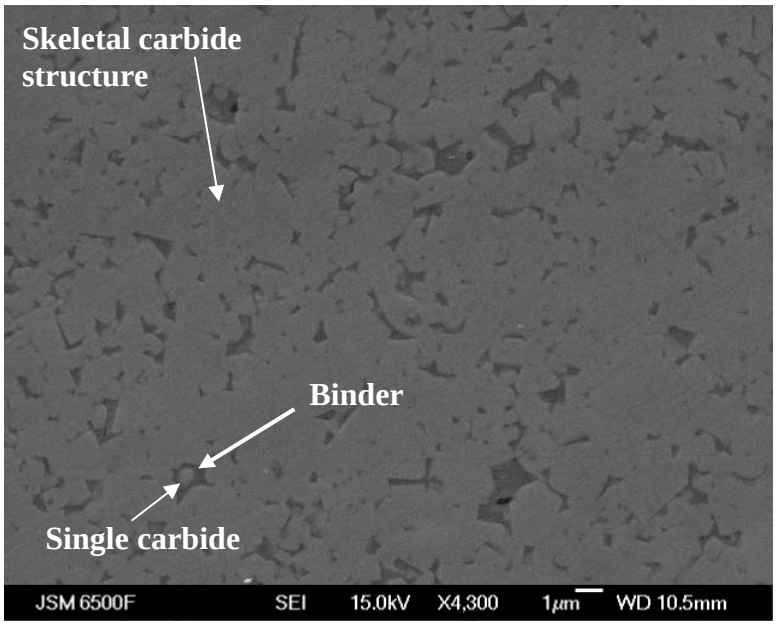

Figure 3.2: Polished surface of a sintered WC-5.7Co-0.3Cr sample showing the typical skeletal structure of the carbides.

The inhomogeneous structure of the coating is also reflected in the larger scatter (± 100 Hv) seen for the hardness measurements of the sprayed coatings compared to the smaller scatter (± 45 HV) seen for sintered samples. The SEM micrograph also reveals the non-uniform size distribution of the carbide grains in the coatings. The coating appears to have larger carbide (3-4 μm) grains towards the centre of the splats and finer carbide grains less than 1 μm in size along the splat boundary. This is likely to occur because of the higher degree of decarburising of WC grains along the splat boundary as the temperature along the splat boundary is expected to be relatively higher than at the centre of the splat. The SEM micrograph of a polished cross-section of WC-10Co-4Cr coating is shown in Figure 3.3b. The cross section also shows the presence of carbide and binder rich areas in the coating along with a possible splat boundary. In general, it was observed that the splats were approximately 50 μm wide and 10 μm thick.

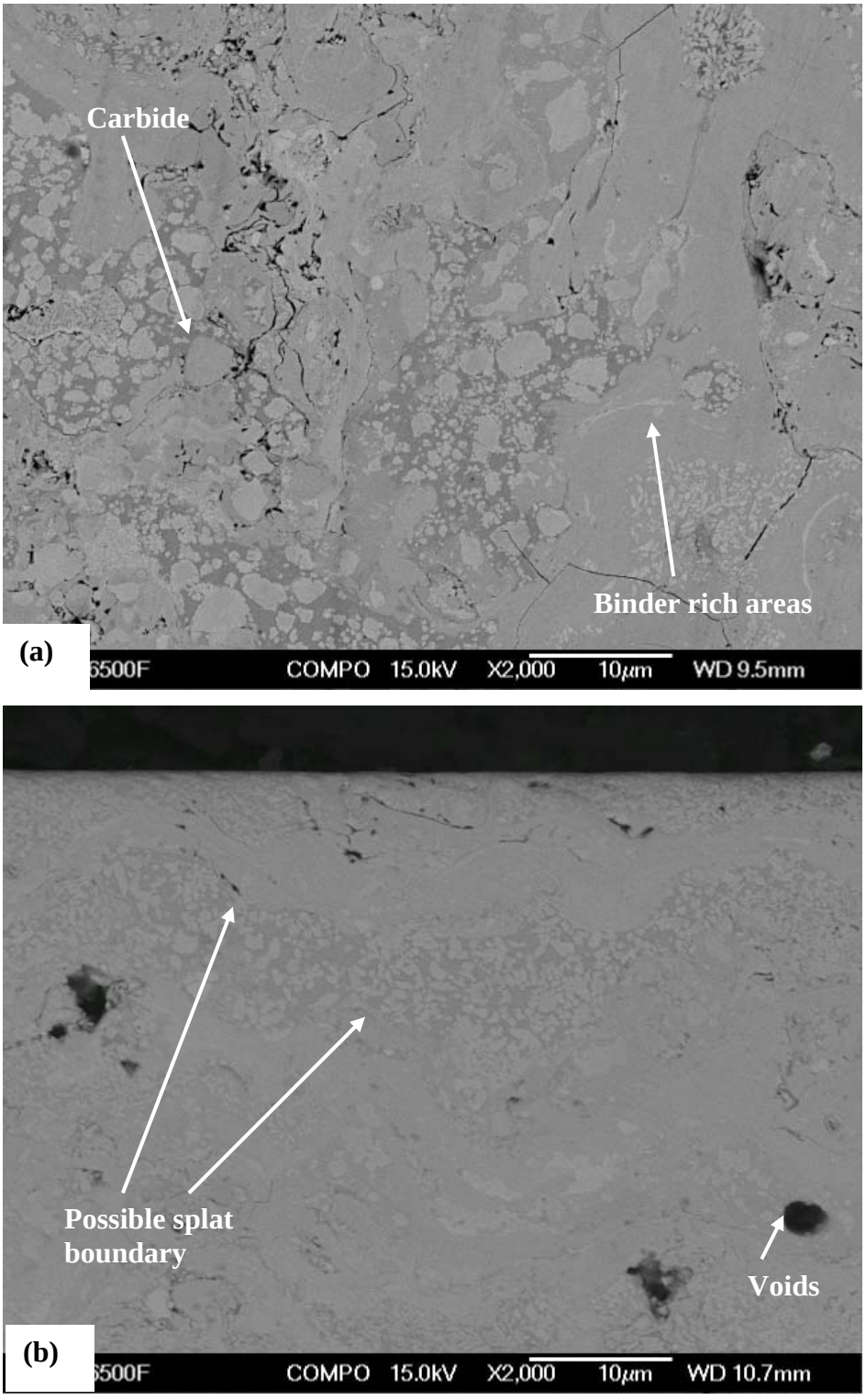

Figure 3.3:SEM micrographs showing (a) SEM (BEI) image of a polished surface of WC-10Co-4Cr and (b) SEM (BEI) image of the polished cross section of WC-10Co-4Cr coating.

3.3 Exposure to test solutions

Downhole drill tool components are exposed to alkaline environments during long service hours and long durations when the tool is idle in downhole conditions. To mimic this exposure, sintered and coated samples of 20 mm x 10 mm were exposed to an alkaline solution prior to wear testing. Samples were either exposed to a Bentonite mud based drilling fluid of pH 11 or a NaOH solution of pH 11 for 168 h (1 week) under naturally aerated conditions at room temperature. The drilling fluid was provided by MI Drilling Fluids (Aberdeen) and was made from Bentonite mud and NaOH solution (the exact composition is commercially sensitive). Prior to exposure, the sprayed sample edges and rear surfaces (substrate) were sealed using a Type 45 stopping off lacquer to prevent galvanic coupling between the substrate and the coating such that only the coated surface of 20 mm x 10 mm was exposed to the test solution. The immersed samples were allowed to freely corrode in the test solution. For comparison, both sintered and sprayed samples were also exposed to distilled water (pH 7) for 1 week prior to micro-abrasion tests.

3.4 Potentiodynamic polarisation

Potentiodynamic polarisation tests were conducted on duplicate samples immersed in a corrosion cell (shown in Figure 2.26, Chapter 2) in the same test solution type as that used for exposure (drilling fluid or NaOH solution). This was done to understand the corrosion kinetics of the exposed samples under static conditions. The corrosion cell comprised of the specimen as the working electrode (WE) held in a Teflon specimen holder, exposing a surface area of 1 cm^2, a graphite rod as the counter electrode (CE) and a 3M silver/silver chloride (Ag/AgCl) reference electrode (3M Ag/AgCl = 0.235 V *vs*. SHE [120]) immersed in the electrolyte. The corrosion cell assembly was placed in a Faraday cage to minimise electrical interferences. The WE was polarised from -0.250 V to 1.00 V at a sweep rate of 1 mV s^{-1} while recording the current density (μA cm^{-2}) using a Gamry Instruments PC4/750 potentiostat and CMS100 software. Potentiodynamic polarisation plots were used to calculate the corrosion potential (E_{corr}) and corrosion current density (i_{corr}) (A cm^{-2}) for all the samples using the Tafel extrapolation method. Using Faraday's law, the average penetration rate ($\Delta x/t$) (cm s^{-1}) was calculated for the known hardmetal density (ρ), on the assumption that the metallic component are oxidised to W^{2+}, Co^{2+}, Cr^{2+} and Ni^{2+} during dissolution and assuming uniform corrosion across the surface of the sample. The corrosion rate (cm s^{-1}) was then converted to *SWR* (m^3 N^{-1} m^{-1}) for known values of sliding distance, load and time, in attempt to compare the loss of material due to pure corrosion with the material loss due to abrasive wear, see Equation 3.1.

$$SWR = \left(\frac{\Delta x}{t}\right)\left(\frac{100 \times t' \times a'}{L \times W}\right) \quad \textbf{3.1}$$

Where, a' is the area in m^2, t' is time in seconds; L is the sliding distance in m and W is the applied load in N for micro-abrasion test. Despite the accurate estimate of mass loss due to corrosion there are some disadvantages of using this procedure. While it assumes uniform corrosion of all the species on the localised sample surface, corrosion actually occurs selectively on the surface due the natural development of active and passive regions.

3.5 Micro-abrasion testing

Micro-abrasion tests were conducted using a TE66 micro-scale abrasion tester (Phoenix Tribology Ltd., Newbury, UK.) developed by Rutherford and Hutchings [153]. A schematic of the apparatus is shown in Figure 2.21, Chapter 2. Samples were mounted on the pivoted arm to allow a point contact between the sample and the ball which is clamped between coaxial shafts. Abrasive slurry is entrained between the ball and the specimen by means of a peristaltic pump which is part of the test rig.

To mimic micro-scale wear in downhole environments of pH 11, micro-abrasion-corrosion tests were conducted with a slurry of SiC particles (Grade F1200, Washington Mills Ltd. Manchester, UK) suspended in a NaOH test solution (pH 11). The mean SiC abrasive particle size was 4.5 μm (Figure 3.4). Micro-abrasion-corrosion tests were conducted on both freshly polished surfaces and samples exposed to alkaline conditions for 1 week. Details of the test conditions are presented in Table 3-2. For comparison, micro-abrasion tests were also conducted on fresh (polished to 1 μm diamond finish) samples with an abrasive slurry of SiC particles suspended in a distilled water (pH 7.0). A constant applied load of 0.2 N and 0.166 v/v abrasive volume fraction (129 g of SiC suspended in 200 ml solution) were used in order to produce three-body rolling wear [49]. Each sample was tested for a sliding distance over a range of 30 m to 90 m. This was done to achieve wear scar depth ranging from 1-10 carbides deep. In order to perform abrasion tests with corrosive media and maintain a constant surface finish, a zirconia ball of 25.4 mm diameter (R_a =0.043 μm) was used as counterface material. The ball rotation speed was kept constant at 0.05 m s^{-1} while the abrasive slurry was fed at a constant feed rate of 0.1 cm^3 s^{-1}. Prior to the actual tests, the ball was conditioned by running against sintered WC samples with identical test conditions, in order to produce 3-4 wear tracks on the ball.

Table 3-2: Test conditions used for micro-abrasion testing

Load	0.2 N
Abrasive slurry	SiC particles (mean particle size of 4.5 μm, standard deviation ±1.3 μm [49]) suspended in NaOH solution of pH 11 or distilled H_2O.
Slurry concentration (v/v)	0.166
Slurry feed rate	0.1 cm^3 s^{-1}
Counterface material	Zirconia (Hardness = 1150 HV, R_a =0.043 μm)
Counterface ball diameter	25.4 mm
Speed of rotation	0.05 m s^{-1}
Sliding distances	30 m, 45 m, 60 m, 75 m, 90 m

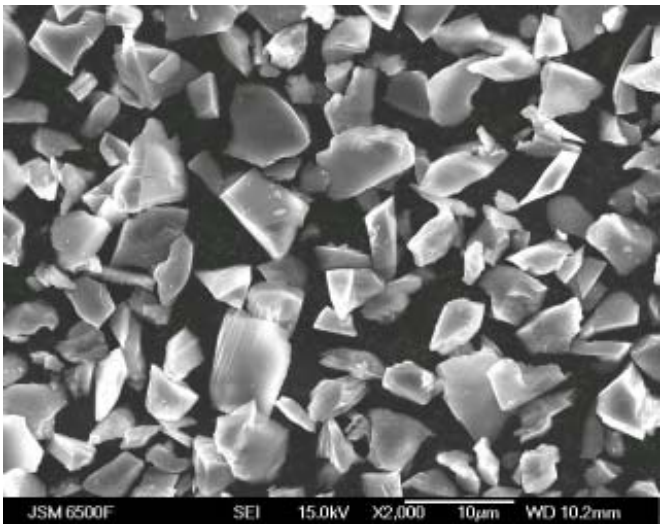

Figure 3.4: SEM micrograph of SiC abrasives.

The resultant wear scars, in the form of a spherical cap were measured using an optical microscope mounted on the rig. The wear volume and *SWR* were calculated as explained in Section 2.2.5.2, Chapter 2. Further analysis was done on the wear scars by examining them under a FEG-SEM and selected samples were scanned using a TaiCaan optical surface profiler or a Taylor Hobson 2-D Talysurf 120L surface profilometer.

3.6 Anodic treatment of WC-10Co-4Cr coated samples

Anodic treatment of WC-10Co-4Cr samples was achieved by holding the samples potentiostatically at 0.20 V above the open circuit potential, i.e. E_{corr} measured in NaOH solution i.e. in the active region as shown in the potentiodynamic polarisation plot in Figure 3.5 (see, Figure 2.27 for the different regions on the polarisation plot). Anodic treatments were performed using a Gamry Instruments PC4/750 potentiostat and ESA400 software. The experimental set-up of anodising the samples was similar to that previously described in section 3.4. Duplicate samples were anodised for a duration of 1 h and 24 h. Micro-abrasion tests were conducted on one set of samples and potentiodynamic polarisation tests were conducted on the other.

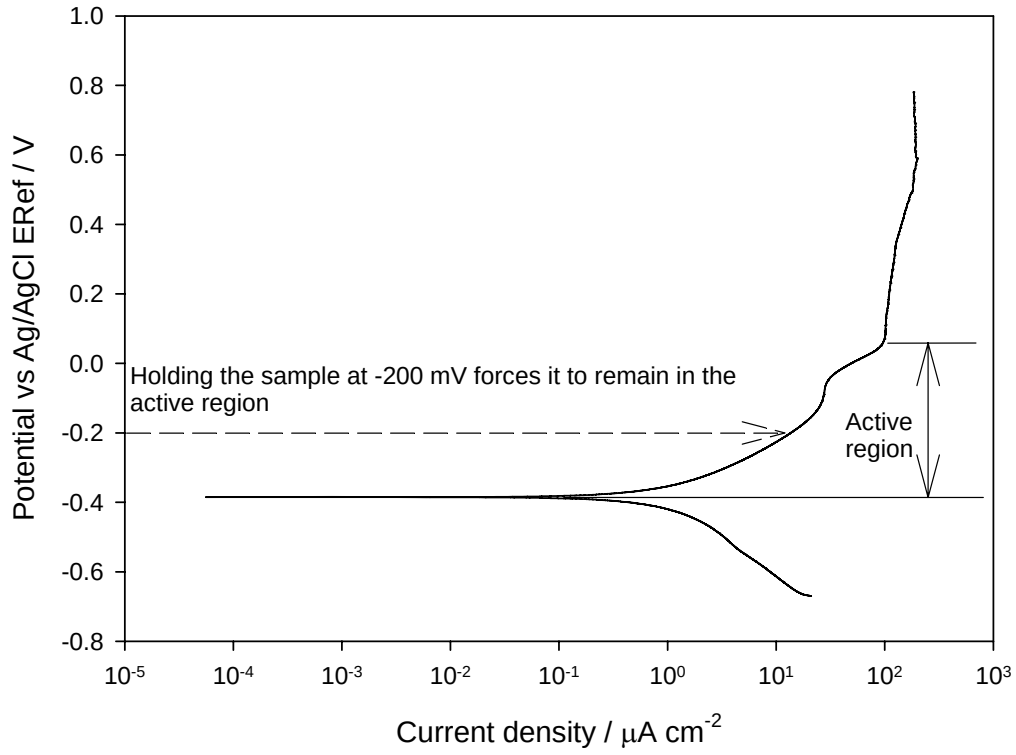

Figure 3.5: Potentiodynamic polarisation plot for a fresh WC-10Co-4Cr coated sample in pH 11 NaOH solution at room temperature showing active region and the potential at which the samples were anodised.

3.7 XPS of fresh and exposed samples

X-ray photoelectron spectroscopy (XPS) was carried out on fresh and exposed (pH 7 and pH 11) samples of WC-10Co-4Cr coating. For comparison, XPS analysis was also done on fresh

and exposed (pH 7 and pH 11) samples of sintered WC-5.7Co-0.3Cr. XPS analysis was done using a Scienta ESCA300 spectrometer (monochromatic Al Kα radiation at 14 keV and 200 mA) at the National Centre for Electron Spectroscopy and Surface Analysis (NCESS), Daresbury Laboratory, UK. A pass energy of 300 eV was used for the survey spectra and 150 eV for the high-resolution spectra scans of selected regions. The slit width of the electron analyser was set at 1.9 mm for the former and 0.5 mm for the latter. Take-off-angles relative to specimen surfaces of 45º and 90º were employed. Charge compensation was accomplished with an electron flood gun operating at an electron energy of 4 eV-6 eV. The carbon C1s line at 285 eV was used to reference the spectra. The relative concentrations of the elements were calculated using appropriate atomic sensitivity factors specific to the Scienta ESCA300. Curve fitting after background subtraction was conducted assuming a complex mixed Gaussian–Lorentzian peak shape.

3.8 Focussed ion beam (FIB) sectioning of exposed WC-10Co-4Cr coating

FIB sectioning of the WC-10Co-4Cr coated samples exposed to pH 11 NaOH solution allowed the corrosion features of corroded WC grains to be observed in cross-section. The FIB sectioning was done using a Nova Nanolab200 Small Dual Beam (SDB). Prior to FIB preparation, a thin layer of Pt was deposited on the whole sample in a sputter coater to avoid charging. After this deposition a 1.5 μm Pt layer is deposited in the FIB on the region of interest to protect the sample during FIB milling. Using the FIB it is possible to mill a hole in the surface with one steep edge (oriented perpendicular to the sample surface) at the region of interest and a step like construction at the opposite side. In this way it is possible to make a cross-section which can be studied by tilting the sample. The milling is done using 30 kV Ga-ions. Figure 3.6 shows the SEM micrograph of a milled slot.

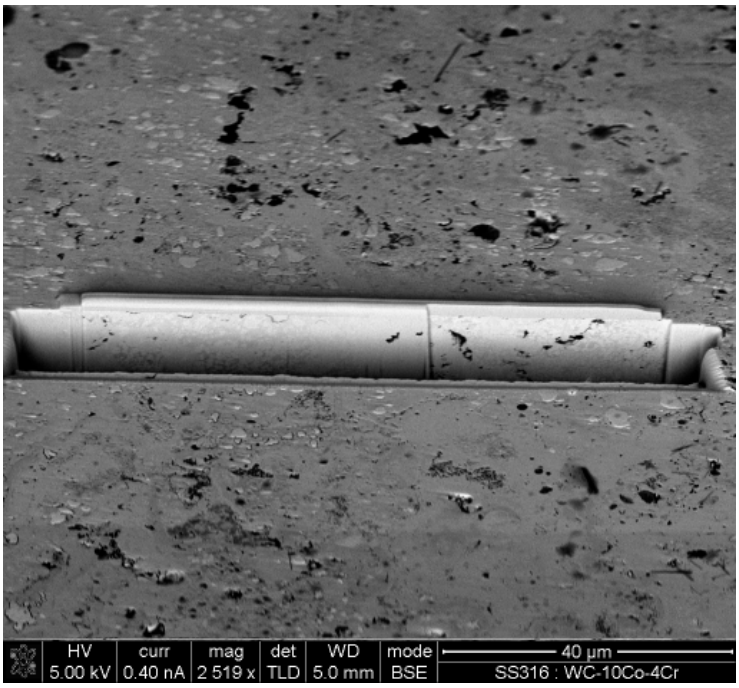

Figure 3.6: SEM micrograph of the WC-10Co-4Cr coated sample showing the focussed-ion beam milled slot.

3.9 Micro-abrasion with *in situ* electrochemical current noise measurements

Figure 3.7 shows the modified micro-abrasion tester capable of *in situ* electrochemical current noise measurements. It combines the conventional micro-abrasion tester (shown in Figure 2.21, Chapter 2) with a three-electrode corrosion cell (shown in Figure 2.26, Chapter 2). The arm was made of polymer and had no metal fixtures to ensure electrical isolation of the electrodes embedded on it. A platinised titanium counter electrode (William Gregor Limited, UK) of dimensions 20 mm x 20 mm and a modified Ag/AgCl reference electrode were embedded in the micro-abrasion tester. A working electrode was connected to the back of the sample being worn (dimensions 10 mm x 20 mm) by means of a spring. The sample was secured to the arm by means of two Derylin clamps and screws. A non-corrosive silicone rubber sealant (RS) was used to seal the rear of the sample to prevent the slurry from seeping into the electrical contact. The edges of the samples were masked off using a Type 45 stopping off lacquer to prevent galvanic coupling between the coating and UNSS316 stainless steel substrate. The three electrodes were connected to a potentiostat and using ESA400 software such that potential could be applied to the working electrode during the micro-abrasion test. To maintain a continuous electrical contact between the three electrodes, the setup was immersed in a slurry tank, as shown in the Figure 3.7. The liquid level in the tank was maintained by means of a draining pipe. This is to ensure that the area of working electrode exposed to the solution in the tank (10 mm x 5 mm) remains constant throughout the duration of the test. The height of the liquid level in the tank was maintained such that the contact between the rotating ball and the sample occurred above the liquid level. This was to ensure comparability with the conventional arm in terms of contact conditions and slurry entrainment between the ball and the sample. Details of the test conditions and the various wear-corrosion interaction components assessed using the modified arm are tabulated in Table 3-3 and 3-4, respectively.

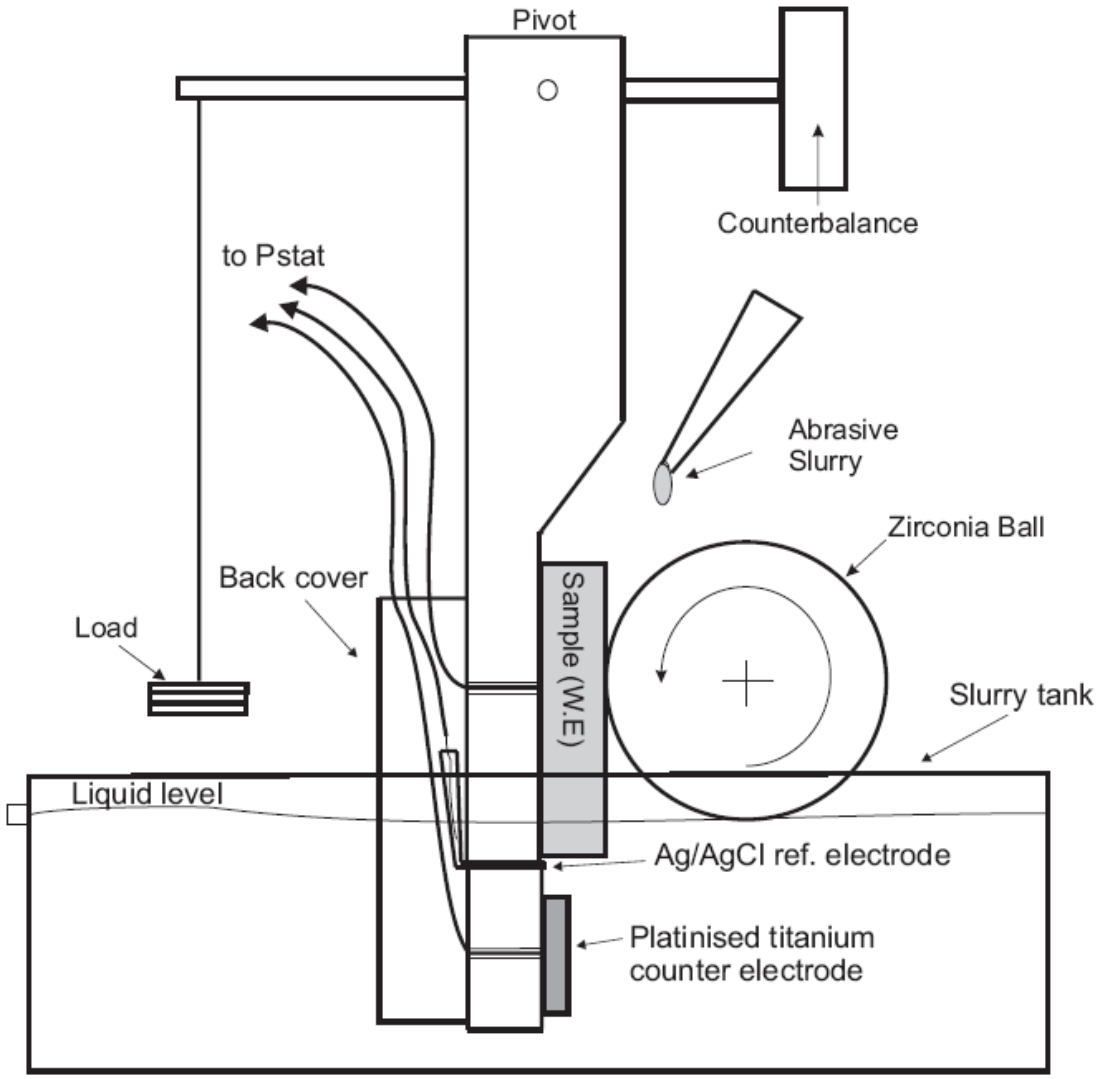

Figure 3.7: Modified micro-abrasion tester with slurry tank and electrochemical cell added to a conventional micro-abrasion arm.

Table 3-3: Test conditions used for micro-abrasion test with *in situ* electrochemical current noise measurements

Load	0.2 N
Abrasive slurry	SiC particles (mean particle size of 4.5 μm) suspended in NaOH + $NaNO_3$ (0.1M) solution of pH 11 or $NaNO_3$ (0.1 M) of pH 7.
Slurry concentration (v/v)	0.166
Slurry feed rate	0.1 cm^3 s^{-1}
Counterface material	Zirconia (Hardness = 1150 HV, R_a =0.043 μm)
Counterface ball diameter	25.4 mm
Speed of rotation	0.05 m s^{-1}
Sliding distances	37.8 m
Electrochemical condition	Samples held at their OCP (abrasion-corrosion) or cathodic protection (CP) applied (pure abrasion)

Table 3-4: Wear-corrosion interaction components and corresponding test conditions

Wear-corrosion components (SWR / m^3 N^{-1} m^{-1})	**Component details**	**Test conditions**
SWR_{Total}	Total wear under abrasion-corrosion condition	Calculated from the wear-scar area at the end of abrasion-corrosion test
SWR_{Elec}	Electrochemical component of total wear	Calculated using the electrochemical current noise data obtained during abrasion-corrosion test (Faraday's law).
SWR_{Mech}	Mechanical component of total wear	$SWR_{Mech} = SWR_{Total} - SWR_{Elec}$ [136]

Due to the low electrical conductivity of NaOH solution of pH 11, a background electrolyte was added to improve the electrical conductivity. 0.1 M solution of $NaNO_3$ was added to 1M NaOH solution and adjusted to give different pH levels between pH 7 and pH 13, see Table 3-5. The conductivity of the solutions prepared is given in Table 3-5. To ensure that there was no influence of the background electrolyte on corrosion behaviour; static potentiodynamic polarisation tests were carried out in the buffered solution and compared with the potentiodynamic polarisation tests done in ph 11 NaOH solution, see Figure 3.8.

Table 3-5: Electrical conductivity of different solutions used for micro-abrasion testing

Solution	pH	Conductivity
NaOH	pH 11	0.6 mS cm^{-1}
Distilled water	pH 7	0.05 mS cm^{-1}
$NaNO_3$ (0.1 M)	pH 7	10.3 mS cm^{-1}
NaOH +$NaNO_3$ (0.1 M)*	pH 9	9.2 mS cm^{-1}
NaOH +$NaNO_3$ (0.1 M)*	pH 11	9.4 mS cm^{-1}
NaOH +$NaNO_3$ (0.1 M)*	pH 13	32.6 mS cm^{-1}

** Desired pH achieved by varying the amount of 1M NaOH added to a 0.1M $NaNO_3$ solution.*

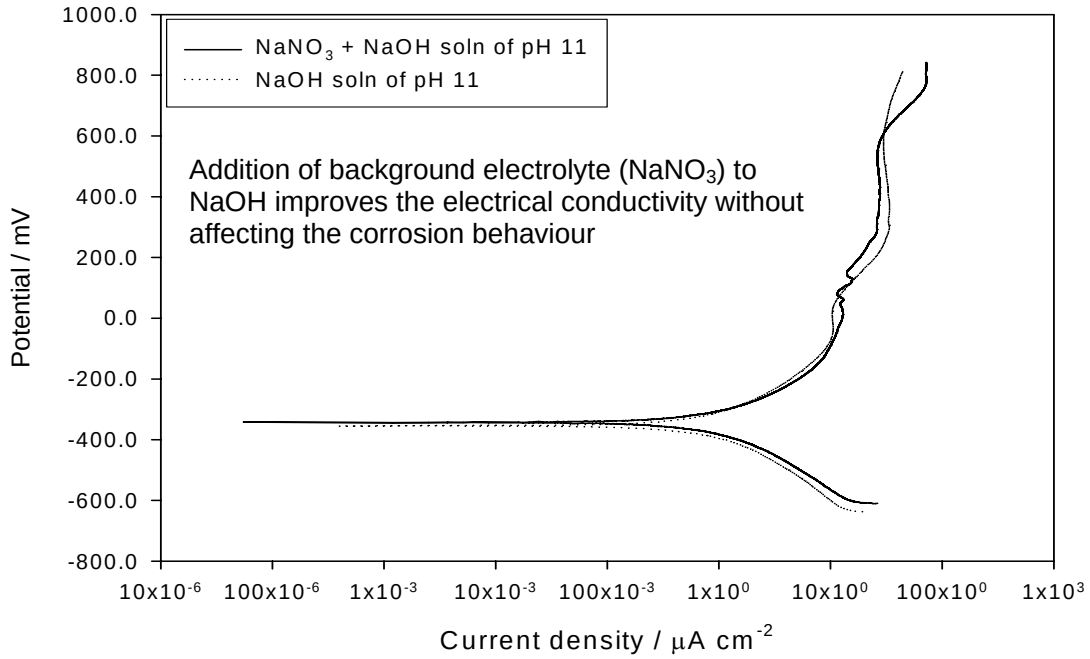

Figure 3.8: Potentiodynamic polarisation curves for WC-10Co-4Cr coated samples with and without the background electrolyte, pH 11.

3.10 Macro-abrasion test (modified ASTM G65, NPL)

Figure 3.9 shows the schematic of the modified ASTM G65 test system. It consists of a sample pressed against a Chlorobutyl rubber (Shore hardness A-60) rimmed steel wheel of 220 mm diameter under dead-weight loading. The thickness and the width of the rubber rim was 12.5 mm. A constant load of 20 N was applied for the duration of the test. The sliding distance selected for the test was 942 m. For the first time, SiC abrasives of 4.5 μm, 17.5 μm

and 180 μm in size were used in this test. Abrasives were fed onto the rubber wheel from a hopper using a slotted drum mechanism. The drum rotation speed was maintained such that abrasives were fed at a constant feed rate of 120 g min^{-1}. To replicate downhole conditions, the tests were carried out under wet conditions.

A fluid feed located in front of the abrasive feed with the nozzle placed close to the test wheel was used to feed NaOH solution of pH 11 directly on the rubber wheel. To replicate prolonged exposure to alkaline conditions as expected downhole, selected samples were exposed to NaOH solution of pH 11 for 168 h prior to testing. For comparison, wear tests were also conducted using distilled H_2O of pH 7. Due to the inconsistent flow of 4.5 μm SiC abrasives under dry conditions, they were pre-mixed in the liquid slurry and fed along with the liquid feed instead of the hopper-slotted drum mechanism.

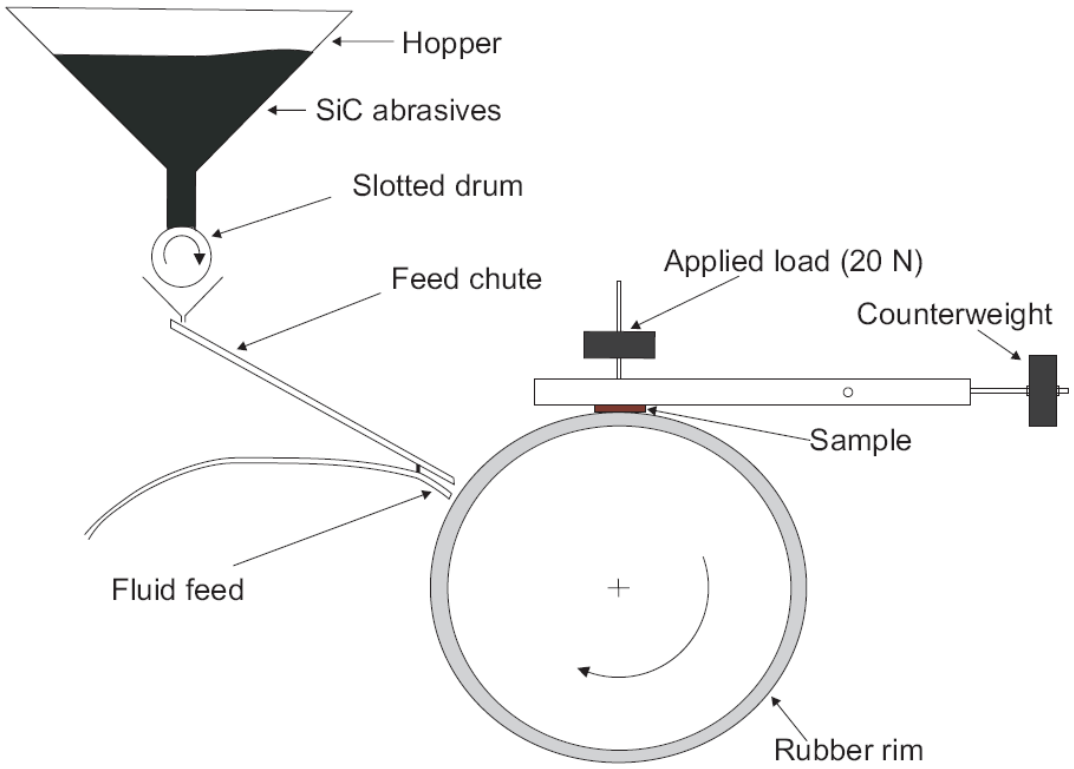

Figure 3.9: Modified ASTM G65 test rig, NPL.

Table 3-6: Test conditions used during macro-abrasion testing

Load	20 N
Fluid feed	NaOH solution of pH 11 or distilled water.
Abrasives	SiC abrasives
Abrasive size/ feed	180 μm (fed via hopper), 17.5 μm (fed via hopper), 4.5 μm (pre-mixed slurry)
Abrasive feed rate	120 g min^{-1}
Slurry feed rate	180 cm^3 min^{-1}
Counterface material	Chlorobutyl rubber (Shore hardness A-60)
Wheel diameter	228 mm
Speed of rotation	0.7 m s^{-1}
Sliding distances	942 m

A detailed test matrix is shown in Table 3-6. SEM micrographs of the three different abrasives used for the test are shown in Figure 3.10. The shape and the angularity of the three abrasives appear to be very similar despite the difference in their sizes. Samples of dimensions 40 mm x 20 mm x 5 mm were used for the macro-testing. The test samples were ground using a resin bonded grinding wheel and polished using 6 μm and 1 μm diamond paste. The process of grinding is likely to generate residual stress in WC samples. However, some residual stress relieving is achieved by polishing the ground samples [154]. Prior to wear testing the samples were cleaned with acetone, dried and weighed using a weighing scale (least count: 0.01 mg). This procedure was repeated after the test and mass loss was for each sample was measured. Each measurement was repeated five times. The specific wear rate (m^3 N^{-1} m^{-1}) was calculated by converting mass loss to volume loss (for known density) and dividing by the sliding distance (942 m) and applied load (20 N).

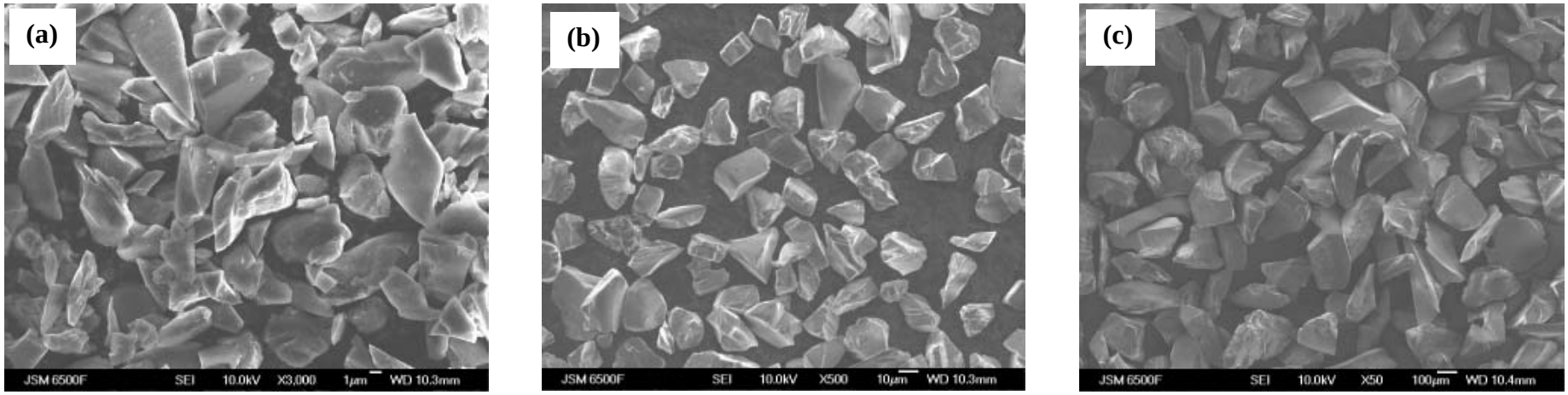

Figure 3.10: Comparison of the abrasives used for the macro-abrasion tests on the modified ASTM G65 rig; (a) 4.5 μm, (b) 17.5 μm and (c) 180 μm abrasive.

3.11 Sample nomenclature

Chapters 5, 6, 7 and 8 discuss the wear-corrosion and static corrosion tests conducted on sintered as well as sprayed samples. For clarity, all the samples are designated according to their nominal composition (see Table 3-1) followed by the test conditions used (e.g. fresh/ exposed, abrasion using pH 7 / pH 11 slurry). All possible sample conditions are tabulated in Table 3-7. For example, WC-10Co-4Cr coating exposed to drilling fluid for 168 h is referred to as WC-10Co-4Cr-df-exp.

Table 3-7: List of tests conducted and sample notations used.

Sample notation	**Condition**
pH 7	Fresh sample abraded using pH 7 distilled water based slurry.
pH 7-exp	Sample exposed to pH 7 distilled water and abraded using pH 7 distilled water based slurry
pH 9	Fresh sample abraded using pH 9 NaOH based slurry.
pH 11	Fresh sample polarised using pH 11 NaOH electrolyte / abraded using pH 11 NaOH slurry
pH 11-exp	Sample exposed to pH 11 NaOH solution for 168 h, polarised using pH 11 NaOH electrolyte / abraded using pH 11 NaOH slurry
df	Fresh sample polarised using pH 11 drilling fluid (*for abrasion refer to pH 11*)
df-exp	Sample exposed to pH 11 drilling fluid for 168 h, polarised using pH 11 drilling fluid / abraded using pH 11 NaOH slurry
pH 13	Fresh sample abraded using pH 9 NaOH based slurry.
anodic-1h	Sample anodically treated in pH 11 NaOH solution for 1 h, polarised using pH 11 NaOH electrolyte / abraded using pH 11 NaOH slurry
anodic-24h	Sample anodically treated in pH 11 NaOH solution for 24 h, polarised using pH 11 NaOH electrolyte / abraded using pH 11 NaOH slurry

4 Initial work

4.1 Preliminary test 1: silica sand abrasives in micro-abrasion

4.1.1 Introduction

As discussed in the Introduction (Chapter 1), the 3rd year undergraduate project [8] sponsored by Schlumberger assessed the feasibility of using silica sand (SiO_2) and Bentonite mud based drilling fluid as an abrasive slurry in the micro-abrasion wear test. The 3rd year project aimed at mimicking the wear in downhole conditions by incorporating downhole environment (silica sand and drilling fluid) into a highly reliable wear test. However, the presence of the non-Newtonian drilling fluid in the abrasive slurry altered the contact conditions during the test and adversely affected the repeatability of the micro-abrasion test.

Hence, this initial test aimed at further simplifying the contact conditions by using an abrasive slurry of silica sand particles suspended in distilled water to assess the effectiveness of silica sand as abrasives for micro-abrasion test. In order to do this, a series of test were conducted on SS316 samples using SiO_2 abrasives instead of the conventional SiC abrasives.

Table 4-1: Comparison of test conditions for the preliminary tests with Bello *et al.* [155]

	Preliminary Test	**Bello *et al.*[155]**
Sample Material	SS 316	SS 316
Abrasive Slurry	Silica sand + distilled water (5-50 μm size distribution)	SiC + distilled water (4.2 μm -average particle size)
Counterface material	Zirconia (d = 25.4 mm Hardness = 1150 HV)	Alumina (d = 22 mm, Hardness = 980 HV)
Loads used	0.25 N	0.25 N
Slurry Concentrations (v/v)	0.006, 0.030, 0.072, 0.135, 0.238	0.006, 0.030, 0.072, 0.135, 0.238
Sliding Distances	37.8 m, 180 m	37.8 m, 180 m
Ball Speed	0.05 m s^{-1}	0.05 m s^{-1}
Slurry feed rate	0.1 cm^3 s^{-1}	0.1 cm^3 s^{-1}

All other test conditions used (see Table 4-1) were same as those used in a study done by Bello *et al.* [155] on the wear-corrosion of SS316. Prior to the micro-abrasion testing, the

SS316 samples were ground (coarse and fine) using SiC abrasive paper and polished using 1 μm diamond paste. The micro-abrasion test conditions used for this preliminary study are tabulated in Table 4-1.

4.1.2 Results and Discussion

The results obtained by Bello *et al.* [155] follow the Adachi-Hutchings wear model and show a transition from grooving (2-B) to rolling (3-B) mode of abrasion as the slurry concentration increases. The increase in the slurry concentration also results in an increase in the wear as seen from the graph of specific wear rate vs. slurry concentration, Figure 4.1. However, such a trend was not visible in the tests done using SiO_2 abrasives. Figure 4.2 compares the SEM of wear scars using SiC and SiO_2 abrasives for different volume concentrations. At low concentrations (0.006), SiC abrasives result in 2-B grooving (Figure 4.2a) while the SiO_2 abrasives result in mixed mode (Figure 4.2d). The wear scar (Figure 4.2d) shows multiple indents, characteristic of 3-B rolling and a random distribution of 2-B grooves. The clear transition from 2-B grooving to 3-B rolling seen for samples worn by SiC abrasives (Figure 4.2a- 4.2c) is absent for the samples worn by SiO_2 abrasives. This lack of wear mode transition resulted in similar wear rates being observed for all slurry concentrations of SiO_2 abrasives hence do not follow the prediction of the Adachi-Hutchings wear mode map [49] for micro-abrasion. The failure of the SiO_2 abrasives to follow the wear mode transition was due to the lack of consistent entrainment into the ball-sample contact during micro-abrasion test, which resulted from an uneven size distribution of SiO_2, see Figure 4.3.

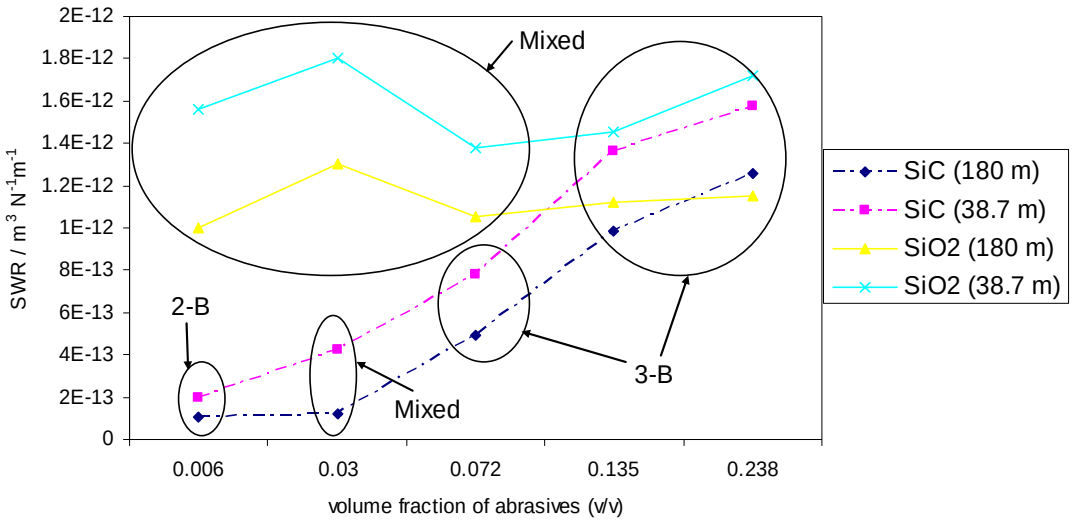

Figure 4.1: *SWR* against concentration plotted for SiC and SiO_2 abrasives showing the difference in the wear rates and wear modes on SS316 samples for identical test conditions.

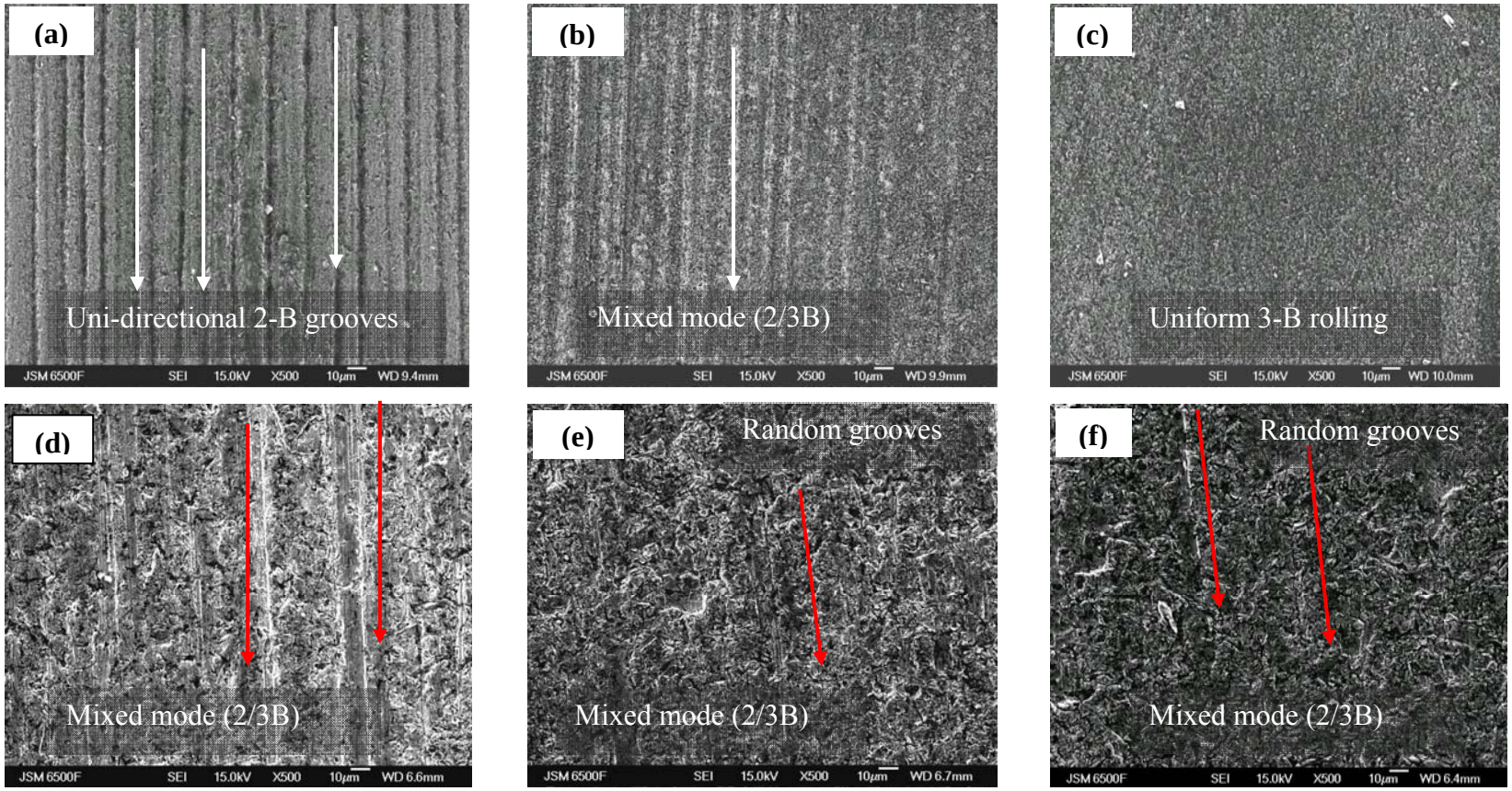

Figure 4.2: SEM micrographs of SS316 stainless steel abraded using (a) 0.006, (b) 0.03, (c) 0.135 volume fractions of SiC abrasives suspended in distilled water; SEM micrographs of SS316 abraded using (d) 0.006, (e) 0.03 and (f) 0.135 volume fractions of SiO_2 abrasives suspended in distilled water.

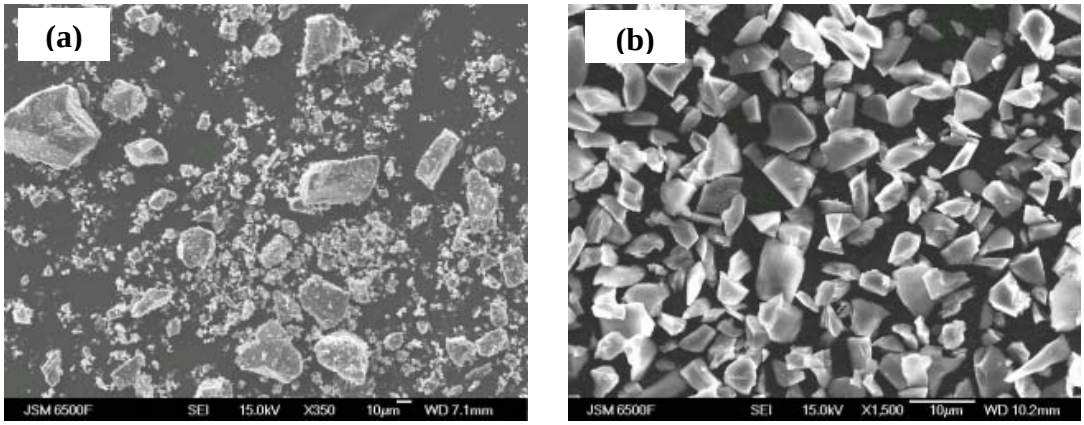

Figure 4.3: Size distribution of (a) SiO_2 and (b) 4.5 μm SiC abrasives.

The results also demonstrated the inability of micro-abrasion tester to accommodate abrasives with uneven size distribution and for more consistent results it was necessary to use abrasives with a controlled size distribution. Study of available abrasives showed that it was very difficult to obtain silica sand of 5 μm size (controlled size distribution). For this reason, it was decided to use F1200 grade black SiC abrasives with mean particle size of 4.5 μm for subsequent micro-scale abrasion testing. It was also obvious from the preliminary tests that abrasive particles of different size are likely to result in different *SWR*, further justifying the need for a dual approach, discussed in Chapter 1. Clearly, the micro-abrasion tester was inadequate to test abrasive wear by large abrasives (≤10 μm). Hence, the modified ASTM G65 tester was needed to study the wear-corrosion performance of candidate materials using large abrasives.

4.2 Preliminary test 2: micro-abrasion of WC-based hardmetals exposed to NaOH solution

4.2.1 Introduction

The literature review suggests that the corrosion rates of WC-based hardmetals in alkaline conditions are very low as compared to acidic conditions [103]. However, some workers have found high wear rates when using alkaline slurries, similar to those observed using acidic slurries [135] suggesting a strong influence of wear-corrosion interaction. Hence it was necessary to evaluate the synergistic effects of exposure to alkaline conditions on the abrasive wear resistance of WC-based hardmetals. Due to the long duration of exposure of wear resistant materials to alkaline environments in downhole conditions, selected samples were exposed to NaOH solution (pH 11) for 168 h, prior to micro-abrasion test. The duration of exposure was fixed as 168 h was representative of 1 week of idle time in downhole condition.

The test programme comprised of the following three tests.

- Static immersion of WC samples in NaOH (pH 11) solution for 168 h.
- Micro-abrasion tests on exposed WC samples using NaOH (pH 11) + SiC abrasives (0.16 v/v).
- Micro-abrasion tests on fresh WC samples using NaOH (pH 11) + SiC (abrasion-corrosion) and distilled water + SiC abrasives (0.16 v/v).

WC-based hardmetals available within the Surface Engineering and Tribology group were selected for the trial tests. Details of the samples used for this test, sintered S6, S11, V12, P6 and D-gun sprayed WC-10Co-4Cr are given in Table 3-1 in Chapter 3. The micro-abrasion test conditions used for the test are tabulated in Table3-2 in Chapter 3.

4.2.2 Results and Discussion

Figure 4.3 shows the *SWR* obtained by the four samples under different conditions. Clearly, for all the sintered hardmetals tested, exposure to pH 11 NaOH solution resulted in an increase in *SWR*. Interestingly, the lowest *SWR* among the sintered samples was observed for the Co-based S6. Despite corrosion resistant binders, the V12 (12% Ni) and P6(6% Co-Ni-Cr) show higher *SWR* as compared to the Co-based S6 and S11. Human *et al.*[147] observed that under abrasion dominated conditions, binders with higher wear-resistance and better binder-carbide interfacial bonding are likely to result in lower wear rates than corrosion resistant binders. Interestingly, V12 and P6 have similar *SWR* for pH 7 and pH 11

conditions, indicating that change in the pH of abrasive slurry does not significantly influence their wear mechanisms. However, both V12 and P6 show a sharp increase in the *SWR* after exposure to pH11 NaOH for 168 h. Clearly, the prolonged exposure to alkaline conditions possibly accelerates the binder dissolution and results in an increase in *SWR*. The wear-corrosion resistance of Co-based S6 was found to be promising and needed to be investigated further. Contrary to the expectations, WC-10Co-4Cr coating showed a lower *SWR* after exposure to pH 11 NaOH solution. The wear resistance of WC-10Co-4Cr coating shows an improvement, i.e. decrease in *SWR*, when the abrasive slurry is changed from neutral to alkaline. This is likely to be due to the influence of the passive films formed on the binder-rich regions which alter the contact conditions during abrasive wear.

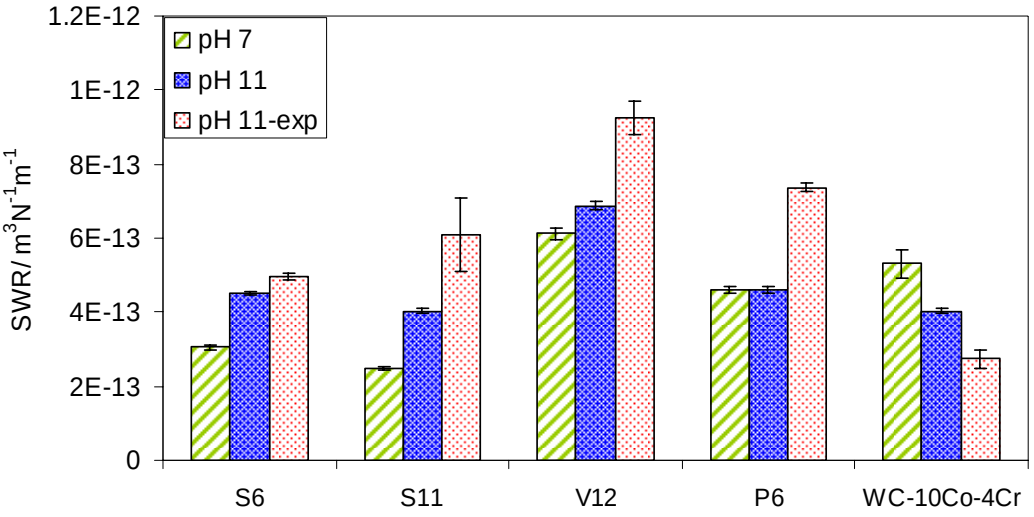

Figure 4.4: Comparison of *SWR* for the selected materials under fresh and pre-exposed conditions.

Clearly, using alkaline abrasive slurry and prolonged exposure to alkaline conditions result in an increase in the *SWR* for sintered hardmetals. Interestingly, the WC-10Co-4Cr coating showed improvement in its wear-corrosion performance after exposure to NaOH solution. The possible corrosion interactions occurring on the surface of WC-based sintered hardmetals and sprayed coatings need detailed investigation using electrochemical techniques. The possible influences of surface corrosion on the wear-corrosion interactions need to be analysed using SEM analysis and surface profilometry techniques. It was also necessary to investigated if similar wear-corrosion interactions were observed after exposure to Bentonite mud based alkaline drilling fluid.

4.3 Conclusions

- Uneven size distribution of silica sand hampers the consistent entrainment of particles during micro-abrasion tests.

- For consistent entrainment of abrasives during micro-abrasion tests, 4.5 μm SiC abrasives need to be used for subsequent wear-corrosion tests.

- Abrasive particles of different size are likely to result in different *SWR*, further justifying the need for a dual approach discussed in Chapter 1.

- The second trial test demonstrated that the pH of abrasive slurry and exposure to alkaline solution strongly influences the *SWR*. It was necessary to evaluate if the observed wear-corrosion interactions were repeatable in drilling fluid of pH 11.

- Sintered WC-6Co (equivalent to S6) and D-gun sprayed WC-10Co-4Cr coating are obvious candidate materials for subsequent wear-corrosion tests. For comparison, sintered WC-6Ni and HVOF sprayed WC-10Co-4Cr need to be tested.

5 Exposure to drilling fluid and micro-abrasion

5.1 Introduction

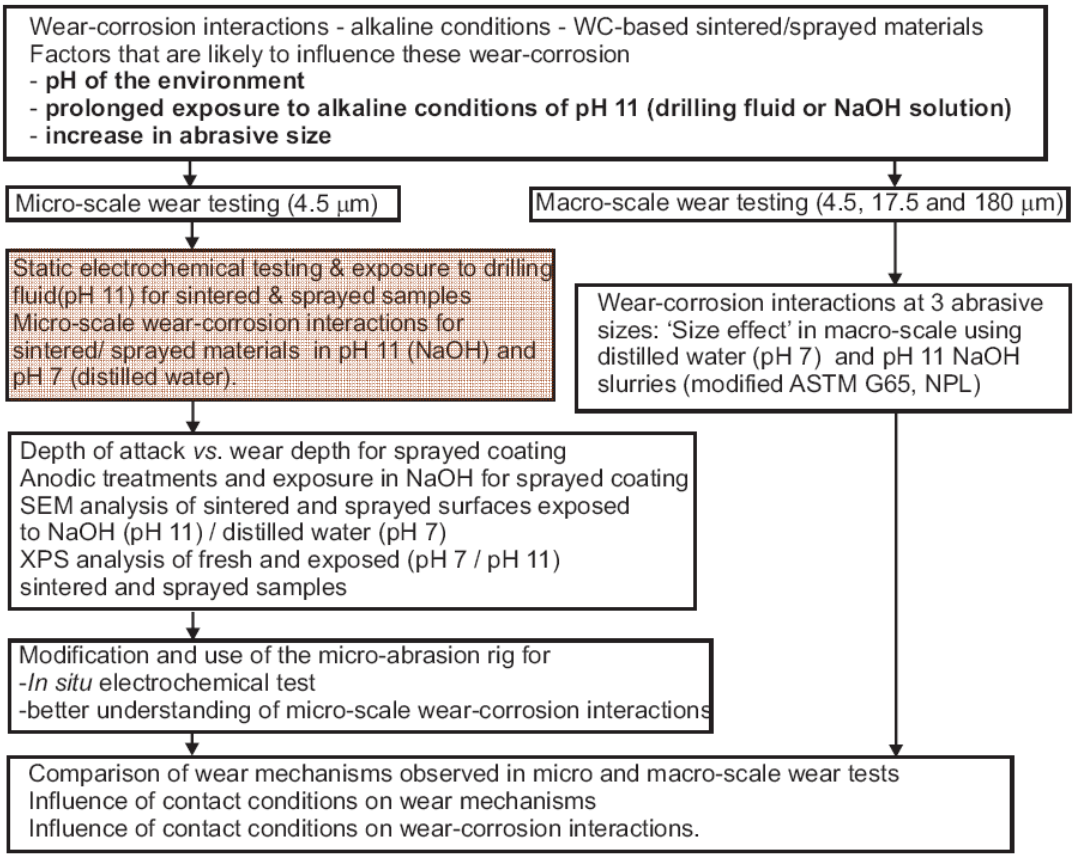

Figure 5.1: Experimental flow chart showing the test programme discussed in Chapter 5 (highlighted).

The preliminary tests detailed in Chapter 4 demonstrated that micro-abrasion tests on sintered samples exposed to pH 11 NaOH solution resulted in an increase in the *SWR* compared to pH 7 samples. Interestingly, for the D-gun sprayed WC-10Co-4Cr coating, a decrease in *SWR* was observed for samples exposed to pH 11NaOH solution. Clearly, exposure to NaOH solution led to an added wear resistance. The preliminary tests also compared the wear-corrosion performance of sintered hardmetals with different binder compositions. The performance of these hardmetals informed the selection of hardmetals to be tested in this Chapter. The aim of this Chapter was to investigate the effects of exposure to a pH 11 alkaline drilling fluid on the wear-corrosion interactions of selected WC-based hardmetals and coatings. Electrochemical techniques such as potentiodynamic polarisation test and surface characterisation techniques such as SEM microscopy and 2-D surface profilometry were used to investigate the corrosion and wear-corrosion mechanisms

observed. This chapter presents the details of exposure to drilling fluid, potentiodynamic polarisation at 0h and 168h after exposure and the micro-abrasion tests conducted on the fresh and exposed samples using pH 11 (NaOH based) and pH 7 (distilled water based) slurries.

The Co-based S6 tested in Chapter 4 resulted in the least *SWR*. A sintered hardmetal with similar composition (WC-5.7Co-0.3Cr) was selected for this test programme. For comparison, a Ni-based hardmetal (WC-6Ni) with similar binder content and carbide size was selected. Both the sintered hardmetals were supplied by Dymet Alloys, UK. Due to the interesting performance of the D-gun sprayed WC-10Co-4Cr coating, it was retained for this test programme. For comparison, a HVOF coating with identical nominal composition was selected (WC-10Co-4Cr). The coatings, WC-10Co-4Cr (D-gun sprayed) and G-WC-10Co-4Cr (HVOF) were supplied by Praxair Surface Technologies Ltd (D-Gun) and Greenhey Engineering Services (G-gun, HVOF), respectively. Details of the properties, composition and designations are given in Table 3-1 in Chapter 3.

The test programme comprised of the following three tests.

- Static immersion of WC samples in Bentonite mud based drilling fluid (df) of pH 11 for 168 h with potentiodynamic polarisation measurements at the start and end of the exposure.
- Micro-abrasion tests on df-exp WC samples using NaOH (pH 11) + SiC abrasives (0.16 v/v).
- Micro-abrasion tests on fresh WC samples using NaOH (pH 11) + SiC and distilled water (pH 7) + SiC abrasives (0.16 v/v).

For comparison with *SWR* obtained during the wear-corrosion tests, the mass loss per unit time ($\Delta x/t$) calculated from the potentiodynamic polarisation test (see Equation 2.33, Chapter 2) was converted to *SWR* as explained in Chapter 3, see Equation 3.1.

5.2 Results and discussion

5.2.1 Potentiodynamic polarisation measurements during exposure to water based drilling fluid

Figure 5.2a and Figure 5.2b show the potentiodynamic polarisation curves for the sintered WC-5.7Co-0.3Cr and WC-6Ni samples at the start (df) and at the end of the exposure (df-exp) to drilling fluid. The anodic behaviour of both the hardmetals is very similar with no clear evidence of 'classic' passivation, i.e. no change in current density over a range of potential (Figure 2.27, Chapter 2). However, the WC-5.7Co-0.3Cr-df-exp and WC-6Ni-df-exp curves show a slight decrease in the rate of anodic kinetics as compared to the WC-5.7Co-0.3Cr-df and WC-6Ni-df curves respectively. Also, WC-5.7Co-0.3Cr-df-exp and WC-6Ni-df-exp curves show a slight increase in the E_{corr} value which indicates that the sample surface has become less active over the duration of the exposure. This decrease in the overall reactivity of the samples is likely to be due to the depletion of the reactive surface components or due to the formation of an oxide film on the sample surface. However, the electrochemical behaviour of sprayed WC-10Co-4Cr and G-WC-10Co-4Cr was different from the sintered hardmetals. The E_{corr} values for the coatings were lower than the sintered hardmetals which was likely to be due to the differences in microstructure and surface composition between the sintered and coated samples. As seen from the microstructural analysis of sintered and sprayed samples in Chapter 3, the sintered hardmetals have a skeletal structure of carbides with the binder evenly dispersed within this structure while the sprayed hardmetals display an inhomogeneous microstructure with an uneven distribution of carbide-rich and binder-rich areas which strongly influences their corrosion behaviour. Although initially the sprayed hardmetals have lower E_{corr} values, a significant change in their corrosion behaviour is observed with the decrease in the rate of anodic behaviour as seen from Figure 5.3a and Figure 5.3b. The WC-10Co-4Cr-df-exp and G-WC-10Co-4Cr-df-exp curves show a decrease in the rate of anodic reactions compared to the WC-10Co-4Cr-df and G-WC-10Co-4Cr-df curves which strongly indicates that the surface chemistry has undergone a modification over the period of exposure. This decrease in the anodic reaction is likely to be associated with the active-passive behaviour of the Co-Cr binder and the WC rich carbide phase. Although the WC-10Co-4Cr-df curve shows some tendency to passivate, no clear evidence of passivation is observed in any other curve.

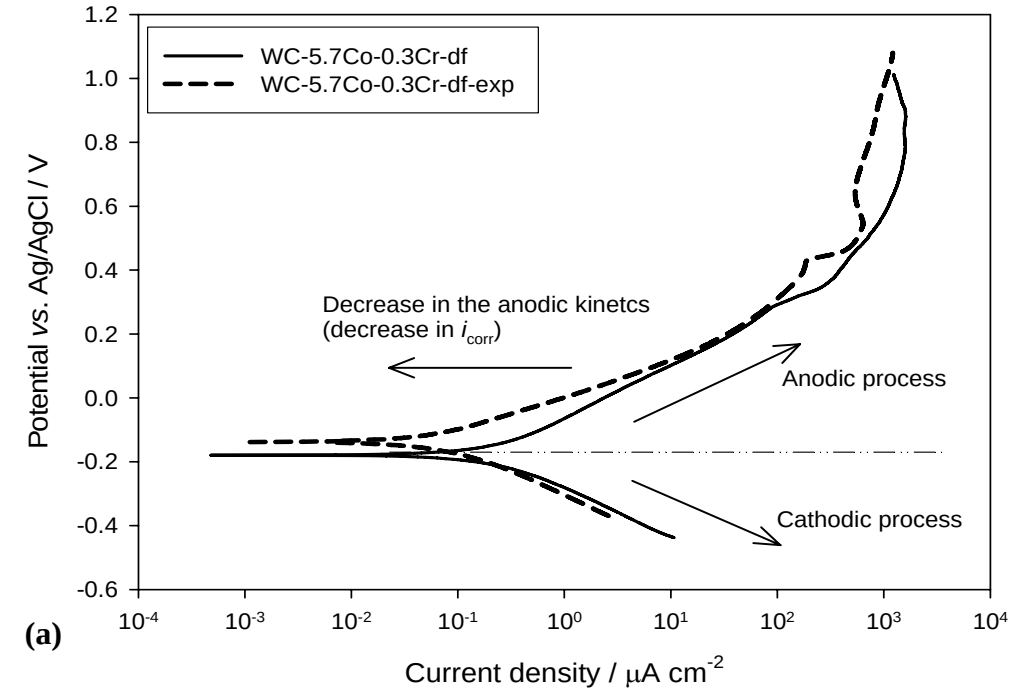

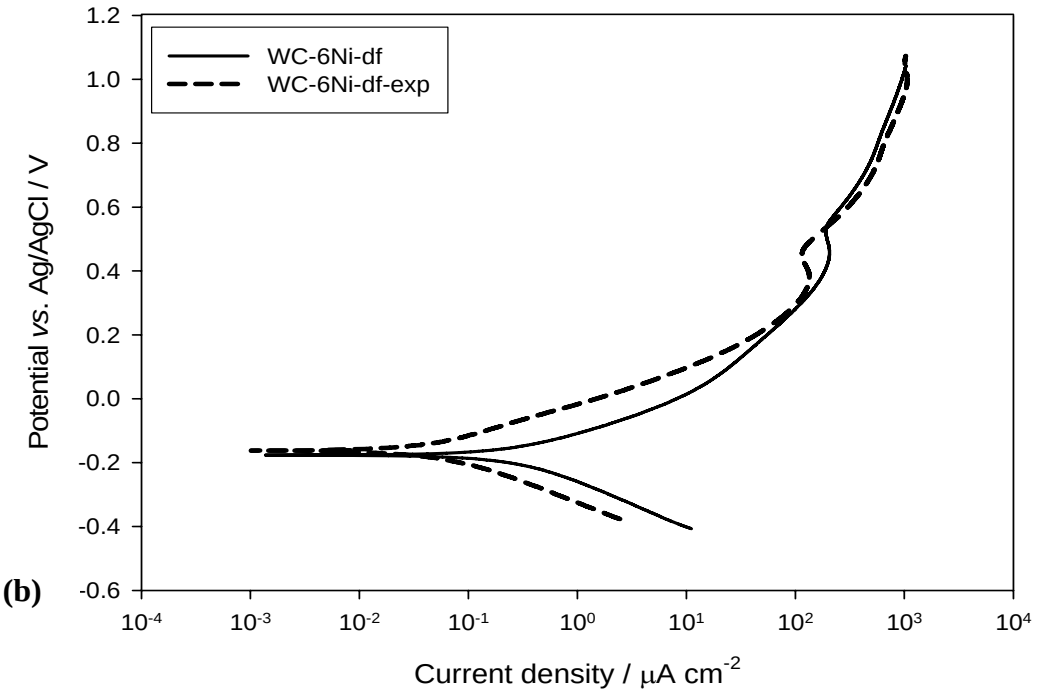

Figure 5.2: Potentiodynamic polarisation curves at the start and at the end of 168 hours of exposure to drilling fluid for WC-5.7Co-0.3Cr and WC-6Ni sintered hardmetals.

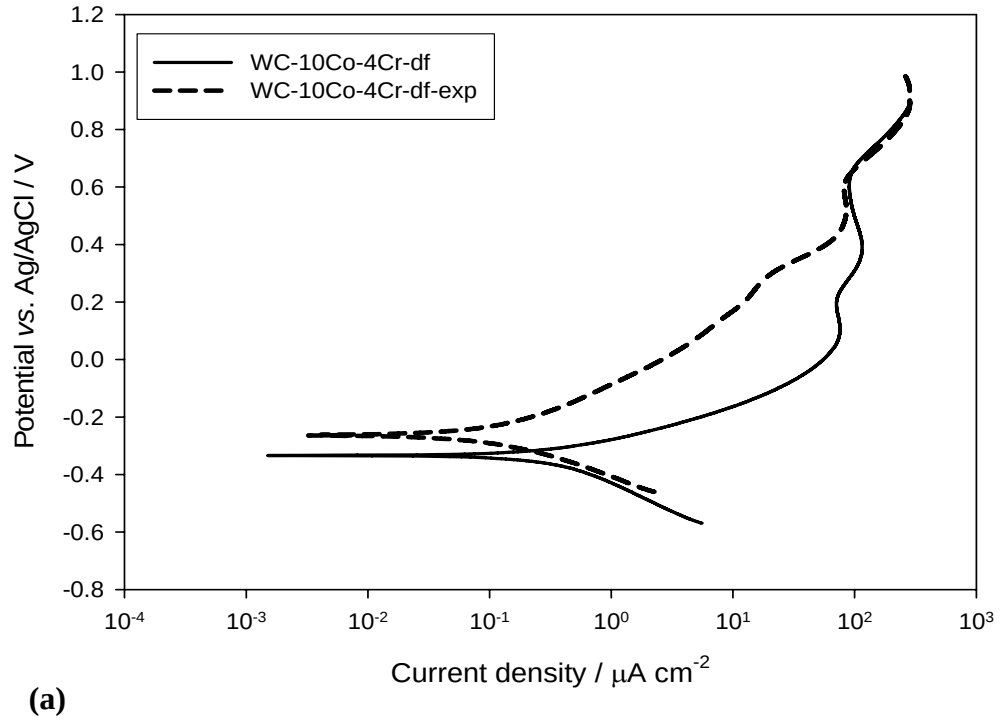

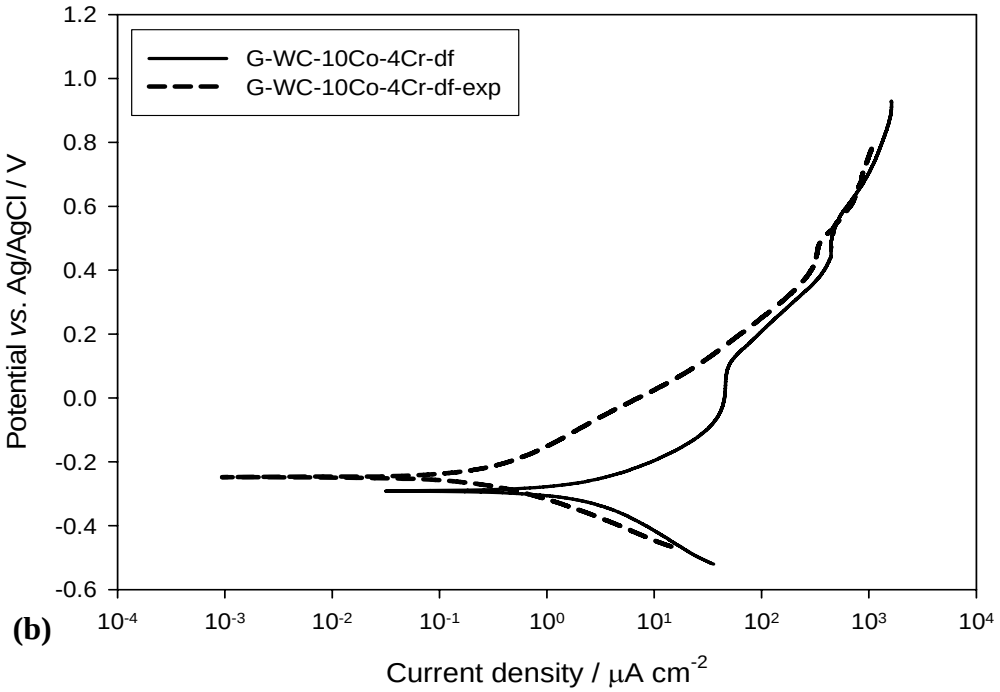

Figure 5.3: Potentiodynamic polarisation curves at the start and at the end of 168 hours of exposure to alkaline drilling fluid for WC-10Co-4Cr and G-WC-10Co-4Cr coatings.

Table 5-1 compares the E_{corr} and i_{corr} densities at the start and the end of exposure to the drilling fluid. The i_{corr} values were determined using the Tafel extrapolation method and were converted to a specific wear rate as discussed in Chapter 3 (Equation 3.1). The samples were ranked according to their *SWR* to reflect their pure-corrosion behaviour. The least *SWR*

was observed for WC-6Ni sample which is expected to be due to the superior corrosion resistance offered by Ni in alkaline conditions. Although the sprayed hardmetals show a larger increase in ΔE_{corr}, the overall pure corrosion performance of WC-6Ni and WC-5.7Co-0.3Cr is found to be better than WC-10Co-4Cr and G-WC-10Co-4Cr. Clearly, the homogeneous skeletal structure appears to offer better corrosion resistance than the inhomogeneous structure of the sprayed hardmetals. This result also suggests that the sprayed samples are more likely to suffer from corrosion during exposure than the sintered samples. This can also be observed from the Figure 5.5 and Figure 5.6 which compare fresh and df-exp surfaces of sintered and sprayed samples respectively and will be discussed later. It also appears that an increase in the binder content leads to an increase in the rate of corrosion, suggesting that the binder-phase is the reactive component in WC-based hardmetals and coatings.

Table 5-1: Evaluation of the E_{corr} and i_{corr} values obtained from the polarisation curves and the *SWR*calculated from the mass loss obtained from the i_{corr} value at the end of exposure (168 hrs).

	E_{corr} (0 hrs) (V)	E_{corr} (168 hrs) (V)	ΔE_{corr} (V)	i_{corr} (0 hrs) ($\mu A\ cm^{-2}$)	i_{corr} (168 hrs) ($\mu A\ cm^{-2}$)	Δi_{corr} ($\mu A\ cm^{-2}$)	*SWR* (C_{168}) ($m^3\ N^{-1}\ m^{-1}$) $\times 10^{-15}$	Rank
WC-5.7Co-0.3Cr	-0.179	-0.138	-0.041	0.177	0.068	-0.109	0.440	2
WC-6Ni	-0.176	-0.162	-0.014	0.33	0.052	-0.278	0.336	1
WC-10Co-4Cr	-0.334	-0.264	-0.070	0.352	0.163	-0.19	0.969	3
G-WC-10Co-4Cr	-0.292	-0.248	-0.044	2.09	0.322	-1.768	1.916	4

5.2.2 Micro-abrasion and wear-corrosion interaction

Figure 5.4 summarises the results of the micro-abrasion tests performed on the pH 7, pH 11 and df-exp samples of the four hardmetals under neutral and alkaline conditions. The *SWR* for the WC-6Ni are higher in alkaline slurries as compared with the neutral slurry. Exposure to drilling mud further increased the *SWR* for WC-6Ni. Nothing can be concluded about the performance of the Co-Cr based WC-5.7Co-0.3Cr due to the observed scatter in the results. However, despite the scatter in the results, WC-5.7Co-0.3Cr has the lowest *SWR* among all the samples tested. The performance of the WC-10Co-4Cr and G-WC-10Co-4Cr samples is very similar, with the lowest wear rate observed for the df-exp condition. This result is contrary to the expectation that localised corrosion of carbide species and the binder matrix would accelerate the wear process and result in an increase in *SWR*. The highest wear in WC-10Co-4Cr and G-WC-10Co-4Cr was observed for pH 7 samples. For further understanding of the wear-corrosion performance of the sintered and sprayed samples, worn and unworn samples have been examined under a scanning electron microscope (SEM).

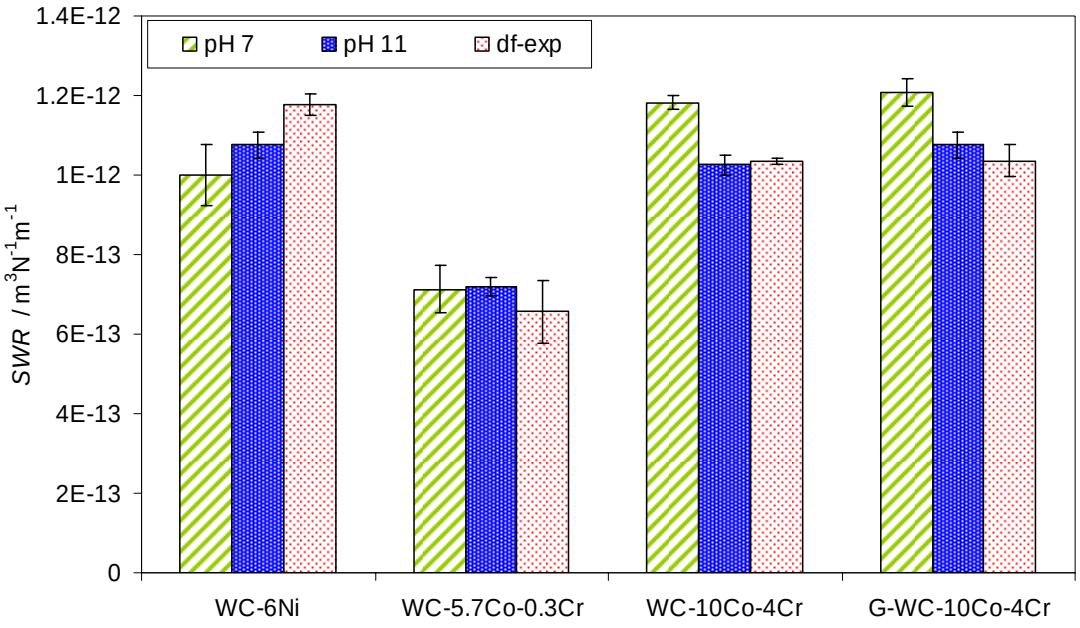

Figure 5.4: Summary of the micro-abrasion test results on pH 7, pH 11 and df-exp samples.

Figure 5.5a and Figure 5.5b compares the unworn surface of fresh and pH 11-exp WC-6Ni. There appears to be no obvious corrosive damage to the df-exp surface. Similarly, Figure 5.5c and Figure 5.5d compares the unworn surfaces of fresh and df-exp WC-5.7Co-0.3Cr. The df-exp surface does not show any significant binder depletion or corrosion of the hard-phase. This is consistent with the potentiodynamic polarisation curves for WC-5.7Co-0.3Cr

and WC-6Ni (Figure 5.2), which showed only a slight decrease in the rate of anodic reactions (curves WC-5.7Co-0.3Cr-df-exp and WC-6Co-df-exp).

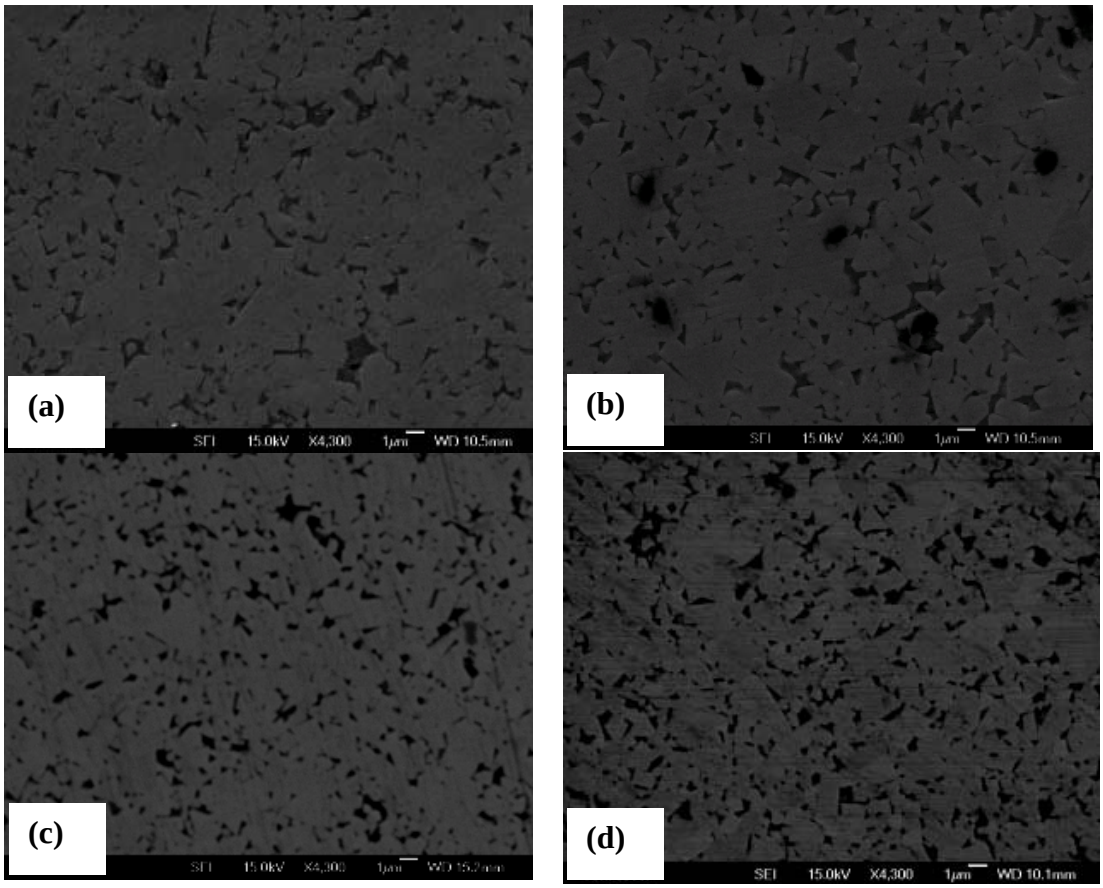

Figure 5.5: Comparison of unworn surfaces of fresh and df-exp samples: (a) fresh WC-6Ni; (b) WC-6Ni-df-exp; (c) fresh WC-5.7Co-0.3Cr and (d) WC-5.7Co-0.3Cr-df-exp.

However, unlike the sintered hardmetals, the df-exp surfaces of WC-10Co-4Cr and G-WC-10Co-4Cr coatings show some evidence of localised corrosion along the binder-carbide interface as seen in Figure 5.6b and Figure 5.6d. Formation of localised 'corrosion trenches' at the carbide edges has been previously observed and has been attributed to the presence of a discontinuous Cr_2O_3 passive film formed on the Co-Cr binder [117, 119]. The potentiodynamic polarisation curves WC-10Co-4Cr-df-exp and G-WC-10Co-4Cr-df-exp (Figure 5.3) also suggest a change in the corrosion kinetics, possibly due to film forming and/or dissolution (corrosion) of the most active component. As discussed in Chapter 2, Pourbaix diagrams for Cr [102] have established the formation of an insoluble Cr_2O_3 film under the conditions similar to those used in this investigation (pH 10 to 11 and a corrosion potential of -0.070 V Ag/AgCl), see Figure 2.24. For a similar potential range Ni and Co are likely to form stable hydroxides of $Ni(OH)_2$ and $Co(OH)_2$ respectively which are also likely to influence the local chemistry. The anodic dissolution of tungsten has been studied previously, however, the overall mechanism has not been clearly established [152]. It is

reported that under alkaline conditions, W is likely to form an oxide WO_3 which can dissolve in the form of WO_4^{2-} at higher potentials [108].

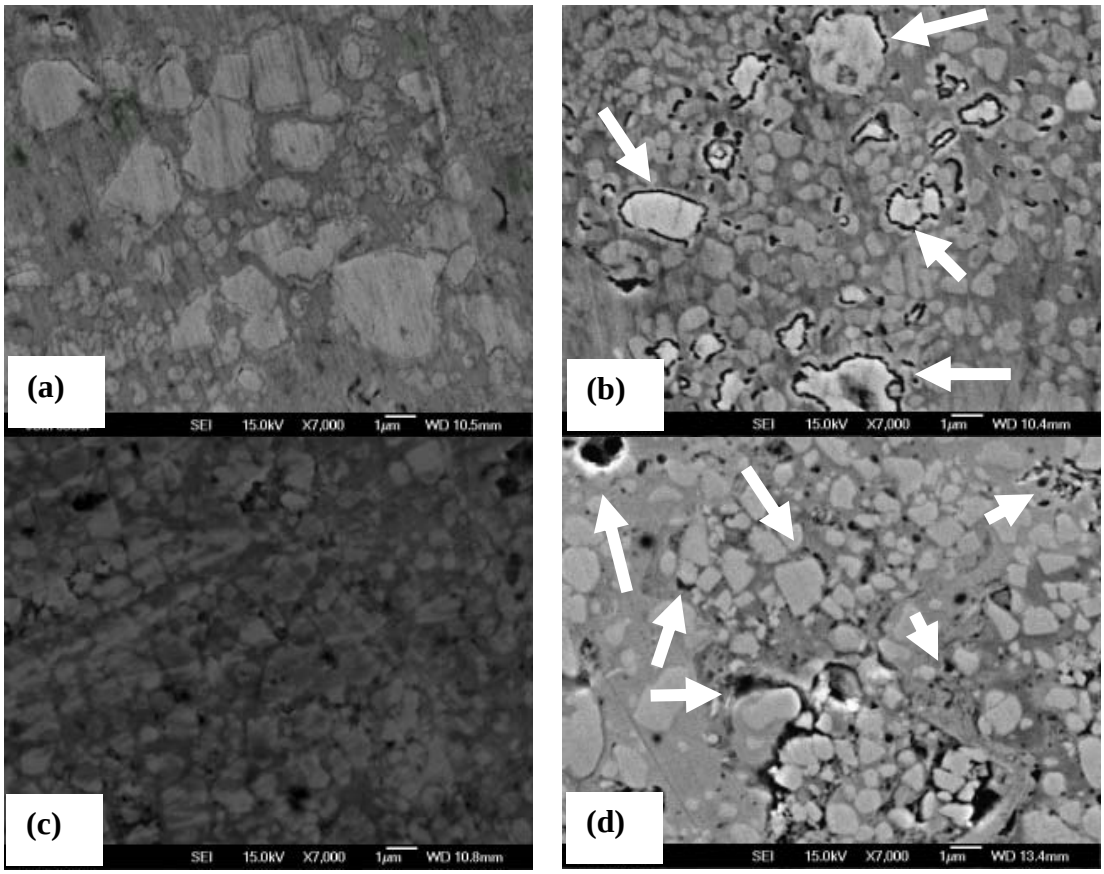

Figure 5.6: Comparison of unworn surfaces of fresh and df-exp coated samples: (a) fresh WC-10Co-4Cr; (b) WC-10Co-4Cr-df-exp; (c) fresh G-WC-10Co-4Cr and (d) G-WC-10Co-4Cr-df-exp, showing evidence of localised corrosion along the periphery of carbide particles.

The corrosion of the binder-carbide interface is very similar to that reported by Souza *et al.* [117] (see Figure 2.25, Chapter 2). However, from the SEM micrographs in Figure 5.6b and Figure 5.6d it appears that the corrosion has progressed towards the carbide phase which is likely to occur in presence of metallic W formed along the carbide grain boundary due to decarburising during the spray process. Presence of re-precipitated metallic W and decarburised W_2C phases along the periphery of WC grains has been identified by Verdon *et al.* [156] by TEM analysis of the coating microstructure.

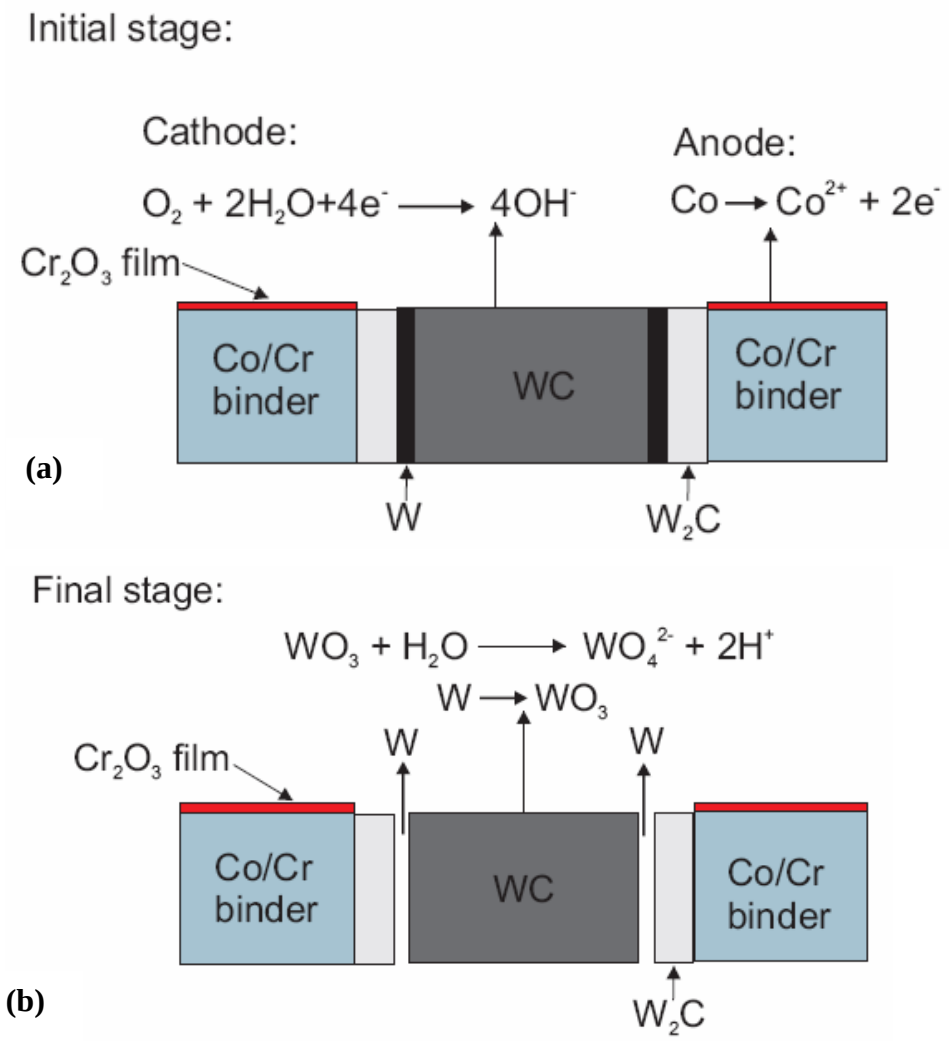

Figure 5.7: Two-step corrosion mechanism proposed for WC-10Co-4Cr coating [141].

As discussed in Chapter 2, section 2.3.3, the corrosion of sintered WC-Co was studied by Hochstrasser *et al.*[106]. A similar mechanism of corrosion for the WC-10Co-4Cr coating is proposed here as shown schematically in Figure 5.7. The corrosion of WC-10Co-4Cr coating is a two-step process. The initial anodic reaction occurs on the binder-phase and results in the formation of Cr_2O_3 / $Co(OH)_2$ passive film on the binder-rich regions. The corresponding cathodic reaction occurs on the carbide particle and results in the formation of OH^- ions, increasing in the local pH. The stability of metallic W reduces with increase in the pH and the subsequent anodic reaction results in the dissolution of metallic W within the carbide-phase. The corrosion of metallic W present between W_2C phase and WC phase leads to the formation of 'corrosion trenches' within the carbide grains.

Figure 5.8 compares the SEM micrographs of wear scars on pH 7, pH 11 and df-exp WC-6Ni and WC-5.7Co-0.3Cr samples. The WC-6Ni wear scars, Figures 5.8a, 5.8b and 5.8c, show a uniformly worn surface with exposed carbides revealing the skeletal structure of the

carbide grains. The df-exp wear scar (Figure 5.8c) shows larger blocks of exposed carbides compared to the pH 7 wear scar (Figure 5.8a) which indicates an increase in binder depletion consistent with an increase in the wear rate as observed in Figure 5.4. However, for WC-5.7Co-0.3Cr, Figures 5.8d, 5.8e and 5.8f, the wear scars show exposed carbide grains in addition to evidence of some intra- carbide grain cracking as highlighted by the arrow markers. This is obvious from the fact that although the carbide size for WC-5.7Co-0.3Cr (2.3 μm) is slightly greater than WC-6Ni (2.0 μm) the wear scars show larger carbides in WC-6Ni as compared to WC-5.7Co-0.3Cr. Also, the pH 7 wear scar for WC-5.7Co-0.3Cr (Figure 5.8d) shows a greater number of exposed carbide grains as compared to the df-exp wear scar (Figure 5.8f). Thus, wear of WC-6Ni appears to have occurred predominantly by binder depletion which has led to the removal of unsupported carbides (undermining), while WC-5.7Co-0.3Cr appears to have suffered to some extent from transgranular carbide cracking along with binder depletion as shown schematically in Figure 5.9. WC-5.7Co-0.3Cr appears to have suffered lesser binder loss as compared to WC-6Ni resulting in overall lower specific wear rate. Clearly, the wear-corrosion performance of the Co-Cr binder is better than the Ni binder which is likely to be due to the superior wear resistance of the Co-Cr binder. It has been previously observed [149] that under wear dominated situations, binders which offer better hardness and deformation characteristics are likely to perform better.

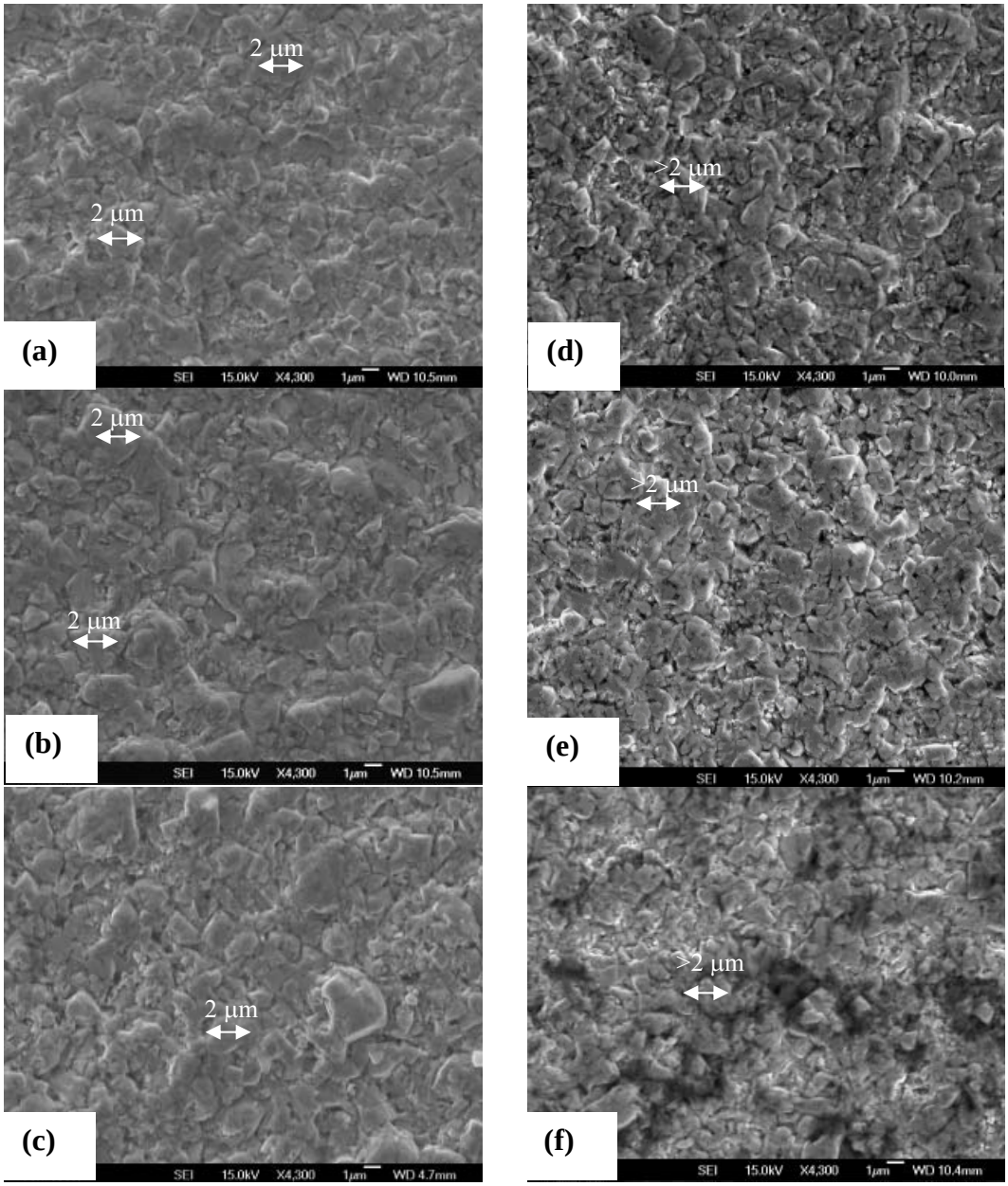

Figure 5.8: Comparison of wear scars of WC-6Ni and WC-5.7Co-0.3Cr: (a) WC-6Ni-pH 7; (b) WC-6Ni-pH 11; (c) WC-6Ni-df-exp; (d) WC-5.7Co-0.3Cr-pH 7; (e) WC-5.7Co-0.3Cr-pH 11 and (f) WC-5.7Co-0.3Cr-df-exp.

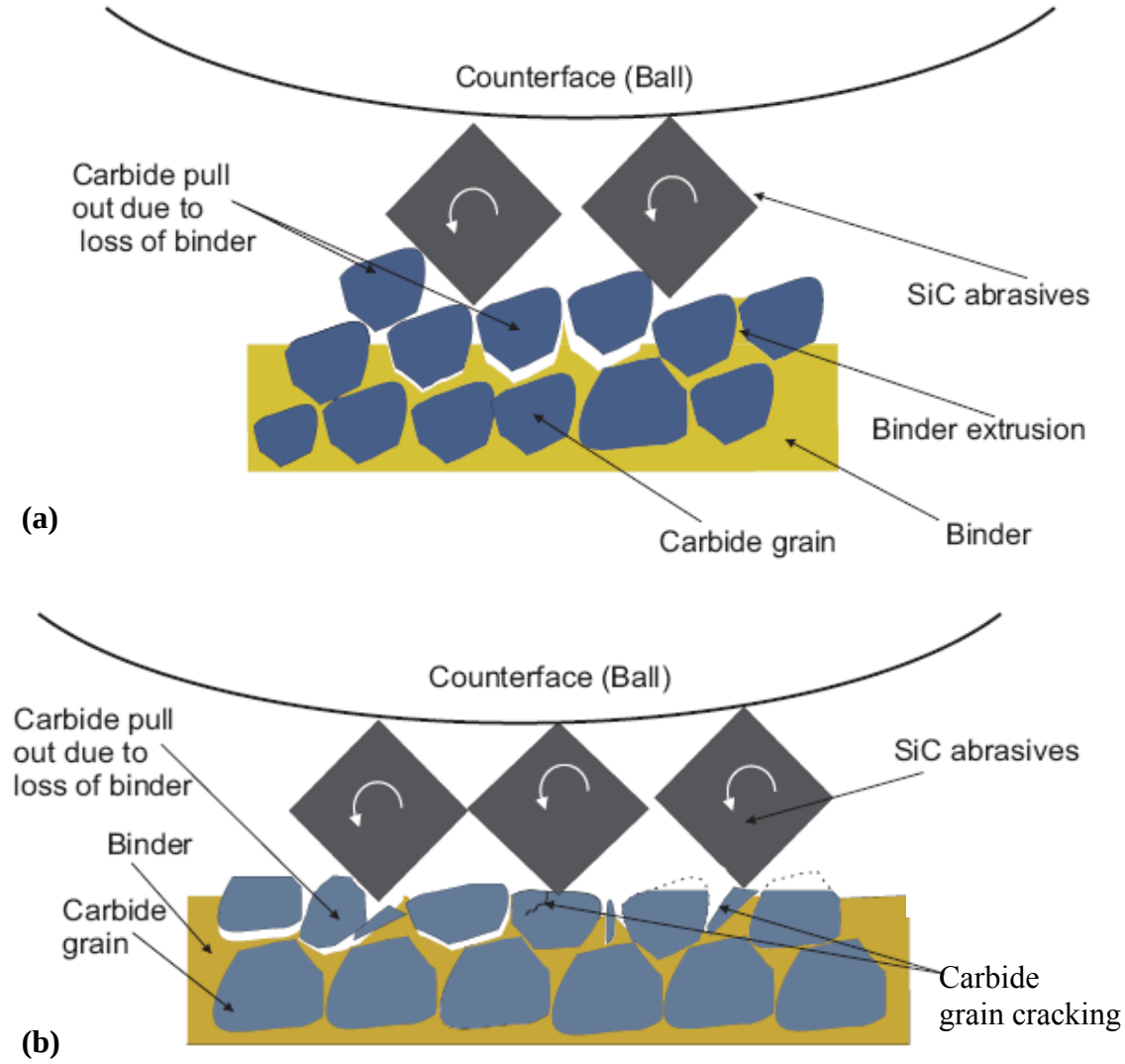

Figure 5.9: Schematic showing the process of abrasive wear (a) Undermining of unsupported carbides as observed in WC-6Ni and (b) carbide cracking and their subsequent removal in WC-5.7Co-0.3Cr.

SEM micrographs of wear scars formed on the pH 7, pH 11 and df-exp WC-10Co-4Cr and G-WC-10Co-4Cr coatings are shown the Figure 5.10. The wear scars show uniform three-body indentations and reveal the non-skeletal carbide distribution in the coatings. Unlike the sintered hardmetals, both the coatings show very similar wear patterns with very little difference in the overall appearance between the pH 7 (Figure 5.10a and Figure 5.10d) and the df-exp wear scars (Figure 5.10c and Figure 5.10f). Significantly, the worn surfaces do not show presence of localised corrosion trenches seen on the unworn surfaces, see Figure 5.6.

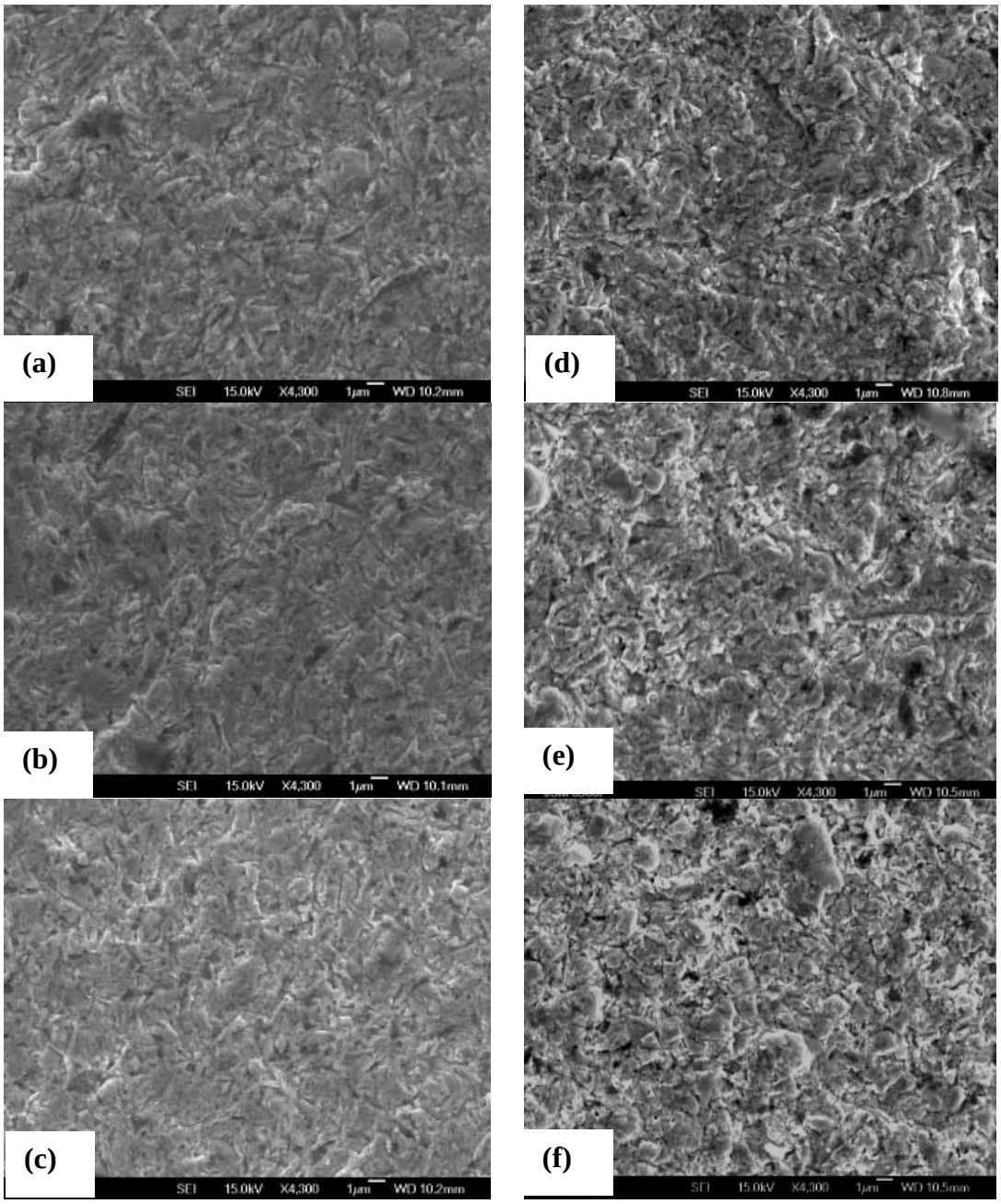

Figure 5.10: Comparison of wear scars of WC-10Co-4Cr and G-WC-10Co-4Cr: (a) WC-10Co-4Cr-pH7; (b) WC-10Co-4Cr-pH 11; (c) WC-10Co-4Cr-df-exp; (d) G-WC-10Co-4Cr-pH 7; (e) G-WC-10Co-4Cr-pH 11 and (f) G-WC-10Co-4Cr-df-exp.

Figure 5.11 compares the 2D surface profiles of the wear scars for the WC-5.7Co-0.3Cr-df-exp and WC-10Co-4Cr-df-exp samples. A noticeable difference in the roughness of the wear scars on sintered and sprayed samples is evident, possibly due to the difference in the wear mechanisms observed. The wear scar on the sintered sample appears to be 7 to 8 carbides deep in the centre. The profile also shows peak to valley features which are multiple carbides deep and as such is representative of the wear mechanism observed in the sintered hardmetals. Similar features were observed on the profiles of other sintered samples. Although similar in depth, the WC-10Co-4Cr coating wear scars appear to be less

rough in nature. The features within the wear scar crater are not as prominent as for WC-5.7Co-0.3Cr. The indents (caused due to rolling abrasive wear) observed in the wear scar are comparable to the size of SiC abrasives used. Also, Figure 5.11b fails to show any evidence of the dislodging of whole splats from the coating surface showing good integrity of splat boundaries.

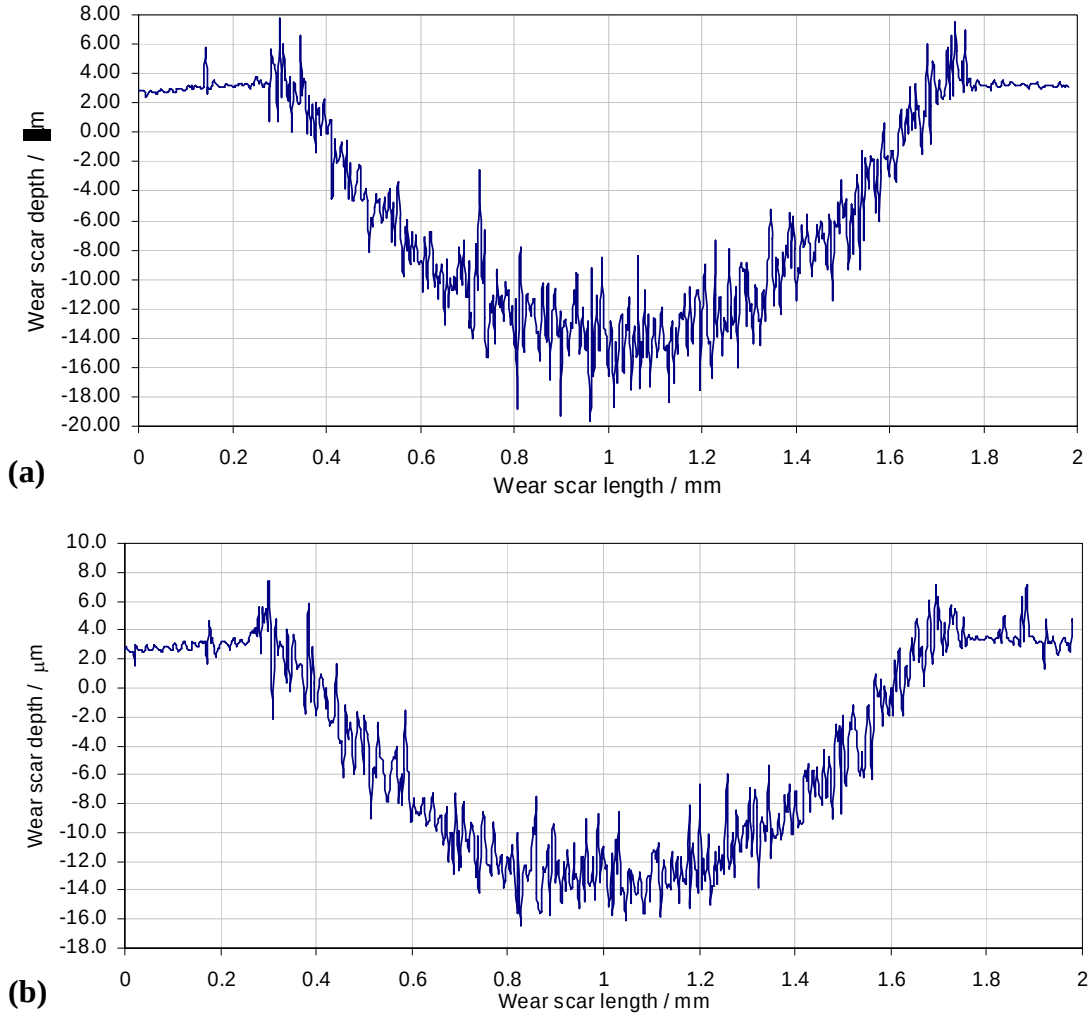

Figure 5.11:Wear scar profiles obtained on df-exp samples of (a) sintered WC-5.7Co-0.3Cr sample and (b) sprayed WC-10Co-4Cr sample showing the difference in the texture of the wear scars due to the difference in the microstructure of the sintered and sprayed samples.

Table 5-2 compares the roughness values calculated from the wear scars of sintered and sprayed samples. Overall, the sprayed coatings had lower roughness values compared with the sintered hardmetals possibly related to single carbide pull-out wear mechanism compared to multiple carbide pull-out mechanism seen on the sintered carbide surface inferred from the peak-valley distances in sintered (4-8 µm) and sprayed hardmetals (2-3 µm).

Table 5-2: Wear scar crater surface roughness.

	***R*a in the crater (μm)**	***R*a outside the crater (μm)**
WC-5.7Co-0.3Cr	1.633	0.101
WC-6Ni	1.611	0.106
WC-10Co-4Cr	1.231	0.155
G-WC-10Co-4Cr	1.216	0.177

Table 5-3 lists the mechanisms which are likely to influence the wear-corrosion interactions. The lowering of wear-rates due to exposure to drilling fluid and when using alkaline slurries observed for WC-10Co-4Cr and G-WC-10Co-4Cr coatings can be attributed to added wear-resistance due to corrosion. Negative wear-corrosion interactions or 'synergies' have not been reported previously for the HVOF sprayed WC-10Co-4Cr and therefore this is an exciting/important finding for which further investigation is needed. The lowering of *SWR* may be influenced by the formation of discontinuous passive films [117, 119] and/or localised corrosion along the periphery of the carbide grains (Figure 5.6b and 5.6d). Negative synergies have been reported by Tan *et al.* [139] in their work on erosion-corrosion of HVOF nickel-aluminium-bronze and were attributed to the presence of a strong passive film which altered the contact conditions between the coating and the erosive particles. In addition, plastic deformation and induced strain in the initial surface can also influence the hardness and affect the wear performance of the sprayed sample. However, it can also be argued that the presence of a passive film or effects of strain hardening, influenced by exposure to alkaline conditions delay the onset of wear and lead to lower wear rates (i.e. negative wear-corrosion interaction) being measured for a short duration test, see Figure 5.12, which may not be the case with long duration tests and during field operation. This possibility needs to be investigated using the modified micro-abrasion tester capable of *in situ* electrochemical measurements.

Table 5-3: Overview of processes that could lead to negative wear-corrosion interaction during abrasion-corrosion

Factors	Effects
Surface Roughness *R*a	Surface roughness influences the contact mechanics of angular particles and the surface. Increase in *R*a could reduce contact stresses and stress distribution [140].
Plastic deformation/strain	Strain hardened surfaces increases hardness and could reduce corrosion due to change in microstructure [157].
Passive film state	Oxide layer could decrease friction between abradants and the bulk material. Also, denser oxide layer could offer extra protection during wear process [139].
Dissolution of the active components	Dissolution of active components on the surface are likely to alter the surface composition with time (Ref: this work).

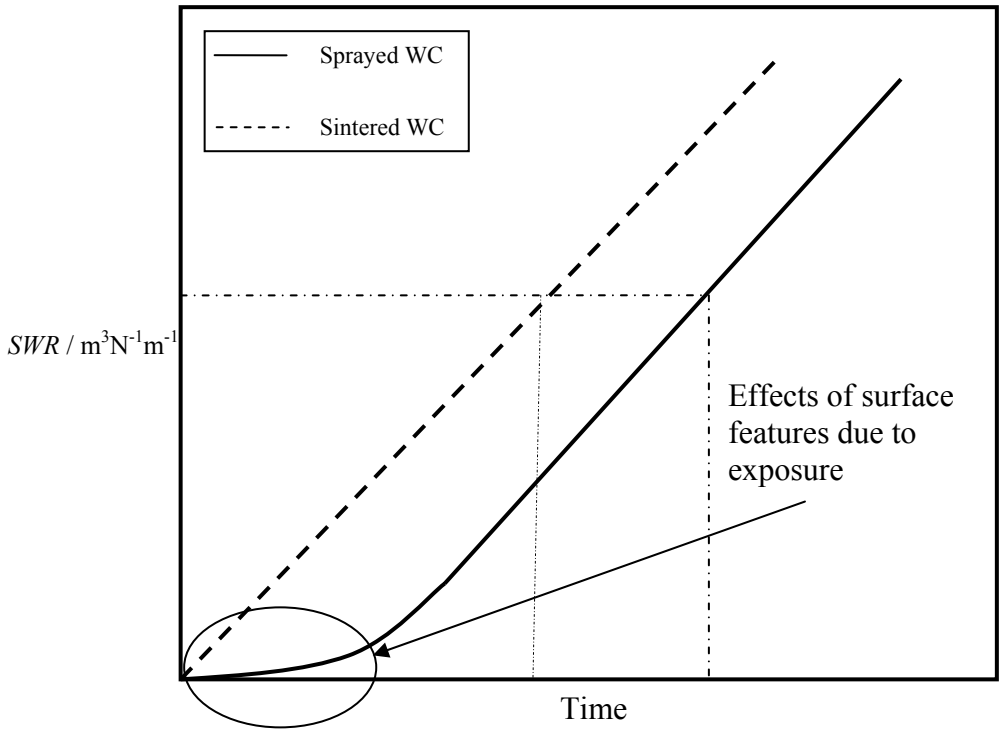

Figure 5.12: Effect of time on the SWR of sintered and sprayed samples.

5.3 Conclusions

- The sintered Ni based WC-hardmetal WC-6Ni shows an increase in *SWR* due to exposure to alkaline drilling fluid and results in a mild positive wear-corrosion interaction. The observed wear mechanism indicates that abrasive wear occurs by the preferential loss of the binder that subsequently exposes the carbide grains which are removed by further abrasive damage. The mild positive wear-corrosion interaction observed in WC-6Ni is likely to be influenced by the dissolution of active components present on the surface of the sample in alkaline conditions.

- The abrasion-corrosion performance of Co-Cr based sintered WC WC-5.7Co-0.3Cr was not as clearly defined, a slight decrease in *SWR* was observed after exposure to the alkaline drilling fluid; however it is difficult to quantify the wear-corrosion interaction which appears to be very mild. The wear mechanism seen on the WC-5.7Co-0.3Cr sample was a combined action of binder loss and cracking of carbide grains.

- The abrasion-corrosion performance of the WC-10Co-4Cr and G-WC-10Co-4Cr coatings was found to be similar to each other which could be due to their similar microstructure and composition. Exposure to alkaline drilling fluid resulted in the lowering of *SWR*. This performance has been attributed to surface chemistry effects due to the exposure to alkaline conditions, i.e. passive film formation in binder-rich areas and formation of corrosion trenches around the carbide grains which is likely to alter the surface composition with time and lead to possible improvement in the surface compliance of the coating.

- The corrosion trenches along the periphery of WC grains in WC-10Co-4Cr coating result from the corrosion of decarburised metallic W formed during the coating process. Micro-galvanic coupling between the WC and Co-Cr binder results in the selective dissolution of metallic W.

- Clearly, there is a need to better understand why WC-10Co-4Cr coating gives lower wear rates under alkaline conditions so that surfaces can be designed to enhance this property. Advanced surface analysis techniques need to be deployed to fully understand the local chemistry likely to occur during exposure and the properties of the resulting surface.

6 Surface analysis and wear-corrosion interactions

6.1 Introduction

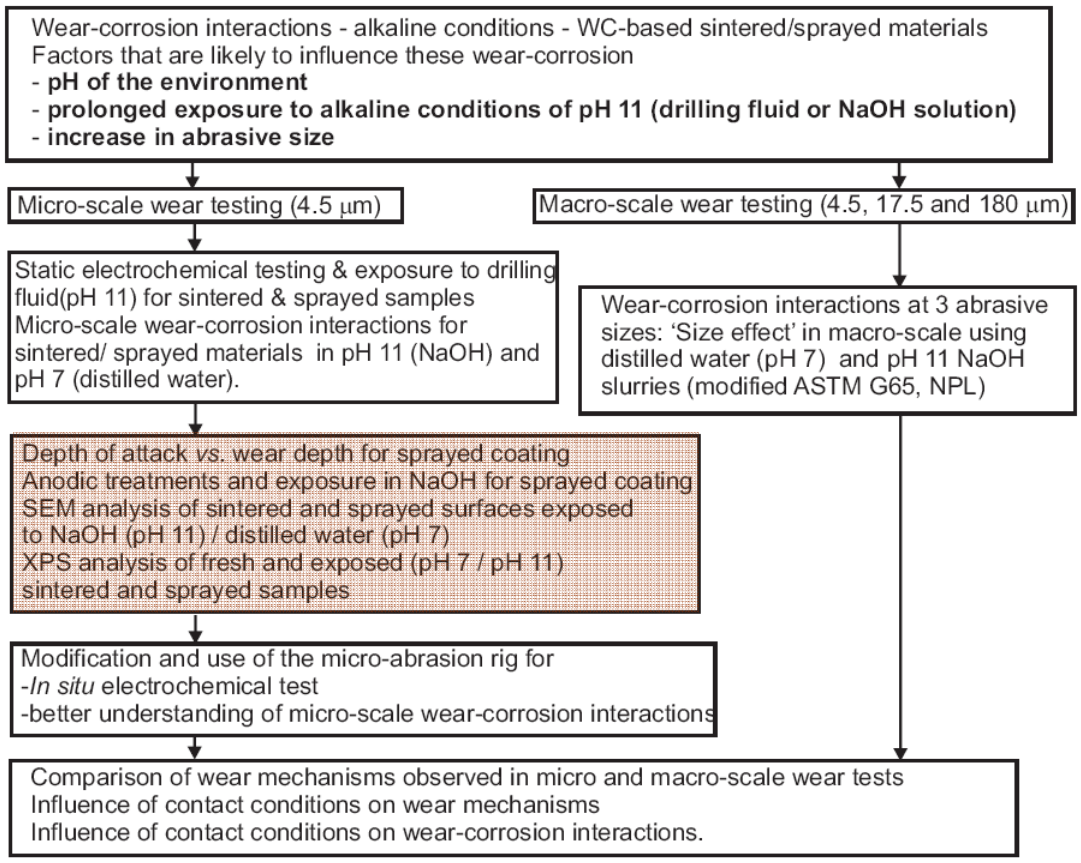

Figure 6.1: Experimental flow chart showing the test programme discussed in Chapter 6 (highlighted).

The wear-corrosion performance of fresh and exposed WC-based sintered hardmetals and sprayed coatings were investigated in the previous chapter (Chapter 5). Among the sintered samples, WC-6Ni showed a slight increase in the *SWR* after exposure to pH 11 drilling fluid, there was no obvious influence on the *SWR* of WC-5.7Co-0.3Cr. In case of the coatings, both WC-10Co-4Cr and G-WC-10Co-4Cr showed a slight decrease in the *SWR* after exposure to pH 11 drilling fluid. This was despite the presence of corrosion trenches on the surface of exposed samples. It was proposed that the lower *SWR* observed for the coatings was due to the possible altering of contact conditions by the selective passivation of the binder-phase and the presence of loosely held carbide grains within the corrosion trenches. It was also proposed that the corrosion trenches formed along the periphery of WC grains were formed due to the preferential corrosion of decarburised metallic W ring around the WC grains. This chapter investigates the wear-corrosion performance of WC-10Co-4Cr coating and

characterises the effects of exposure by advanced surface analysis techniques such as SEM imaging, XPS analysis and FIB sectioning. For comparison, SEM imaging and XPS analysis was also done on sintered WC-5.7Co-0.3Cr. WC-10Co-4Cr coating and sintered WC-5.7Co-0.3Cr were selected for further analysis in this Chapter as they had the lowest *SWR* among the coatings and the sintered samples tested in the Chapter 5 respectively. Due to the complex nature of drilling fluids and concerns over possible degradation of the drilling fluid chemistry over time, subsequent exposures and analysis was done using a more controlled environment of pH 11 NaOH solution. This chapter aimed at gaining a physical understanding of the negative wear-corrosion interactions (i.e. lowering of *SWR* as compared to pH 7 conditions) observed for the WC-10Co-4Cr coating. The influence of corrosion depth *vs.* the wear depth was investigated by conducting micro-abrasion tests for sliding distances between 30 m and 90 m. Anodic treatments were carried out on the WC-10Co-4Cr coating to accelerate the effects of exposure and replicate the corrosion features observed.

The test programme comprised of the following tests.

- Micro-abrasion tests on fresh and exposed WC-10Co-4Cr coating using pH 11 and pH 7 slurries for sliding distances of 30 m, 45 m, 60 m, 75 m and 90 m.
- Anodic treatment of WC-10Co-4Cr coating for 1 h and 24 h in NaOH solution (-0.2 V *vs.* Ag/AgCl) followed by potentiodynamic polarisation of the anodically treated samples.
- Micro-abrasion tests on duplicate samples of WC-10Co-4Cr coating anodically treated for 1 h and 24 h.
- SEM analysis of WC-10Co-4Cr coating before and after exposure to pH 11 NaOH solution and pH 7 distilled water (for comparison). For comparison, SEM analysis was also done on sintered WC-5.7Co-0.3Cr coating before and after exposure to pH 7 distilled water and pH 11 NaOH solution.
- XPS analysis of fresh and exposed (to pH 7 and pH 11) samples of WC-10Co-4Cr coating and sintered WC-5.7Co-0.3Cr (for comparison).
- FIB cross-sectioning of WC-10Co-4Cr coating exposed to pH 11 NaOH solution for cross-sectional examination of the corrosion trenches observed.

The detailed experimental procedures are as described in Chapter 3.

6.2 Results and Discussion

6.2.1 Micro-abrasion for sliding distances between 30 m and 90 m

Figure 6.2 shows the *SWR* for pH 7, pH 11 and pH 11-exp samples plotted against the sliding distance for WC-10Co-4Cr coating. Although there is some scatter in the results, the pH 7 samples show a higher wear volume than the pH 11-exp or the pH 11 samples for all the sliding distances.

The wear scars obtained on the pH 7, pH 11 and pH 11-exp wear scars were measured using a Taylor Hobson form Talysurf 2-D profiler, see Table 6-1. Clearly, the differences in the wear scar depth between pH 7 and pH 11 / pH 11-exp samples are more evident for sliding distances greater than 60 m. A slight difference in the wear scar depth is also observed for sliding distance of 45 m. Figure 6.3 superimposes the depth of the wear scars obtained on the pH 11-exp samples at different sliding distances on an SEM-BSE cross-section. The SEM-BSE image shows the uneven distribution of binder-rich regions and carbides in the coating and reveals the lamellar structure of the splats which are approximately 10 μm thick. As seen from the superimposed wear scar depths, the depth of wear scars for 75 m and 90 m are at the average thickness of the splats.

The difference in the wear scar depth observed for pH 7, pH 11 and pH 11-exp samples can be related to the coating microstructure. As discussed in Chapter 2, Stewart *et al.* [30] predicted a model for the cooling of a typical WC-Co splat during the coating process. The higher temperatures at the splat boundary lead to higher amount of metallic W being dissolved in the binder-phase. This leads to the formation of the nano-crystalline binder phase being predominantly present along the splat boundaries making them weaker. The centre of the splat is expected to retain higher amounts of WC grains making the centre of the splat more wear resistant (due to higher wear resistance of the carbide-rich regions in the splat) as compared to the splat boundary. Micro-abrasion for 60 m and above leads to the wear scar abrading past the wear resistant/ carbide rich centre of the splat. As discussed in the previous chapter, the wear mechanism observed for sprayed coatings is the preferential removal of the binder-phase leading to the undermining of carbide grains. Hence, under alkaline conditions, the passivation of the binder-phase appears to lower the rate of binder depletion leading to a noticeable difference in the wear rates/ wear scar depths. The inhomegenity in the coating structure is also evident from the absence of Archard-like behaviour by the coating, see Figure 6.2. While typical Archard-like behaviour should be

independent of sliding distance, the random distribution of hard and soft phases in the coating results in the variation of *SWR* with increase in the wear-scar depth / sliding distance.

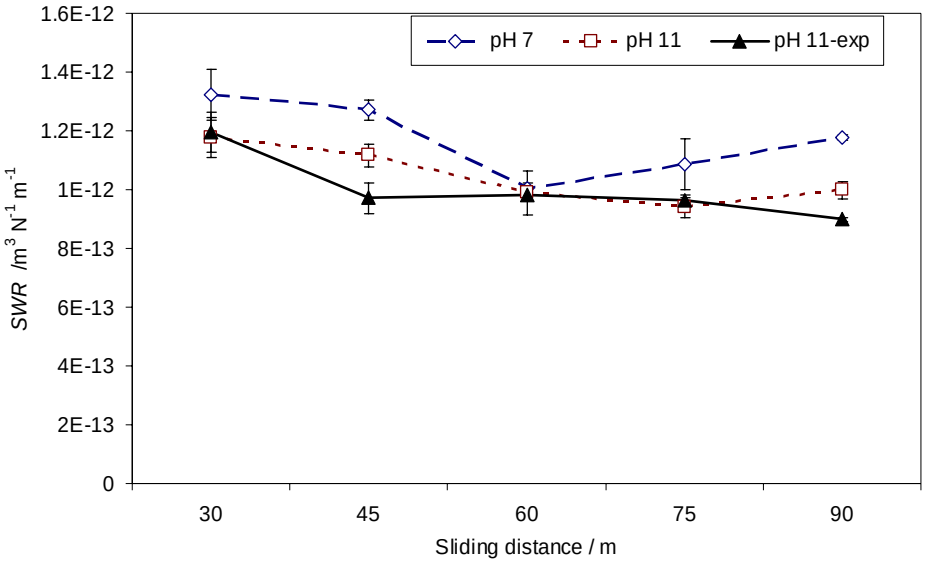

Figure 6.2: *SWR vs.* sliding distance for micro-abrasion of fresh and pH 11-exp samples.

Table 6-1: Wear scar depth recorded for pH 7, pH 11 and pH 11-exp samples for different sliding distances.

	30 m	45 m	60 m	75 m	90 m
pH 7 (μm)	9.5	11	12	15	17
pH 11 (μm)	9	10	11	12	15
pH 11-exp (μm)	9	9.5	11	13	14

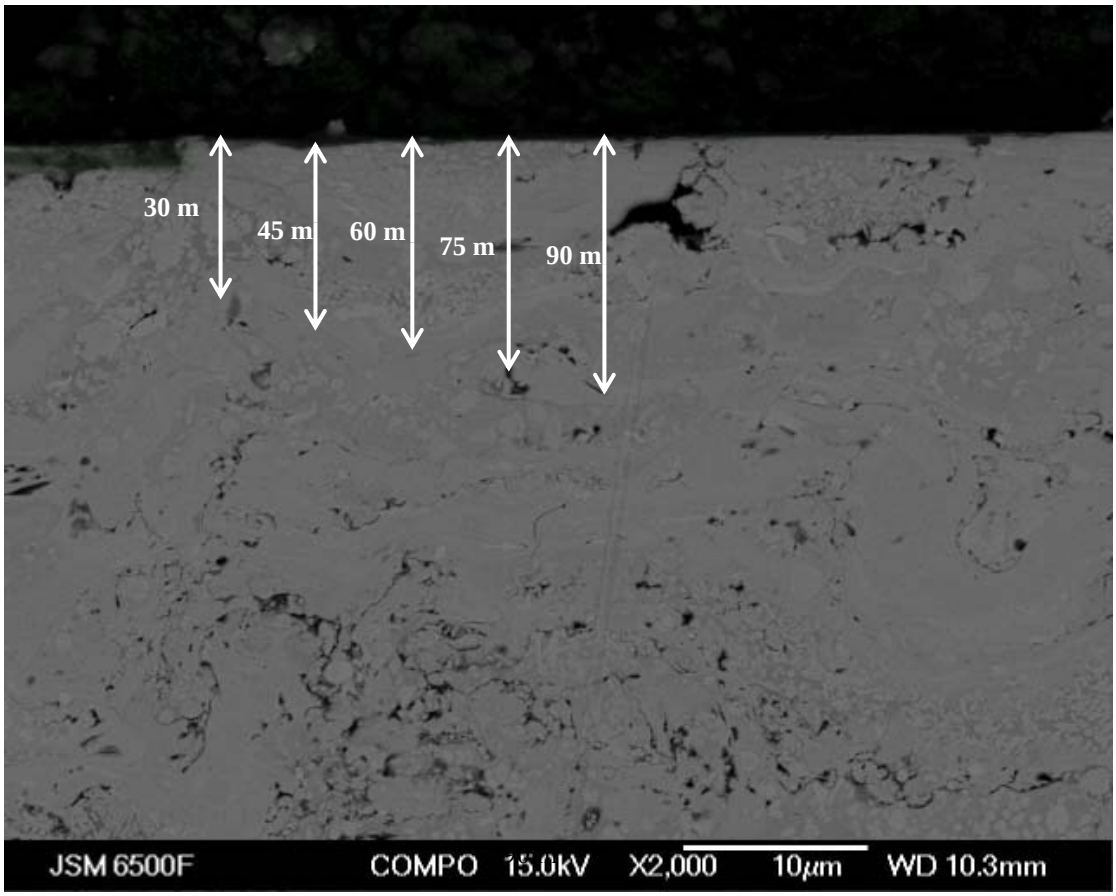

Figure 6.3: SEM-BSE micrograph of the cross section of pH 11-exp sample showing the depth of the wear scars for sliding distances between 30 m and 90 m.

6.2.2 Anodic pre-treatments and micro-abrasion

Figure 6.4 shows the potentiodynamic polarisation curves for fresh (pH 11), exposed (pH 11-exp) and anodically treated samples (anodic-1h, anodic-24h) in NaOH solution of pH 11. E_{corr} and i_{corr} values calculated using the Tafel extrapolation method are tabulated in Table 6-2.

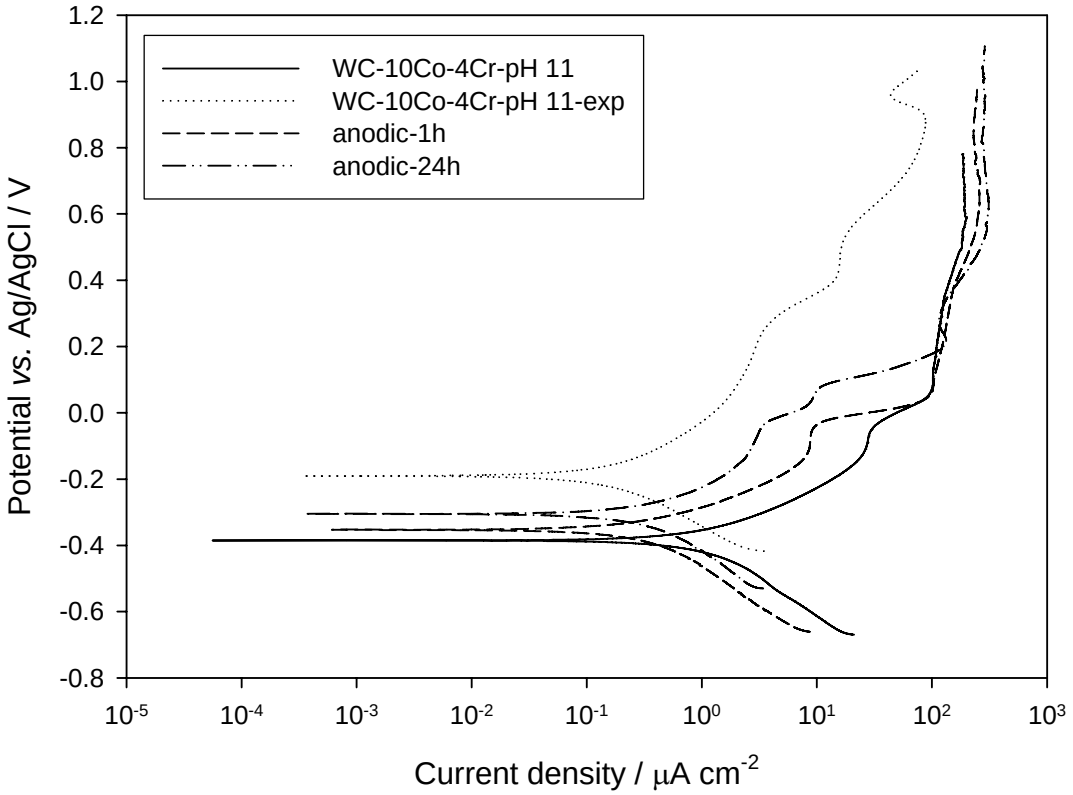

Figure 6.4: Potentiodynamic polarisation curves for WC-10Co-4Cr: pH 11, pH 11-exp, anodic-1h and anodic-24h samples in pH 11 NaOH solution.

Potentiodynamic polarisation curves for fresh and df-exp samples of WC-10Co-4Cr coating have been studied in Chapter 5 and their behaviour is similar on exposure to pH 11 NaOH solution, see Figure 6.4. As in case if exposure to df, exposure to pH 11 NaOH solution results in an increase in the E_{corr} value accompanied by a decrease in the i_{corr} value. This behaviour is expected as the active components such as metallic W and decarburised W_2C on the surface are depleted which results in a change in the surface composition. Although the pH 11-exp curve shows a decrease in the rate of reaction on the sample surface, it does not show typical 'passive' behaviour. This is expected as only the binder-rich areas on the surface are expected to passivate in alkaline conditions. The metallic W present at the sample

surface is expected to undergo dissolution at pH 11 [102]. Although the potentiodynamic polarisation curves for the anodically treated samples show a decrease in the E_{corr} value compared to the pH 11 sample, this decrease is not as dramatic as observed for the pH 11-exp sample. It was expected that the process of anodising of samples would result in active dissolution of soluble and active species on the sample surface resulting in replication of the surface composition achieved by exposure. The E_{corr} values of the anodically treated samples show some increase compared to pH 11 sample but are not as high as the pH 11-exp sample. Although there appears to be some improvement in the corrosion resistance of the anodically treated sample (due to an increase in the E_{corr} value and a decrease in the i_{corr} value as compared with a fresh sample), it is not as much as observed for the pH 11-exp sample.

Table 6-2: E_{corr} and i_{corr} values for fresh, pH 11-exp and anodically treated samples polarised in NaOH solution of pH 11.

Condition	E_{corr} (V)	i_{corr} (μA cm^{-2})
anodic-1h	-0.353	0.551
anodic-24h	-0.305	0.471
pH 11	-0.385	1.573
pH 11-exp	-0.190	0.315

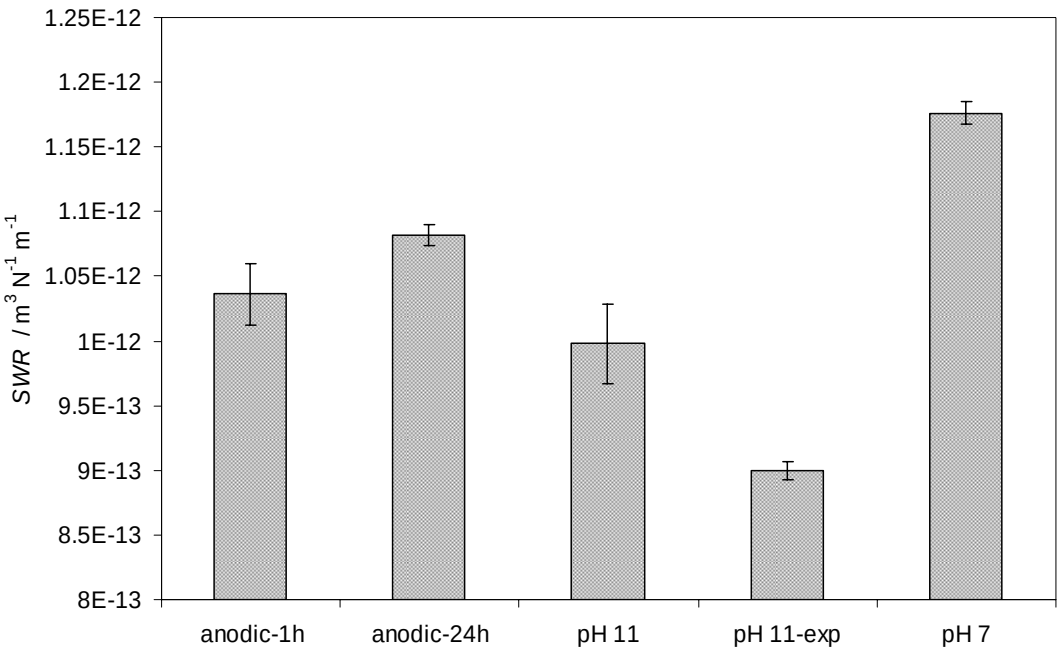

Figure 6.5: *SWR* for WC-10Co-4Cr coated samples (anodic, pH 11 and pH 11-exp) after 90 m sliding.

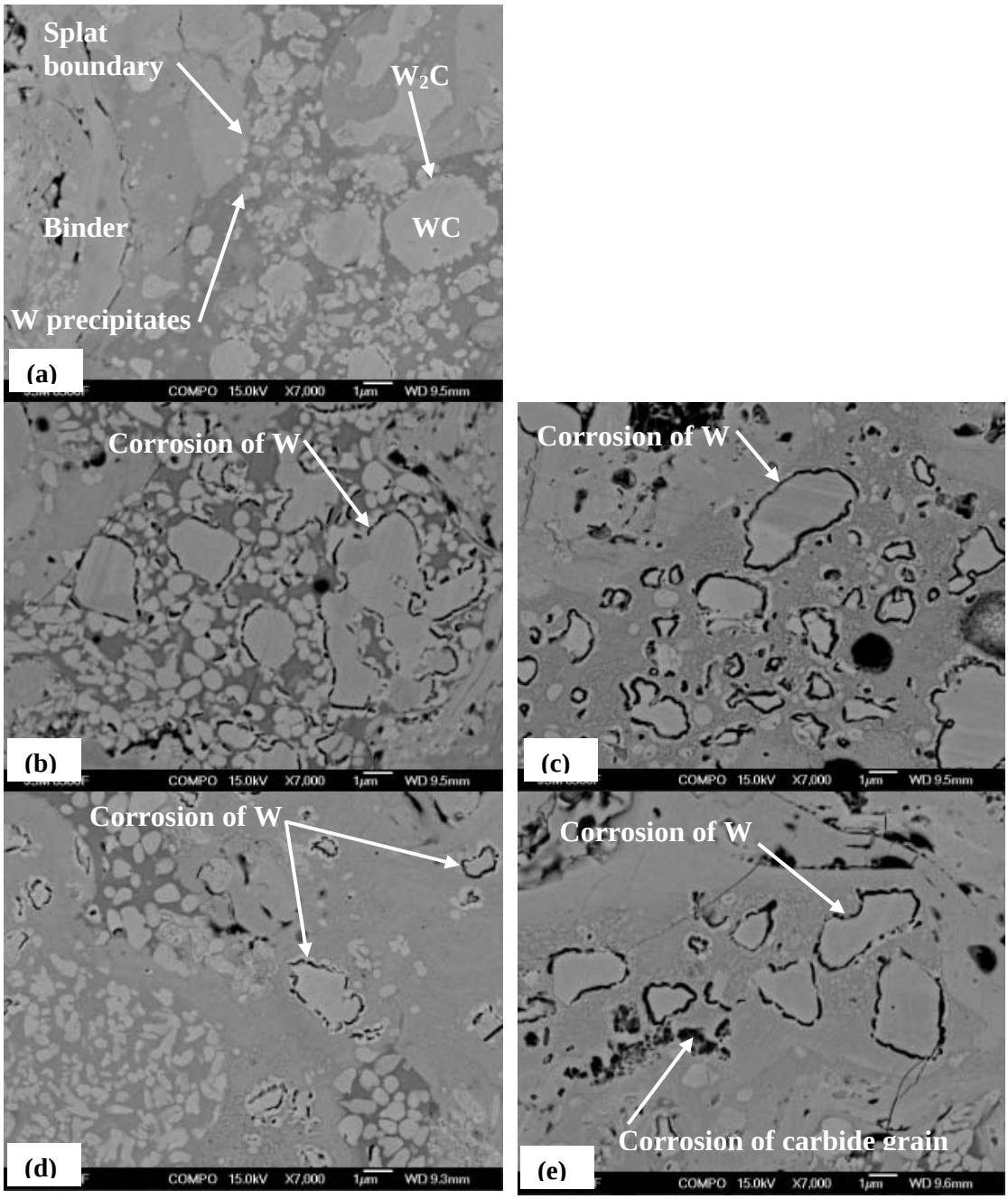

Figure 6.6: SEM micrographs of WC-10C0-4Cr coating; (a) fresh, (b) exposed to drilling fluid for 168h, (c) exposed to NaOH for 168 hrs, (d) after anodic treatment in NaOH solution of pH 11 for 1 h and (e) anodic treatment for 24 h.

Figure 6.5 shows the *SWR* for the pH 11, anodic (1h and 24h) and pH 11-exp samples after micro-abrasion using abrasive slurry of SiC particles suspended in NaOH solution (other test conditions are detailed in Table 3-2, Chapter 3). The results show that the anodically treated samples result in a slightly lower *SWR* compared to pH 7. However, the *SWR* for anodically treated samples is higher than the pH 11 and pH 11-exp samples. Clearly, anodising the samples has not achieved the exact replication of the conditions which lead to the lowering of *SWR* compared to pH 7 samples. To understand the micro-abrasion-corrosion

performance of the anodically treated samples, SEM micrographs of anodically treated surfaces (unworn) were examined.

Figure 6.6 compares the SEM-BSE images of the polished surfaces of fresh, exposed and anodically treated samples. Figure 6.6a shows a fresh surface with carbide grains ranging from less than 1μm to 4 μm. As discussed in Chapter 2, during the process of spraying, the WC grain undergoes decarburising and forms W_2C and metallic W along the grain boundary [29, 30]. Verdon *et al*. [29] found that apart from the decarburising of WC along the grain boundaries, colonies of tungsten precipitates of ≈100 nm in size are formed along the splat boundary due to the melting of WC particles and precipitation of W on subsequent cooling. Figure 6.6b and c compare the surfaces exposed to drilling fluid of pH 11 (Chapter 5) and NaOH solution of the same pH respectively. The micrographs show similar features with preferential corrosion along the periphery of the carbide grain i.e. in regions which are likely to have formed metallic W. The micrographs of exposed samples also reveal that the localised corrosion observed along the carbide grain boundary progresses towards the carbide grain and not towards the binder. This is likely to be due to the selective passivation of the binder phase observed by other workers [113, 119]. Figure 6.6d and e compare the surfaces of samples anodically treated for 1 h and 24 h respectively. The sample anodically treated for 1 h shows some corrosion along the carbide grain, although to a lesser extent than what is observed in the exposed samples.

Table 6-3: Summary of results for samples tested under different conditions.

	pH 11	pH 11-exp	df-exp	anodic-1h	anodic-24h	pH 7
SWR ($m^3N^{-1}m^{-1}$) (90m)	9.98	9.00	10.4	10.36	10.81	11.8
E_{corr} (V)	-0.39	-0.19	-0.26	-0.35	-0.30	NA
i_{corr} (μA)	1.57	0.32	0.16	0.55	0.47	NA

The sample anodically treated for 24 h shows similar features as observed for the exposed samples. Interestingly, the sample anodically treated for 24 h shows complete dissolution of small WC grains and precipitated W particles, suggesting that exposure to alkaline conditions for extended durations could lead to complete dissolution of WC particles.

Table 6-3 summarises the results (*SWR*, E_{corr} and i_{corr}) for pH 7, pH 11, df-exp, pH 11-exp and anodically treated samples. Figure 6.7 shows *SWR* plotted against the E_{corr} for all the samples tabulated in Table 6-3. The observed trend of E_{corr} vs. *SWR* is not linear. Despite being more electropositive, the anodically treated samples show a higher *SWR* as compared

to the pH 11 sample. However, the exposed sample has a higher E_{corr} than the anodically treated samples and it also displays a lower *SWR*. The lowest *SWR* was observed for the pH 11-exp sample. The same sample also shows the highest E_{corr} value. It appears that for the exposed samples, an increase in the E_{corr} results in a corresponding decrease in *SWR* while for the anodically treated samples, an increase in the E_{corr} results in an increase in the *SWR*. Clearly, the active dissolution which results from anodic treatment of the samples (and leads to a subsequent decrease in the E_{corr} value) does not replicate the exposed surface and results in an increase in *SWR* despite an increase in E_{corr}. The possible reasons for this difference in performance are discussed below.

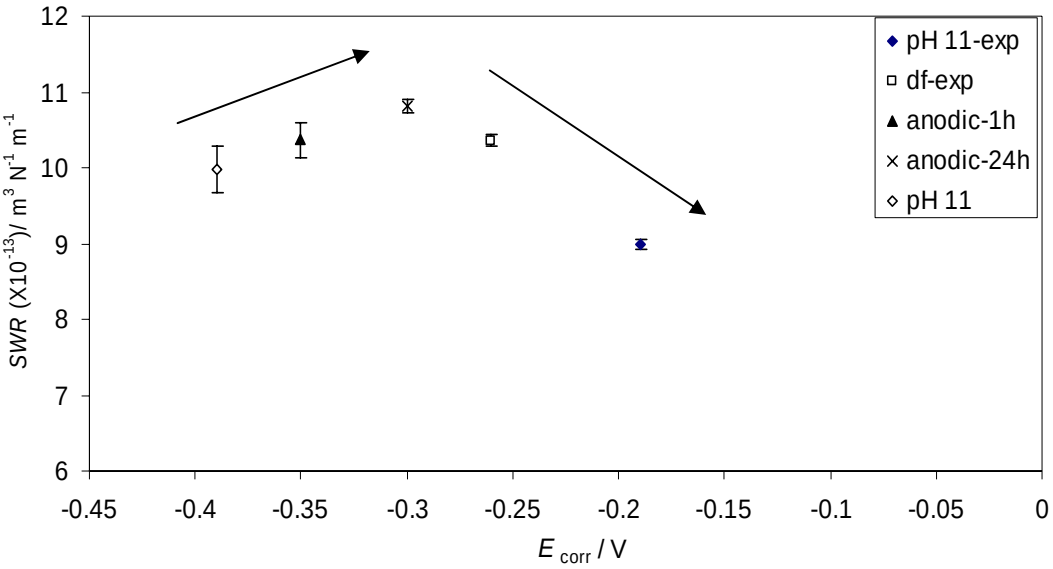

Figure 6.7: *SWR* vs. E_{corr} for all WC-10Co-4Cr coating samples.

While anodic treatment holds the whole sample at -200 mV (i.e. all anodic), exposure allows anode/cathode sites to develop naturally. The anodic treatments of the sprayed samples result in the preferential corrosion of metallic W and replicate the corrosion trench formed due to exposure. However, anodically treated surface does not result in the passivation of the binder-rich regions. Hence, anodically treated surfaces do not replicate the surface chemistry and exact contact conditions resulting from exposure to alkaline conditions leading to a difference in the *SWR*. Clearly, it is necessary to investigate the nature of the passive films on the exposed surfaces and the possible modification in the contact due to the formation of the trench around the carbide grains.

6.2.3 Exposure to distilled water/ pH 11 NaOH solution for 1 week

6.2.3.1 Sprayed WC-10Co-4Cr coating

Figure 6.8 compares the SEM micrographs of (a) freshly polished (b) pH 11-exp and (c) pH 7-exp WC-10Co-4Cr coated samples. Interestingly, corrosion of the metallic W ring at the periphery of the WC grains is observed for samples exposed to pH 7 as well as pH 11; see Figure 6.8 (b & c).

Table 6-4: States of Cr, Co and W as described in their Pourbaix diagrams [102] under neutral and alkaline conditions.

pH	Cr	Co	W
7	Passive	Corrosion	Corrosion
	$Cr(OH)_3$	(Co^{2+})	(WO_4^{2-})
11	Corrosion	Passive	Corrosion
	(CrO_4^{2-})	$Co(OH)_2$, Co_3O_4	(WO_4^{2-})

For the sprayed coatings, the presence of metallic W and large binder-rich regions on the surface would lead to the preferential corrosion of W and form localised corrosion-trenches along the periphery of WC grains in both pH 11 NaOH solution and pH 7. The likely corrosion interactions leading to the formation of localised corrosion-trenches in pH 11 and pH 7 are shown schematically in Figure 6.9. The two-step corrosion reaction for metallic W results in the lowering of local pH within this trench. However, this decrease in local pH is expected be restricted to the corrosion-trenches formed around the carbide grains and is not likely to influence the overall pH of the solution at the coating surface. Hence the localised corrosion of metallic W around the WC grains is not likely to result in the destabilising and dissolution of $Co(OH)_2$ passive film present on the binder.

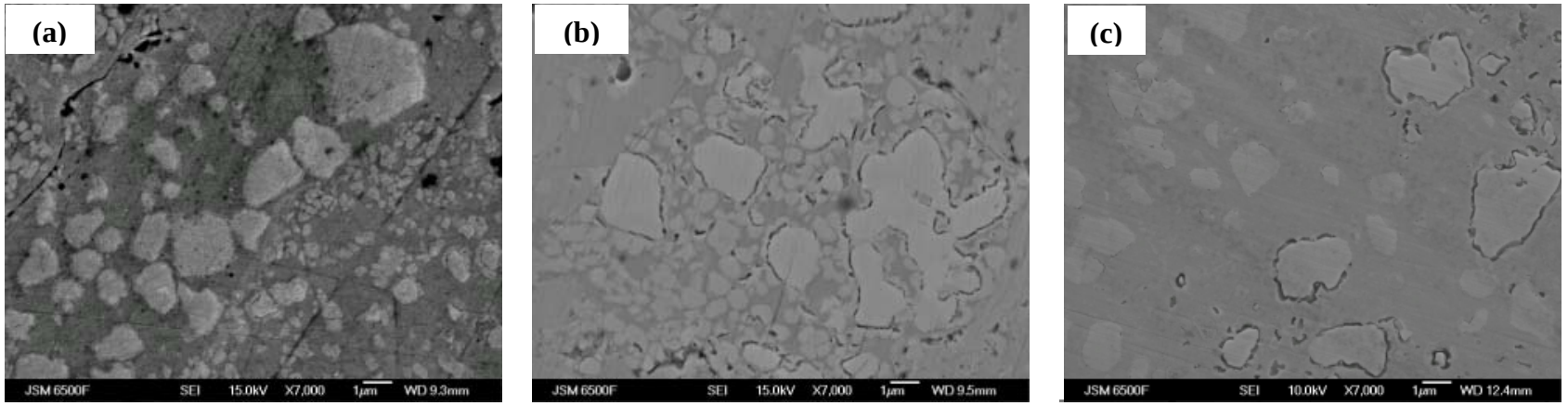

Figure 6.8: Comparison of WC-10Co-4Cr coating; (a) freshly polished surface, (b) exposed to NaOH solution of pH 11 and (c) exposed to distilled water.

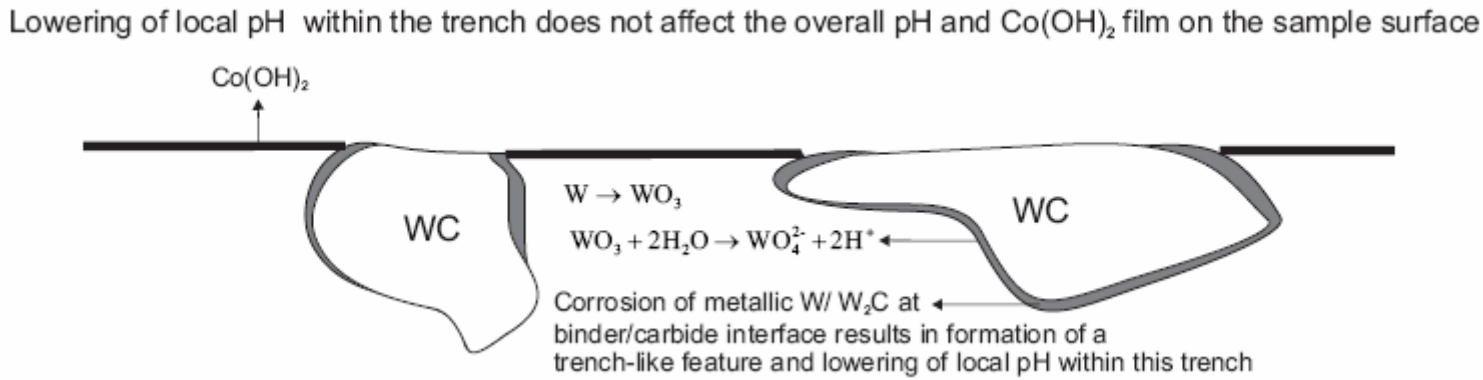

Figure 6.9: Corrosion schematic for sprayed WC-10Co-4Cr coating.

6.2.3.2 Sintered WC-5.7Co-0.3Cr

The corrosion behaviour of the sintered samples is expected to be influenced by the amount of binder in a sintered sample which is significantly lower than that found in sprayed coatings. The surface of sintered samples is rich in WC grains with the binder being present in the gaps between the carbide grains. The Co-rich binder phase is expected to contain metallic W due to its dissolution in the binder phase during the liquid phase sintering process [158, 159]. Figure 6.10(a and b) compare the SEM micrographs of WC-5.7Co-0.3Cr sintered samples before and after exposure to pH 11 NaOH solution (pH 11-exp). Figure 6.10c shows the exposed surface at higher magnification. The pH 11-exp surface shows negligible binder dissolution or corrosion at the binder-carbide interface. Passivation of Co is expected to result in the formation of a stable oxide film comprising of $Co(OH)_2$ and Co_3O_4 [160]. Figure 6.10 (d and e) compare the SEM micrographs of WC-5.7Co-0.3Cr sintered samples before and after exposure to distilled water (pH 7-exp). Figure 6.10f shows the exposed surface at higher magnification. The SEM micrographs clearly show evidence of selective dissolution of the binder phase. Galvanic coupling between metallic W and Co results in the corrosion of W as discussed in Chapter 2. The corrosion of metallic W is expected to result in a drop in the local pH [105]. However, due to the skeletal structure of the sintered samples, a change in the local pH influences the stability of the binder present in the crevices between carbide grains at the sample surface, see Figure 6.10. Lowering of the local pH results in the instability of the passive film formed on Co, see Equation 6.1.

$$Co(OH)_2 + 2H^+ \rightarrow Co^{2+} + H_2O \qquad \textbf{6.1}$$

The corrosion process is shown schematically in Figure 6.11**.** For the samples exposed to pH 11, the drop in local pH from pH 11 is not likely to accelerate binder dissolution as Co is expected to passivate under neutral and weak alkaline conditions, see Figure 6.10c. However, for the samples exposed to distilled water a drop in the local pH from pH 7 is expected to turn the local environment acidic and reduce the stability of $Co(OH)_2$, see Equation 6.1. The corrosion process is also shown schematically in Figure 6.10f.

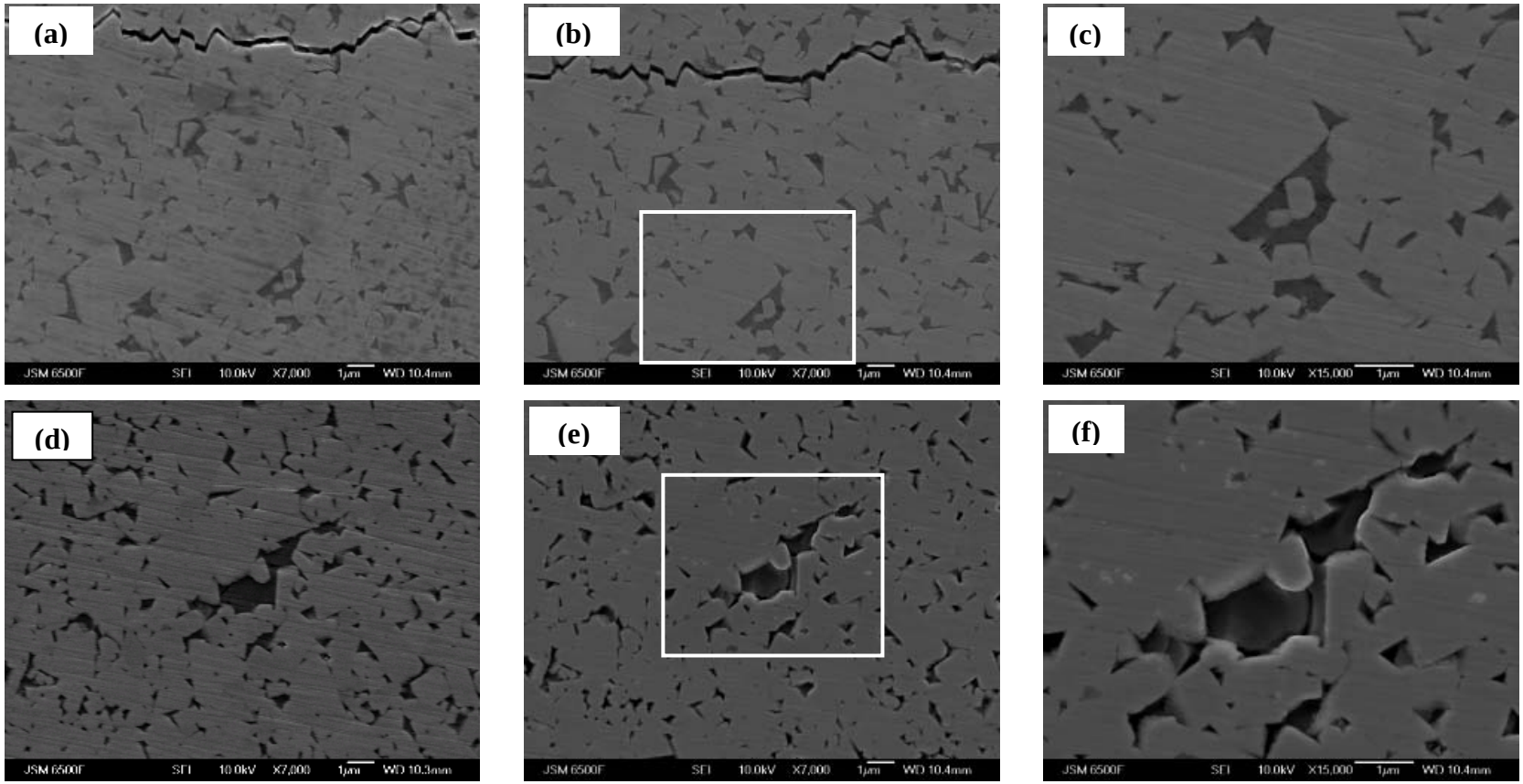

Figure 6.10: Comparison of sintered WC-5.7Co-0.3Cr samples; (a) the freshly polished surface, (b) after exposure to pH 11 NaOH solution (pH 11-exp), (c) high magnification image of area highlighted in (b), (d) the freshly polished surface, (e) after exposure to distilled water (pH 7-exp) and (f) high magnification image of area highlighted in (e).

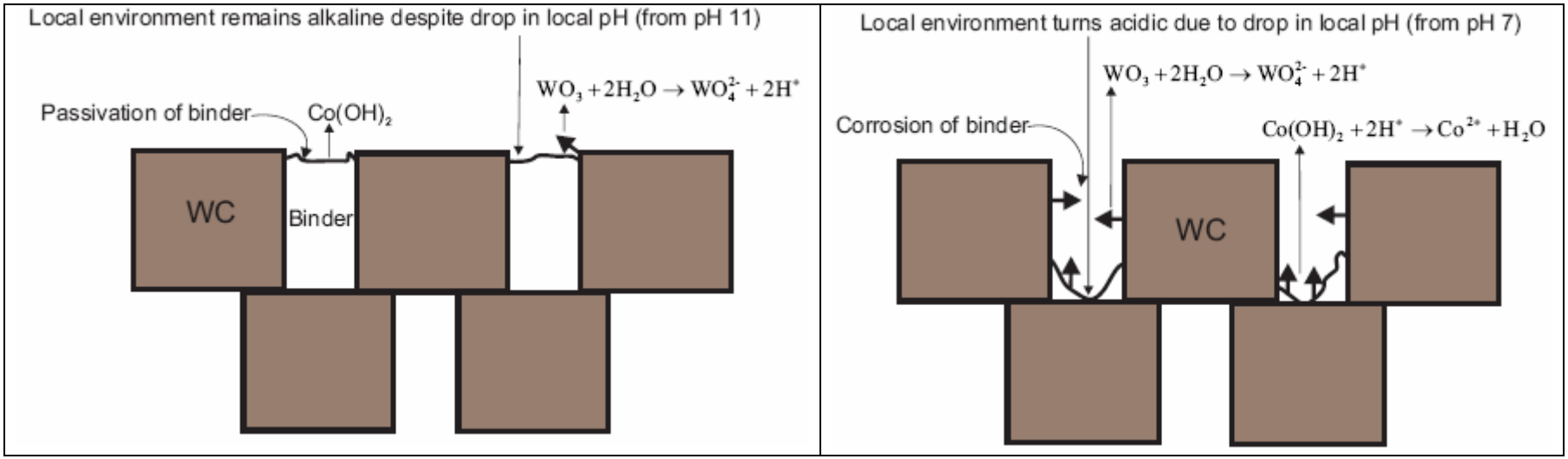

Figure 6.11: Schematic for corrosion occurring on sintered WC-5.7C0-0.3Cr in (a) alkaline environments of pH 11 and (b) neutral environments (pH 7).

6.2.4 XPS analysis on fresh and exposed samples

X-ray photoelectron spectroscopy (XPS) analysis was performed on fresh and exposed (pH 7 and pH 11) samples of WC-10Co-4Cr coating and sintered WC-5.7Co-0.3Cr to characterise the changes in the surface composition as a result of exposure to pH7 and pH 11 conditions. National Institute of Standards and Technology (NIST) XPS online database [161] has been used to compare binding energies observed in the species observed on the fresh and exposed surfaces.

6.2.4.1 Sprayed WC-10Co-4Cr coating

Figure 6.12 compares the Co(2p) signals from fresh and exposed samples. As seen in Figure 6.12a, the main peak for Co(2p) signal at 778.3 eV indicates the presence of metallic Co on the surface of the sample. A weak signal in the range of 781.0 eV suggests presence of an oxide film on the surface. As the binding energies for CoO, $Co(OH)_2$ and Co_3O_4 are similar, it is not possible to identify the exact composition of the oxide film from the Co(2p) spectra. However, as discussed in the section 6.2.3, Pourbaix diagrams [102] for Co in neutral and alkaline conditions suggest a passive film of $Co(OH)_2$. A passive film of $Co(OH)_2$ was also identified by Hochstrasser [105] on the binder-phase of sintered WC-6Co.

Figure 6.12b and Figure 6.12c show the Co(2p) spectra for WC-10Co-4Cr coating exposed to pH 7 and pH 11 respectively. Clearly, both the spectra show the main peak of Co(2p) signal at 781 eV indicating that an oxide film is present on the Co-phase. This is also corroborated by the weak signal in the range of 778.2 eV, corresponding to metallic Co. Similarly, the XPS spectra for Cr on the fresh sample shows a peak at 574.2 eV corresponding to metallic Cr, see Figure 6.13a. The fresh sample also shows a weak signal in the Cr(2p) range of 577.1 eV, where Cr_2O_3 is expected. As observed for Co(2p) peaks, the Cr(2p) spectra for WC-10Co-4Cr coating exposed to pH 7 and pH 11 reveal the main peak for Cr(2p) signal at 577.2 eV indicating that the metal Cr phase is covered by an oxidised surface layer of Cr_2O_3. Similar oxide peak was identified by Souza and Neville [117] during the XPS analysis of anodised WC-10Co-4Cr samples. Figure 6.14 shows the C(1s) spectra for fresh and exposed samples of WC-10Co-4Cr coating. While the fresh sample shows a distinct peak corresponding to the binding energy of WC, the exposed samples show a single peak at 285 eV corresponding to C. This further corroborates that there is dissolution of W occurring on the sample surface. While the corrosion of metallic W and subsequent decrease in the local pH leads to the formation of corrosion trenches on the surface of the coating, the absence of a distinct peak corresponding to WC in the C(1s) spectra is also likely to be due

to the formation of WO_3 oxide on the carbide surfaces of pH 7-exp and pH 11-exp samples as observed from their respective W(4f) peaks, see Appendix 1. Clearly, the XPS analysis of the WC-10Co-4Cr coating showed the presence of $Co(OH)_2$, Co_3O_4 on the surface of the exposed coating and the absence of metallic W suggesting that the binder rich regions passivate while the metallic W corrodes leading to the formation of a localised corrosion-trenches along the periphery of WC grain as seen in Figure 6.8(b and c).The XPS results are also tabulated in Table 6-5.

Table 6-5: XPS results for fresh and exposed (pH 7, pH 11) WC-10Co-4Cr coating

Sample condition	**Element**	**Detected species**	**Binding Energies (eV)***
Fresh	Co(2p)	Co	778.3
	Cr(2p)	Cr	574.2
		Cr_2O_3	577.1
	C(1s)	WC	283.0
Exposed (pH 7)	Co(2p)	$Co(OH)_2$.	781.0
	Cr(2p)	Cr_2O_3	577.1
Exposed (pH 11)	Co(2p)	$Co(OH)_2$.	781.0
	Cr(2p)	Cr_2O_3	577.1

** Binding energies compared with the NIST online database [161]*

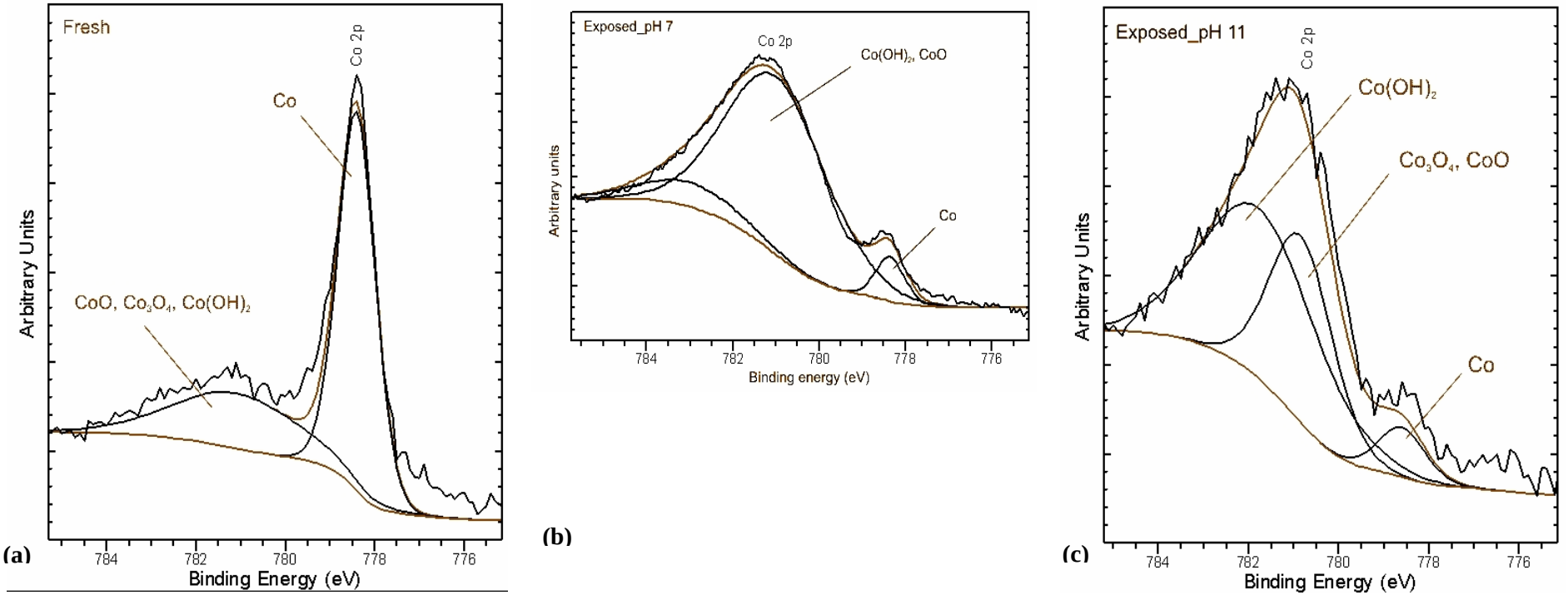

Figure 6.12: XPS of Co(2p) peak from the surface of WC-10Co-4Cr coating (a) fresh, (b) exposed to pH 7 and (c) exposed to pH 11.

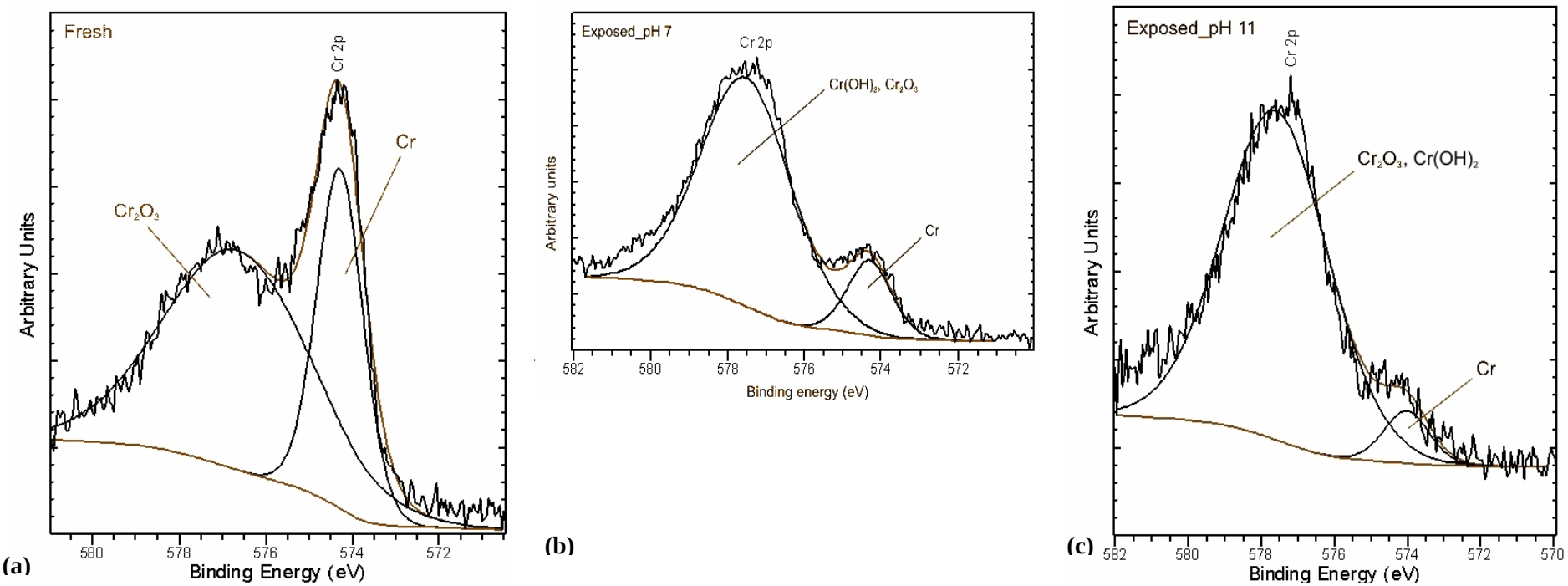

Figure 6.13: XPS of Cr(2p) peak from the surface of WC-10Co-4Cr coating (a) fresh, (b) exposed to pH 7 and (c) exposed to pH 11.

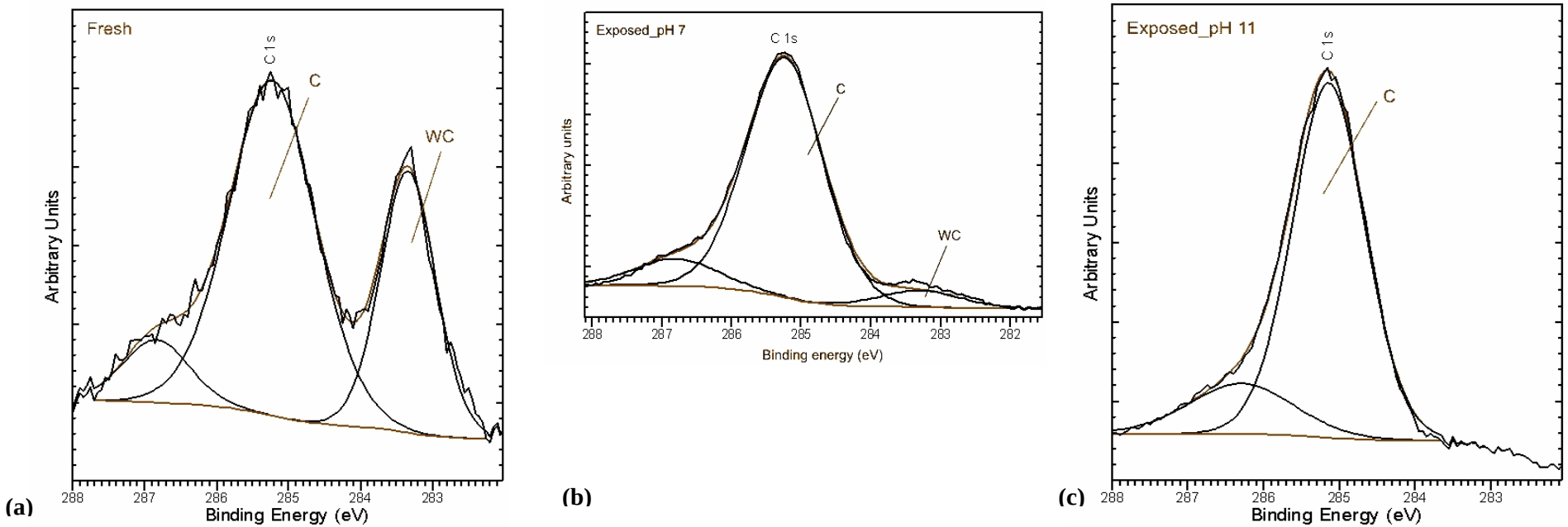

Figure 6.14: XPS of C(1s) peak from the surface of WC-10Co-4Cr coating (a) fresh, (b) exposed to pH 7 and (c) exposed to pH 11.

6.2.4.2 Sintered WC-5.7Co-0.3Cr

Figure 6.15 compares the Co(2p) spectra for fresh and exposed samples of sintered WC-5.7Co-0.3Cr. The Co(2p) spectra for the fresh sample reveals a main peak at 778.2 eV indicating the presence of metallic Co on the surface. As observed by Hochstrasse [105], Co-phase in sintered samples readily passivate to $Co(OH)_2$, as can be corroborated from the smaller peak in the Co(2p) spectra at 781 eV indicating the presence of $Co(OH)_2$ (781.0eV). The Co(2p) spectra for sintered samples exposed to pH 7 and pH 11 show the main peak signal at 780.9 eV, suggesting that the Co binder is covered with an oxide surface layer.

The selective dissolution of W out of the WC phase is likely to result in the formation of a carbon-enriched zone on the surface, which prevent re-oxidation of W (to WO_3) [105]. This is corroborated by the comparison of C(1s) spectra for fresh and exposed samples, see Figure 6.16 . The C(1s) spectra for the fresh sample reveals a main peak at 283.1 eV indicating the presence of WC on the surface. However, the C(1s) spectra for the exposed surfaces show a relatively weak signal at 283.1 eV, indicating the dissolution of metallic W and the formation of a carbon-enriched zone. The lack of WO_3 oxide formation on the exposed surfaces is also corroborated by the absence of a distinct peak corresponding to WO_3 in the W(4f) spectra, see Appendix 1.

Clearly, the XPS analysis of the fresh and exposed surfaces provides evidence of dissolution of metallic W and the formation of oxides on the binder-rich areas. As discussed in the section 6.2.3, dissolution of W leads to the drop in the local pH and subsequent localised dissolution of $Co(OH)_2$ film on the binder-rich areas. The XPS results for fresh and exposed sintered WC-5.7Co-0.3Cr are also tabulated in Table 6-6.

Table 6-6: XPS results for fresh and exposed (pH 7, pH 11) sintered WC-5.7Co-0.3Cr

Sample condition	Element	Detected species	Binding Energies (eV)*
Fresh	Co(2p)	Co	778.3
	C(1s)	WC	283.0
Exposed (pH 7)	Co(2p)	$Co(OH)_2$.	781.0
	C(1s)	WC	283.0
Exposed (pH 11)	Co(2p)	$Co(OH)_2$.	781.0
	C(1s)	WC	283.0

** Binding energies compared with the NIST online database [161]*

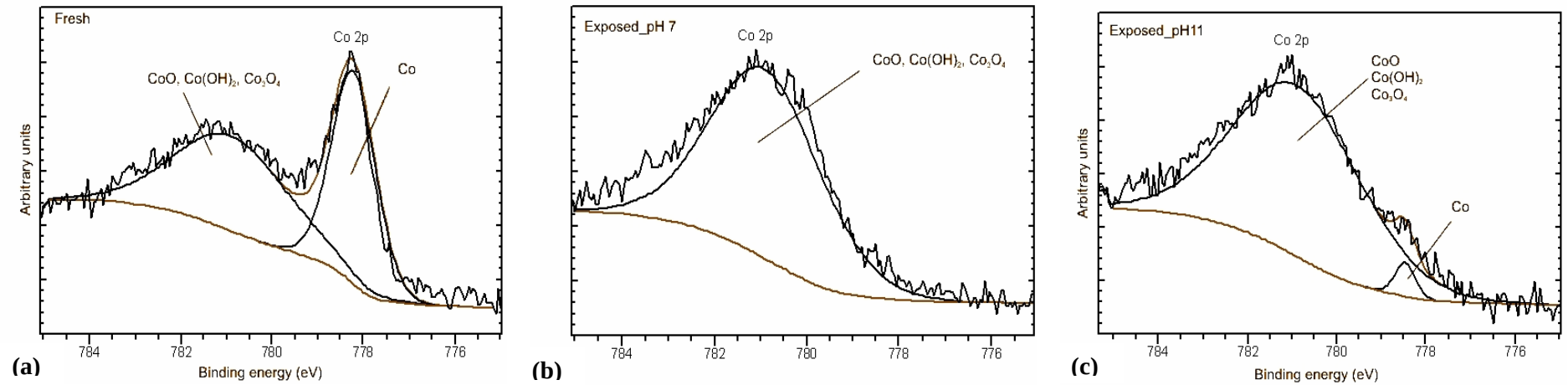

Figure 6.15: XPS of Co(2p) peak from the surface of sintered WC-5.7Co-0.3Cr (a) fresh, (b) exposed to pH 7 and (c) exposed to pH 11.

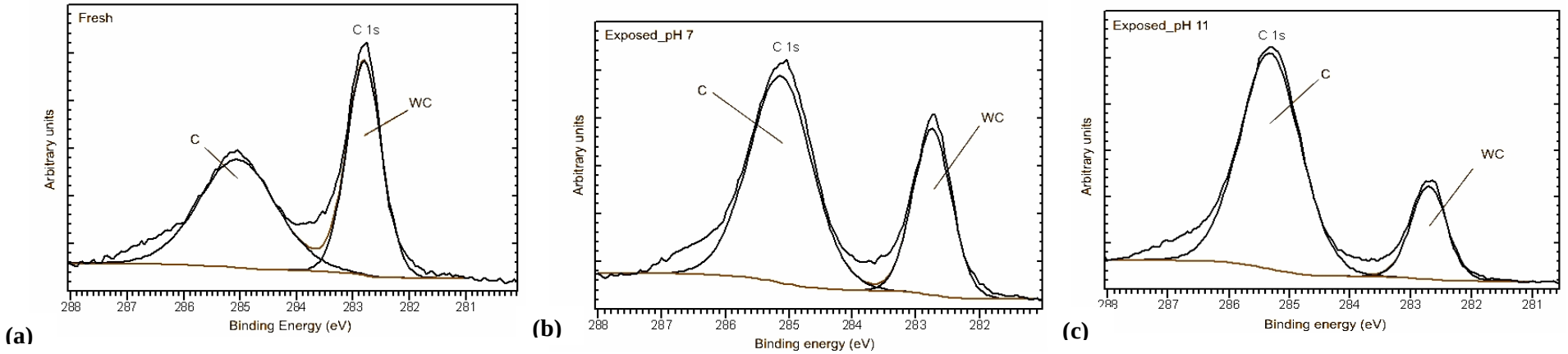

Figure 6.16: XPS of C(1s) peak from the surface of sintered WC-5.7Co-0.3Cr (a) fresh, (b) exposed to pH 7 and (c) exposed to pH 11.

6.2.5 FIB sectioning of the exposed WC-10Co-4Cr coating

As discussed earlier (Chapters 5 and 6), the wear-corrosion interactions of the WC-10Co-4Cr coating appear to be influenced by the contact conditions due to the presence of corrosion trenches around WC grains. Conventional sample sectioning using a precision saw and grinding/polishing for SEM analysis does not preserve these corrosion features. Hence it is not possible to accurately estimate the depth of corrosion attack around the carbide grains using conventional approaches. However, FIB sectioning allowed the exposed sample to be sectioned without damaging the corrosion features, particular the carbide grains which were presumed to be loose within the corrosion cavity. Figure 6.17 shows the FIB milled slot revealing the cross-section of the coating. Clearly, as predicted, selective dissolution of the metallic W results in the corrosion trench propagating underneath the carbide grain resulting in the carbide grain being loose in the cavity. The SEM micrograph also reveals that the selective dissolution of W phase only occurs on the carbides at the surface. There is no evidence of corrosion on the sub-surface carbide grains. Clearly, the corrosion attack appears to be one-carbide deep. Also, the depth of corrosion attack is not uniform as can be seen from the partially formed corrosion trench, see Figure 6.18.

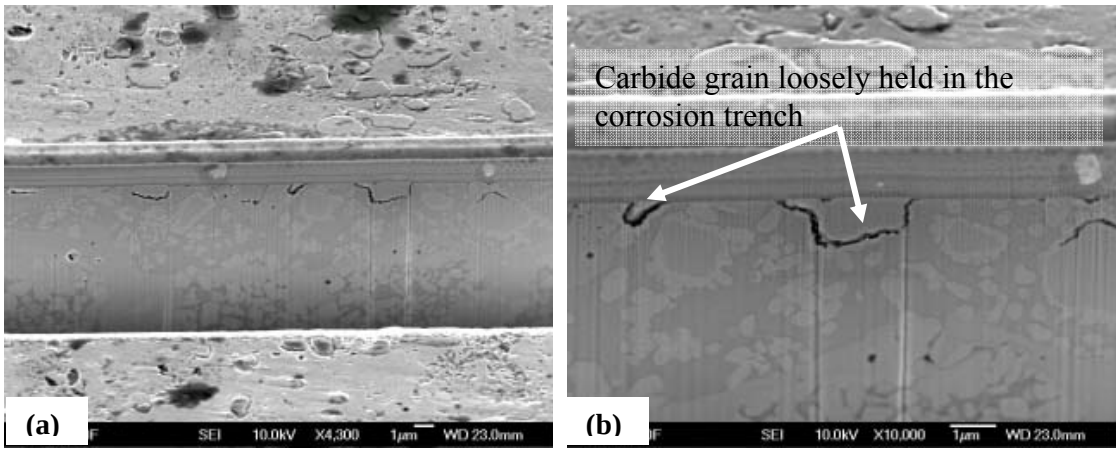

Figure 6.17: FIB section of pH 11-exp WC-10Co-4Cr coating revealing the corrosion of metallic W around the WC grain (a) low magnification image and (b) high magnification image.

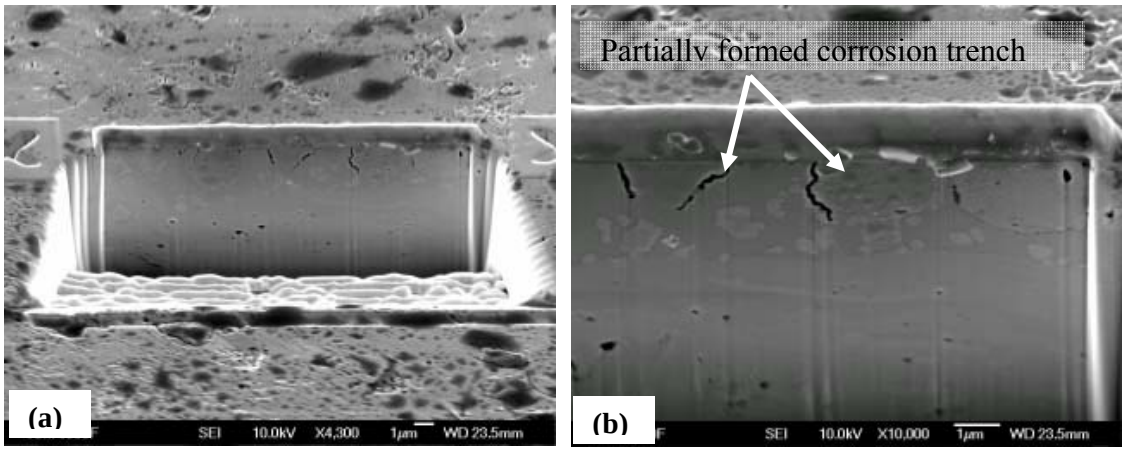

Figure 6.18: Partially formed corrosion trench due to the selective dissolution of metallic W.

6.2.6 Summary

Clearly, as predicted in the Chapter 5, corrosion trenching around the carbide grain results in the carbide grain becoming loose within the corrosion cavity. Loosely held carbides are likely to offer additional surface compliance during abrasive wear, a possible reduction in contact stress along with an effective crack arrest due to the detached nature of the carbides, all of which possibly leads to a decrease in the *SWR* observed for exposed samples. Although the anodic treatments of the WC-10Co-4Cr coating result in the formation of similar corrosion trenches on the surface, it does not result in a similar decrease in the *SWR,* possibly due to the absence of passive film on the surface of anodically treated samples. The XPS analysis confirms the presence of a passive film on the binder-rich regions of the WC-10Co-4Cr coating rich in $Co(OH)_2$. The presence of $Co(OH)_2$ is known to result in the lowering of friction between the abrasive particle and the coating surface [35]. A decrease in the friction between abrasive and the surface and the presence of loose carbides on the surface are likely to influence the particle entrainment in the contact. According the model for particle entrainment predicted by Shipway [50], the transition from sliding to rolling occurs at a critical value of the turning moment on the particles. A decrease in the friction and increase in surface compliance is likely to encourage sliding / grooving of the particles instead of rolling. It has been observed earlier that for the micro-abrasion test, grooving mode of abrasive wear results in lower wear as compared to rolling mode. However, as observed in Figure 6.3, the wear scars are well are approximately 15 μm deep (4-5 carbides) while the corrosion trench due to exposure is 3-4 mm deep (1 carbide). Clearly, for the corrosion trenches to influence the wear-corrosion process, the rate of corrosion in the coating should be faster than the rate of wear. It is essential to know the corrosion kinetics occurring during wear-corrosion process for an accurate estimation of the corrosion rate during wear. Hence, a

micro-abrasion tester capable of *in situ* electrochemical measurements needs to be deployed for monitoring the corrosion kinetics (repassivation/depassivation, corrosion of metallic W on the wear scar) during wear-corrosion.

6.3 Conclusions

- No simple relationship between E_{corr} and *SWR* due to different surface chemistry and sub-surface corrosion attack. Anodic treatment of the WC-10Co-4Cr coating results in the preferential corrosion of metallic W ring along the periphery of the carbide grains and results in the formation of corrosion trenches for samples exposed to pH 11 NaOH solution for 1 week.

- Anodic treatment of the coating also revealed that the preferential corrosion initiated at the metallic W ring along the periphery of the carbide grain propagates towards the centre of the carbide grain and not towards the binder-phase as thought previously. However, anodic treatments do not replicate the contact conditions generated due to exposure to pH 11, possibly due to the lack of selective passivation on binder-rich regions

- Interestingly, exposure to pH 7 conditions result in the preferential dissolution of the binder-phase in the sintered WC-5.7Co-0.3Cr samples. This is due to the local drop in the pH leading to crevice-type corrosion of the binder-phase. However, crevice-type corrosion of the binder-phase is not observable in sintered samples exposed to pH 11 NaOH solution.

- Corrosion trenches are also observed in WC-10Co-4Cr coating exposed to pH 7. Clearly, corrosion features observed on sintered as well as sprayed samples on exposure to pH 7 indicates that pH 7 should not be considered as a "corrosion free environment".

- XPS analysis of sprayed WC-10Co-4Cr coating confirmed the presence of Cr_2O_3 and $Co(OH)_2$ films on the binder rich regions along with the preferential depletion of metallic W from the surface of samples exposed to pH 7 and pH 11 conditions. XPS analysis of sintered WC-5.7Co-0.3Cr also confirmed the preferential dissolution of metallic W and the formation and formation of $Co(OH)_2$ on the binder-rich areas.

- The FIB sectioning of WC-10Co-4Cr coating exposed to pH 11 revealed that the depth of preferential corrosion attack of the metallic W ring is one-carbide deep and results in the loosening of the carbide grain. This is likely to influence the contact

mechanics during micro-abrasion. It is likely that the lowering of *SWR* observed for the exposed WC-10Co-4Cr coating is due to the subtle changes in contact conditions by the combined effect of increased surface compliance and selective passivation of the binder-phase altering friction values between abradant and coating surface.

- However, the corrosion trenches observed are one-carbide deep whereas the wear scar is 4-5 carbides deep. For the corrosion trenches to influence the contact conditions during wear-corrosion, the rate of corrosion of metallic W should be faster than the rate of abrasion. Deployment of a modified micro-abrasion tester capable of *in situ* electrochemical measurements is necessary to monitor corrosion kinetics occurring during wear-corrosion and will be dealt with in Chapter 7.

7 *In situ* electrochemical current noise measurements during micro-abrasion

7.1 Introduction

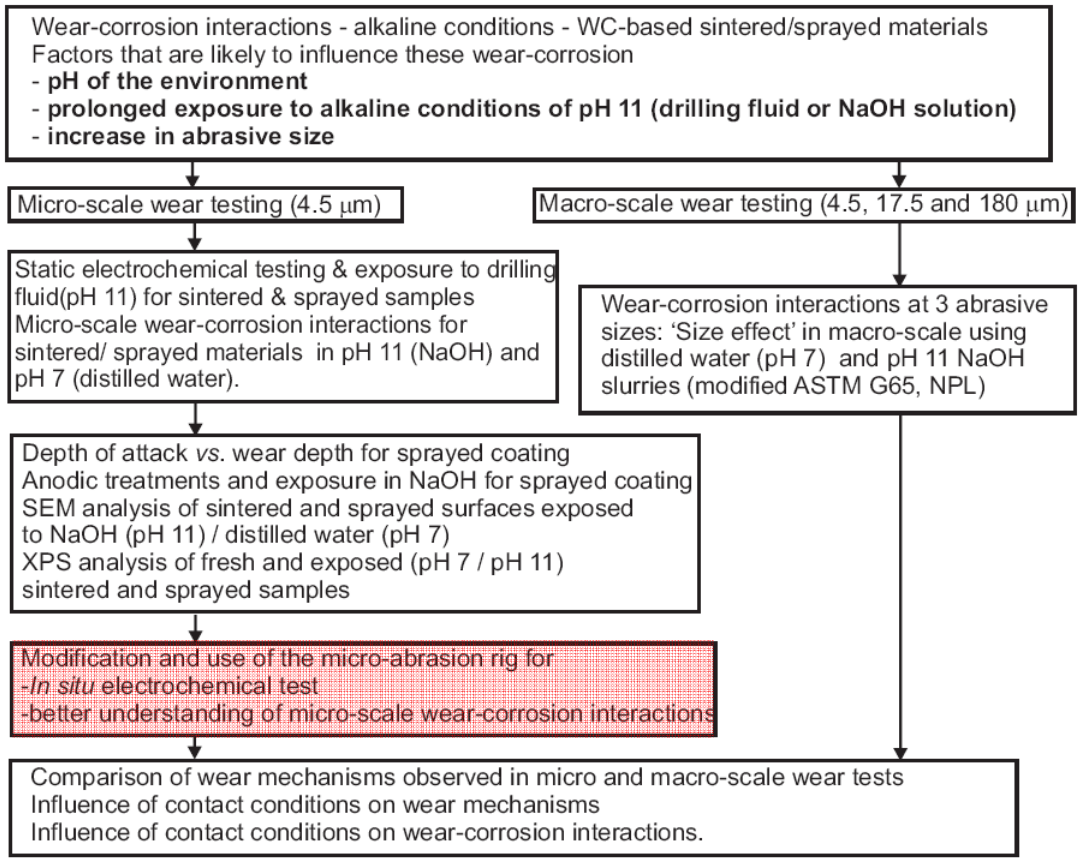

Figure 7.1: Experimental flow chart showing the test programme discussed in Chapter 7 (highlighted).

In previous chapters (Chapter 5 and Chapter 6), elucidating the wear-corrosion interactions was attempted during micro-abrasion tests by comparing the specific wear rates (*SWR*) obtained using neutral (pH 7) and alkaline (pH 11) slurries. The electrochemical activity was inferred based on the *SWR* observed. Clearly, corrosion features observed on WC-based sintered hardmetals and sprayed coatings exposed to neutral conditions revealed that neutral conditions can not be considered as 'corrosion free' environment. Also, this arrangement does not provide any understanding of the electrochemical response to abrasive wear i.e. repassivation within the wear scar during abrasion test and the influence of abrasive wear on corrosion. Hence, in this chapter, a modified micro-abrasion tester capable of *in situ* electrochemical measurements is deployed to monitor fluctuations in current (referred to as

noise). Conducting micro-abrasion tests on a sample partially immersed in test solution of the same pH as the abrasive slurry and measuring the current-noise before (stationary ball in contact with the sample with load applied), during (ball rotating against the sample) and after (stationary ball in contact with the sample) the micro-abrasion test provides invaluable information about the corrosion kinetics during wear-corrosion. The current-noise response observed can be used to establish a relationship between the ability (or inability) of the sample to passivate during micro-abrasion test and the pH of the abrasive slurry. The area under the current (I) *vs.* time (t) curve is known as electrochemical charge (Q), which represents corrosion occurring due to abrasive wear. Q can be converted to a mass loss using Faraday's law. The test set-up and test procedures are detailed in Chapter 3 along with sample preparation.

Due to the possible inaccuracies in the estimation of pure abrasion (PA) using CP and pure corrosion (PC) (discussed in Chapter 2), the use of PC, PA and ΔPA_C, ΔPC_A to calculate wear-corrosion interactions has been deliberately avoided. Instead, as discussed in the Chapter 2, wear-corrosion interactions were calculated by the equation proposed by Jemmely *et al.* [125], see Equation 7.1

$$SWR_{Mech} = SWR_{Total} - SWR_{Elec} \qquad \textbf{7.1}$$

Where, SWR_{Total} represents the total wear due to wear-corrosion interactions and is obtained by measuring the wear-scar on the sample. SWR_{Elec} represents the electrochemical component of the wear-corrosion interaction and SWR_{Mech} represents the mechanical component of wear-corrosion interaction. For comparison, wear tests was also done in pH 11 conditions by applying a negative potential (300 mV below OCP) to the sample leading to cathodic protection (CP) of the sample from corrosion (avoiding hydrogen evolution and calcification). The test conditions and the setup are discussed in detail in Chapter 3. Details of the test matrix are shown in Table 7-1.

Table 7-1: Matrix showing the test conditions, i.e. OCP (values) / CP (values)

	Fresh				**Exposed**	
	pH 7 (mV)	**pH 9 (mV)**	**pH 11 (mV)**	**pH 13 (mV)**	**pH 7 (mV)**	**pH 11 (mV)**
WC-10Co-4Cr coating	OCP (-190)	OCP (-250)	OCP (-250) / CP (-550)	OCP (-400)	OCP (-252)	OCP (-240)
Sintered WC-5.7Co-0.3Cr	OCP (-210)	OCP (-130)	OCP (-250) / CP (-130)	OCP (-270)	OCP (-150)	OCP (-110)

7.2 Results and Discussion

7.2.1 Micro-abrasion with *in situ* electrochemical current noise measurement

The next two sections discuss the wear-corrosion interactions that occur under neutral and alkaline conditions for sintered and sprayed samples in terms of the effects of exposure time, microstructure and electrochemical current-noise data. The results provide an insight to the influence of microstructure and pH of abrasive slurry on repassivation kinetics for WC-based sintered and sprayed coatings.

7.2.1.1 Sprayed WC-10Co-4Cr

Figure 7.2 shows the electrochemical current noise response for the WC-10Co-4Cr coating during micro-abrasion tests for different pH. The *It* curves show a sharp rise in the current immediately after the abrasion test begins. This sharp rise in current is observed due to the removal/ damage of the passive $Co(OH)_2$ film on the binder rich areas. After the initial rise in the current it attains a relatively steady value, see Region 'A' in Figure 7.2. The current levels do not change substantially for the remaining duration of the micro-abrasion test despite the increase in the wear scar area. This is due to the repassivation occurring within the wear scar in binder-rich areas not being abraded at that instant. This is also corroborated by the observation of Region 'B' in the *It* curves, see Figure 7.2. The fluctuation in the current occurring in Region 'B' is due to the spontaneous repassivation within the wear scar and subsequent depassivation due to the action of abrasive particles. This process is discussed in detail in the next paragraph. At the end of each test the current levels sharply drop to similar values as seen before abrasion. This is due to the repassivation of the wear-scar after the ball rotation stopped. This further corroborates that binder-rich areas within the wear scar readily passivate in the absence of abrasion. A similar current-noise behaviour was observed during the reciprocating-sliding wear of passive metals (SS316, Cr and Ni)by Mischler *et al.*[136]. It was reported that the variation of the measured anodic current was the measure of the electrochemical metal removal rate in the wear scar.

The abrasive wear in WC-10Co-4Cr coating occurs by multiple indents of the size of abrasive particles (three-body) which also damages the passive film on the binder. Three-body rolling abrasion occurring in the wear scar is schematically shown in the Figure 7.3. Binder-rich areas not abraded at that instant repassivate, depending on the pH of the abrasive slurry (see Table 7-2). The preferential removal of the binder-phase exposes the carbides to

the abrasive particles. Loosening of exposed carbides occurs due to their fragmentation leading to the removal of unsupported fragments as shown in the Figure 7.3. Wear debris such as fractured carbides, oxide particles and abrasive particle fragments are likely to be ejected from the contact or re-embed within the wear scar leading to the modification of the contact conditions within the wear scar. Re-embedment of wear debris in the wear scar can result in an improvement in wear-resistance. Micro-galvanic coupling within the wear scar occurs due to the random distribution of carbide-rich and binder rich areas. Presence of re-embedded wear-debris is also likely to accelerate the micro-galvanic coupling by creating active-passive sites within the wear scar. Figure 7.3 also shows the micro-galvanic coupling between the worn and the unworn areas on the sample. The depassivation and repassivation occurring within the wear-scar is a complex process and is influenced by factors such as the size of the indentation caused by abrasive particles, applied load, concentration of abrasive particles within the abrasive slurry and pH of the abrasive slurry. The three-body indentation of the binder-rich region is shown schematically in Figure 7.4. Multiple indentations by abrasive particles result in the breaking of the passive film along with the abrasive wear of the binder phase and generate wear debris (oxide particles and fragments of abrasives). The removal of the passive film on the binder-rich areas exposes fresh surface underneath to the abrasive slurry. Partial repassivation of the freshly exposed surface depends on the ability of Co to passivate at the pH of the abrasive slurry (see Table 7-2).

Table 7-2: States of Cr, Co and W as described in their Pourbaix diagrams [102] under neutral and alkaline conditions under potentials used during wear-corrosion testing (between 100 mV and -200 mV *vs.*SHE).

pH	Cr	Co	W
7	Passive	Corrosion	Corrosion
	$Cr(OH)_3$	(Co^{2+})	(WO_4^{2-})
9	Passive	Corrosion/ Passive	Corrosion
	$Cr(OH)_3$	(Co^{2+})/ $Co(OH)_2$, Co_3O_4	(WO_4^{2-})
11	Corrosion	Passive	Corrosion
	(CrO_4^{2-})	$Co(OH)_2$, Co_3O_4	(WO_4^{2-})
13	Corrosion	Passive/ Corrosion	Corrosion
	(CrO_4^{2-})	$HCoO_2^-$	(WO_4^{2-})

The time taken for the repassivation of the wear scar calculated from the *It* curves assuming a second order exponential decay, see Figure 7.5 (an example of curve fitting shown in *Appendix 1*). The repassivation time observed for WC-10Co-4Cr coating is between 0.4 and 0.6 s when abraded using pH 7, pH 9 and pH 11 slurries. However, for the pH 13 conditions,

the WC-10Co-4Cr coating takes longer to repassivate due to the tendency of W and Co to remain electrochemically active as summarised in Table 7-2.

As shown in Figure 7.2, the maximum current levels observed for pH 7, pH 9, pH 11, pH 11-exp are similar (less than 5 μA). However, higher current values are observed for pH 7-exp samples (10 μA) and pH 13 samples (25 μA). Interestingly, the current observed for pH7-exp samples was higher than for the pH 7 samples. This is likely to be due to the micro-galvanic coupling between the nascent surface in the wear scar and the surrounding area of the pH 7-exp sample leading to increased electrochemical dissolution. The wear scar is expected to be more active as compared to the relatively passive surrounding (due to exposure) leading to higher corrosion within the wear scar. Micro-galvanic coupling between the active wear scar and the relatively passive unworn areas is likely to occur for all samples. The high current values observed for pH 13 samples are expected due to the greater tendency of W, Co and Cr to corrode at pH 13. This is also corroborated by the slower repassivation observed at the end of the micro-abrasion test, see Figure 7.5.

Figure 7.6 shows the wear-corrosion rates (SWR_{Total}) for the fresh and exposed WC-10Co-4Cr coatings abraded using neutral and alkaline slurries. The lowest SWR_{Total} is observed for pH 11 and pH 11-exp samples while the highest SWR_{Total} is observed for the pH 13 sample. As discussed in Chapter 6, at pH 11 Co is expected to form a passive oxide film ($Co(OH)_2$, see Table 7-2) which is likely to lower the rate of binder removal. As seen from the Figure 7.6, the use of *CP* for pH 11 has resulted in a lower SWR_{Total} as compared to pH 7. This further corroborates the argument that pH 7 should not be considered as a corrosion-free condition.

SEM micrographs of worn samples were studied to determine the wear mechanisms that occurred on the sprayed coatings. Figure 7.7 compares the unworn surface of the WC-10Co-4Cr coating to the wear scars on pH 11-CP, pH 7, pH 11, pH 7-exp and pH 13 samples. For consistency, SEM micrographs were obtained from the centre of the wear scar for all samples. Due to the non-uniform microstructure of the coating (see Figure 7.7a) the number of carbides exposed in each case is expected to differ. In general for all samples, the SEM micrographs reveal that wear has occurred by preferential removal of binder around the carbide grains, this leads to them cracking and their subsequent removal as shown schematically in Figure 7.3. The preferential binder removal leads to the formation of a 'moat-like' feature around the carbide grains. This feature is observed on all worn surfaces

and appears to be principally in the direction of the motion of abrasive slurry and is formed due to the preferential depletion of the binder-phase around the carbide grains.

Wear-scar areas from the micro-abrasion of the WC-10Co-4Cr coating for sliding distances between 15 m and 45 m, as discussed in the Chapter 6 have been used to plot the wear scar area *vs.* time, see Figure 7.8. Figure 7.8 suggests that after the initial 'running-in' period, the wear scar grows linearly during the course of the micro-abrasion test. This assumption was used to determine the growth in the wear-scar depth per minute during micro-abrasion, see Figure 7.9. Assuming that corrosion of the binder-rich areas occur at a constant rate, the depth of corrosion per minute is calculated from the electrochemical charge (Q) measured during micro-abrasion using Faraday's law, see Figure 7.9. Figure 7.9 suggests that while the depth of the wear-scar grows at a rate of 1 μm min^{-1}, the corrosion of the binder phase is between 1 and 5 nm min^{-1}. Clearly, mechanical damage of the surface during abrasion is three orders of magnitude greater than the electrochemical effects, i.e. preferential corrosion of metallic W. Figure 7.9 also shows that the dependence of depth corrosion attack depends on the pH of the abrasive slurry. The growth rate of the wear-scar also suggests that the presence of corrosion trenches on exposed coatings, discussed in Chapters 5 and 6, are not expected to influence the wear-corrosion performance of the coating as the corrosion trenches are 3-5 μm deep and are thus likely to be abraded in the initial stages of the micro-abrasion test (depth of wear-scar growth is 1 μm min^{-1}). Interestingly, similar corrosion trenches are formed on unworn surface of a sprayed coating exposed to pH 13 solution for the duration of the micro-abrasion test, see Figure 7.10. In this instance, the dissolution of Co ($HCoO_2^-$) and W (WO_4^{2-}) is expected at pH 13 as established in Table 7-2.

Corrosion trenches around WC grains are observed on pH 11-exp, pH 7-exp as well as pH 13 samples. However, unlike the pH 11-exp samples, there is no decrease in SWR_{Total} for the pH 7-exp and pH 13 samples with respect to the pH 11-CP sample. The decrease in SWR_{Total} observed for pH 11 and pH 11-exp samples (also discussed in Chapter 5 and Chapter 6) appears to result from a decrease in the binder-phase removal. As previously discussed in Chapter 6, the XPS analysis of the WC-10Co-4Cr coating exposed to a pH 11 solution revealed the presence of a $Co(OH)_2$ rich oxide film on the surface. Presence of a passive film is likely to alter the stiffness between the abrasive particle and the binder-rich areas. It has been proposed in Chapters 5 and 6 that the passivation of the binder-rich areas is also likely to result in a reduced friction between the abrasive and the sample surface. Also, the repassivation times calculated from the *It* curves suggest a relatively high repassivation rate (0.5 s) of the binder-phase under pH 11 conditions. The observed wear mechanism of

preferential removal of the binder phase and the undermining/ fragmentation of the carbide grains and the higher repassivation rate of the binder-phase strongly suggest that a decrease in the rate of binder depletion results in the lowering of the SWR_{Total} for pH 11 and pH 11-exp samples during abrasive wear. This is corroborated by the increase in SWR_{Total} observed under pH 13 conditions due to the reduced passivation and consequent increase in the removal of the binder. This is further corroborated by plotting the average current measured during micro-abrasion against the SWR_{Total}, see Figure 7.11. SWR_{Total} increases linearly with increase in the corrosion current (I) suggesting that an accelerated binder removal results in an increase in SWR_{Total}. Despite measurable corrosion current, pH 11 and pH 11-exp samples have the lowest SWR_{Total}. Clearly, the wear-corrosion interactions (depassivation/ repassivation of the binder-phase, re-embedding of wear debris) occurring under pH 11 conditions result in the improvement in the wear-corrosion performance of the WC-10Co-4Cr coating.

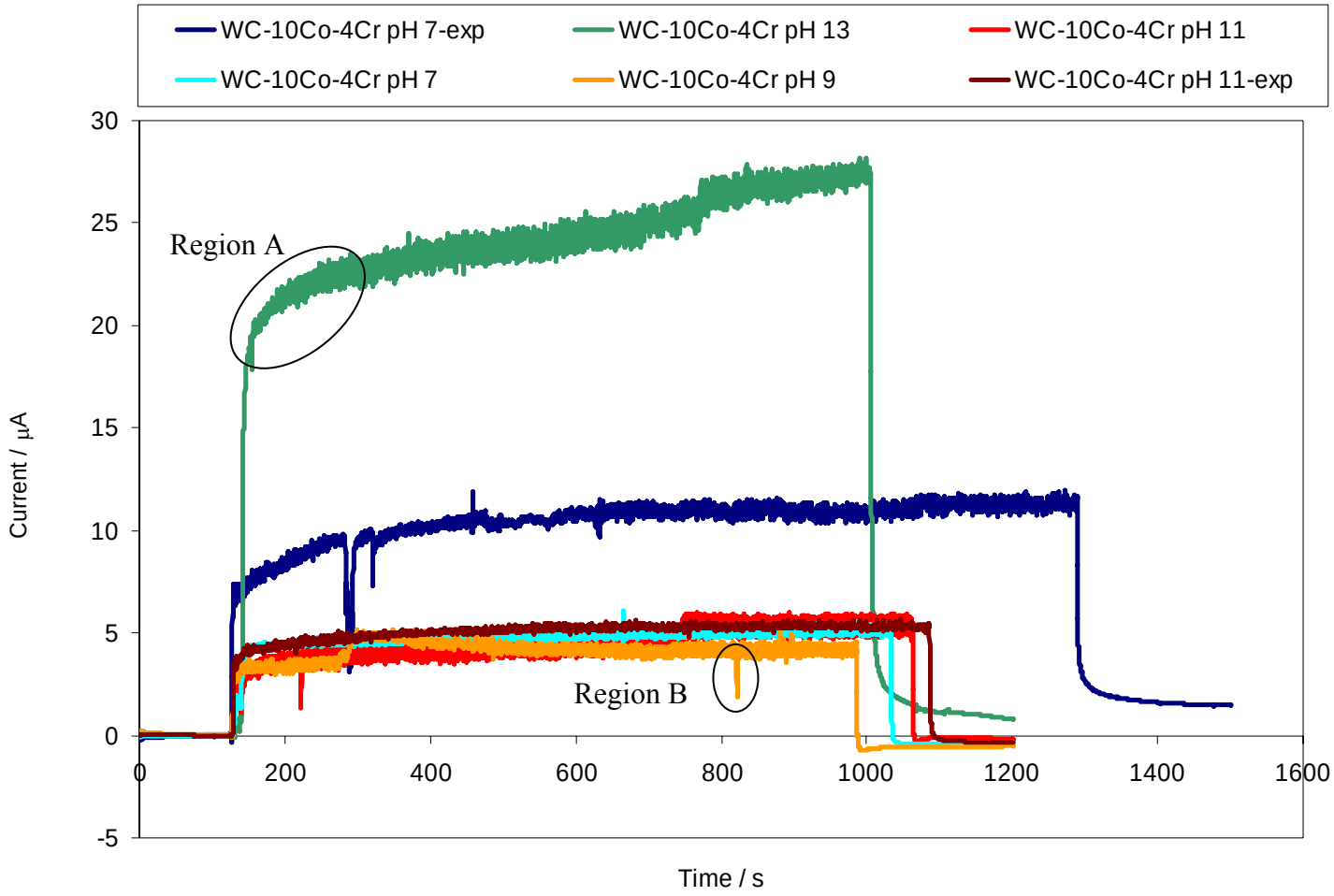

Figure 7.2: Current *vs*. time plots obtained during *in situ* micro-abrasion of WC-10Co-4Cr coating.

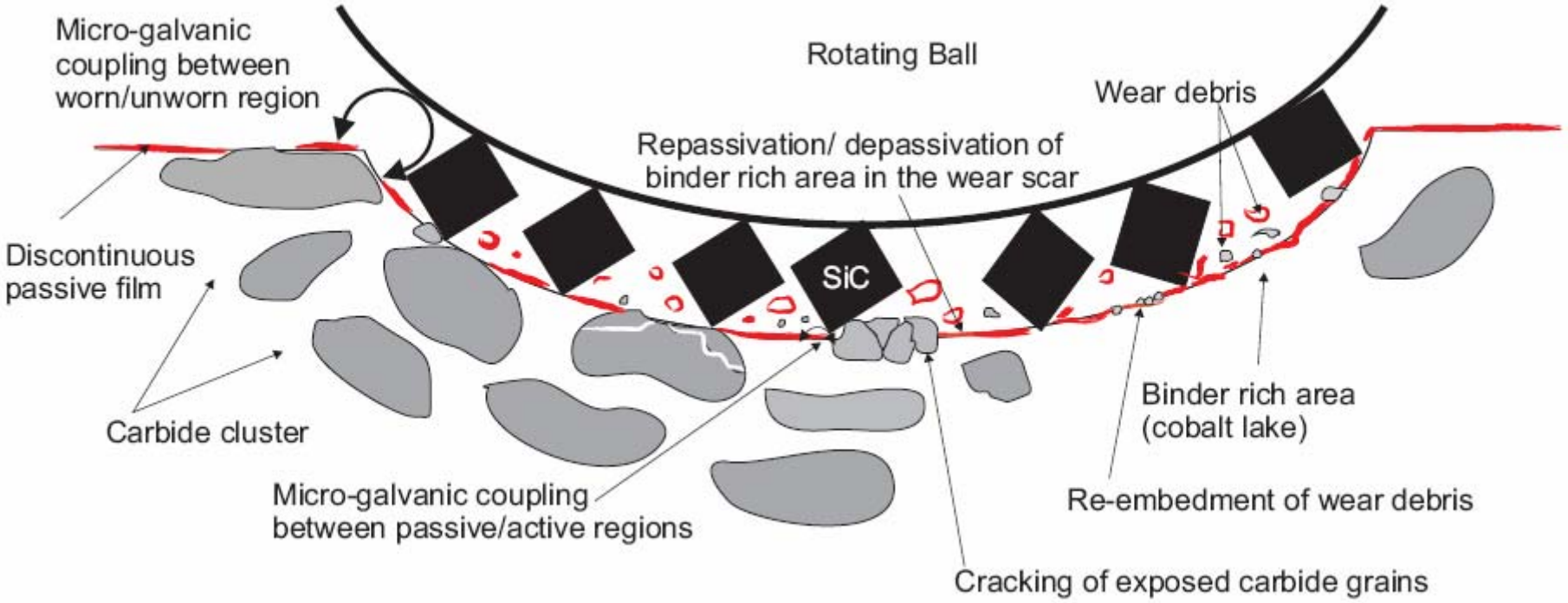

Figure 7.3: Schematic of wear-corrosion process during micro-abrasion of sprayed WC-10Co-4Cr coating.

.

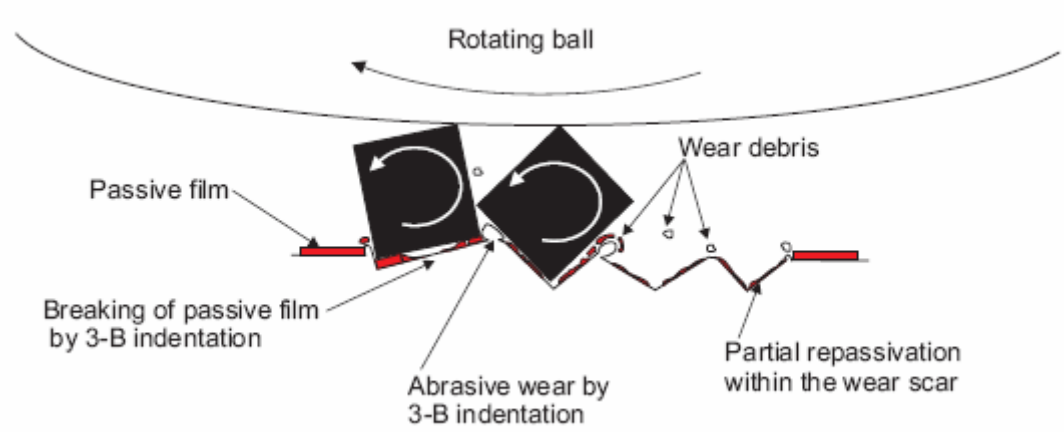

Figure 7.4: Mechanism of depletion of the binder and removal of passive film by 3-B indentations.

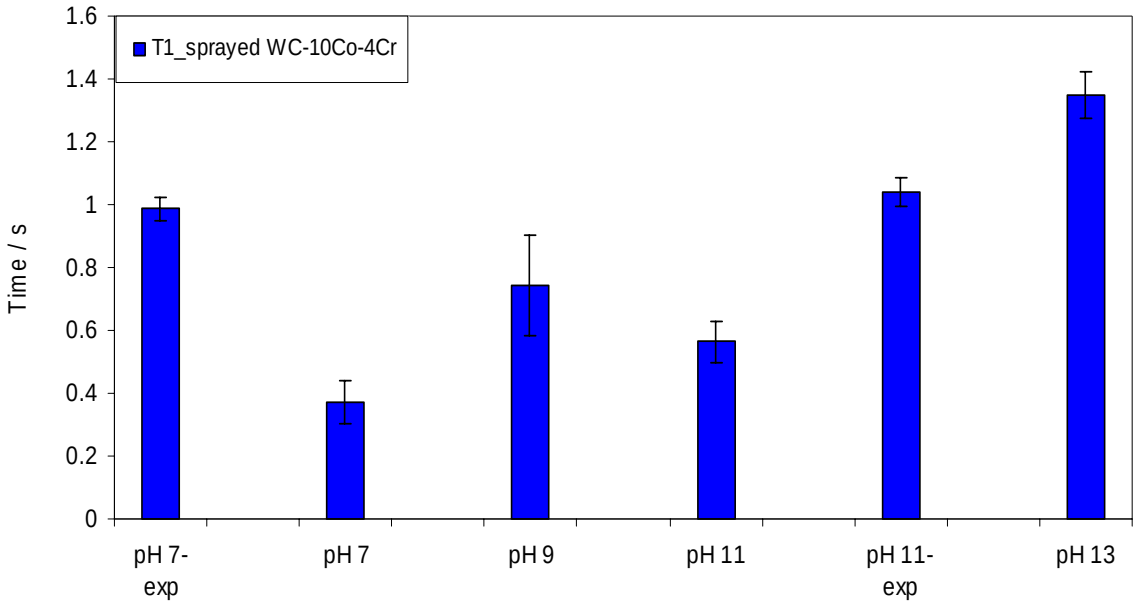

Figure 7.5: Repassivation times calculated from the *It* curves.

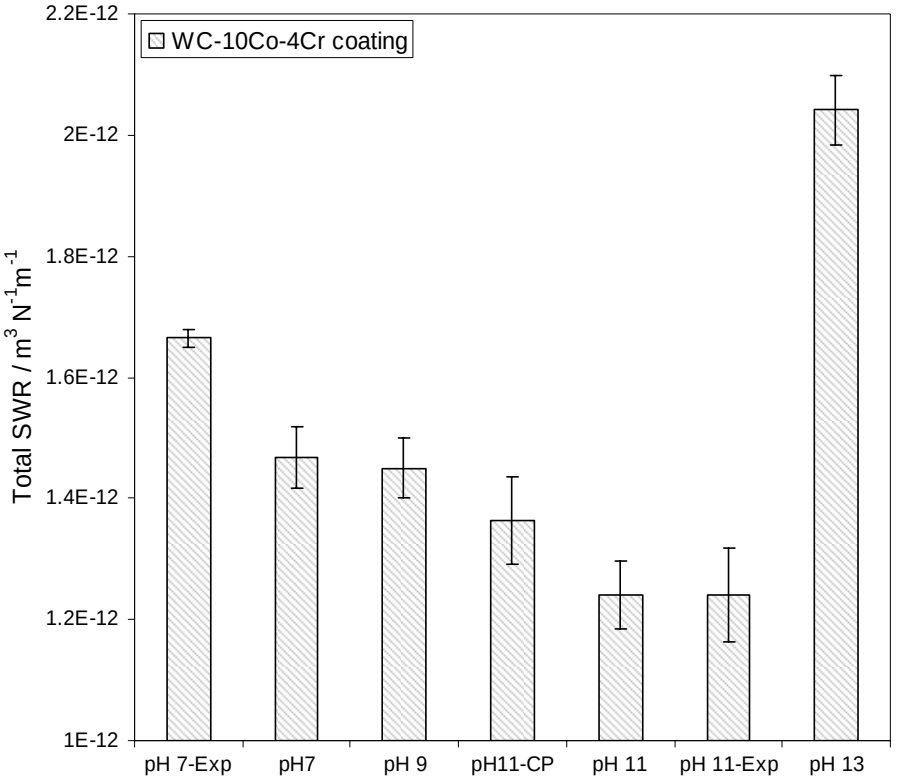

Figure 7.6: Specific wear rates for WC-10Co-4Cr coating under different pH conditions.

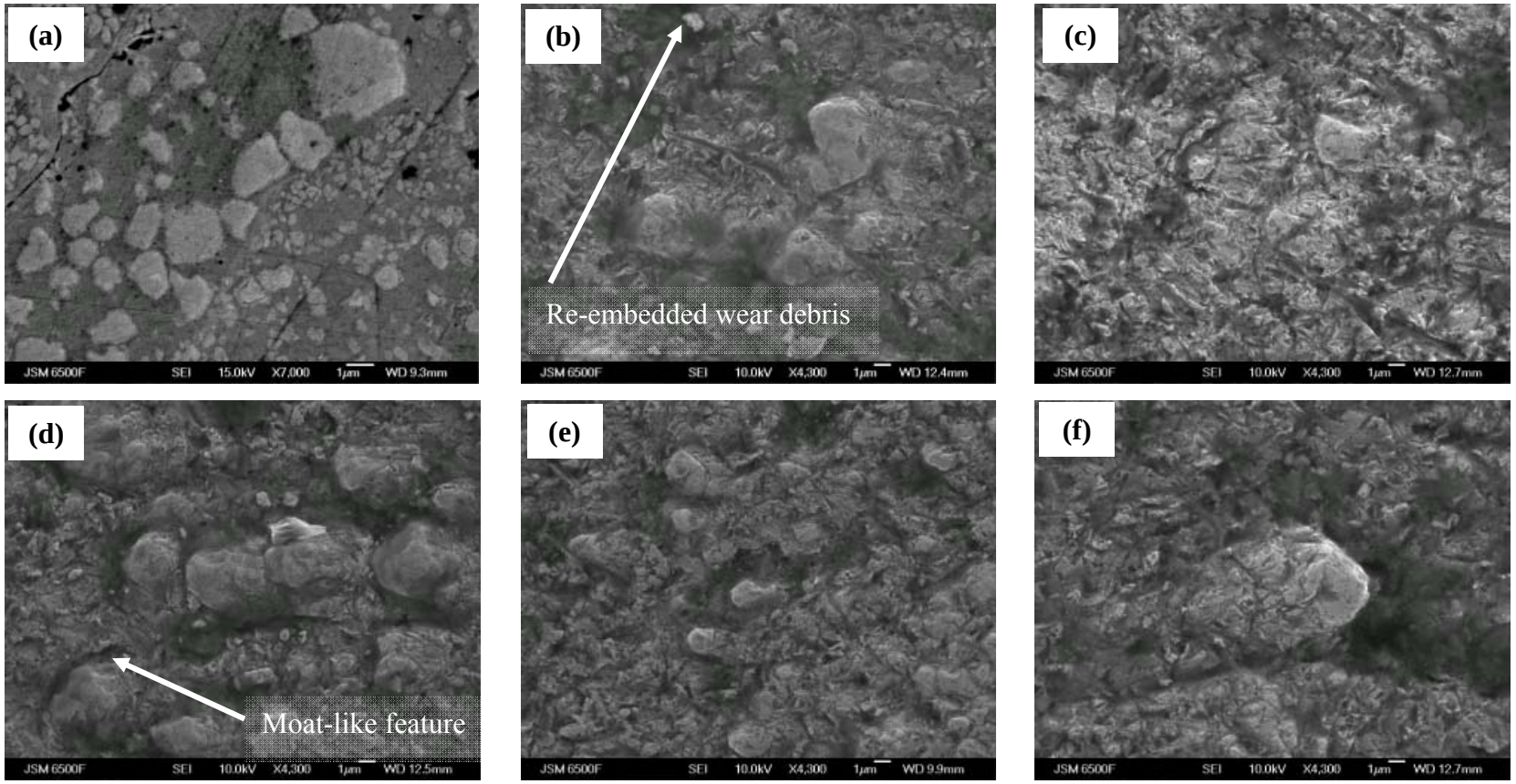

Figure 7.7: SEM micrographs of wear scars on sprayed coatings; (a) Unworn surface for comparison, (b) pH 11_CP, (c) pH 7, (d) pH 11,(e) pH 7-exp and (f) pH 13.

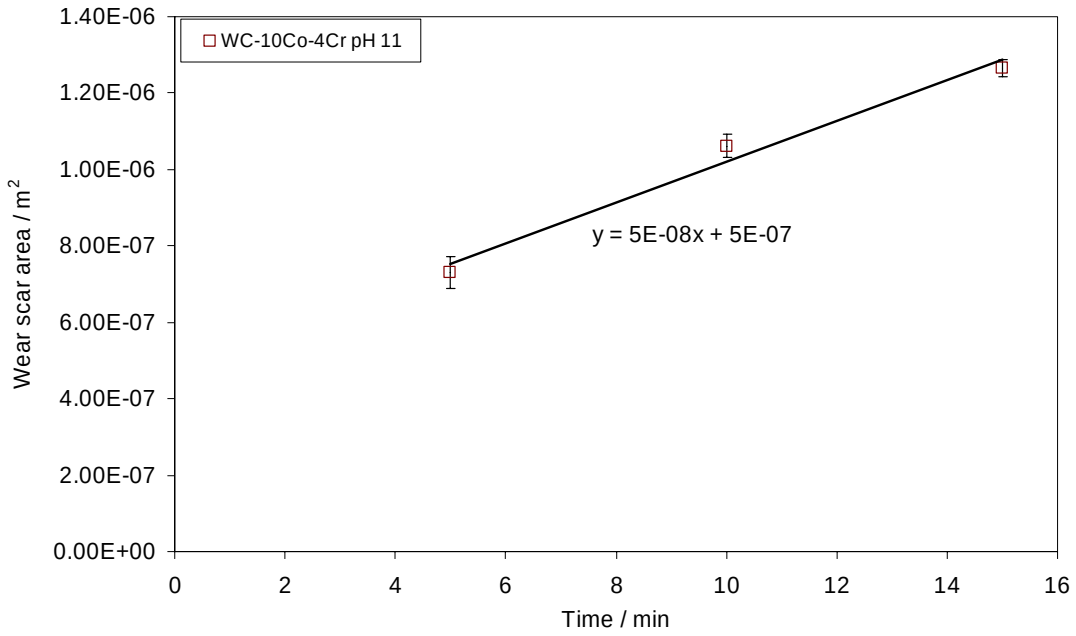

Figure 7.8: Increase in wear-scar area with time (plotted from the data discussed in Chapter 6).

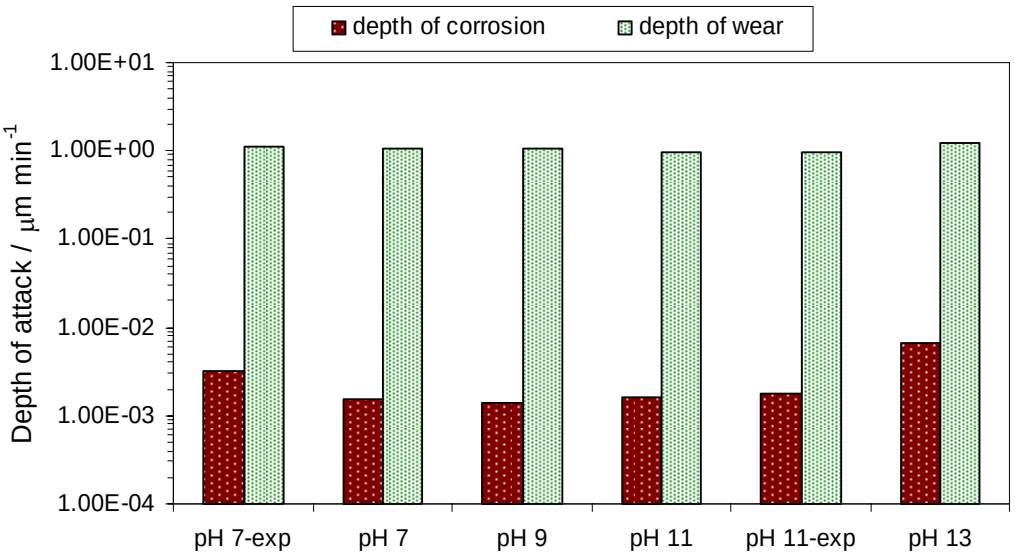

Figure 7.9: Corrosion and wear per minute during the micro-abrasion test.

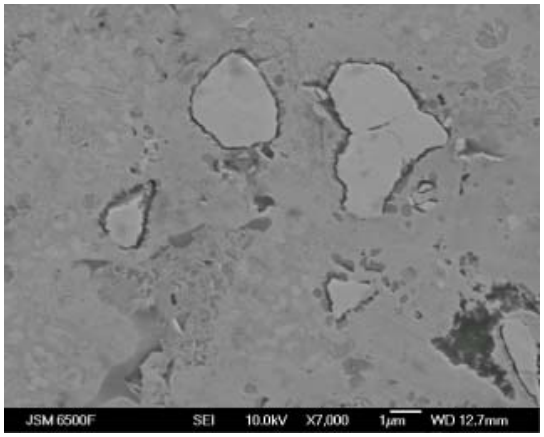

Figure 7.10: Localised corrosion features on unworn WC-10Co-4Cr coating adjacent the wear scar exposed to pH 13 slurry.

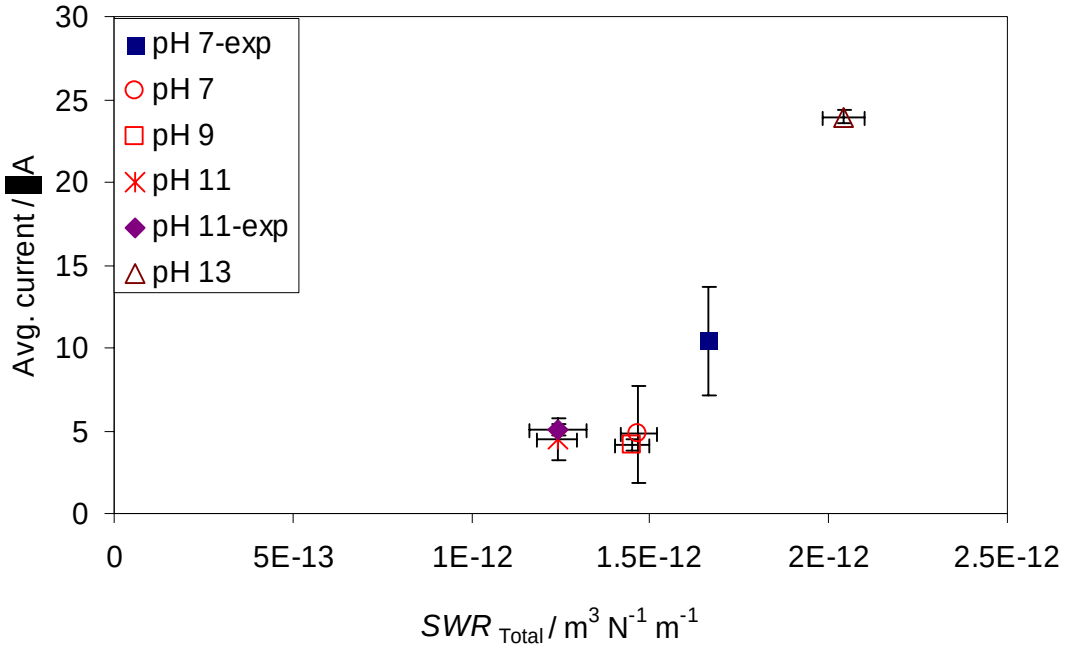

Figure 7.11: Relation between average current and SWR_{Total} for WC-10Co-4Cr coating.

7.2.1.2 Sintered WC-5.7Co-0.3Cr

Figure 7.12 compares the current-noise response for fresh and exposed sintered WC-5.7Co-0.3C samples obtained during the micro-abrasion tests using alkaline (pH 9, pH 11 and pH 13) and neutral (pH 7) abrasive slurries. The shape of the *It* curves for the sintered samples are distinctly different to those seen for the sprayed coatings. There is no sharp increase in the current at the start of the abrasion. Instead, the current gradually increases throughout the duration of the wear test associated with the increase in the wear scar area as the tests progress. However, it also suggests that, unlike the sprayed samples, the wear scar in sintered samples does not readily repassivate when it comes in contact with neutral and alkaline slurries. Figure 7.13 shows a schematic depicting the possible wear-corrosion interactions occurring on the sintered sample surface during micro-abrasion. The microstructure of sintered samples is rich in WC grains and does not have distinct binder rich areas which can repassivate during the wear test. For the same reason, abrasive wear in sintered hardmetals is very different from that observed in the WC-10Co-4Cr coating. As shown in the Figure 7.13, wear-corrosion occurs by the fragmentation and subsequent removal of carbides within the wear scar. As observed for the WC-10Co-4Cr coating, re-embedment of fragmented carbides in the wear-scar is likely to result in an increased wear-resistance. Unlike distinct depassivation / repassivation of the binder-phase observed in the WC-10Co-4Cr coating, localised corrosion of the binder present in the crevice-type features is likely to occur depending on the local pH. This is likely to result in an increased corrosion rate as compared to the sprayed samples.

The much slower repassivation in WC-rich structure also results in an increase in the current as the wear scar increases during micro-abrasion test. This is corroborated by the absence of features ‘A’ and ‘B’ seen in the *It* curves for sprayed samples (Figure 7.2). At the end of each micro-abrasion test on sintered samples, the current level gradually decreases and does not return to the similar values as observed at the start of the test with the exception of the pH 11 sample. This is contrary to the sharp drop in the current observed at the end of the wear test for sprayed coatings. This was further corroborated by calculating the time taken by the sintered samples to repassivate from the *It* curves assuming a second order exponential decay as shown in Figure 7.14. Clearly, while the wear scar on WC-10Co-4Cr coatings takes between 0.4 and 0.6 s to repassivate, the wear scar on the sintered WC-5.7Co-0.3Cr takes approximately 3 s to repassivate. The much slower repassivation of the sintered surface during micro-abrasion also leads to current values typically three times greater than those for the sprayed coatings. The current levels and the shape of the curves observed for

pH7, pH 9, pH 11 and pH 11-exp samples are generally similar (less than 30 μA). However, higher current values are observed for pH7-exp sample (80 μA) and pH 13 sample (90 μA). The shape of the *It* curves for pH 7-exp and pH 13 samples are distinctly different from the other sintered samples. A steep rise in current is observed between 100 and 200 seconds after abrasion began, particularly for the pH 7-exp sample. This is likely to be due to the effects of exposure to distilled water. As discussed in Chapter 6, binder dissolution is observed on the surface of pH 7-exp sample. The higher current observed for pH 7-exp samples is likely to result from the increased electrochemical dissolution of the binder-phase on the wear scar due to micro-galvanic coupling between the nascent wear scar (freshly exposed surface) and the unworn area of the pH 7-exp sample. The wear scar is expected to be more active as compared to the passive surrounding (due to exposure). Micro-galvanic coupling between the active wear scar and the relatively passive unworn areas is likely to occur for all samples. However, the absence of active species on the surface due to exposure is likely to result in higher currents for the pH 7-exp sample. Similarly, an increased dissolution of the binder-phase is likely to result in increase in the current-noise.

Figure 7.15 compares the wear-corrosion rates (SWR_{Total}) for fresh and exposed samples of sintered WC-5.7Co-0.3Cr abraded using neutral and alkaline slurries. The highest SWR_{Total} is observed for the pH 13 samples. The SWR_{Total} observed for pH 7-exp, pH 7, pH 9, pH 11, pH 11-exp, pH 11-CP are generally similar and within the limits of the error bars. The results suggest that under neutral and weakly alkaline conditions, abrasive slurry pH does not significantly influence the SWR_{Total}. Despite the higher current noise, pH 7-exp samples do not show higher SWR_{Total} as compared to pH 11-CP samples. Clearly, the corrosion at the binder/carbide interface observed after exposure and the galvanic coupling between WC and Co-binder results in an increase in the current noise but does not lead to a noticeable increase in the wear-corrosion rates. This is likely to be due to the lack of accelerated binder-phase removal by the abrasive slurry at pH 7. As discussed in Chapter 2 (Literature Review), the microstructure of sintered samples is skeletal in nature and is rich in WC. However, due to a higher hardness as a result of the carbide-rich structure, the SWR for sintered samples is an order of magnitude lower than the sprayed coatings. Micro-abrasion studies on sintered WC-based hardmetals have found that wear occurs by a combination of preferential depletion of binder around the carbide grains / binder extrusion between the carbide grains which initiates the fracture and cracking of the carbide grains [71, 72]. Gee *et al.* [72] have studied the micro-abrasion of WC-based sintered hardmetals using acidic and alkaline abrasive slurries. While reporting no visible difference in wear rates when using neutral and mild acidic / mild alkaline slurries, the wear rate noticeably increased when using strong acidic or alkaline

slurries (pH 1, pH 2 and pH 13). They concluded that the higher wear rates observed in strong acidic and alkaline slurries was due to the accelerated binder depletion due to wear-corrosion interactions.

To study the wear mechanisms occurring in the sintered samples, SEM micrographs of worn samples were investigated. Figure 7.16 compares the unworn surface of sintered WC-5.7Co-0.3Cr to the wear scars generated using neutral / alkaline slurries. For consistency, SEM micrographs are obtained from the centre of the wear scar for all samples. The SEM micrographs reveal that the worn surfaces of the sintered samples are devoid of any binder, compared with the unworn surface (Figure 7.16a). The carbide grains within the wear scar appear to have suffered from repeated fragmentation and fracture. Removal of small amounts of binder from between the carbide grains at the surface results in propagation of surface cracks within a carbide grain which accelerates wear. The size of the fragmented carbides in neutral and weak alkaline conditions (pH 7, pH 9, and pH 11) is similar, which indicates that the rate of binder dissolution suffered by these samples is also similar, see Figure 7.15. This has also resulted in these samples having similar SWR_{Total}. However, pH 13 sample (Figure 7.16f) shows a presence of severely fragmented carbide grains on the surface which is likely to be caused by excessive binder depletion during micro-abrasion. This is further corroborated by the SEM micrograph of the unworn surface of the pH 13 sample exposed to the abrasive slurry, see Figure 7.17. Clearly, the surface has suffered from binder depletion around the carbide grains due to the possible micro-galvanic coupling between the Co-binder and the WC grains. A similar reaction in the wear scar is likely to accelerate binder depletion leading to increased fragmentation of the carbide grains and subsequent increase in the SWR_{Total}.

As in case of the WC-10Co-4Cr coatings, after the initial 'running in' period, a linear growth of the wear scar area is observed for the sintered WC-5.7Co-0.3Cr, see Figure 7.18. Assuming that corrosion of binder-rich areas occurs at a constant rate throughout the micro-abrasion test, wear scar depth and corrosion depths in μm min-1 are calculated, see Figure 7.19. The rate at which wear-scar increases is less for the carbide-rich sintered WC-5.7Co-0.3Cr as compared to the WC-10Co-4Cr coating despite an order of magnitude increase in the corrosion rate. Clearly, as proposed earlier in this Chapter, the rate of binder dissolution in sintered WC-5.7Co-0.3Cr is higher due to the skeletal carbide structure. Although the rate of corrosion attack is relatively high (as compared to the WC-10Co-4Cr coating), the mechanical damage (wear scar growth) will always supersede the rate of corrosion damage during the micro-abrasion test and hence, under neutral and alkaline conditions, the increase in the depth of wear-scar is not influenced by the rate of increase in corrosion depth. This

also corroborates that while the wear of WC-10Co-4Cr coating strongly depends on the pH of the abrasive slurry due to the preferential removal of the binder and undermining of the carbide grains, abrasion of the sintered WC-5.7Co-0.3Cr is not strongly influenced by weak alkaline and neutral conditions as wear occurs by fragmentation and loosening of the carbide grains. This is further corroborated by plotting the average current values measured during micro-abrasion against the SWR_{Total}. No obvious relationship exists between increase in average current and the SWR_{Total} under neutral and weak alkaline conditions. However, maximum current is observed for pH 13 samples which also result in the highest SWR_{Total}, possibly due to the excessive rate of binder depletion observed under pH 13.

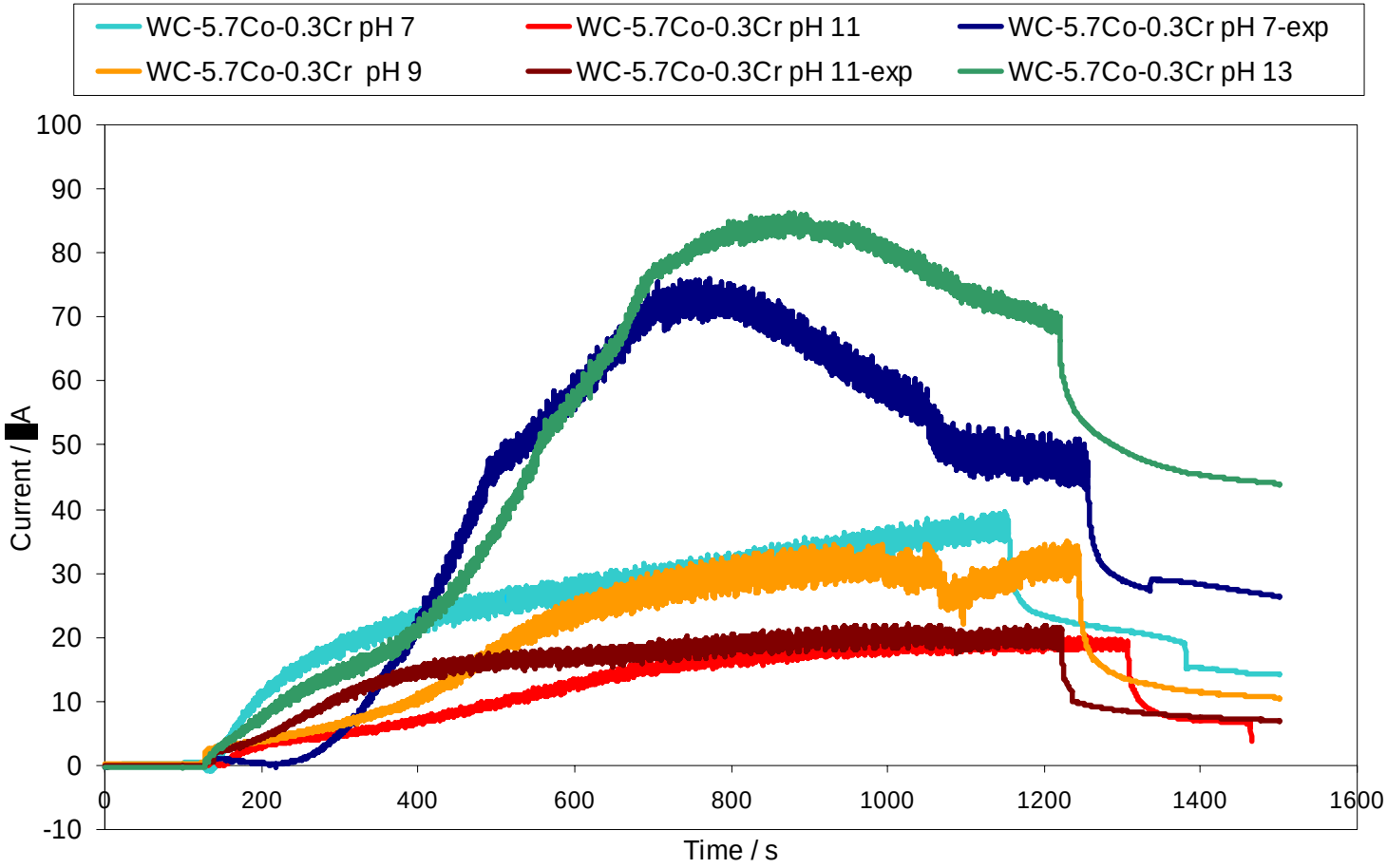

Figure 7.12: Current *vs*. time plots obtained during *in situ* micro-abrasion of sintered WC-5.7Co-0.3Cr samples.

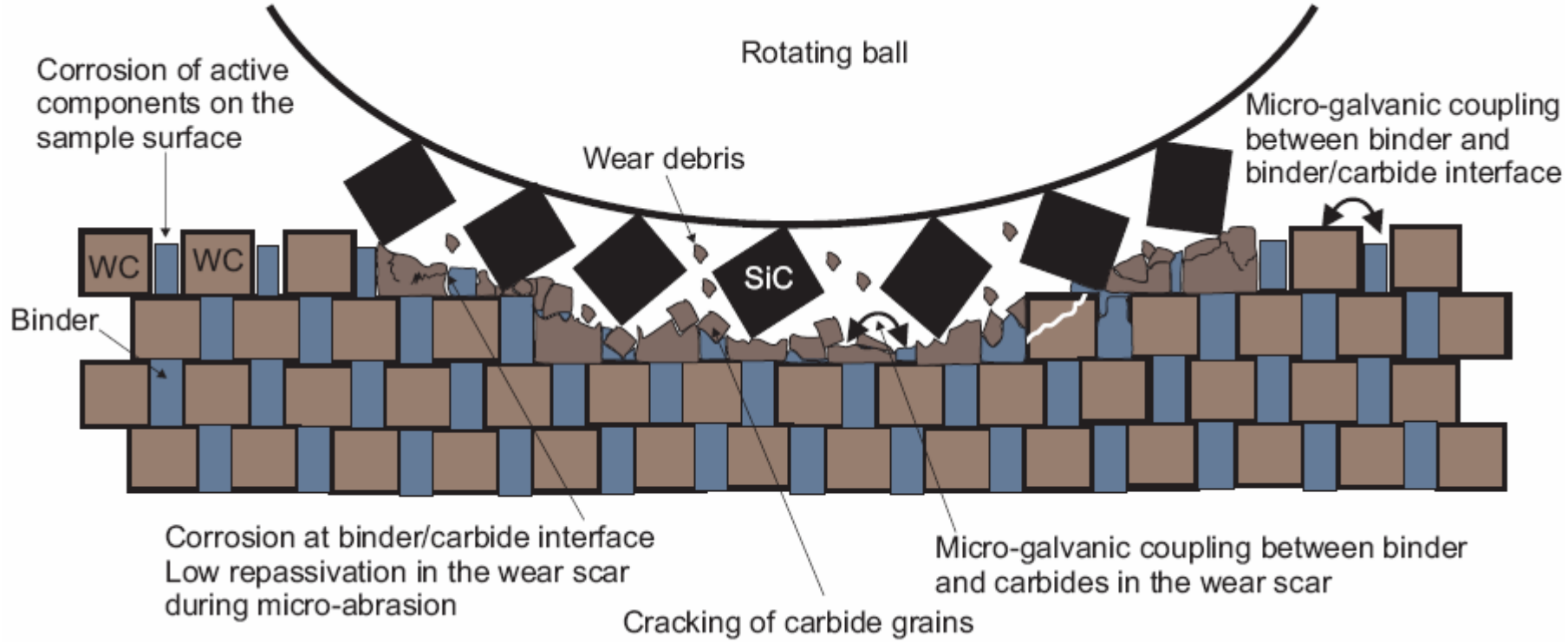

Figure 7.13: Schematic of wear-corrosion process occurring during micro-abrasion of sintered WC-5.7Co-0.3Cr samples.

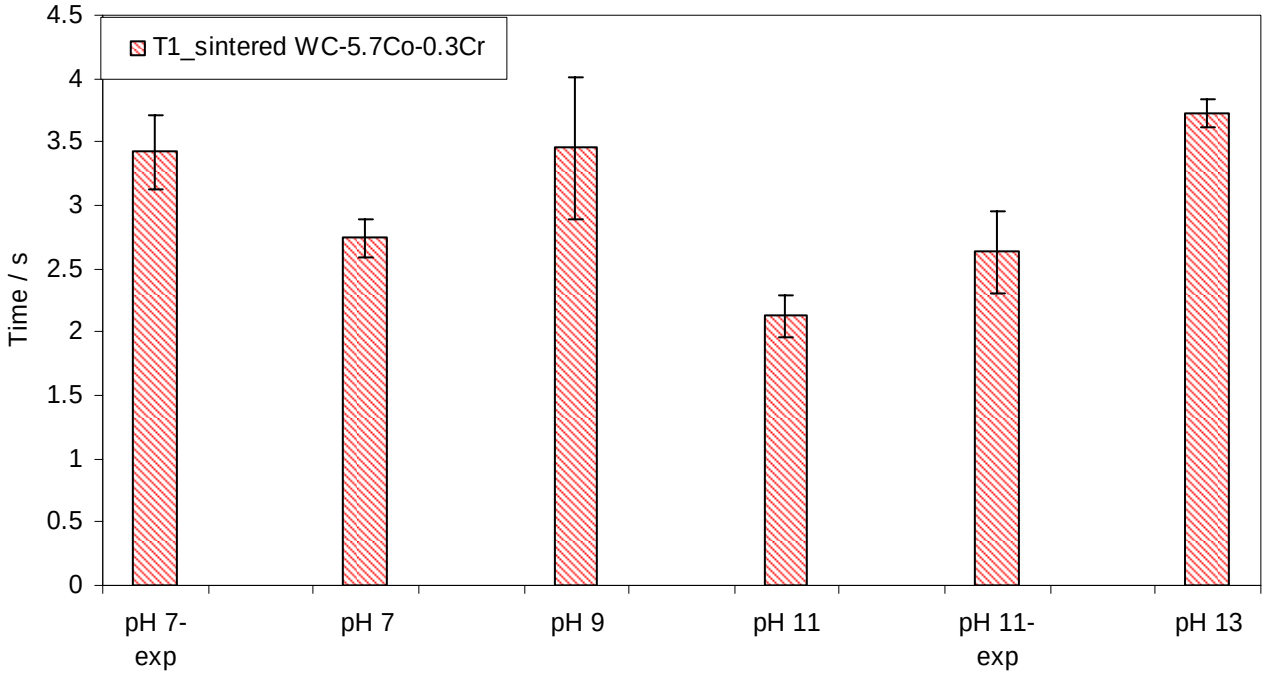

Figure 7.14: Repassivation time calculated form the *It* curves.

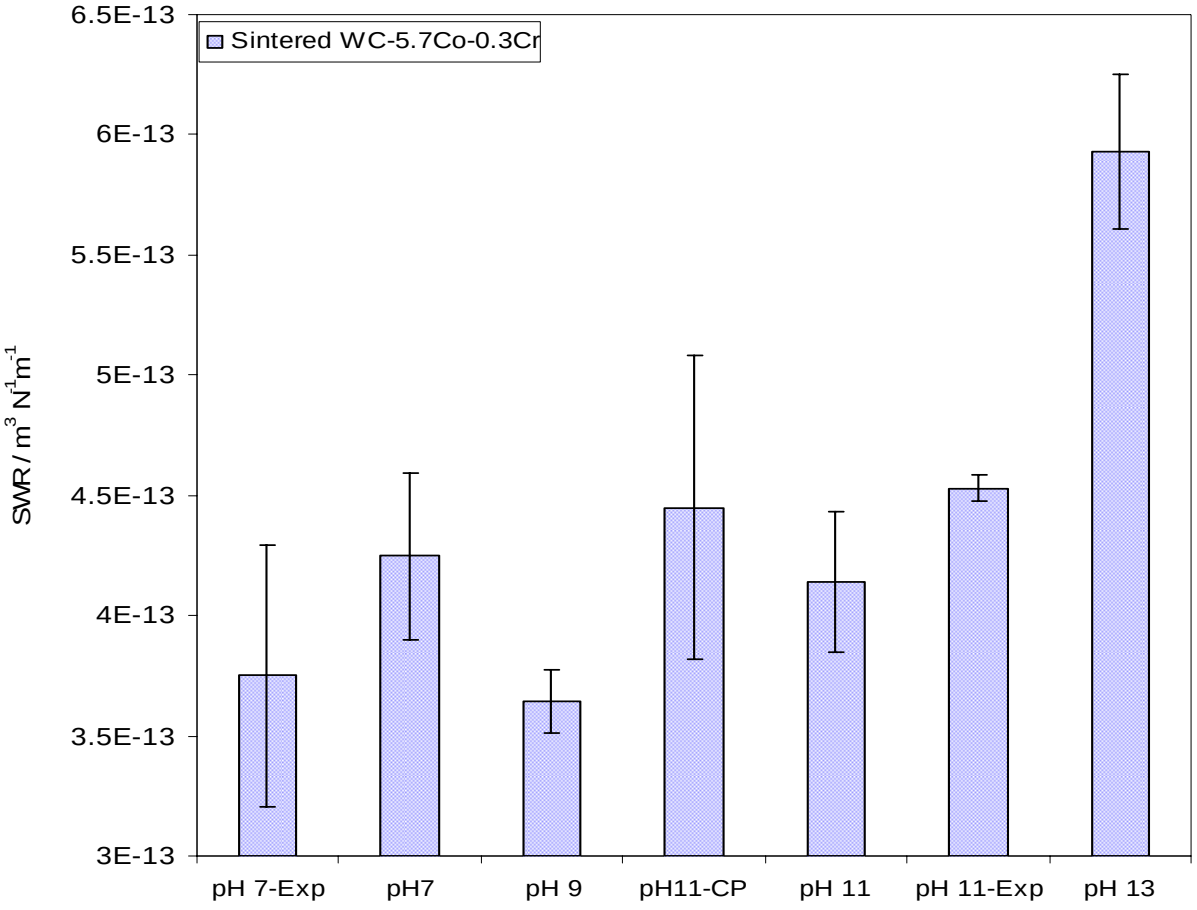

Figure 7.15: Specific wear rates for sintered WC-5.7Co-0.3Cr under different pH conditions.

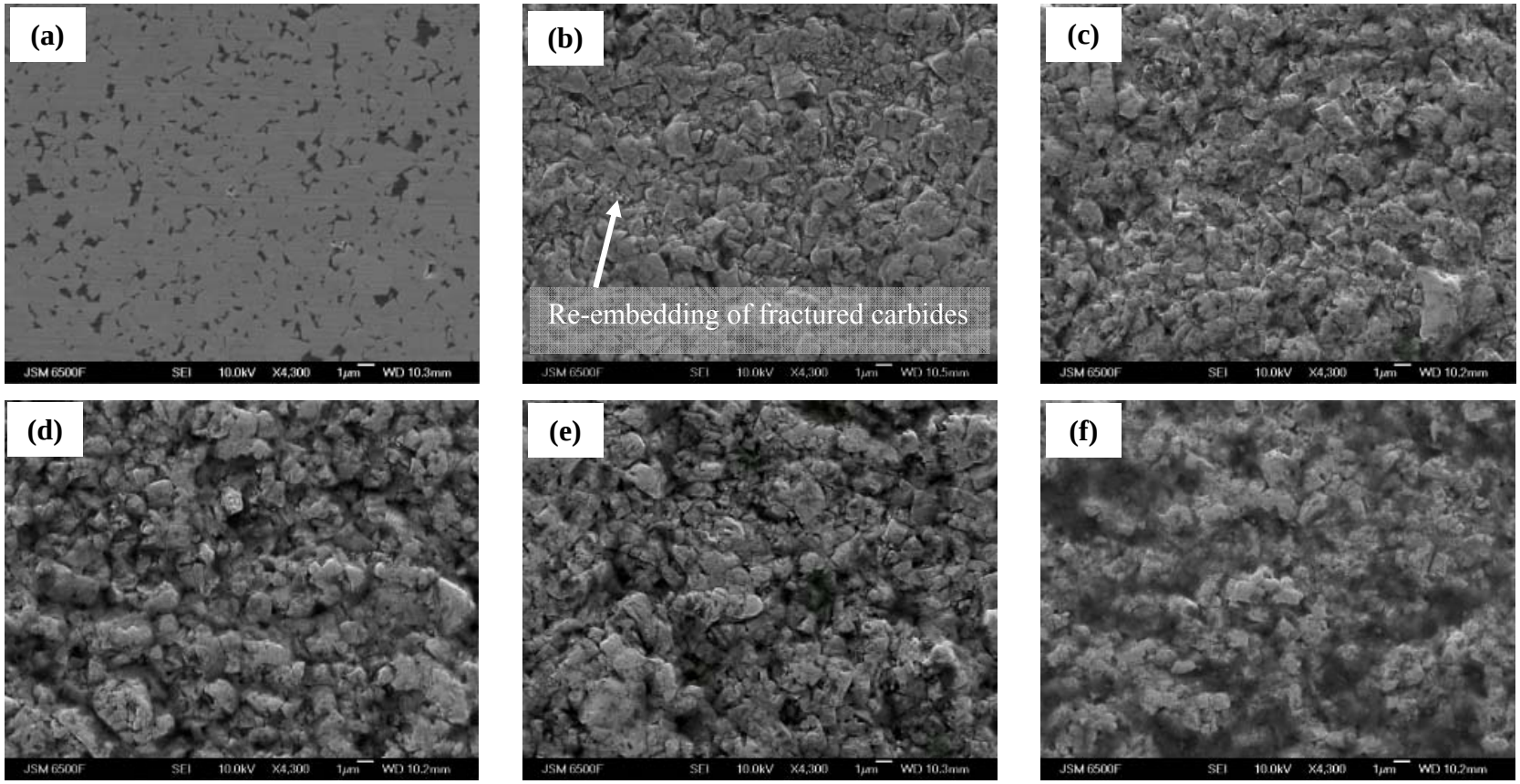

Figure 7.16: SEM micrographs of wear scars on sintered; (a) Unworn surface for comparison, (b) pH 11-CP, (c) pH 7 (d) pH 11, (e) pH 7-exp and (f) pH 13.

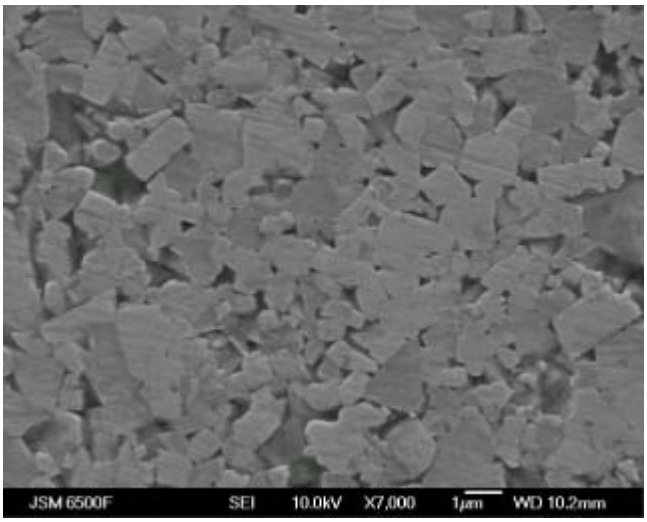

Figure 7.17: Localised corrosion features on unworn sintered WC-5.7Co-0.3Cr adjacent the wear scar exposed to pH 13 slurry.

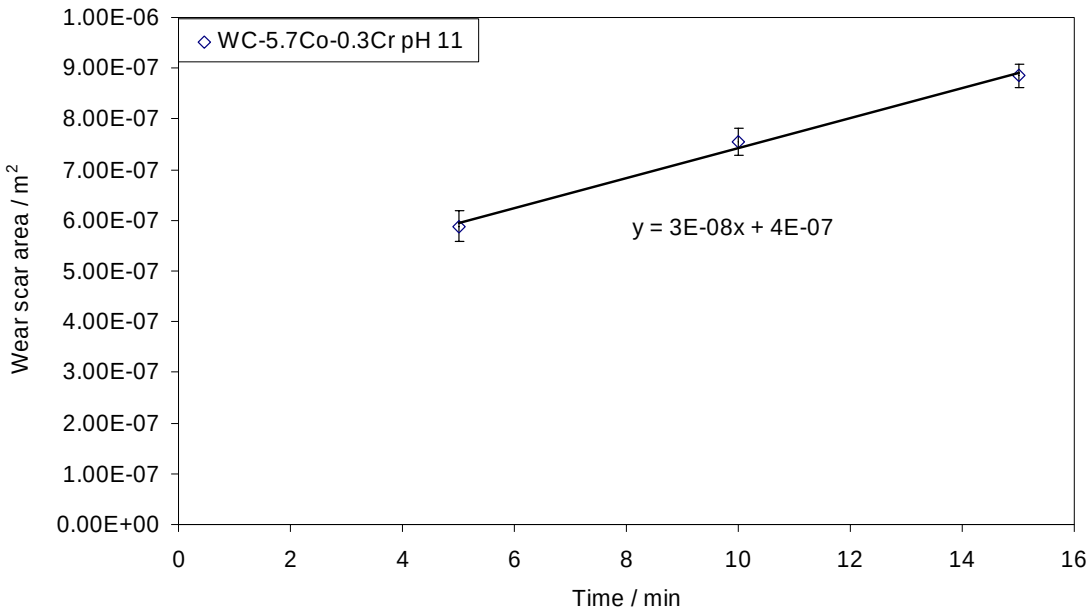

Figure 7.18: Increase in wear-scar area with time for sintered WC-5.7Co-0.3Cr abraded for 15 m, 30 m and 45 m using SiC abrasives suspended in pH 11 NaOH slurry.

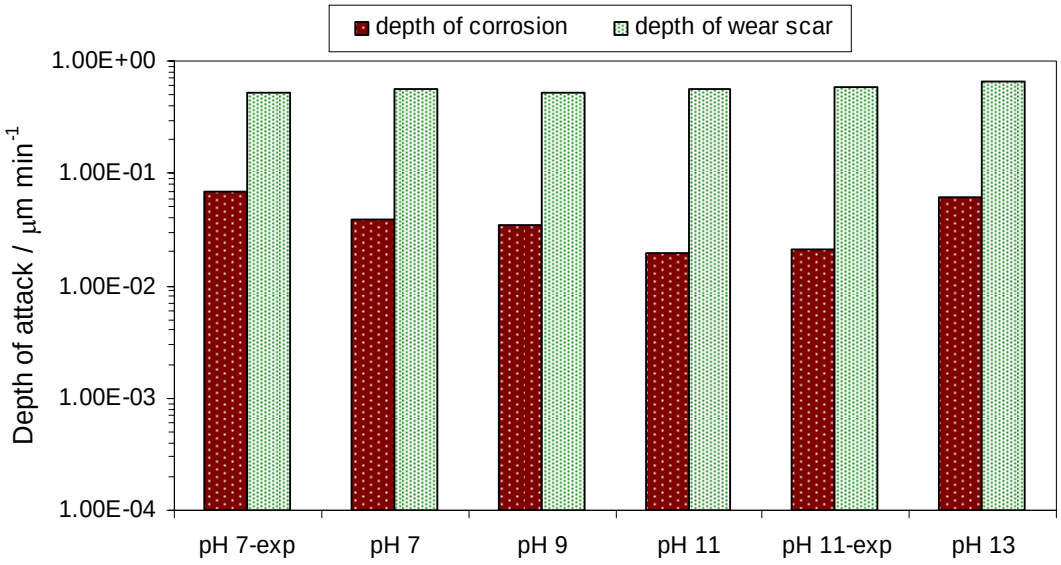

Figure 7.19: Corrosion and wear per minute during the micro-abrasion test.

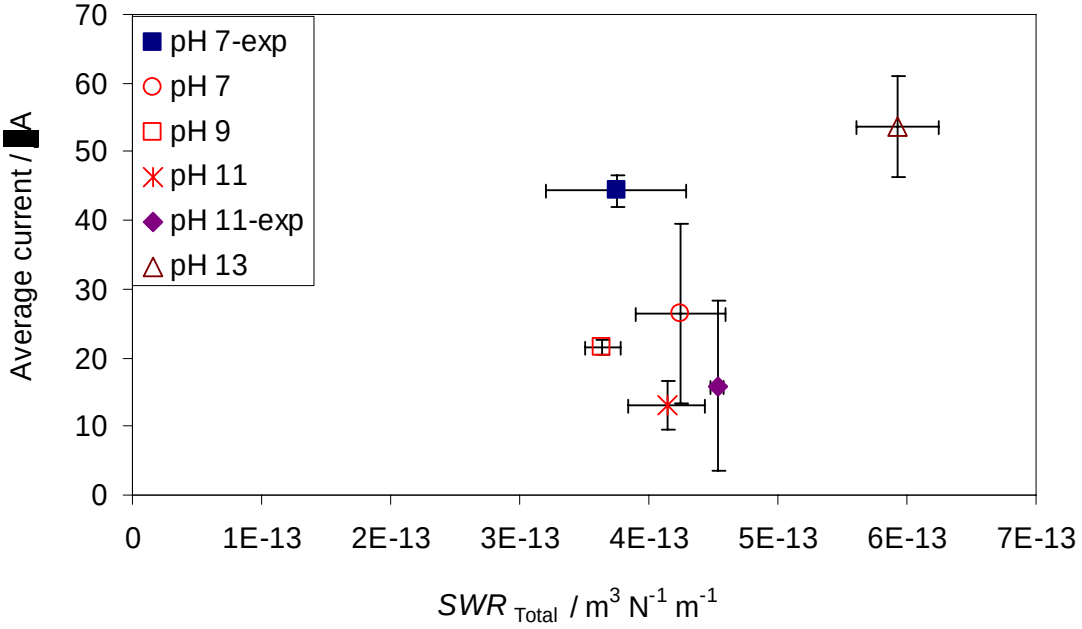

Figure 7.20: Relation between average current and SWR_{Total} for WC-10Co-4Cr coating.

7.2.1.3 Electrochemical wear rates

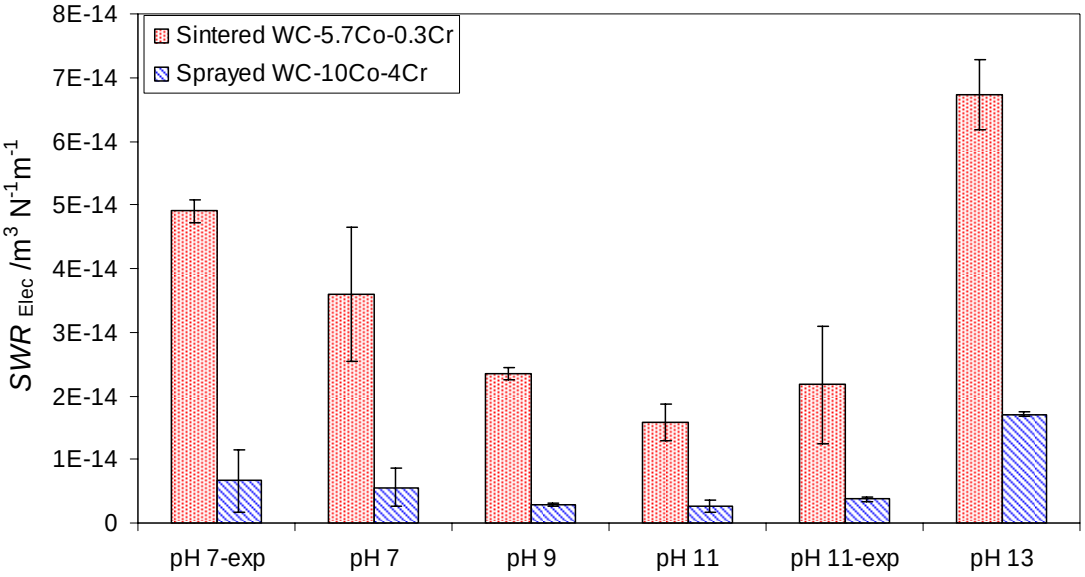

Figure 7.21: Specific wear rates obtained from electrochemical current noise data during micro-abrasion under different pH conditions.

Using Faraday's law (assumes equal number of electrons, as detailed in the Chapter 3), the mass loss was converted to SWR_{Elec} for known specimen density, applied load and sliding distance for the micro-abrasion test, see Figure 7.21. Highest SWR_{Elec} is observed for pH 13 samples while the least SWR_{Elec} is observed for pH 11 samples. SWR_{Elec} can be related to the active/ passive states of Co and W in neutral and alkaline conditions, see Table 7-1. Clearly, SWR_{Elec} values demonstrate a strong dependence on the ability of Co to passivate as can be seen from the comparison of values obtained for pH 7, pH 13 and pH 11 samples for both sintered and sprayed hardmetals. Also, a higher Co content in the sprayed coating has resulted in reduced SWR_{Elec} as compared to sintered samples. The exposure of sintered hardmetals and sprayed coatings to pH 7 conditions and the use of *in situ* electrochemical technique demonstrate that measurable electrochemical activity is observed under neutral conditions (pH 7) and hence it can not be considered as a 'corrosion-free' environment for comparison with acidic and alkaline conditions.

Figure 7.22 and Figure 7.23 compare the 'recovery ratio' for WC-10Co-4Cr coating and sintered WC-5.7Co-0.3Cr respectively. Recovery ratio is defined as the ratio of repassivation current (current at the end of the test) and the maximum current measured during the test and is a measure of the repassivation of the wear-scar at the end of micro-abrasion test.

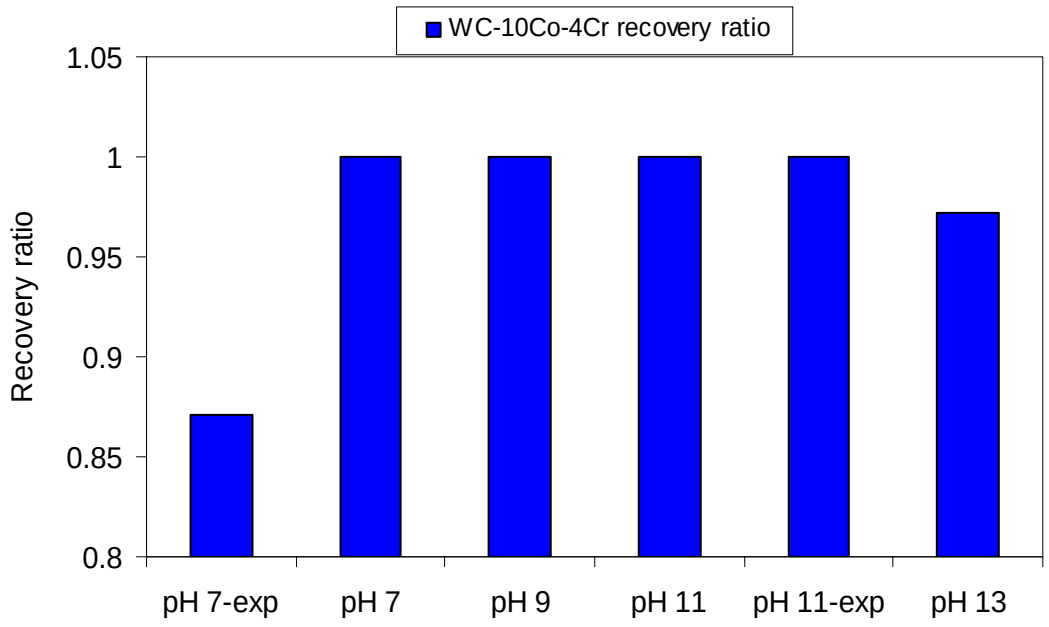

Figure 7.22: Recovery ratio at the end of the micro-abrasion test.

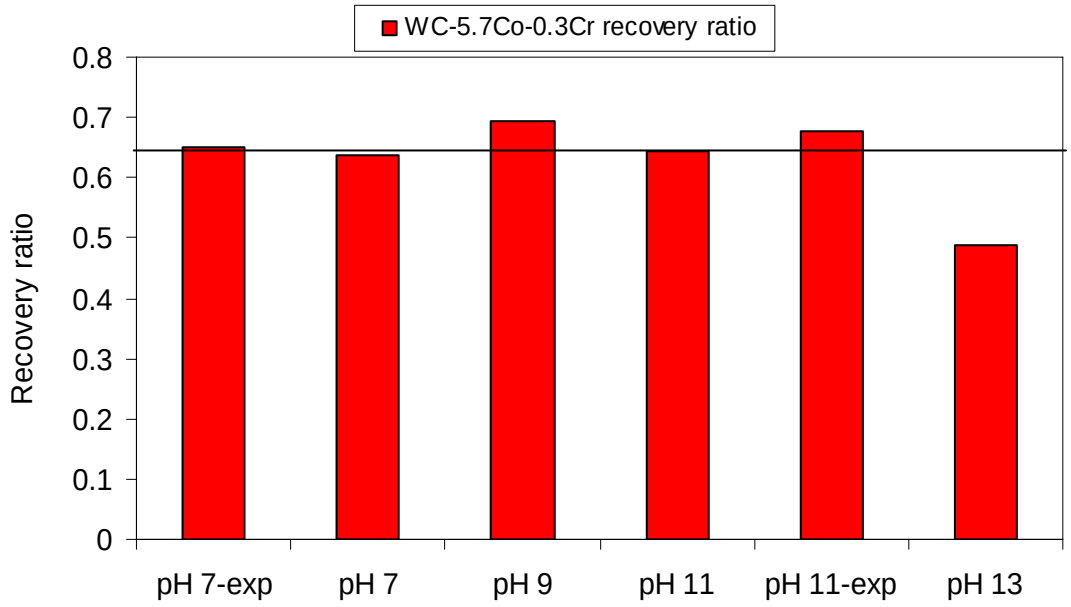

Figure 7.23: Recovery ratios at the end of micro-abrasion test.

Hence, a recovery ratio of 1 indicates that the surface has fully repassivated at the end of the test as is the case of pH 7, pH 9, pH 11 and pH 11-exp samples of WC-10Co-4Cr coating. This further suggests that the WC-10Co-4Cr coating has the ability to readily repassivate when exposed to weak alkaline conditions. However, this is not the case with pH 13 and pH 7-exp samples of WC-10Co-4Cr coating. This suggests that the exposed wear-scar area remains electrochemically active at the end of the wear test. This is due to the lack of

repassivation within the wear-scar. This is also likely to be due to an increase in the surface area within the wear scar and possible micro-galvanic coupling between the worn area and the unworn areas on the coating surface.

Interestingly, the recovery ratio is lower for the sintered samples compared to the sprayed. This is due to the absence of binder-rich areas which readily passivate in weak alkaline conditions. Also, the worn surface of the sintered samples is expected to provide a larger surface area as compared to a polished surface. Presence of fractured carbides is also likely to result in the formation of crevice-type features and encourage localised corrosion of the binder-phase. Possible micro-galvanic coupling between the wear-scar and the unworn area is also likely to result in further increase in the electrochemical activity on the worn surface. Clearly, abrasive wear of sintered WC-5.7Co-0.3Cr results in an increased electrochemical activity on the worn surfaces. The effects of increased electrochemical activity on the subsequent wear-corrosion performance of the sintered WC-5.7Co-0.3Cr need to be investigated.

7.2.1.4 Wear-corrosion interaction maps

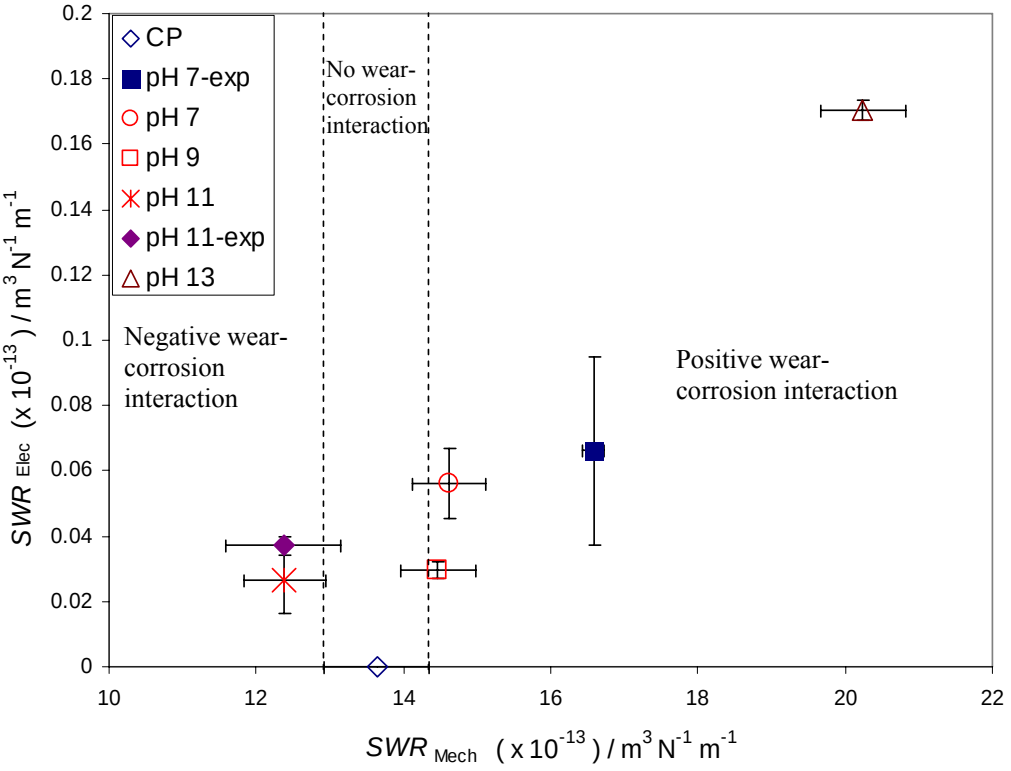

Figure 7.24: Electrochemical wear vs. mechanical wear for sprayed WC-10Co-4Cr coating.

As discussed in the previous section, SWR_{Elec} was calculated from the area under the current noise curve during micro-abrasion. Whereas, the SWR_{Mech} is the difference between the SWR_{Total} obtained from the wear test and the SWR_{Elec} (Equation 7.1). pH 11-CP sample is considered as the baseline condition as the SWR_{Elec} for pH 11-CP is zero.

Figure 7.24 shows the graph of SWR_{Elec} *vs*. SWR_{Mech} for the fresh and exposed samples for the WC-10Co-4Cr coatings. Wear-corrosion of sprayed coatings in pH 13 abrasive slurry results in an increase in SWR_{Elec} and consequently results in an increase in SWR_{Mech}. This behaviour is in accordance with the observed wear mechanism. An increase in SWR_{Elec} results in an increase in the rate of binder removal from the sample surface which leads to an increase in undermining of carbides leading to an increase in the SWR_{Mech}. Despite the fact that the electrochemical wear is three orders of magnitude lower than the wear-corrosion rates observed for all sprayed coatings, the ability of the binder to resist corrosion / passivate appears to be closely related to the wear-corrosion performance. pH 11 and pH 11-exp

samples show that a decrease in the rate of binder removal results in a decrease in the SWR_{Mech}.

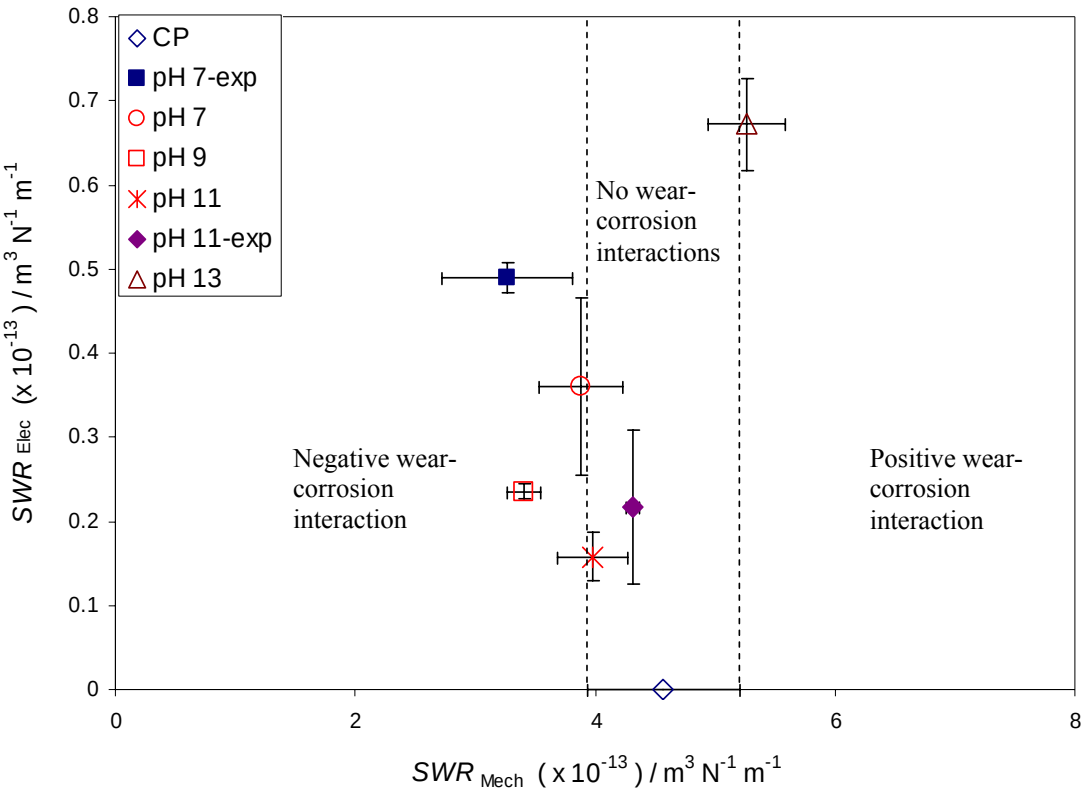

Figure 7.25: Electrochemical wear vs. mechanical wear for sintered WC-5.7Co-0.3Cr samples.

However, the SWR_{Elec} *vs*. SWR_{Mech} relationship is more complex for the sintered samples, see Figure 7.25. The higher SWR_{Elec} is due to the poor repassivation performance of sintered WC-5.7Co-0.3Cr compared to the WC-10Co-4Cr coating. However, an increase in the SWR_{Elec} does not lead to any appreciable change in the SWR_{Mech}, except for the pH 13 samples. The rate of binder depletion/ extrusion is known to influence the wear-corrosion of sintered hardmetals [103]. However, under neutral and weak alkaline conditions depletion of binder is not significantly accelerated and therefore does not change the SWR_{Mech}. This was also observed from the SEM micrographs of the worn samples which showed similar levels of carbide grain cracking; see Figure 7.16 and the comparison between the depth of wear and corrosion attack (Figure 7.17). Higher SWR_{Elec} and SWR_{Mech} observed in pH 13 samples is due to increase in the binder depletion occurring under strong alkaline conditions, see Figure 7.17. Also, as there is no obvious relationship between the SWR_{Elec} and pH, PA can not be calculated using the approach of extrapolation of SWR_{Elec} *vs* pH curve to obtain the pH value corresponding to zero SWR_{Elec} as discussed in Chapter 2.

7.2.1.5 Summary

In summary, the wear-corrosion performance of sintered WC-5.7Co-0.3Cr and sprayed WC-10Co-4Cr was studied under neutral and alkaline conditions and the influence of factors such as prior exposure to pH 7 / pH 11 solutions and abrasive slurry pH on the observed wear-corrosion mechanisms have been investigated.

The wear-corrosion performance of the WC-10Co-4Cr coating showed a strong dependence on the pH of the abrasive slurry. Overall, the lowest SWR_{Total} was observed for pH 11 condition while the highest SWR_{Total} was observed for pH 13. SEM investigation of wear-scars revealed that the wear mechanism strongly depended on the rate of binder removal within the wear scar and undermining of the carbide grains. Comparison of repassivation times at the end of the micro-abrasion test (Figure 7.5) and the average current levels (Figure 7.11) observed during the micro-abrasion tests suggest that the binder-removal rate during micro-abrasion was influenced by the ability of the binder to repassivate. Hence under conditions where the binder-phase was likely to form a predominantly Co-based passive film (pH 11), the rate of binder removal, and hence the SWR_{Total} was lower. It was also observed that abrasion leads to acceleration in corrosion due to an increase in the surface area and stripping of passive film formed on the surface. However, under neutral and mild alkaline conditions, the wear-scar readily repassivated when micro-abrasion stops. The SWR_{Elec} observed during micro-abrasion in pH 7 conditions resulted in an increase in the SWR_{Total} and confirms that pH 7 condition cannot be considered as a corrosion-free environment. It was also obvious from the rate of mechanical and electrochemical attack that the 1-carbide deep corrosion trenches observed on exposed samples do not influence the SWR_{Total} as they are removed within the initial stages of abrasion. Clearly, the SWR_{Total} is controlled by the rate of binder-removal which is influenced by the pH of the abrasive slurry.

The wear-corrosion performance of sintered WC-5.7Co-0.3Cr was less dependent on the abrasive slurry pH as compared to WC-10Co-4Cr coating. SEM micrographs of the wear-scars revealed that wear occurs predominantly by the fragmentation of the carbide grains followed by the removal of unsupported carbide grain fragments. The high SWR_{Elec} observed for sintered samples was due to the low repassivation rate observed for the sintered samples, see Figure 7.14. Under weak alkaline and neutral conditions, the removal of the binder-phase was not affected, resulting in a relatively uniform SWR_{Total}. However, there was a marked increase in the SWR_{Total} when using a pH 13 abrasive slurry as the binder-phase depletion is accelerated (Figure 7.17 and Figure 7.19). Thus, overall the wear-corrosion analysis of

sintered hardmetal and sprayed coating reveal that the wear-corrosion interactions are expected to be the lowest under pH 11 conditions.

Interestingly, it was observed that the slow repassivation coupled with the absence of readily passivating binder-rich areas lead to a marked increase in corrosion at the end of the wear test. Low recovery ratios of 0.65 were observed. This behaviour was due to the microstructure of the sintered hardmetals. Abrasive wear leads to a substantial increase in the surface area of the sample along with the formation of crevice-type features between fractured carbides. Increase in corrosion is likely to be due to the drop in local pH within the crevice-type features and possible micro-galvanic coupling between the unworn area and the wear scar. Presence of corrosion at the end of the micro-abrasion test is likely to weaken the skeletal carbide structure and could be detrimental to the subsequent wear-corrosion performance and needs further investigation.

7.3 Conclusions

Sprayed WC-10Co-4Cr coating:

- Comparison of the depth of wear and depth of corrosion during abrasion calculated using current-noise trends reveal that the mechanical damage always supersedes the electrochemical damage and is two-orders of magnitude greater. The corrosion trenches observed on exposed samples (pH 7-exp, pH 11-exp) are one-carbide deep and are likely to be removed in the initial stages of abrasion. Hence, these corrosion trenches are not expected to have any influence on the final SWR_{Total}.
- SEM micrographs of worn samples reveal that wear occurs by preferential removal of binder around the carbide grains exposing them to the abrasives which subsequently leads to their cracking and pull-out.
- Among the pH values examined in this chapter, the least SWR_{Total} was observed using abrasive slurry of pH 11 (pH 11 and pH 11-exp samples). The repassivation times at the end of the micro-abrasion test and the average current levels observed during the micro-abrasion tests suggest that the binder-removal rate during micro-abrasion was influenced by the ability of the binder to repassivate. Under conditions where the binder-phase was likely to form a predominantly $Co(OH)_2$ passive film, the rate of binder removal, and hence the SWR_{Total} was lower. This was also corroborated by the trend observed between SWR_{Elec} and SWR_{Mech}. As proposed in Chapter 6, the passivation of the binder-rich areas was also likely to result in a reduced friction between the abrasive and the sample surface resulting in the lowering of SWR_{Total}.

Sintered WC-5.7Co-0.3Cr:

- SEM micrographs of the wear scars reveal that wear occurs predominantly by the fragmentation of carbides and their subsequent removal by abrasion.
- Comparison of SWR_{Elec} and SWR_{Mech} for all the conditions reveals that increase in SWR_{Elec} does not lead to an appreciable change in SWR_{Mech}, except for pH 13 samples which is due to the excessive binder depletion observed for pH 13 samples. Under neutral and weak alkaline conditions, SWR_{Mech} is independent of the SWR_{Elec} and is largely dependent on the ability of the carbide grains to resist fracture.
- Although SWR_{Elec} is higher than that observed for sprayed coatings under weak alkaline and neutral conditions, this is due to the inability of the WC-rich sintered surface to readily passivate.

- Despite the higher corrosion rates observed for sintered hardmetals, their superior wear resistance offered by the skeletal carbide structure. The ability of the carbides to resist fragmentation is crucial for improving the wear-corrosion resistance of sintered hardmetals.
- However, inability of the carbide-rich sintered structure to readily repassivate leads to the presence of corrosion at the end of micro-abrasion test is likely to weaken the skeletal carbide structure and could be detrimental to subsequent wear-corrosion performance and needs further investigation. Intermittent use of the sintered hardmetals in corrosive environments can accelerate the wear-corrosion in the hardmetal.

8 Effects of increase in abrasive size on wear mechanisms and wear-corrosion interactions

8.1 Introduction

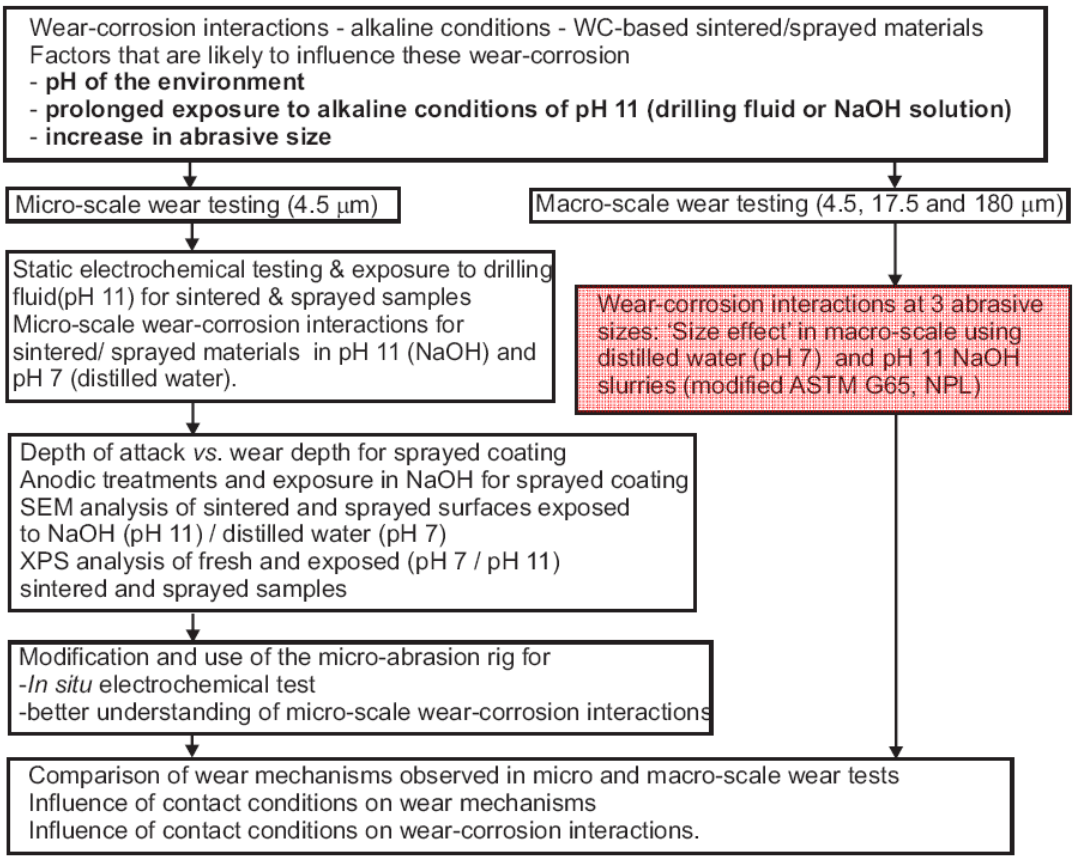

Figure 8.1: Experimental flowchart showing the test programme discussed in Chapter 8.

As discussed in the Chapter 1, downhole drilling operation exposes WC-based sintered hardmetals and sprayed coatings to abrasive particles of up to 500 μm suspended in alkaline drilling fluids (pH 9-11) [6]. The influence of abrasive size on wear was discussed in detail in the literature review (Chapter 2). The literature review concluded that although the effect of abradant size on the abrasive wear of metals has been extensively studied the effect on abrasive wear of WC-based sintered hardmetals and sprayed coatings has not been widely researched. Micro-abrasion studies on WC-based sintered hardmetals and sprayed coatings (Chapters 5, 6 and 7) reveal that the wear-corrosion of such surfaces is complicated due to the presence of hard and soft phases within the microstructure which respond differently during abrasive wear. The response to abrasive wear may be further influenced by the environmental pH and the corrosion performance of the WC-based hardmetals.

The complexity of evaluating the size effect of abrasives arises from the difficulty of entraining abrasives of different sizes as most wear-tests are designed to entrain abrasives of a specific size. Comparison of the wear mechanisms observed in the micro-abrasion tester (using 4.5 μm abrasives) and ASTM G65 rubber/ steel wheel test (abrasive size of 180-220 μm) can provide some understanding of the wear mechanisms that are likely to occur when the abrasive particle size changes. However, this does not give a true reflection of the 'size effect' due to the inherent differences in the contact conditions and hence can not be used to compare wear rates. To overcome these difficulties, it is necessary to adapt/ modify a well-characterised test set-up to conduct wear tests using abrasives of different sizes. This chapter investigates the size effect of abrasive particles on the abrasion-corrosion of WC-based sintered WC-5.7Co-0.3Cr and sprayed WC-10Co-4Cr coating using a modified ASTM G65 tester. For the first time, SiC abrasives particles, 4.5 μm, 17.5μm and 180 μm in size (an abradant/carbide size ratio of 1, 10 and 100), were successfully entrained on the modified ASTM G65 wear tester. The details of the experimental set-up and test conditions were discussed in detail in Chapter 3. An overview of the test matrix is given in Table 8-1

Table 8-1: Test matrix for the macro-scale abrasion test

Condition	**pH 7**			**pH 11**			**pH 11-exp**		
Abrasive size (μm)	**4.5**	**17.5**	**180**	**4.5**	**17.5**	**180**	**4.5**	**17.5**	**180**
Sintered WC-5.7Co-0.3Cr	X	X	X	X	X	X	X	X	X
Sprayed WC-10Co-4Cr	X	X	X	X	X	X	X	X	X

8.2 Results and Discussion

8.2.1 WC-10Co-4Cr coating

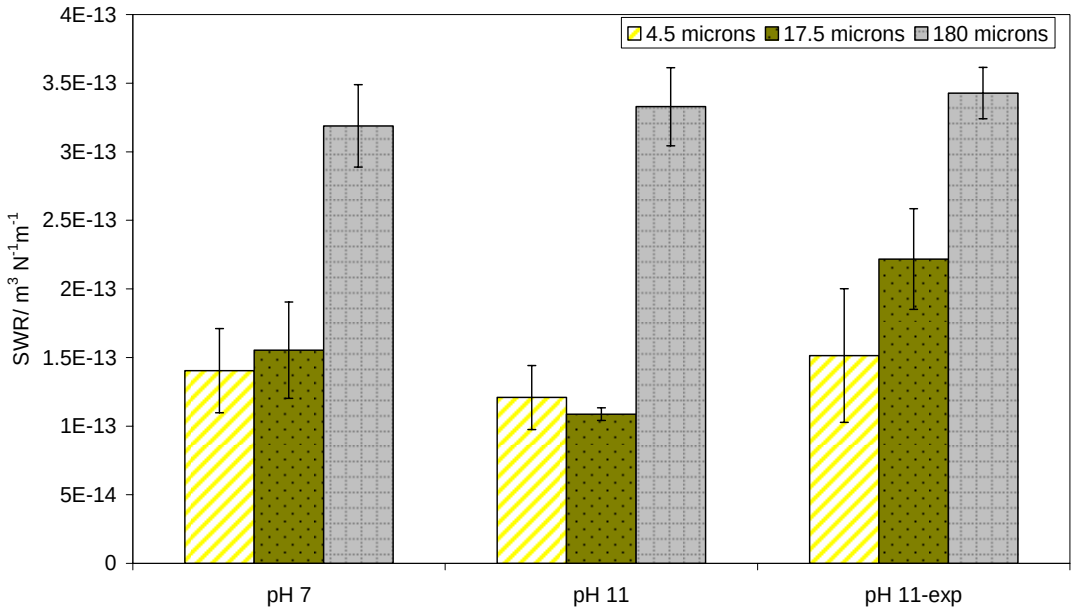

Figure 8.2: Specific wear rates for WC-10Co-4Cr coating using similar volume fractions of 4.5 μm, 17.5 μm and 180 μm SiC abrasives suspended in pH 7 and pH 11 slurries.

Figure 8.2 shows the specific wear rates (*SWR*) for pH 7, pH 11 and pH 11-exp samples of sprayed WC-10Co-4Cr coating abraded using 4.5 μm, 17.5 μm and 180 μm SiC abrasives. As seen in Figure 8.2, the influence of pH on the *SWR* appears to be very subtle and will be discussed later in the chapter. Figure 8.2 also shows that for all pH conditions, the *SWR* observed for the 4.5 μm and 17.5 μm abrasives are very similar which could be due to similar wear mechanisms. However, the *SWR* doubles for the 180 μm abrasives indicating that there may be a change in the wear mechanism for180 μm abrasives. SEM micrographs of the worn pH 11 surfaces were examined to determine the wear mechanisms occurring. For consistency, SEM analysis was performed on the centre of the wear scar in all samples

8.2.1.1 4.5 μm SiC abrasive

Figure 8.3a shows an unworn surface of a WC-10Co-4Cr sprayed coating revealing its microstructure of randomly distributed binder-rich and carbide-rich areas. Figure 8.3b shows a wear scar with grooves of the size of the abrasives (4-5 μm wide) caused by the ploughing action of the abrasives. The grooves appear to be prominent in binder rich regions. Clearly, abrasive wear of the binder-phase has occurred by two-body (2-B) grooving mechanism. In regions rich in carbide grains, there appears to be preferential removal of binder-phase as highlighted in the Figure 8.3c. The preferential removal of the binder-phase around the carbides is likely to be caused by fragmented abrasive particles which are smaller than 1 μm in size. The rotation of the rubber wheel at a high velocity of 0.9 m s^{-1} is also likely to cause slurry washing of the binder-phase from between the carbides, as can be seen from the Figure 8.3c. The observed wear mechanism in the carbide-rich areas is similar to equal pressure on the phases (EP) mode of the model predicted by Axen *et al.*[68]. Equal pressure on the phases results in the preferential abrasion of the softer phase (binder) leading to the 'undermining' of the harder phase (carbides). This result in the ejection of loosely held carbides from the surface as can be inferred from the presence of cavities in the wear scar, see Figure 8.3b. Also, preferential removal of the binder-phase exposes the carbides to the abrasive particles resulting in their fragmentation. Preferential removal of the binder-phase around the carbide grains is likely to occur if the abrasive particles are of same size or smaller than the carbide grains as observed by Chen *et al.* [85] and Liao *et al.* [87]. Grooves caused by abrasive particles ploughing through binder rich regions are also observed in the cross-section of the worn sample; see Figure 8.4b. Clearly, abrasion in binder-rich areas of the coating has been caused by 2-B grooving of the abrasives. Also, the stresses induced by the contact of 4.5 μm abrasives do not cause any sub-surface cracking as seen from the cross-section of the worn coating. Hence, wear of the coated surface occurs by a combination of 2-B grooving in the binder-rich areas and preferential removal of the binder phase/ undermining of carbide grains in the carbide rich areas. The different wear mechanisms observed in the carbide-rich and binder-rich regions of the coating are due to the inhomogeneous microstructure of the coating and abrasion by abrasive similar in size to that of the carbide grains.

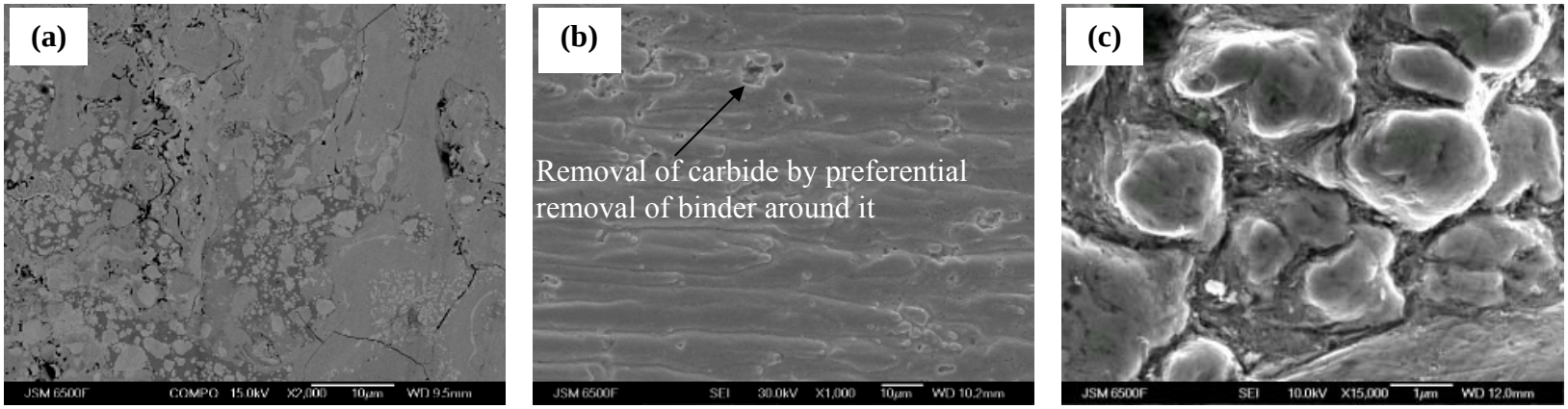

Figure 8.3: Comparison of WC-10Co-4Cr coating; (a) unworn area, (b) pH 11 sample worn using 4.5 μm abrasives and (c) high magnification image of (b) showing preferential binder removal around a cluster of carbide grains (direction of abrasive motion: left to right).

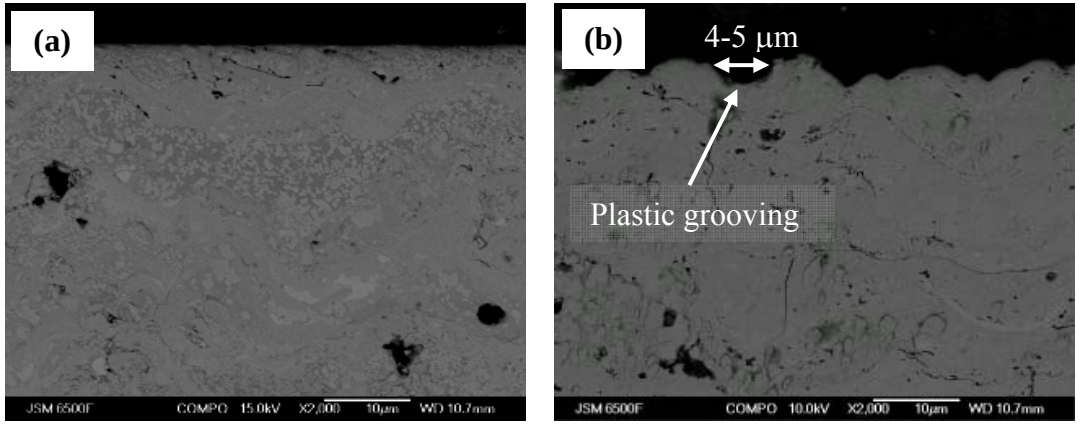

Figure 8.4: Comparison of WC-10Co-4Cr coating cross-sections; (a) unworn area and (b) pH 11 sample worn using 4.5 μm abrasives showing grooves of the size of the abrasives.

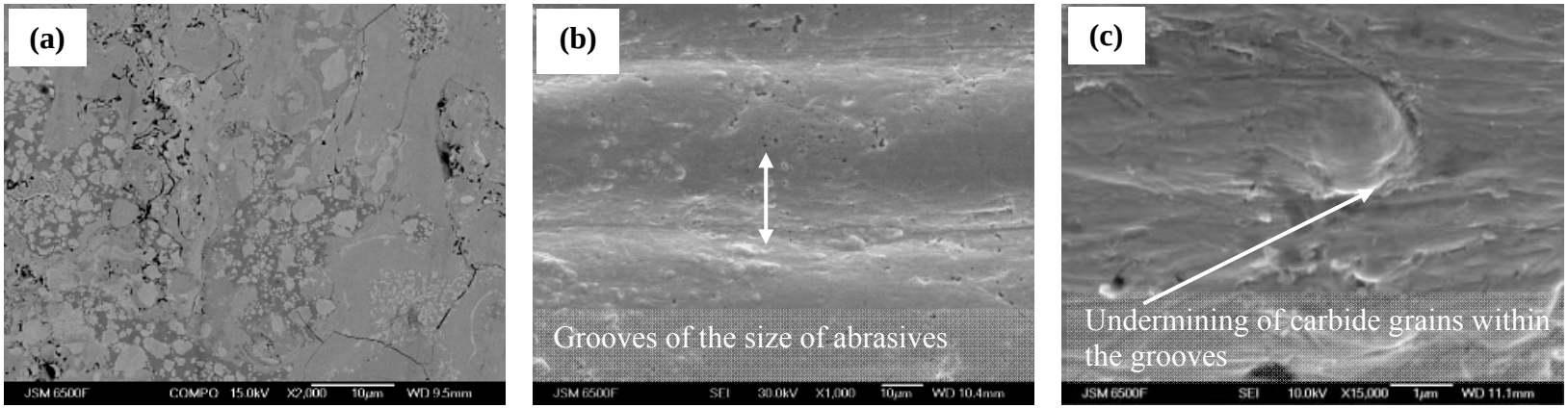

Figure 8.5: Comparison of WC-10Co-4Cr coating; (a) unworn area, (b) pH 11 sample worn using 17.5 μm abrasives and (c) high magnification image of (b) (direction of abrasive motion: left to right).

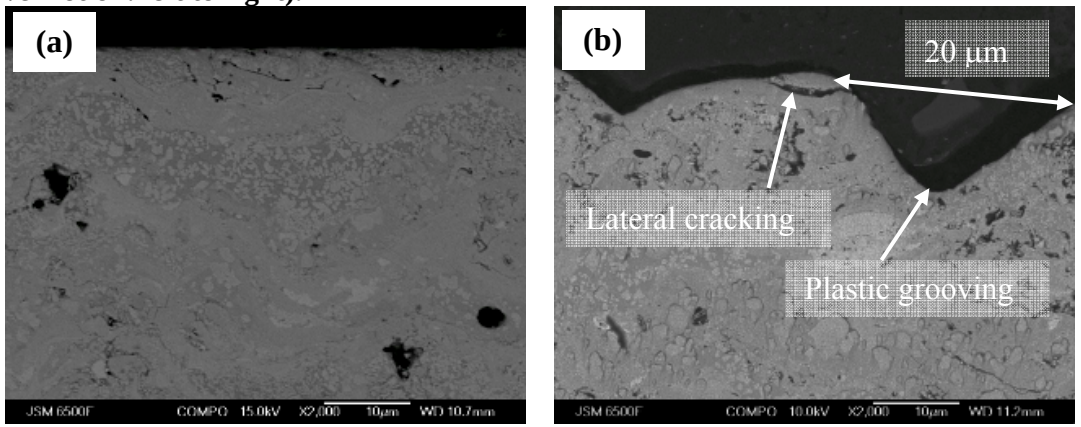

Figure 8.6: Comparison of WC-10Co-4Cr coating cross-sections; (a) unworn area and (b) pH 11 sample worn using 17.5 μm abrasives showing grooves of the size of the abrasives and lateral cracks formed due to the large grooves.

8.2.1.2 17.5 μm SiC abrasive

Figure 8.5 are micrographs of (a) an unworn surface and (b) a worn area on the sprayed WC-10Co-4Cr abraded using 17.5 μm SiC abrasives. The worn area reveals the grooved surface of the coating, see Figure 8.5b. The grooves are significantly wider and there are fewer carbide grains present within the grooves as compared to the sample worn using the 4.5 μm abrasive. Figure 8.5c shows a high magnification SEM of a region in the groove and shows a carbide grain within the groove. Some / limited preferential binder depletion has occurred around the carbide grain exposing it to abrasive particles. The removal of the carbides from the coating surface by the 17.5 μm abrasive is likely to be due to a combined action of fragmentation and the removal of unsupported carbide grains. The preferential removal of the binder-phase around the carbide grains leading to their undermining is likely to be more effective with the smaller 4.5 μm abrasive, see Figure 8.3c and Figure 8.5c.

The 17.5 μm abrasive particles plough through the coating forming grooves of similar size as can be seen in the cross-section of a worn surface in Figure 8.6b. Clearly, the grooves appear to increase in size with a corresponding increase in the size of the abrasive as can be seen from the Figure 8.4b and Figure 8.6b. The high level of plastic deformation due to the grooving observed in coated samples worn by 17.5 μm abrasive also leads to the lateral cracking in the coating which can further accelerate wear by delamination, as highlighted in Figure 8.6b. Liao *et al* [87] observed a similar wear mechanism when studying the abrasive wear of HVOF WC-17Co coating using abrasives larger than the carbides. It was reported that the larger abrasives cut or plough through the coating fragmenting carbide particles in the process which are subsequently gouged out by the action of abrasive particles.

The coating wear using 17.5 μm abrasive occurs by the formation of grooves of the size of the abrasives and removal of carbides within the grooves by a combination of fragmentation of the carbides leading to the removal of unsupported carbide grains. The plastic deformation caused by grooving of 17.5 μm abrasive also leads to some lateral cracking of the coating.

8.2.1.3 180 μm SiC abrasive

Figure 8.7 shows the SEM micrographs of (a) an unworn surface and (b) a worn area on the sprayed WC-10Co-4Cr abraded using the 180 μm SiC abrasive. The worn surface of WC-10Co-4Cr coating shows the presence of fine grooves, see Figure 8.7b. Unlike the worn surfaces abraded using 4.5 μm and 17.5 μm abrasives, the grooves on the surface are not similar in size to that of the abrasive used (180 μm). Also, the surface of the worn sample does not show the presence of any worn/ fractured carbides. This can also be confirmed from the higher magnification SEM of the worn surface, see Figure 8.7c. The SEM shows that the grooves on the worn surface are ~1 μm wide and the surface shows no evidence of any worn carbides. Clearly, the absence of any fractured carbides suggests that either the carbides have suffered severe fragmentation leading to their removal from the coating surface or have been removed in large splat-size debris. The absence of any cavities formed due to the undermining of carbide grains on the wear scar surface indicates that the carbides are removed in spat-sized debris. This is further corroborated by the presence of transverse cracks on the coating surface suggests that the coating failure occurs by crack propagation through the binder-phase. The cross-sections of worn coatings were studied for a better understanding of the observed wear mechanism. Figure 8.8a and Figure 8.8b compare the cross sections of an unworn and worn coated sample. The cross-section of the worn coating reveals the presence of sub-surface transverse and lateral cracks propagating through the binder-phase along the splat boundary.

Brittle fracture of HVOF WC-Co coating has been observed during indentation by hard particles either in the form of Palmqvist cracks or Median cracks (half penny crack) depending on the indentation loads [88]. Propagation of cracks initiated due to the indentation by hard particles can lead to the delamination of the coating in splat-sized debris. Lopez-Cantera and Mellor [37] studied the fracture toughness and erosion-resistance of the WC-10Co-4Cr coating and observed that the ability of the coating to resist fracture is related to its erosion-resistance. Stewart *et al*. [94] found that propagation of sub-surface transverse cracks was the controlling factor for material removal in abrasive wear of plasma sprayed WC–Co coatings using macro-scale abrasives (200 μm). They reported that vertical cracks are formed during the initial stage of the material loss by the indentation of the abradant into the coating. The vertical cracks propagated through the coating until they reached either the binder phase or the splat boundaries. On reaching the binder-phase or the splat boundary, they propagate parallel to the coating surface removing material in ‘splat-size’ debris as shown in Figure 8.9. A similar mechanism of development and propagation of sub-surface

cracks during erosive wear has been reported by a number of studies [27, 92]. This is also corroborated by the observation that crack propagation parallel to the coating /substrate interface in WC-based coatings is easier than crack propagation transverse to the coating/ substrate interface [37]. The removal of large sections of the coating during the abrasion-corrosion process using 180 μm abrasives results in doubling of the wear rates as compared to the abrasion-corrosion due to 4.5 μm and 17.5 μm abrasives. The removal of coating debris along the binder phase also explains the absence of carbide particles on the worn surface.

The wear-corrosion tests on the sprayed WC-10Co-4Cr clearly show that there is a change in wear-mechanism as the abrasive size increases. Figure 8.10 compares the wear mechanisms observed for the coating using 4.5 μm, 17.5 μm and 180 μm abrasives. Depth of the wear scars was estimated from the wear scar volume measured gravimetrically and the approximate wear scar area. The wear scars were found to be approximately 1 splat deep (3-4 carbides) for WC-10Co-4Cr coating abraded using 4.5 μm and 17.5 μm SiC abrasives. Also, for 4.5 μm and 17.5 μm abrasives, a similar wear mechanism of plastic grooving of the binder phase followed by undermining and fragmentation of the carbide grains leads to a similar *SWR*. Interestingly, there is a very subtle increase in the *SWR* for the pH 11-exp samples abraded using 4.5 μm and 17.5 μm SiC abrasives. As observed from the FIB cross-sections of the WC-10Co-4Cr coating exposed to pH 11(Chapter 6), corrosion attack was one carbide deep (4-5 μm). Due to the larger wear scar area and relatively low wear scar depth as compared to the micro-abrasion tests, the *SWR* in the modified ASTM G65 test are influenced by the pre-induced corrosion features on the surface of WC-10Co-4Cr coating. As discussed in Chapter 6, corrosion of metallic W around the periphery of the carbide grains leads to loosening of carbide grains. The undermining and removal of unsupported carbides on the coating surface leads to an increase in *SWR* (pH 11-exp) when abraded 4.5 μm and 17.5 μm abrasives. This is further corroborated by the observation that sprayed samples worn by 180 μm abrasive do not show any influence of the pH of the abrasive slurry or the surface condition (fresh / exposed) as wear is caused by the propagation of lateral cracks and removal of the coating in the form of splat-sized debris. Clearly, the observed wear mechanism is independent of the surface conditions. However, formation and propagation of lateral cracks in the coating also leads to a significant increase in the *SWR*.

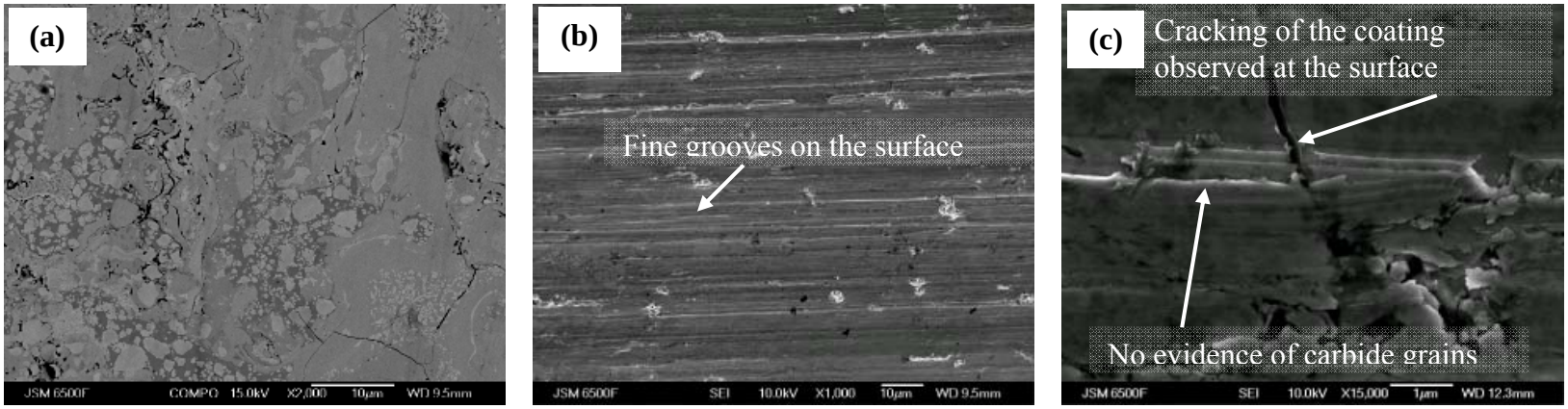

Figure 8.7: Comparison of WC-10Co-4Cr coating; (a) Unworn area, (b) pH 11 sample worn using 180 μm abrasives and (c) High magnification image of (b) showing fine grooves devoid of any carbides (direction of abrasive motion: left to right).

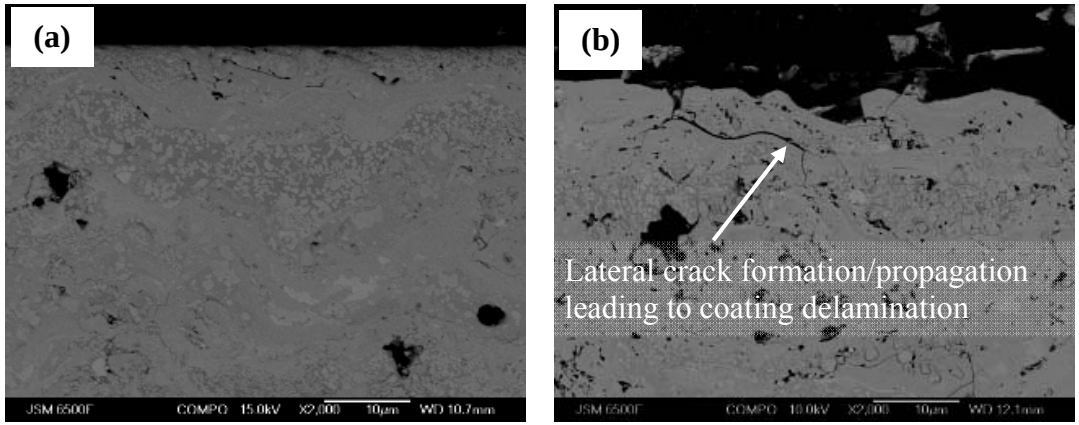

Figure 8.8: Comparison of WC-10Co-4Cr coating cross sections; (a) Unworn area and (b) pH 11 sample worn using 180 μm abrasives showing lateral crack formation which leads to eventual spalling of the coating along the weak splat boundaries.

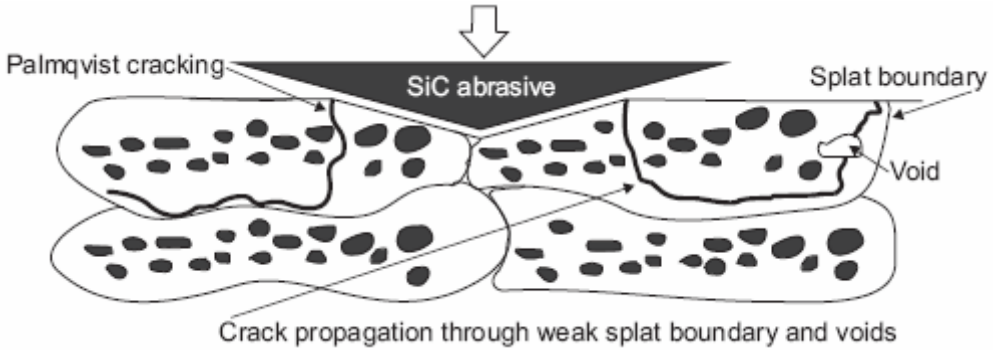

Figure 8.9: Schematic showing the formation and propagation of Palmqvist cracks within the coating due to the indentation of 180 μm SiC abrasives.

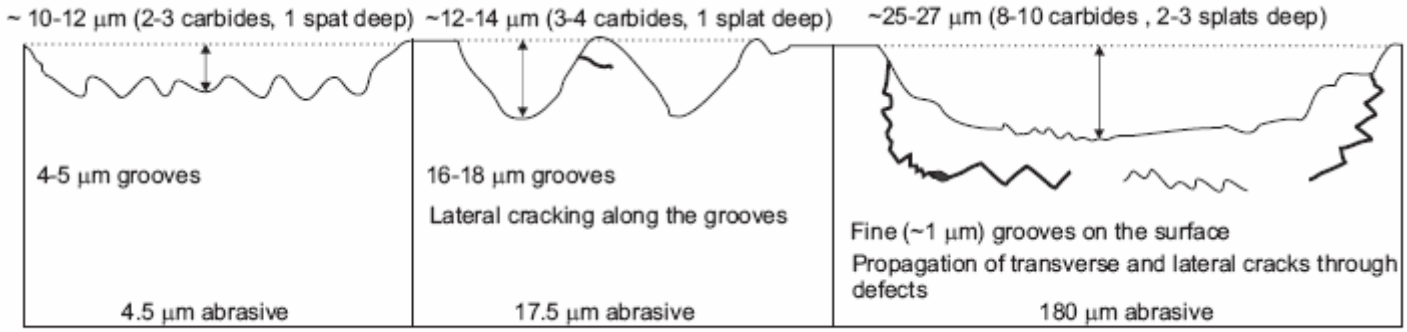

Figure 8.10: Summary of wear mechanisms observed for the sprayed WC-10Co-4Cr coating abraded using 4.5 μm, 17.5 μm and 180 μm abrasives.

8.2.2 Sintered WC-5.7Co-0.3Cr

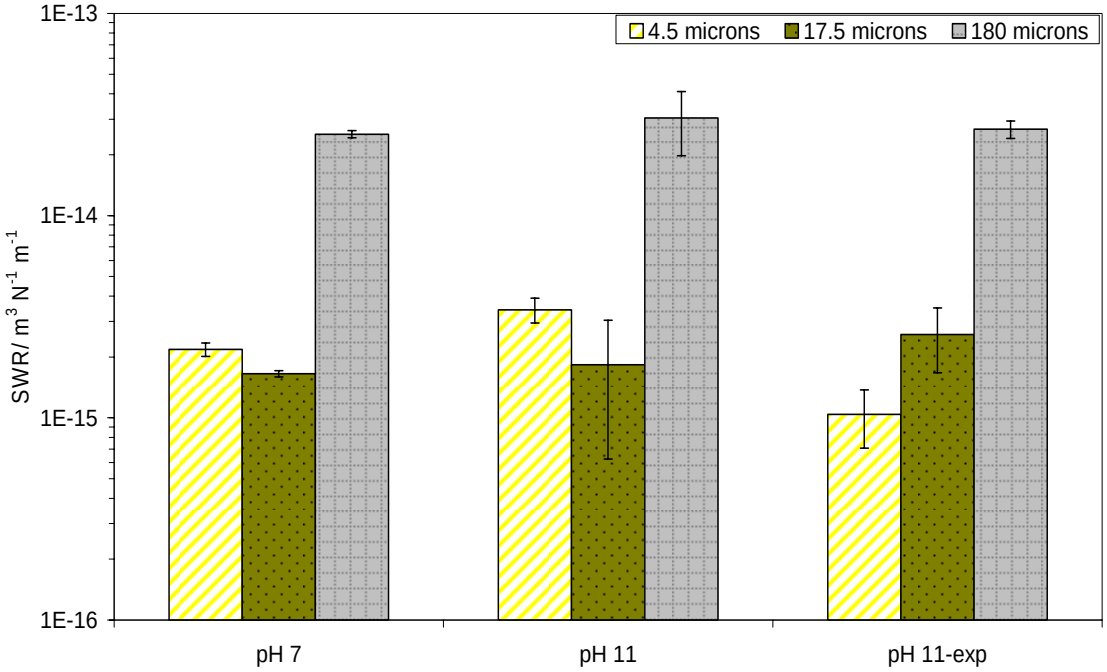

Figure 8.11: Specific wear rates for sintered WC-5.7Co-0.3Cr using similar volume fractions of 4.5 μm, 17.5 μm and 180 μm SiC abrasives suspended in pH 7 and pH 11 slurries.

Figure 8.11 shows the *SWR* for pH 7, pH 11 and pH 11-exp samples of sintered WC-5.7Co-0.3Cr abraded using 4.5 μm, 17.5 μm and 180 μm SiC abrasives. The SWR using 4.5 μm and 17.5 μm abrasives was found to be similar suggesting that comparable wear mechanisms are acting. However, the *SWR* using 180 μm abrasives increased by an order of magnitude signifying a change in the wear mechanism when the abrasive size increases from 17.5 μm to 180 μm. The *SWR* for all three abrasive sizes appears to be insensitive to change in pH (i.e. pH 7, pH 11 and pH 11-exp samples).

SEM micrographs for the worn pH 11 sintered surfaces were examined to determine the wear mechanisms occurring for the 4.5 μm, 17.5 μm and 180 μm abrasives. For consistency, the SEM investigation was undertaken at the centre of the wear scar and the direction of abrasive motion was from right to left.

8.2.2.1 4.5 μm SiC abrasive

Figure 8.12 shows the SEM micrographs of (a) an unworn surface and (b) a worn area on the sintered WC-5.7Co-0.3Cr abraded using 4.5 μm SiC abrasive. The worn surface shows a random distribution of regions with excessive binder depletion. In addition to the preferential binder depletion, Figure 8.12c shows that some of the carbide grains have suffered from surface cracking. The study abrasive wear of WC-based sintered hardmetals using fine abrasives (typically similar in size as the carbide grains) reveals a two-stage wear mechanism as observed by Shipway *et al.* [162]. In the initial stage of abrasive wear, abrasive particles selectively remove the binder phase leading to the formation of small pits with inter-granular facets. As observed by Blombery *et al.* [75], the removal of the binder-phase leads to the lowering of fracture strength and development of plastic strain within the surface layers of the sintered hardmetal. The strain developed is relieved by the formation of cracks within the carbide grains along their slip planes [75, 76]. Lowering of the fracture strength aids the propagation of these cracks which lead to the loosening of carbide grains within the skeletal structure. Subsequent abrasion removes the unsupported and fragmented carbides from the surface. The wear mechanism is also shown schematically in Figure 8.13.

Figure 8.14 compares the cross-sections of an (a) unworn sample and (b) worn sample. Clearly, the worn sample does not show any sub-surface damage to the carbide structure due to abrasion indicating that the effect of the abrasive particles is limited to the carbides at the surface.

8.2.2.2 17.5 μm SiC abrasive

Figure 8.15 compares the SEM micrographs of (a) an unworn surface to (b) a worn area on the sintered WC-5.7Co-0.3Cr abraded using 17.5 μm SiC abrasives. The SEM of the worn area shows preferential removal of the binder-phase around the carbides. The binder removal appears to be less than that for the 4.5 μm SiC abrasive, see Figure 8.12b. The preferential removal of the binder-phase from the surface layers of the sintered hardmetal is clearly an important step in the wear process. However, the skeletal microstructure makes it difficult for abrasives larger than the carbide grains to remove the binder-phase preferentially. Larsen-Basse [73] studied the sliding wear of WC-Co hardmetals and suggested that the binder is squeezed out of the surface by compressive stresses along the direction of sliding. Due to the skeletal carbide structure, there is negligible deformation of the WC grains and hence all the deformation is taken up by the binder-phase. An empirical relationship

proposed by the same author suggested that the amount of binder extruded was directly proportional to the size of carbide particles and the total strain developed within the hardmetal and inversely proportional to the binder mean free path. Removal of the binder-phase results in the lowering of the fracture toughness of the carbide grains. Damage to the carbide structure is caused by the fracturing of the carbide grains due to the reduced resistance to fracture. The preferential removal of the binder-phase and the subsequent fracturing of the carbide grains are shown schematically in Figure 8.16.

Figure 8.17b shows the cross-section of a worn sample. As in case of the sintered samples worn by 4.5 μm abrasive, the extrusion of the binder-phase and subsequent fragmentation of the carbide grains is limited to the carbides on the surface as there is no evidence of sub-surface damage. The level of binder depletion and carbide grain cracking observed for 17.5 μm abrasives was less than 4.5 μm abrasives, which results in the slightly lower *SWR* observed when using 17.5 μm abrasives.

Figure 8.12: Comparison of sintered WC-5.7Co-0.3Cr sample; (a) unworn area, (b) pH 11 sample worn using 4.5 μm abrasives and (c) high magnification image of the worn sample showing preferential binder removal around the carbide grains (direction of abrasive motion: left to right).

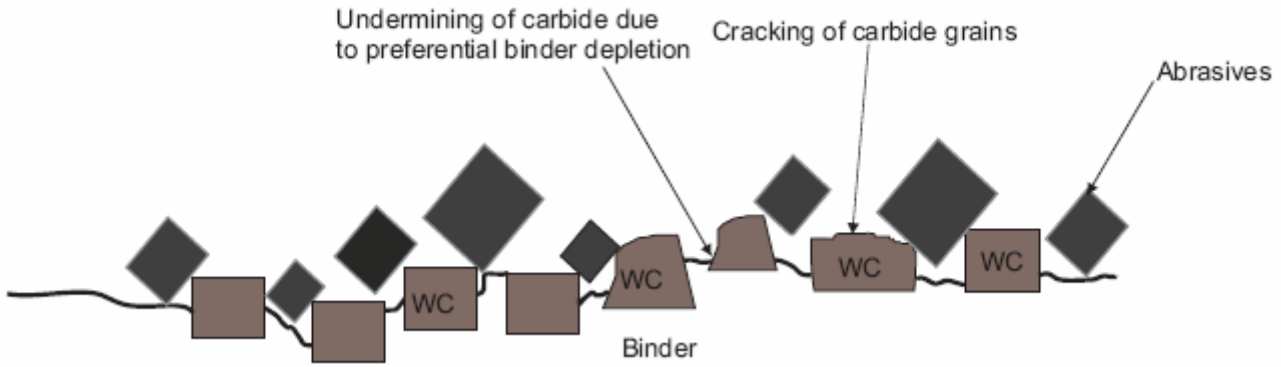

Figure 8.13: Schematic of the wear mechanism observed for sintered WC-based hardmetals abraded using abrasives of similar size as the carbide grains.

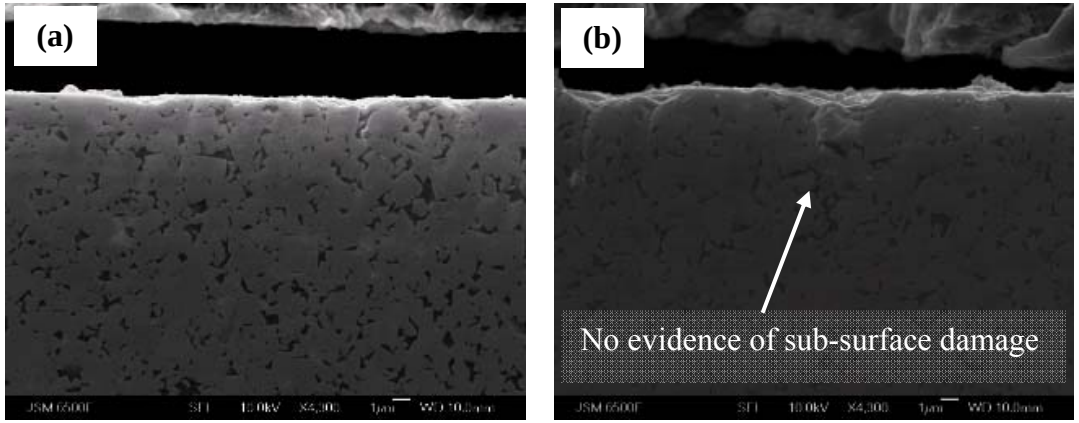

Figure 8.14: Comparison of sintered WC-5.7Co-0.3Cr cross-sections; (a) unworn area and (b) pH 11 sample worn using 4.5 μm abrasives (direction of abrasive motion: left to right).

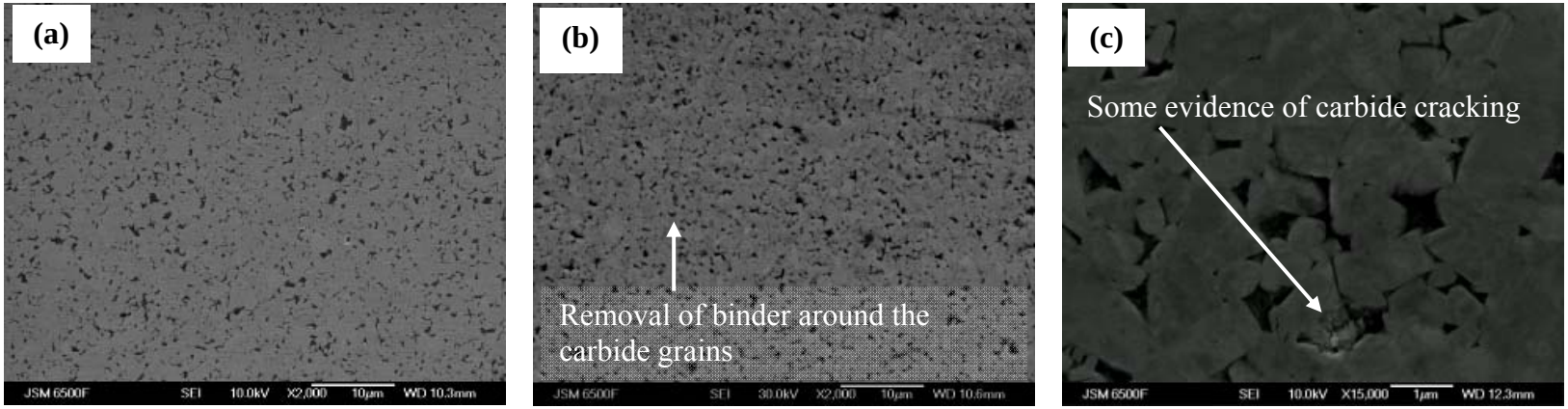

Figure 8.15: Comparison of sintered WC-5.7Co-0.3Cr sample;(a) Unworn area, (b) pH 11 sample worn using 17.5 μm abrasives and (c) high magnification image of the worn sample.

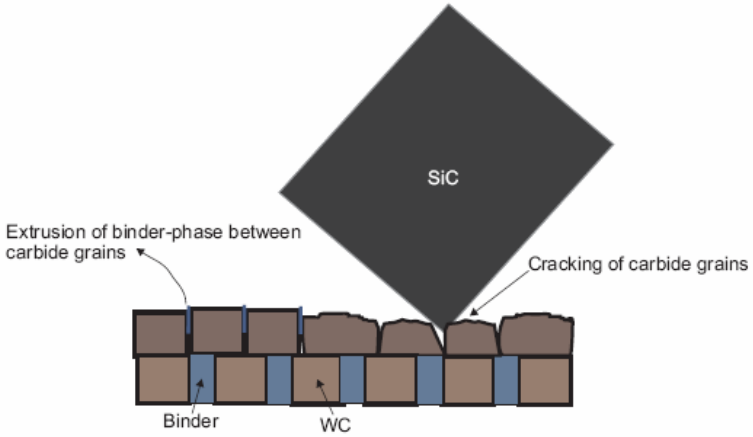

Figure 8.16: Schematic of the wear mechanism observed for sintered WC-based hardmetals abraded using 17.5 mm abrasives.

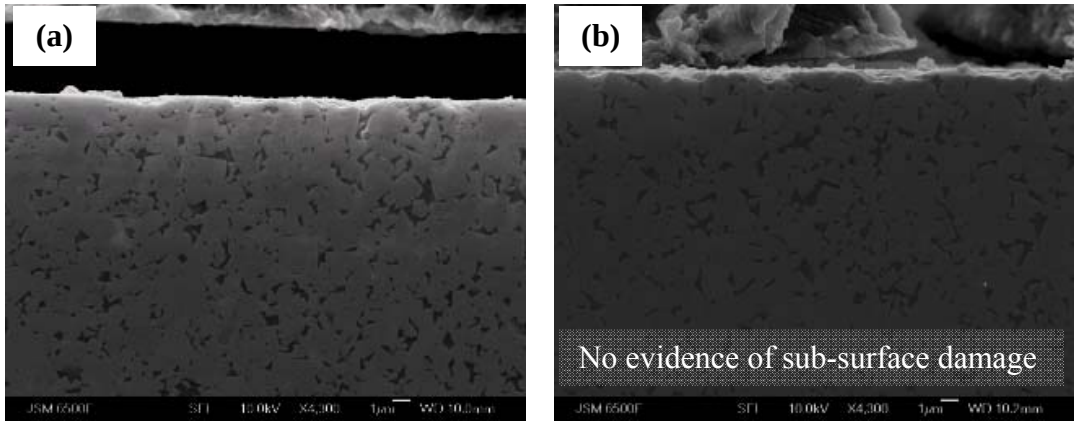

Figure 8.17: Comparison of sintered WC-5.7Co-0.3Cr cross-sections; (a) Unworn area and (b) pH 11 sample worn using 17.5 μm abrasives.

8.2.2.3 180 μm SiC abrasive

Figure 8.18 shows the SEM micrographs of (a) an unworn surface and (b) a worn area on the sintered WC-5.7Co-0.3Cr abraded using 180 μm SiC abrasive. The worn surface shows evidence of extensive carbide grain cracking and binder extrusion. Figure 8.18c shows the high magnification SEM of the worn area. There is also evidence of lateral cracking of individual carbide grain perpendicular to the direction of abrasive motion. Similar cracking of carbides was observed by Gee *et al.* [76, 78] during their study of abrasive wear of sintered WC-Co hardmetals by silica abrasives of similar size. The absence of the binder-phase also suggests that wear occurs by a combination of binder extrusion followed by cracking of the carbide grains along their slip planes. The wear process of sintered WC-based hardmetals using 180 μm abrasives is shown schematically in Figure 8.19. As observed for 17.5 μm abrasives, the preferential removal of binder-phase from the surface layers of the sintered WC-5.7Co-0.3Cr occurs by extrusion. The surface strain due to the preferential removal of the binder-phase is relieved by the cracking of carbides along their slip planes. The presence of increased plastic strain within the surface layers of worn WC-Co samples was confirmed using XPS analysis by Klaasen and Kubarsepp [77]. Removal of the binder-phase also results in the lowering of fracture toughness of the surface layers (3-5 μm, 1-2 carbides deep) of the hardmetal [75]. Presence of cracks within the carbide grains and lower fracture toughness lead to accelerate fragmentation of the carbide grains by subsequent abrasion. Fragmentation of the carbides results in the weakening of the skeletal carbide structure and facilitates the removal of unsupported carbide fragments. The intensity of fragmentation of the carbides appears to be directly related to the size of the abrasive particles.

The wear mechanisms observed for 17.5 μm abrasives and 180 μm abrasives are similar. However, severe fragmentation of carbides observed using 180 μm results in an order of magnitude increase in the wear rates. Unlike abrasion of the WC-10Co-4Cr coating, the presence of cracks is limited to the carbides on the surface of the sample as indicated by the absence of any evidence of sub-surface damage seen in the cross-section of the worn sample, see Figure 8.20b.

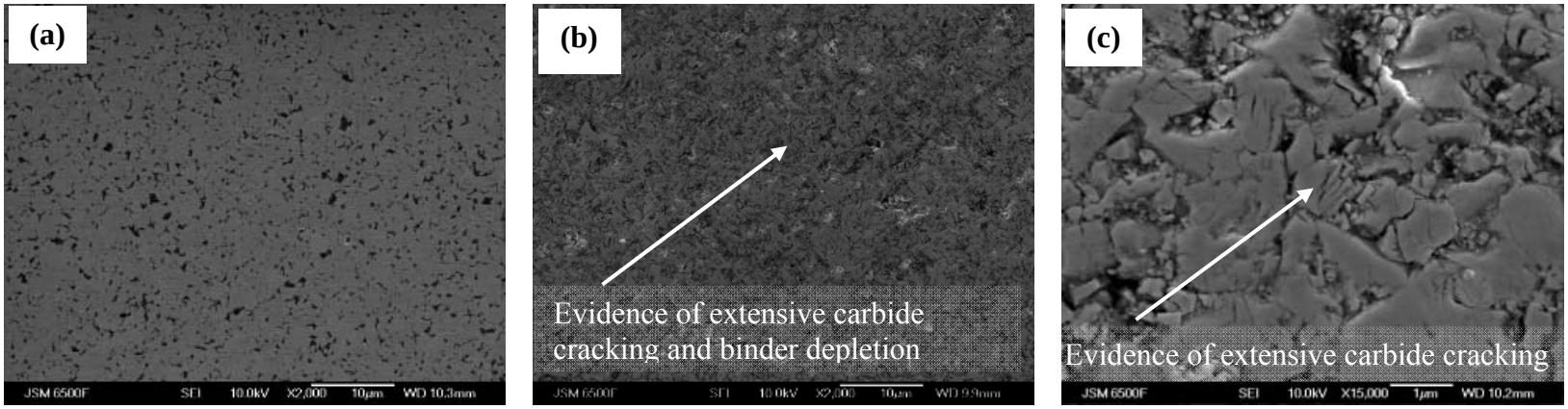

Figure 8.18: Comparison of sintered WC-5.7Co-0.3Cr sample; (a) unworn area, (b) pH 11 sample worn using 180 μm abrasives and (c) high magnification image of the worn sample showing fracture of carbide grains (direction of abrasive motion: left to right).

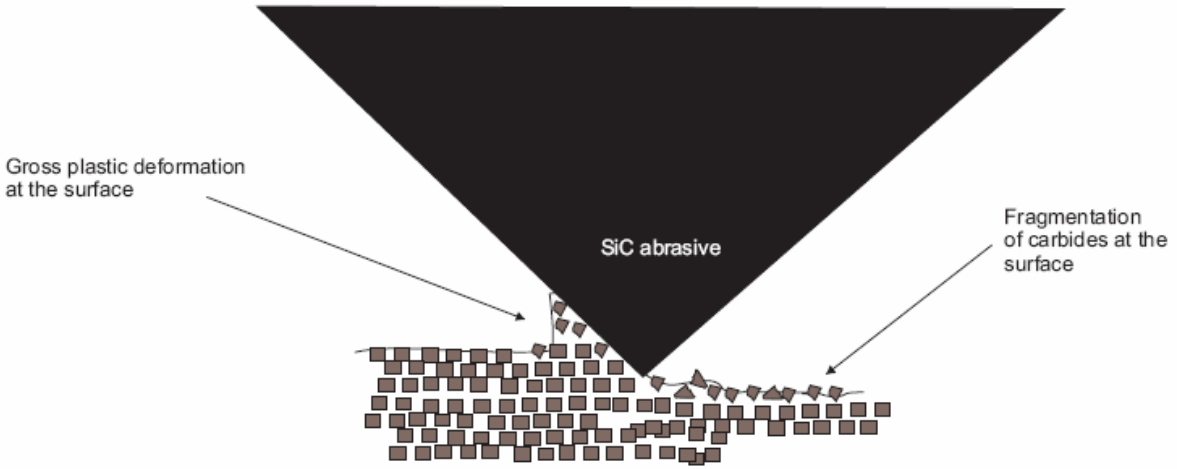

Figure 8.19: Schematic of the wear mechanism observed for sintered WC-based hardmetals abraded using 17.5 mm abrasives.

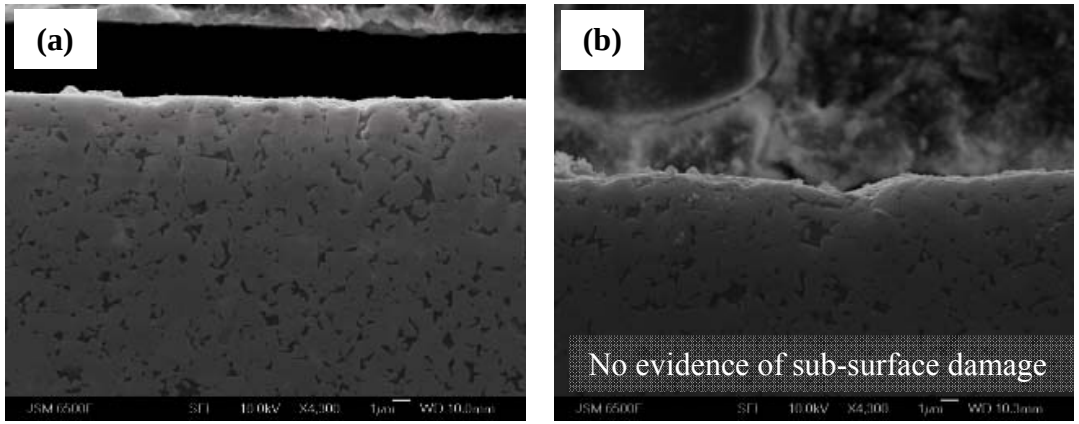

Figure 8.20: Comparison of sintered WC-5.7Co-0.3Cr cross-sections; (a) unworn area and (b) pH 11 sample worn using180 μm abrasives.

8.2.3 Size effect: Sintered WC-5.7Co-0.3Cr and WC-10Co-4Cr coating

The modified ASTM G65 rig was successfully used to entrain abrasives between 4.5 μm and 180 μm in size. This allowed the abrasive/carbide ratio to be varied from 1 to 100 whilst all other test conditions remained constant. For the first time, such a study was conducted to investigate the influence of change in abrasive particle size on the wear-corrosion of WC-based sintered hardmetals and coatings. A distinct 'size-effect' was observed for WC-based sintered hardmetal as well as sprayed coating. Clearly, the size effect results from the change in the wear mechanism observed with an increase in abrasive size.

The study of WC-10Co-4Cr coating showed that for 4.5 μm and 17.5 μm abrasives, abrasive wear occurred by the ploughing of the binder-phase by 2-B grooving. Preferential removal of the binder-phase led to the undermining of the carbides and their removal by subsequent abrasion. As seen from the cross-sections of the samples worn by 4.5 μm and 17.5 μm abrasives, there is no evidence of median cracking typically observed in grooving abrasion of brittle materials. However, abrasion by 180 μm abrasives leads to the formation of lateral cracks (Palmqvist cracking) as observed by Ahn *et al.*[89] and Lima *et al.*[88]. Propagation of the lateral cracks through the binder-rich phase along the weak splat boundary results in the delamination of the coating generating splat-size debris. As observed by Evans and Marshall [163], the wear amount increases when the delamination occurs by the propagation of lateral cracks within the coating. Clearly, the delamination of the coating along the binder-rich regions at the splat boundaries depends on the ease of crack propagation within the coating. As observed by Lopez-Cantera and Mellor [37] and Wheeler and Wood [93], the wear performance of WC-based coatings strongly depends on its fracture toughness. Study of indentation crack in the D-gun sprayed WC-10Co-4Cr coating revealed that the propagation of the cracks occurs along the interface between the outer region of the splats where carbides dissolve during thermal spraying and the inner core where carbides have not reached sufficient temperature to dissolve. As discussed in Chapter 2, during the D-gun spraying process, WC grains react with the metallic binder to form brittle ternary carbides and mixed W-C-M compounds particularly in the outer regions of the splat where the temperatures are higher [27, 30]. Lopez-Cantera and Mellor [37] observed the coating produced by HVOF system produced a denser coating with lesser dissolution of WC in the binder-phase as compared to the D-gun sprayed WC-10Co-4Cr leading to a higher fracture toughness and erosion resistance. Clearly, the delamination of the coating during abrasion and fracture toughness depend on the amount of WC dissolved in the binder phase and

improvement in the abrasion resistance can be obtained by minimising the dissolution of WC in the binder-phase and the subsequent embitterment of the binder-phase.

As seen from the wear mechanisms observed for sintered WC-5.7Co-0.3Cr abraded using 4.5 μm, 17.5 μm and 180 μm SiC abrasives, wear begins with the preferential removal of the binder-phase by abrasive particles similar in size to the carbide grains or by the extrusion of binder by abrasive particles which are larger than the carbide grains. As discussed in the previous section, the preferential removal of the binder-phase results in lowering of the fracture toughness of the surface layers and cracking of the carbides along their slip planes to relieve the accumulated strain. Subsequent abrasion leads to the fragmentation of carbide grains along the cracks formed and removal of unsupported carbides. Similar wear mechanisms were observed by Gee *et al.*[76] during their study of abrasion and erosion, mechanisms for sintered WC/Co hardmetals, who proposed the following steps:

- Removal of the binder-phase from the surface layer
- Plastic deformation and grooving of the binder phase
- Accumulation of plastic strain in WC grains
- Fracture and fragmentation of individual WC grains
- Cracking between WC grains
- Breakaway of unsupported WC grains

Clearly, as seen from the SEMs of worn samples, the intensity of each of the steps in the abrasion of sintered WC-5.7Co-0.3Cr appears to be dependent on the ratio of abrasive to carbide size. Interestingly, although the mechanism for preferential removal of the binder-phase is different for 4.5 μm and 17.5 μm abrasives, the *SWR* obtained is similar. Insignificant amount of fragmentation and fracture of carbides was observed for both 4.5 μm and 17.5 μm abrasives. For 17.5 μm and 180 μm abrasives, preferential binder removal occurred by extrusion, extensive fragmentation of carbides was only observed for 180 μm abrasives, leading to an order of magnitude increase in *SWR*. Clearly, the extensive fragmentation of the carbide grains result in the weakening of the skeletal carbide structure and the breaking-away of unsupported carbides. However, Ogilvy *et al.*[164] studied the indentation fracture of cemented carbides and observed that unlike typical brittle materials, cracks did not propagate radially into the bulk material and instead remained in the near-surface region (3-5 μm, 1-2 carbides deep) of the indentation plastic zone. Clearly, while 180 μm abrasives result in the formation of lateral cracks and delamination of the WC-10Co-4Cr coating (Figure 8.8), the fragmentation of carbides observed on the sintered WC-5.7Co-0.3Cr is limited to the near-surface regions (Figure 8.20). Blombery *et al.*[75] suggested that due to the compressive stresses in the WC grains and tensile stresses in the binder-phase

induced during the sintering process, bulk properties of the WC-Co composite do not encourage propagation of cracks.

The ability of the carbide grains on the surface to resist fracture is likely to result in the lowering of *SWR*. However, as discussed in the previous section, fracture and fragmentation of individual carbides is strongly dependent on the depletion of the binder-phase. As discussed in the Chapter 2 (Literature Review), a decrease in the binder content and in the carbide size results in an increase in the hardness of the sintered hardmetals [21, 25] without a substantial decrease in its fracture toughness [21]. Jia *et al.*[80] compared the abrasive wear performance of conventional (0.7 to 2.5 μm) and nano-structured (0.07 μm) WC-based sintered hardmetals. Clearly, the fracture behaviour of WC grains was related to their size and lowering the size of carbides is expected to result in a higher abrasive wear resistance. Also, according the Larsen Basse [73] model for extrusion of binder during abrasive wear, smaller carbides are expected to result in lesser binder extrusion. Lowering of the amount of binder extruded can also be achieved by improving the flow stress of the binder material.

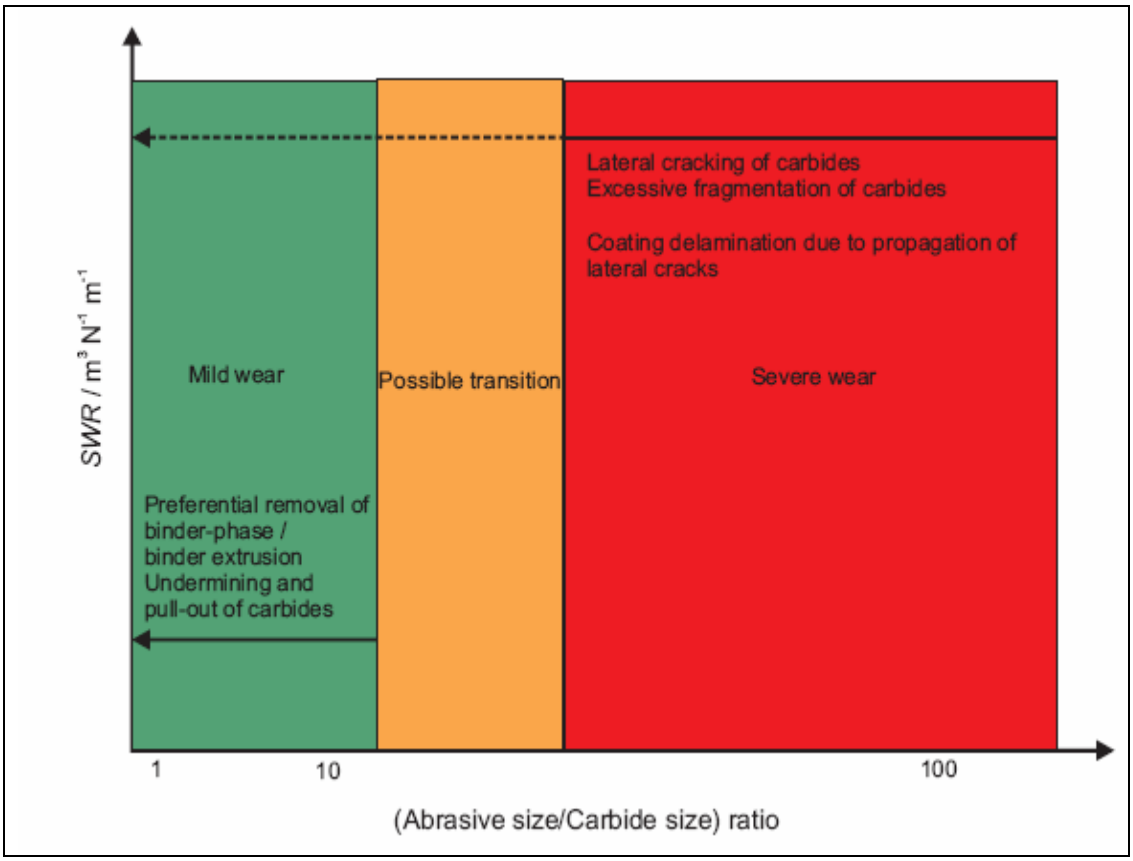

Figure 8.21: Summary of wear mechanisms which lead to the 'size effect' being observed for sintered WC-5.7Co-0.3Cr and sprayed WC-10Co-4Cr.

The influence of change in wear mechanisms caused by a change in abrasive / carbide size ratio on the *SWR* is summarised in Figure 8.21. Based on the *SWR* and the wear mechanisms

observed, the graph can be divided into two distinct regions. The region shown in green is where the abrasive/carbide ratio is between 1 and 10 and has the minimum *SWR*. The region shown in red is where the abrasive/carbide ratio is 100 and has the maximum *SWR*. A possible transition region is shown in orange when the wear mechanism shifts from the preferential binder-phase removal to the more severe cracking of carbides and sub-surface cracking of the coating.

8.3 Conclusions

- For both sintered and sprayed hardmetals, the effects of exposure to alkaline conditions are very subtle.
- Unlike single-phase materials, for WC-based sintered hardmetals and sprayed coatings, an increase in abrasive size leads to a change in wear mechanism.
- Sintered WC-5.7Co-0.3Cr
  - Abrasive wear using 4.5 μm and 17.5 μm abrasives is caused by preferential removal of the binder-phase leading to the undermining and removal of unsupported carbides. Depletion of the binder phase also results in some carbide grain cracking. However, cracking of carbides due to abrasion using 4.5 μm and 17.5 μm abrasives is relatively low and results in mild wear.
  - Abrasive wear using 180 μm abrasives is caused by a combination of binder extrusion and extensive cracking of the carbides. Extensive cracking of the carbides accelerates the undermining and removal of unsupported carbide fragments resulting in severe wear. Severe wear is observed for large abrasive/carbide ratios and leads to an order of magnitude increase in wear rates as compared to mild wear.
  - A decrease in the fragmentation of carbides during wear is likely to result in lower wear rates. Hence, the use of nano-scale carbides needs to be explored.

- Sprayed WC-10Co-4Cr

  - Grooves of the size of abrasives cause abrasive wear with 4.5 μm and 17.5 μm abrasives. For both abrasive sizes, removal of carbide grains occurs by preferential removal of the binder phase around the carbide grains. No sub-surface damage is caused when the abrasive/carbide size ratio is between 1 and 10 (4.5 μm and 17.5 μm abrasives) and results in relatively mild wear (1.5×10^{-13} m^3 N^{-1} m^{-1})
  - Abrasive wear using 180 μm abrasives occurs by a high stress and plastic deformation of the coating which leads to the formation of transverse and lateral sub-surface cracks. Due to the lower lateral fracture toughness, propagation of sub-surface cracks along the weak splat boundaries/ binder phase and results in the delamination of the coating and doubling of *SWR*

(3.0×10^{-13} m^3 N^{-1} m^{-1}). As in case of the sintered hardmetals, large abrasive/carbide ratios result in severe wear.

- Doubling of wear rates results from the formation and propagation of lateral cracks in the coating and depends on the fracture toughness of the coating. Improvement in the fracture toughness of the coating is expected to result in lower wear rates. Limiting the amount of W dissolution during the spraying process can lead to an increase in the fracture toughness.

- Significantly lower wear rates can be achieved by lowering the ratio of abrasive/carbide size by limiting the size of abrasive particles in a contact.

9 Influence of contact conditions on the wear mechanisms and wear-corrosion interactions

9.1 Introduction

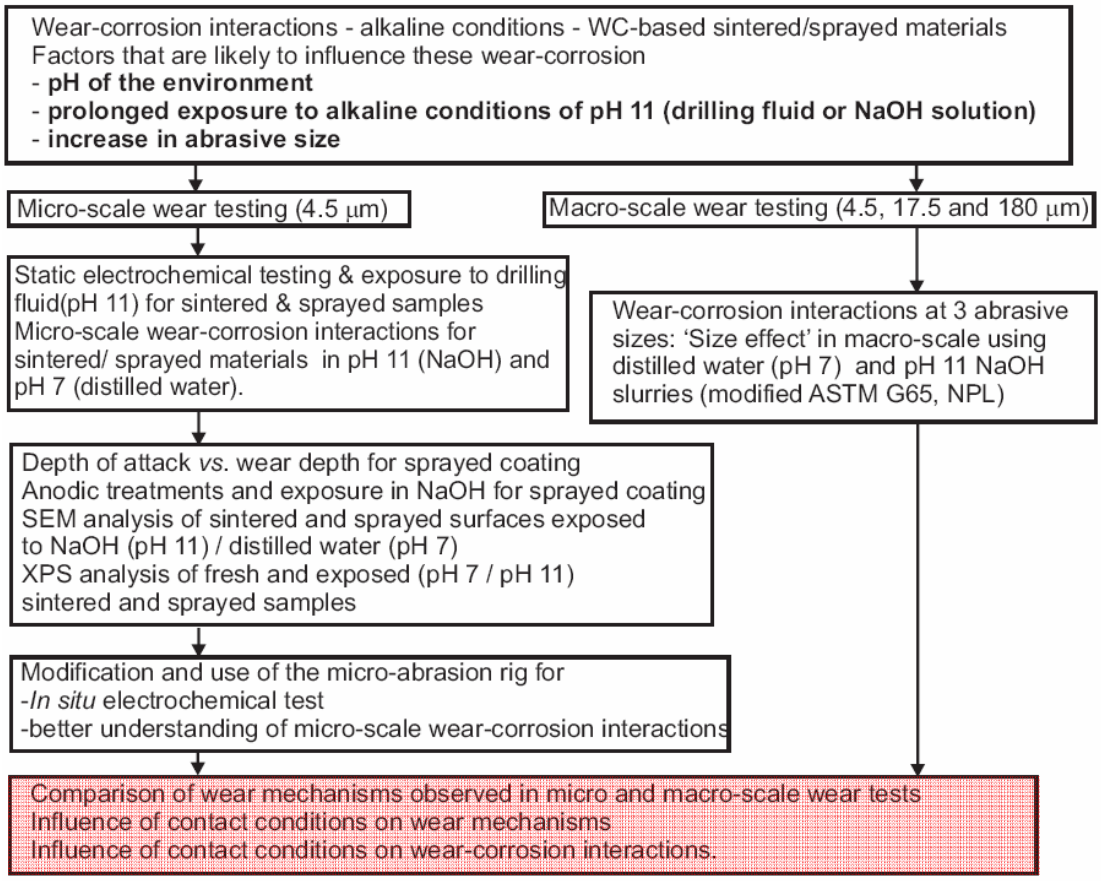

Figure 9.1: Experimental flow chart highlighting the discussion in Chapter 9.

In this Chapter, results from Chapters 7 and 8 are compared for a better understanding of contact conditions on the wear-corrosion interactions and wear mechanisms observed. Chapters 7 and 8 revealed that for both the sintered WC-5.7Co-0.3Cr and WC-10Co-4Cr coating the wear rates are strongly dependent on the prevalent wear-mechanisms. The use of 4.5 μm abrasives in the modified ASTM G65 tester provides an opportunity to compare the wear mechanism observed for the sintered WC-5.7Co-0.3Cr and WC-10Co-4Cr coating during abrasion using the micro-abrasion tester and the modified ASTM G65 and investigate the influences of contact conditions on the wear mechanisms. In this Chapter, the wear mechanisms observed will be compared on the basis of applied load, contact area (relative to the microstructure / splat geometry) and the wear modes observed (rolling/ grooving).

Models available in the literature have been used to predict the severity of the contact and its influence on the *SWR*. This chapter also investigates the effects of exposure (corrosion trenches and selective passivation of the binder-phase) and the influence of contact conditions on the overall wear rates.

9.2 Results and Discussion

9.2.1 Influence of contact conditions and abrasive size on wear mechanism

Figure 9.2 compares the *SWR* observed for sintered WC-5.7Co-0.3Cr and WC-10Co-4Cr coating abraded in the micro-abrasion tester and the modified ASTM G65 (macro) tester using SiC abrasives of different sizes suspended in a pH 11 slurry. For the WC-10Co-4Cr coating, the highest *SWR* is observed during the micro-abrasion test. Interestingly, the *SWR* during micro-abrasion with 4.5 μm abrasive is higher than in the macro test with 180 μm abrasive. To understand the difference in the *SWR* observed during abrasion by the micro-abrasion tester and the modified ASTM G65 tester, it is necessary to closely examine the prevalent wear mechanisms. Figure 9.3 compares the SEM micrographs of WC-10Co-4Cr coating worn using 4.5 mm SiC suspended in pH 11 NaOH in (a) micro-abrasion tester and (b) modified ASTM G65 tester. Figure 9.3a shows the random distribution of indents on the surface, typical of three-body abrasive wear. The SEM also reveals that despite the presence of directionless indents on the surface, there is preferential removal of the binder-phase around the carbide grains highlighted by the ‘moat-like’ features created around the carbide grains. The exposed carbides in the wear-scar also show some signs of fragmentation. The removal of the carbides within the wear scar appears to have occurred by the combination of preferential removal of the binder-phase around them followed by their fragmentation.

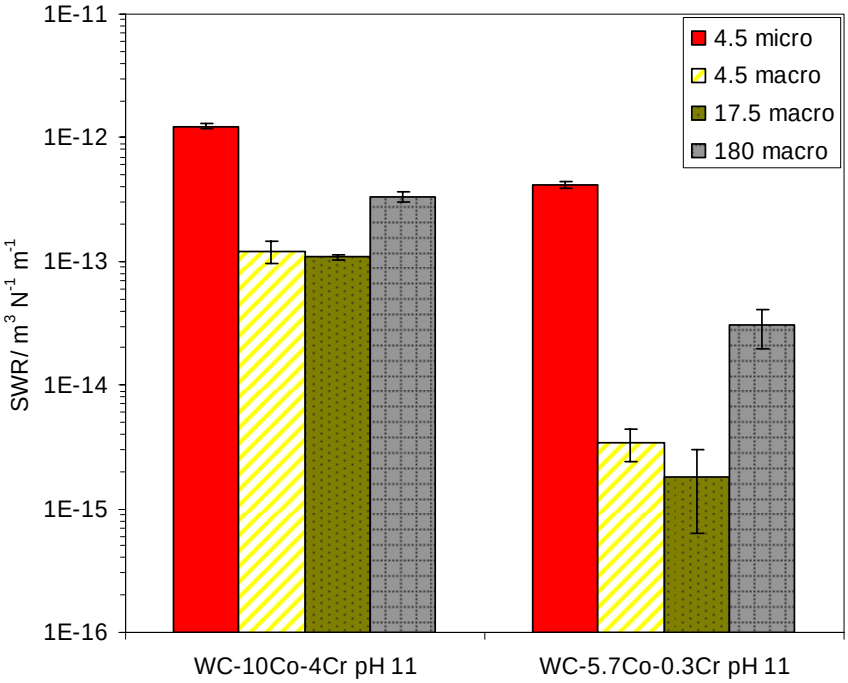

Figure 9.2: Comparison of *SWR* from micro-abrasion and G65 tests using pH 11 NaOH slurry.

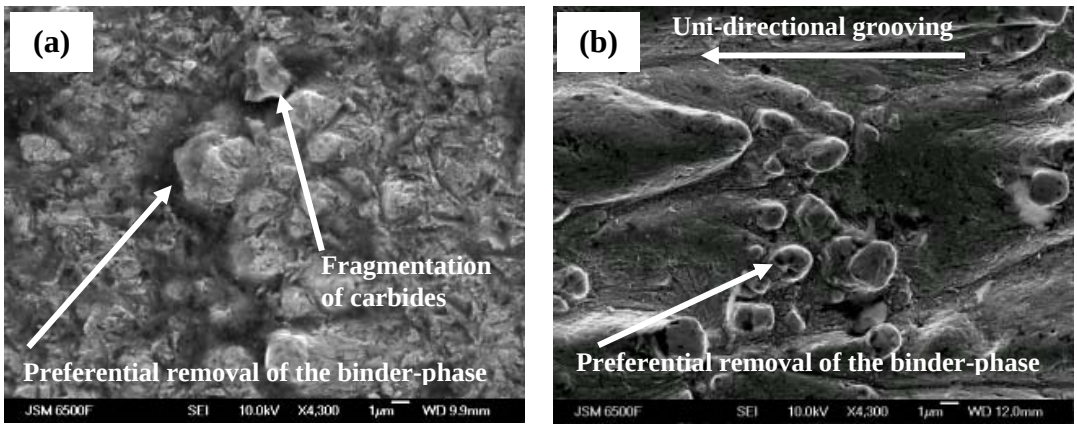

Figure 9.3: SEM micrograph of WC-10Co-4Cr coating abraded using 4.5 μm abrasives using pH 11 NaOH slurry on; (a) micro-abrasion tester showing 3-B rolling and (b) modified ASTM G65 test showing 2-B grooving mode.

Figure 9.3b shows the SEM of the worn WC-10Co-4Cr coating with 4.5 μm SiC on the modified ASTM G65 tester. The worn surface is characterised by uni-directional grooves in the direction of abrasive motion, typical of two-body abrasive wear. Interestingly, despite the different wear mode from that in the micro-scale abrasion, the exposed carbides reveal that preferential binder-phase removal and undermining of carbides appears to be the predominant wear mechanism. The presence of uni-directional binder-phase removal also suggests possible binder depletion from the flow of abrasive slurry at higher velocity likely

to be ~5 m s^{-1} (velocity of the rubber wheel = 0.9 m s^{-1}) compared to the micro-abrasion (velocity of ceramic ball = 0.05 m s^{-1}). Also, unlike micro-abrasion there is no clear evidence of fragmentation of carbides. Clearly, there is an order-of-magnitude increase in the *SWR* during micro-abrasion of WC-10Co-4Cr coating due to the difference in the abrasive particle motion in the contact (3-B rolling/ 2-B grooving) and contact conditions.

Similar differences in the *SWR* are observed for the sintered WC-5.7Co-0.3Cr, see Figure 9.2. SEM micrographs of sintered WC-5.7Co-0.3Cr abraded using 4.5 μm SiC in the micro-abrasion tester and the modified ASTM G65 tester clearly show the differences in the wear-scars, see Figure 9.4. The wear-scar from the micro-abrasion test shows severely fragmented carbides and very little evidence of the presence of binder-phase, see Figure 9.4a. The severe fragmentation of the carbides is caused by the multiple indentations of the abrasives during 3-body rolling mode of abrasion. However, the sintered WC-5.7Co-0.3Cr abraded using 4.5 μm SiC in the modified ASTM G65 tester shows greater evidence of preferential removal of the binder-phase along with some evidence of carbide grain fracture. However, unlike the WC-10Co-4Cr coating, the wear scar shows no clear evidence of uni-directional grooving. Wear occurs by the preferential removal of the binder-phase and fragmentation of exposed carbides. Clearly, an increase in the fragmentation of the carbides appears to have resulted in two orders of magnitude increase in the *SWR*.

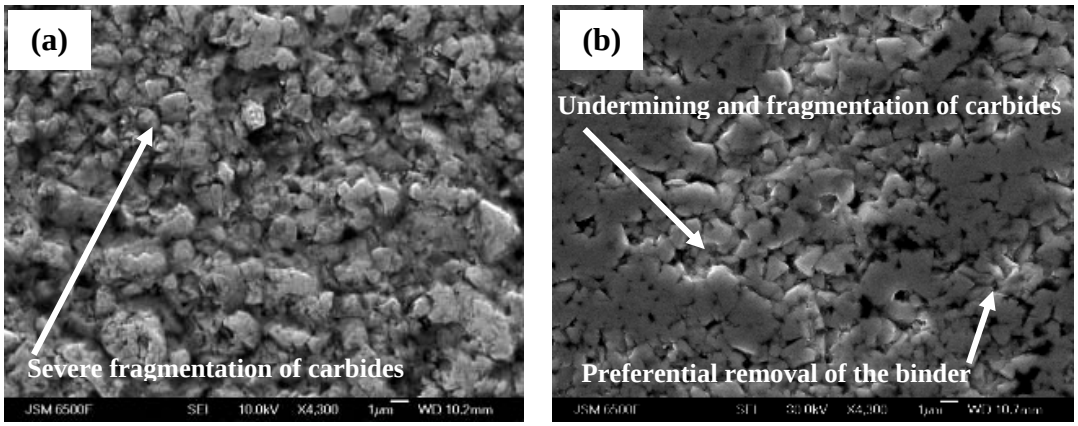

Figure 9.4: SEM micrograph of sintered WC-5.7Co-0.3Cr abraded using 4.5 μm abrasives on; (a)micro-abrasion tester and (b) modified ASTM G65 test.

To understand the overall *SWR* performance due to the change in the particle motion within the contact, it is necessary to review the factors governing them. As discussed in the Chapter 2, attempts have been made at predicting the motion of the abrasive particles within a contact. The Williams and Hyncica [48] model predicted that an abrasive particle between two surfaces undergoes a transition from rolling to grooving when the value for $D/h^* \geq 2$,

where D is the particle major axis and h^* is the separation of surfaces, see Figure 2.11, Chapter 2. However, as found by Shipway [50] and Trezona *et al.*[52] , h^* can not be determined by hydrodynamic lubrication conditions as the surfaces are not supported by a significant hydrodynamic pressure. Hence, the transition between rolling and grooving needs to be determined by the applied load and the number of particles within the contact, i.e. severity of contact as predicted for the micro-abrasion test by Adachi and Hutchings [99]. Trezona *et al.*[52] reviewed the transition between two-body and three-body abrasive wear during micro-scale abrasion and found that despite lower severity of contact, the *SWR* for three-body abrasive mechanism is always higher than that observed for two-body abrasion.

The higher *SWR* observed during micro-abrasion can be justified by the estimation of maximum contact pressure derived from the load per particle during the tests using the following assumptions:

- The shape of the abrasives is independent of its size, i.e. the angularity does not change with size.
- Close packing of the abrasives exists within the contact.
- A circular contact patch used to calculate the number of abrasives
- The contact between the abrasive and sample is Hertzian in nature, i.e. static.

Adachi and Hutchings [49] used the concept of 'interaction area' for the calculation of number of particles in the contact during micro-abrasion area. However, the interaction area was based on a static Hertzian contact between the ball and the sample and can not be applied to the area contact between the rubber wheel and the sample for the modified ASTM G65 test. Table 9-1 tabulates the load per particle and the possible contact pressures considering a Hertzian point contact between the abrasives and the sample. As shown in the Figure 9.6, the contact between the abrasives and the sample was assumed to have the same radius (1 μm) for all three abrasive sizes. Stachowiak and Batchelor [56] examined the abrasivity of different abrasives and found that wear increased with an increase in the abrasivity. In this case, since the abrasive used for all the tests is the same, it was assumed that the abrasivity and hence the contact between the abrasives and the sample was the same for all sizes. For example, in the modified ASTM G65 test, the pressure acting on the sample in the absence of abrasive particles can not possibly explain the difference in the *SWR* due to the different abrasive sizes. However, by considering the number of particles likely to be present in the contact, an increased pressure per particle is observed when using 180 μm abrasives. The contact pressures calculated using this method can explain the cracking of carbides along their slip planes observed when using 180 μm abrasives. However, in the micro-abrasion test, despite the lower contact pressures predicted, severe fragmentation of

carbides occurs. A possible reason for this is the change in the wear mode observed during micro-abrasion. While 2-B grooving abrasion occurs during the ASTM G65 test, 3-B rolling abrasion is observed during micro-abrasion. The estimation of contact conditions used here is not robust and has not accommodated factors such as the ratio between the hardness of the counterface material and the sample, which determines the motion of the abrasives in the contact (2-B or 3-B). However, it is an attempt to understand the influence of contact pressures on the *SWR* and can be used to predict wear under similar wear modes (2-B grooving or 3-B rolling).

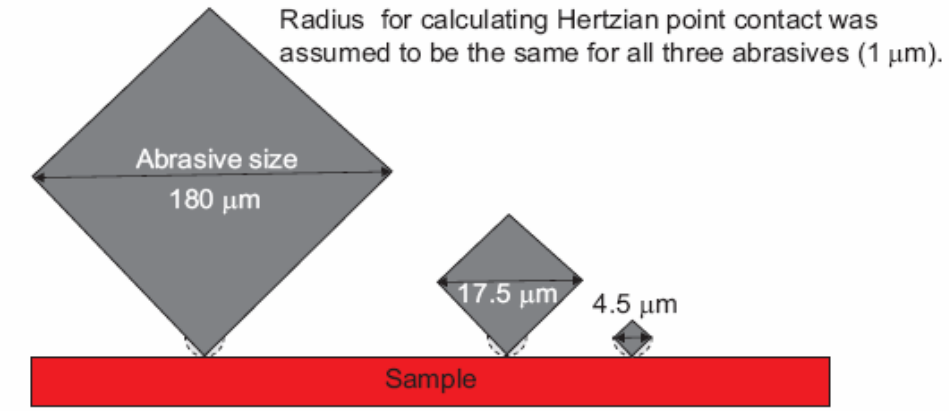

Figure 9.5: Static Hertzian point contact between abrasives and sample.

Table 9-1: Comparison of contact conditions between micro-abrasion and the ASTM G65 tests

Test	G65	G65	G65	Micro-abrasion
Abrasive size (μm)	180	17.5	4.5	4.5
Load (N)	20	20	20	0.2
Wear scar area (μm^2)	1.5×10^8	1.5×10^8	1.5×10^8	3.8×10^5
Number of abrasives in contact *	6×10^3	6.25×10^5	9.3×10^6	2.3×10^4
Load per particle (N)	3.3×10^{-3}	3.2×10^{-5}	2.0×10^{-6}	9×10^{-6}
Max. contact pressure without abrasives (MPa)	5.5	5.5	5.5	200**
Max. contact pressure per abrasive** (GPa)	**70**	**15**	**6**	**10**

** Assuming closed packing*

*** Hertzian point contact, see Figure 9.5*

9.2.2 Influence of contact conditions and abrasive size on wear-corrosion interactions after exposure to pH 11 NaOH

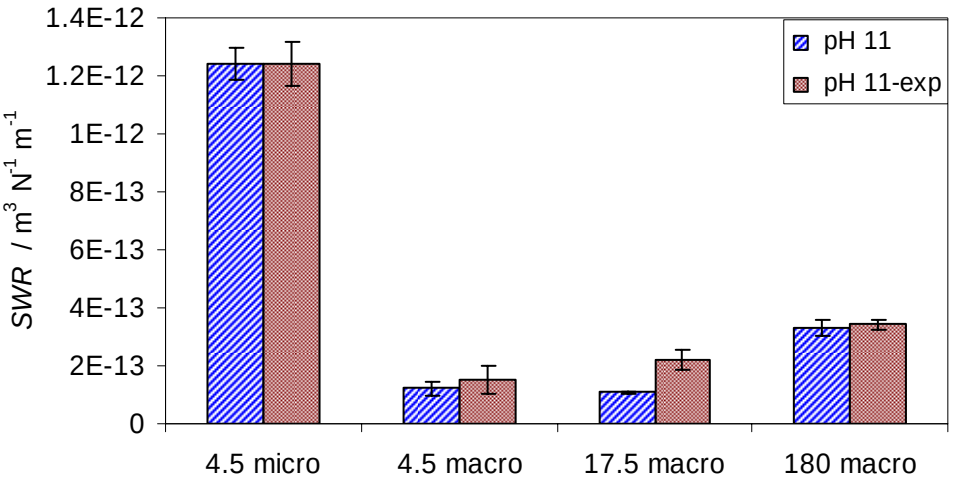

Figure 9.6: pH 11 and pH 11-exp samples of WC-10Co-4Cr coating abraded on the micro-abrasion tester and the modified ASTM G65 using NaOH based slurries.

Figure 9.6 shows the *SWR* for pH 11 and pH 11-exp samples of WC-10Co-4Cr coating. Interestingly, while a similar *SWR* was observed for pH 11 and pH 11-exp samples during micro-abrasion, there appears to be a slight increase in the *SWR* for pH 11-exp samples during abrasion in the modified ASTM G65 test, particularly when using 4.5 μm and 17.5 μm abrasives. The observed trends can be explained by the effects of observed wear mechanisms on the depth of wear and the depth of corrosion attack due to exposure. As discussed in Chapter 6, the depth of corrosion attack in the WC-10Co-4Cr coating due to exposure to pH 11 NaOH solution is one-carbide deep (3-5 μm). However, as observed in Chapters 6 and 7, the wear-scar in the micro-abrasion test rapidly grows in depth and the corrosion affected region on the sample surface is abraded early in the test. As shown in the Figure 9.6, the wear-scar is relatively localised with an average area of 1.1 mm^2 and the wear-scar depth increases rapidly as the test progresses. This results in the corrosion trenches present on the surface after exposure being unable to influence the final *SWR* and therefore the pH 11 and pH 11-exp samples having similar *SWR*.

However, unlike the micro-abrasion test, the wear scar on the modified ASTM G65 test increases in area as the test progresses with an average wear scar area of 225 mm^2. Interestingly after 942 m of sliding, the depth of the wear scar is less than that observed after micro-abrasion for 37.8 m of sliding, see Figure 9.6 and Figure 9.7. Hence, the influence of corrosion trenches will be greater during the abrasion on the modified ASTM G65 tester,

depending on the wear mechanism observed. As discussed in the Chapter 8, for both 4.5 μm and 17.5 μm abrasives, the wear mechanism observed is predominantly grooving of the binder-phase along with the undermining and fragmentation of exposed carbides. Hence, the presence of loosely held carbides in the corrosion trenches is expected to result in their accelerated removal resulting in a slight increase in the *SWR* for pH 11-exp samples. However, as the mechanism observed for 180 μm abrasives is dependent on the formation and propagation of lateral cracks / fracture toughness of the coating, the presence of corrosion trenches on the surface do not significantly influence the *SWR* .Hence, pH 11 and pH 11-exp samples have very similar *SWR*.

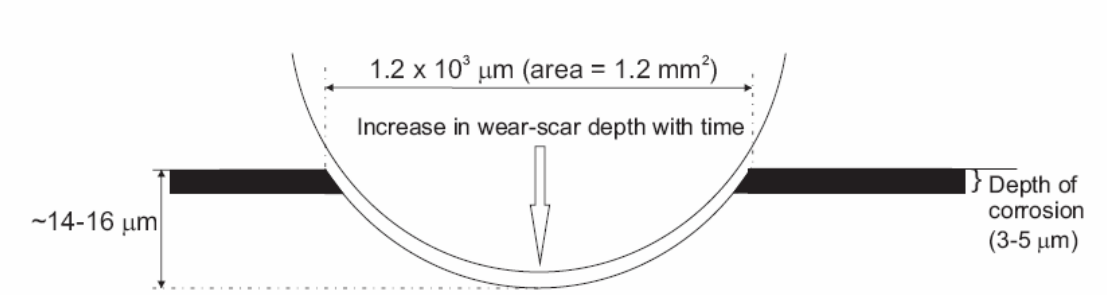

Figure 9.7: Influence of corrosion features on pH 11-exp surface on micro-abrasion (sliding distance =37.8 m, applied load = 0.2 N).

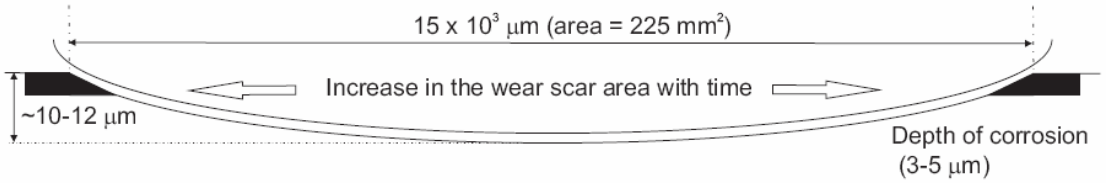

Figure 9.8: Influence of corrosion features on pH 11-exp surface during abrasion with 4.5 μm abrasives on the modified ASTM G65 test (sliding distance = 942 m, applied load = 20 N).

Figure 9.8 compares the *SWR* observed for pH 11 and pH 11-exp samples for sintered WC-5.7Co-0.3Cr abraded in the micro-abrasion tester and the modified ASTM G65 tester. The *SWR* observed for pH 11 and pH 11-exp samples during micro-abrasion is very similar. As observed from the SEM analysis of pH 11-exp samples in Chapter 6, there is no evidence of preferential binder-dissolution and / or weakening of the carbide structure due to exposure. Also, as discussed in Chapter 6, presence of $Co(OH)_2$ oxide film was detected on the binder phase in the pH 11-exp sintered WC-5.7Co-0.3Cr. As discussed in section 9.2.1, the wear mechanism during micro-abrasion is strongly dependent on the three-body indentation causing severe fragmentation of the carbides and their removal by subsequent abrasion. As the wear mechanism is not influenced by the exposure to alkaline conditions, *SWR* for pH 11

and pH 11-exp samples are similar Also, as observed for the micro-abrasion of the WC-10Co-4Cr coating, the rapid increase in the depth of the wear-scar means no or little influence by pre-exposure being observed.

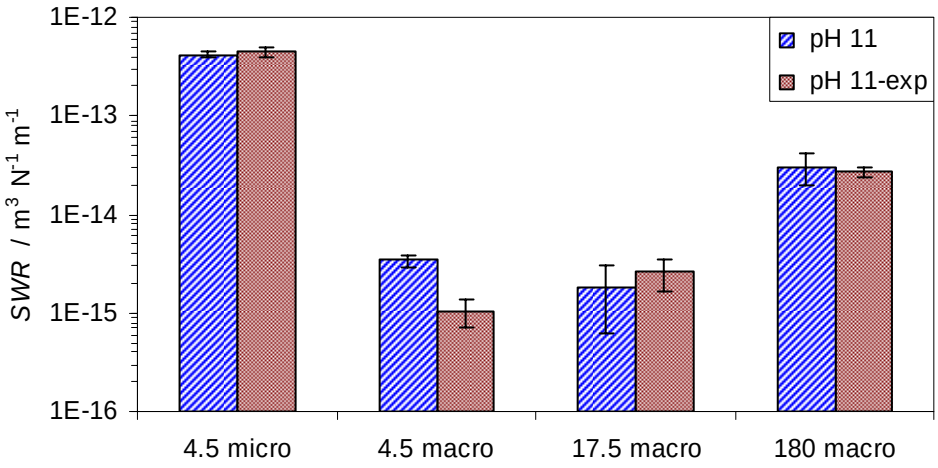

Figure 9.9: pH 11 and pH 11-exp samples of sintered WC-5.7Co-0.3Cr abraded on the micro-abrasion tester and the modified ASTM G65 using NaOH based slurries.

As discussed in Chapter 8, the wear mechanism observed for 4.5 μm SiC is the preferential depletion of the binder-phase resulted in the undermining and fragmentation of the carbide grains. Exposure to pH 11 NaOH solution results in selective passivation of the binder phase and formation of $Co(OH)_2$. The passive oxide film on the binder-phase may reduce friction [35, 73] and lead to a decrease in the preferential binder-phase removal. Consequently, a lower *SWR* is observed for pH 11-exp samples abraded using 4.5 μm SiC. However, the same is not the case with sintered WC-5.7Co-0.3Cr samples abraded using 17.5 μm and 180 μm abrasives. The *SWR* for pH 11 and pH 11-exp samples are similar, due to the wear-mechanism being different than that observed for 4.5 μm SiC. As discussed in Chapter 8, removal of the binder-phase by 17.5 μm and 180 μm abrasives occurs by extrusion between the carbide grains due to the compressive stresses induced in the carbide structure. The SEM micrographs of worn samples revealed that the subsequent fragmentation of carbides causes the bulk of the damage. Hence, *SWR* for pH 11 and pH 11-exp are not influenced by the effects of exposure to a pH 11 NaOH solution.

9.2.3 Conclusions

- For the WC-10Co-4Cr coating, multiple indentation of the binder-phase and the fragmentation of carbides observed when using 4.5 μm SiC in the micro-abrasion tester results in an order of magnitude increase in *SWR* compared to the preferential removal of the binder and undermining of carbides observed for 4.5 μm SiC in the modified ASTM G65.

- For the sintered WC-5.7Co-0.3Cr, severe fragmentation was observed during micro-abrasion with 4.5 μm SiC resulting in two orders of magnitude increase in *SWR* compared to the preferential depletion of the binder-phase and undermining of carbides observed in the modified ASTM G65 test using 4.5 μm SiC. Clearly, the increase in the fragmentation of the carbides on the surface causes this order of magnitude increase in wear.

- For both sintered and sprayed samples, abrasive wear by multiple indentations (3-B rolling) produces more severe damage than grooving wear.

- Clearly, the presence of corrosion-trenches on the WC-10Co-4Cr coating surface results in the lowering of the wear resistance of the affected region (1-carbide deep). However after the removal of the corrosion affected zone by subsequent abrasion, the wear resistance is similar to a fresh (pH 11) sample. The effects of increase in the corrosion rate (depth of attack) on the wear-corrosion performance of the WC-10Co-4Cr coating need to be explored.

- Interestingly, there is a slight improvement in the wear resistance of the corrosion affected region (1-carbide deep) in sintered WC-5.7Co-0.3Cr exposed to pH 11, possibly due to the lowering of friction due to the presence of $Co(OH)_2$ oxide film which decreases the preferential binder removal. However, as in the case of the sprayed coating, after the removal of the corrosion affected zone the wear resistance is similar to the fresh (pH 11) sample.

- In highly loaded contacts the mechanical damage always supersedes the electrochemical damage and hence protection against corrosion is not an important factor. However, due to the higher contact pressures observed in such cases, the use of sintered hardmetals / coatings with high hardness may be beneficial.

- In evenly distributed contacts, large areas of interaction result in the corrosion observed on the surface increasing the overall wear and the use of a more corrosion resistant binder / coating may lower the overall wear rates further.

10 Conclusions and further work

10.1 Introduction

This thesis describes the work carried out to mimic wear-corrosion interactions in downhole conditions and investigates the wear-corrosion performance of candidate downhole materials, i.e. WC-based sintered hardmetals and sprayed coatings in neutral and alkaline conditions. Typical downhole conditions expose these materials to alkaline conditions between pH 9 and 11 for long durations and abrasives of different sizes resulting in severe wear-corrosion.

State-of-the-art understanding of wear-corrosion interactions of WC-based hardmetals and coatings at the beginning of this project:

- Previous work done on wear-corrosion of WC-based hardmetals and coatings was focussed on acidic and neutral conditions and these resulted in large positive wear-corrosion interactions (100% increase in wear using a pH 1.1 abrasive slurry).
- According to the ASTM standards [131] for determining synergism between wear and corrosion, neutral conditions were assumed to be 'corrosion free' and used as 'benchmark-conditions' for calculating wear-corrosion interactions.
- Abrasive size effect has been previously investigated for single-phase materials. However, these effects cannot be applied for metal matrix composites due to the presence of hard and soft phases which are expected to react differently during abrasion.
- Some understanding of corrosion of WC-based sintered materials had been achieved and Hochstrasser [105] proposed a model for corrosion interactions between the WC-phase and metallic binder in neutral, acidic and alkaline environments.
- The corrosion in the WC-based coatings was identified using SEM analysis [113, 151]. Intense localised corrosion (corrosion trenching) around WC grains was observed during potentiodynamic polarisation tests in 3.5 % NaCl [113]. It was understood that due to the discontinuous passive film present on the binder-rich areas, corrosion is initiated at the binder-carbide interface and progresses towards the carbide as well as the binder [117].

Present work:

- Improved the understanding of the effects of prolonged exposure to pH 7 distilled water and pH 11 NaOH conditions.
- Developed a novel technique for *in situ* electrochemical measurements during micro-abrasion for understanding the corrosion kinetics occurring during micro-abrasion.
- Investigated the size effect of abrasives on the wear-corrosion of WC-based sintered hardmetals and coatings.

10.2 Exposure to pH 11 NaOH and pH 7 distilled water

- Prolonged exposure to pH 7 distilled water and pH 11 NaOH resulted in the formation of trench-like features around carbide grains in the WC-based coating. These corrosion trenches have been examined in detail and the corrosion mechanisms were predicted by adapting the Hochstrasser model [106]. This is the first time that the corrosion trenches have been observed and investigated under open circuit conditions.

- FIB sectioning of WC-10Co-4Cr coating exposed to pH 11 NaOH reveals that the depth of preferential corrosion of metallic W is one-carbide deep and results in the carbide grain being loosely held in the corrosion trench. Also, accelerated anodic treatment of the WC-10Co-4Cr coating revealed that the corrosion trench propagates towards the centre of the carbide grain and not towards the binder-phase as previously reported in the literature.

- Prolonged exposure to pH 7 distilled water resulted in the preferential dissolution of the binder-phase in the sintered WC-based hardmetal. However, no such effects are observed in pH 11 NaOH solution. The Hochstrasser model [106] developed for sintered WC-Co hardmetals has been adapted to explain the local change in pH which causes preferential dissolution of the binder-phase in pH 7 distilled water.

- The formation of corrosion trenches in WC-10Co-4Cr coating and the preferential binder dissolution observed for sintered WC-5.5Co-0.3Cr in pH 7 distilled water indicate that wear tests conducted in distilled water should not be considered as ‘pure abrasion’ and questions the use of ASTM standards [131] for determining synergism between wear and corrosion for WC-based sintered hardmetals and coatings.

10.3 Micro-abrasion using *in situ* electrochemical current noise measurements:

- For the first time, a modified micro-abrasion tester capable of *in situ* electrochemical measurements has been developed and used to study the wear-corrosion of WC-based sintered hardmetals and sprayed coatings. This technique has been successfully used to quantify the mechanical and electrochemical performance during micro-scale wear-corrosion in the pH range between 7 and 13.

WC-10Co-4Cr coating:

- The overall wear mechanism observed during micro-abrasion of the WC-based coatings is the preferential removal of the binder-phase due to multiple indentations by abrasives and breaking-away of exposed carbides as shown in the Figure 10.1. The use of *in situ* electrochemical measurements enables the quantification of wear and corrosion in the 'z' direction (depth wise). The electrochemical response during wear suggests that the mechanical damage always dominates the corrosion occurring on the surface, see Figure 10.1

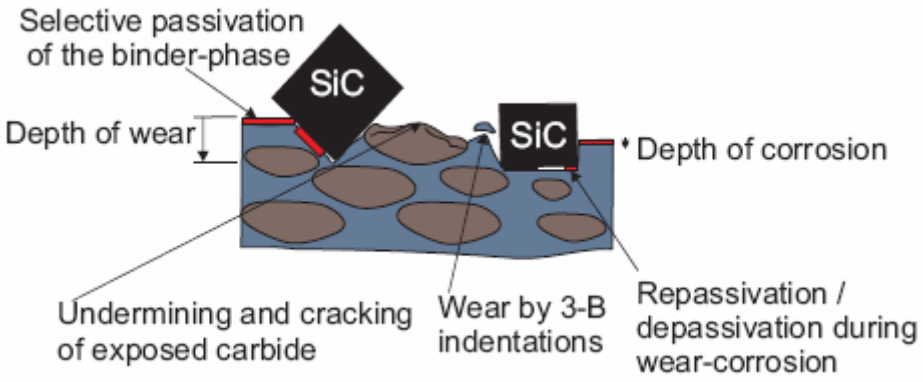

Figure 10.1: Schematic showing the micro-scale wear-corrosion mechanism for the WC-10Co-4Cr coating.

- However, the rate of repassivation of the binder-phase appears to influence the rate of binder-phase removal by altering the stiffness of the abrasive-surface contact and lowering the friction between abrasives and the surface. This was also corroborated by the relationship between electrochemical and mechanical wear, which showed that mechanical wear increased with an increase in the electrochemical wear. Low electrochemical wear was observed under pH 11 conditions due to a high repassivation rate of the binder-phase and leads to a corresponding decrease in the rate of binder-removal and a reduction in overall wear rates. The high repassivation

rates observed for the coating were also corroborated by the instantaneous repassivation of the wear scar at the end of the micro-abrasion test.

- The passivation / corrosion states of Co and W predicted by Pourbaix diagrams were found to be accurate and were validated using XPS and SEM analysis. Figure 10.2 superimposes the Pourbaix diagram for Co on the SWR *vs.* pH graph and highlights the influence of corrosion / passivation of the binder-phase on the wear-corrosion rates during micro-abrasion.

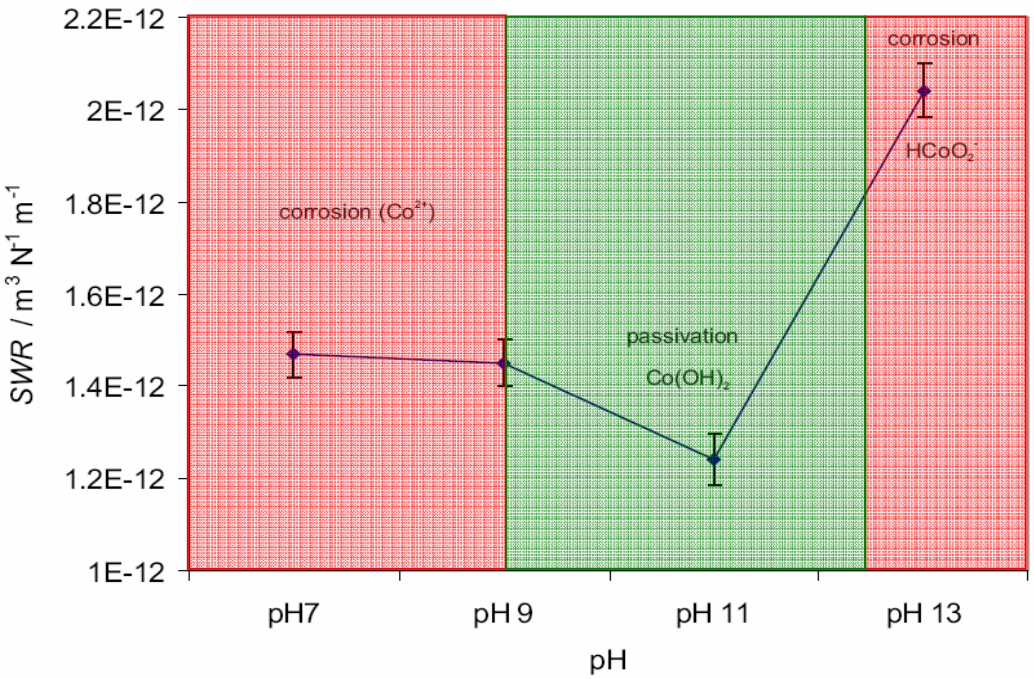

Figure 10.2: Influence of passivation of Co-binder on the *SWR* trend observed for WC-10Co-4Cr coatings between pH 7 and 13.

Sintered WC-5.7Co-0.3Cr:

- Wear-corrosion of the sintered hardmetal occurred by the extrusion of the binder-phase between the carbide grains as predicted by the Larsen Basse model [73] and the subsequent cracking of carbides, see Figure 10.2. The *in situ* electrochemical current noise measured during micro-abrasion showed that there is no significant repassivation occurring within the wear scars resulting in higher corrosion during micro-abrasion, due to the absence of discrete binder-rich regions. However, as in the case of the WC-10Co-4Cr coating, the attack in 'z' direction reveals that wear dominates corrosion occurring at the surface . As the wear mechanism controlled by the cracking of the carbide grains (see Figure 10.3), the variation of the pH between 7 and 11 does not influence the overall wear rates. However, pH 13 conditions result in

an increase in the dissolution of the binder-phase and a consequential increase in the overall wear rates.

- Also, the worn sintered surface reveals the presence of crevice-type corrosion features. Active electrochemical dissolution of the binder-phase occurs within these features as detected by the current-noise measurements at the end of the wear test. This electrochemical activation of the sintered hardmetal is likely to adversely affect its subsequent wear resistance. Hence intermittent use of components made from sintered hardmetals is likely to accelerated wear and shorten component life.

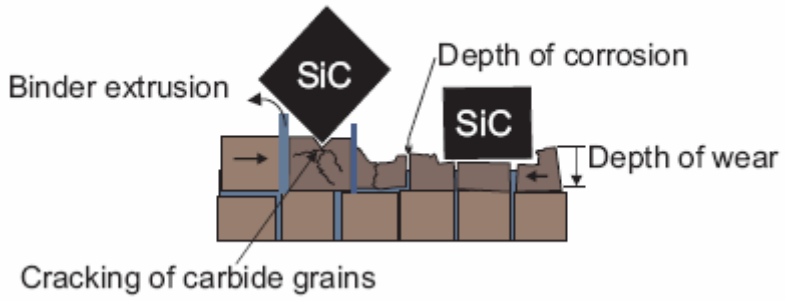

Figure 10.3: Schematic showing the micro-scale wear-corrosion mechanism for the sintered WC-5.7Co-0.3Cr.

10.4 Micro-macro testing and the size effect of abrasives

For the first time, the size effect of abrasives has been studied for WC-based sintered hardmetals and sprayed coatings. Table 10-1 and 10-2 show the wear mechanisms determined under different contact conditions and with different abrasive sizes.

Table 10-1: Micro-scale abrasive wear mechanisms observed for sintered WC-5.7Co-0.3Cr and WC-10Co-4Cr coating

4.5 μm	**Binder**	**Carbide**
Sintered WC-5.7Co-0.3Cr	Extrusion (3-B indentation)	fragmentation and subsequent removal
WC-10Co-4Cr coating	Preferential removal (3-B indentation)	fragmentation and subsequent removal

Table 10-2: Macro-scale abrasive wear mechanisms observed for sintered WC-5.7Co-0.3Cr and WC-10Co-4Cr coating

4.5 μm	**Binder**	**Carbide**
Sintered WC-5.7Co-0.3Cr	Preferential removal (2-B grooving).	Fragmentation / undermining and subsequent removal.
WC-10Co-4Cr coating	Preferential removal (2-B grooving).	Undermining and subsequent removal.
17.5 μm	**Binder**	**Carbide**
Sintered WC-5.7Co-0.3Cr	Extrusion (2-B grooving).	Undermining / fragmentation and subsequent removal.
WC-10Co-4Cr coating	Preferential removal (2-B grooving).	Fragmentation and subsequent removal.
180 μm	**Binder**	**Carbide**
Sintered WC-5.7Co-0.3Cr	Extrusion (2-B grooving).	Fragmentation and subsequent removal.
WC-10Co-4Cr coating	Lateral cracking of the coating leads to its removal in splat-sized debris.	

WC-10Co-4Cr coating:

- The behaviour of the coating does not conform to the current understanding of the size effects. Unlike the single-phase ductile materials, complicated and strongly depends on the ability of the coating to plastically deform without the formation of sub-surface cracks.

- The extent of sub-surface cracking in the coating increases with the size of abrasives and leads to the delamination of the coating due to propagation of lateral cracks. Doubling of wear results from the delamination of the coating and its removal in the form of splat-size debris and is strongly dependent on the lateral fracture toughness of the coating as can be seen from the Figure 10.4.

Sintered WC-5.7Co-0.3Cr:

- It was found that the response of the sintered WC-5.7Co-0.3Cr strongly depends on the ability of the binder-phase to resist plastic formation and the ability of the carbides to resist fracture. An increase in the extent of cracking in the carbide grains increases with the abrasive size. An order of magnitude increase in wear results from the extensive cracking and the subsequent removal of the carbide grains as shown in Figure 10.4.

- The behaviour of WC-based hardmetals is very different from the single-phase materials studied previously. An increase in abrasive size causes a change in wear mechanism and leads to an abrupt increase in wear (order of magnitude). In addition to the size of abrasives the wear rates are dependent on the overall wear mechanisms.

This investigation also found that Archard's law cannot be used directly as inhomohenity in the coating leads to variation in the wear rates. A change in wear mechanism observed with change in the abrasive size, in not accommodated by Archard's law. A change in the wear mode from 2-B grooving to 3-B rolling results in an order of magnitude increase in the wear rates and can not be explained by Archard's law as shown in Figure 10.4.

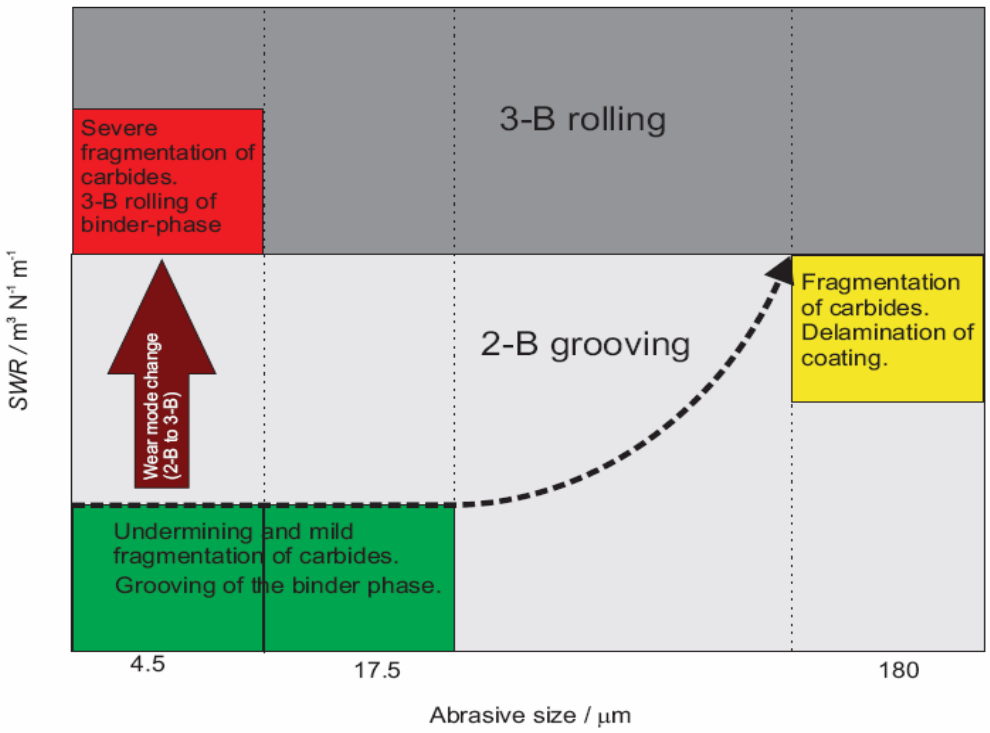

Figure 10.4: Influence of wear mode (2-B grooving / 3-B rolling) and carbide fragmentation on the *SWR* for WC-based sintered WC-5.7Co-0.3Cr and WC-10Co-4Cr coating.

10.5 Recommendations for improving wear-corrosion resistance of WC-based hardmetals and coatings

- Highly stressed contact conditions result in the maximum wear and avoiding such contacts is expected to result in a lowering of wear.
- For both sintered hardmetals and sprayed coatings, an increase in the abrasive size leads to a sharp increase in the wear rates. Improvement in the performance of hardmetals can be achieved by preventing large (< 20 μm) abrasives from being recirculated in the system.
- Maintaining the pH of the drilling fluid close to pH 11 is likely to result in the lowest wear-corrosion in the WC-based coatings.
- Lowering the amount of metallic W dissolved in the binder-phase is likely to results in improving the coating fracture toughness. This would inhibit the formation and propagation of lateral cracks and lower the possibility of wear due to delamination of the coating. Options such as cold spraying of the coating for added corrosion resistance need to be explored. This is expected to better control the dissolution of W in the coating during the spray process.

- Corrosion does not appear to strongly influence the performance of the sintered hardmetal. Having a wear resistant binder is likely to result in more benefits than having a corrosion resistant binder-phase.
- Removal of the binder-phase by extrusion and preferential depletion of the binder-phase can be lowered by increasing the shear strength of the binder-phase.
- Reducing the size of carbide grains used for sintered hardmetals to less than 1 μm (nano-sized) in size is also likely to result in lower binder extrusion as well as reducing cracking of the carbides. The wear-corrosion behaviour of such hardmetals needs to be explored for application in downhole conditions.

10.6 Further work

- Micro-abrasion with *in situ* electrochemical measurements is an excellent tool for studying the wear-corrosion interactions occurring during micro-abrasion of multi-phase materials under different pH conditions and this work should be extended to study the influence of increased corrosion rates on the wear-corrosion interactions.

- Lack of repassivation and the creation of 'crevice-type' corrosion processes on an abraded sintered hardmetal need further investigation. The influence of localised corrosion occurring on the abraded surface on subsequent abrasive wear needs to be assessed.

- The wear-corrosion performance of sprayed coatings with varying binder-content needs to be examined to better understand the influence of selective passivation of the binder-phase and its influence on the overall wear-corrosion interactions.

- Further work should be aimed at incorporating high-temperature / high pressure slurry during wear-corrosion testing. Possible uses of drilling fluids as abrasive slurry also need to be explored.

- Further work should be aimed at populating the size effect of abrasives on the wear of WC-based sintered hardmetals and coatings. Further work also needs to examine the size effect of abrasives on sintered hardmetals with nano-sized carbide grains.

APPENDIX 1

Table A1: Commonly used reference electrodes for electrochemical tests at 20 ^{o}C

Name	Symbol	Electrode	Potential, V-SHE
Standard Hydrogen Electrode	SHE	(Pt)H_2 (a=1)/H^+ (a=1)	0.000
Saturated Silver/ Silver Chloride	Sat Ag/AgCl	Ag/AgCl/SAT KCl	+ 0.196
1 M Silver/Silver Chloride	1 M Ag/AgCl	Ag/AgCl/1 M KCl	+ 0.235
0.6 M Silver/Silver Chloride	0.6 M Ag/AgCl	Ag/AgCl/0.6 M KCl	+ 0.250
0.1 M Silver/Silver Chloride	0.1 M Ag/AgCl	Ag/AgCl/0.1 M KCl	+ 0.288
Saturated Calomel Electrode	SCE	Hg/Hg_2Cl_2/SAT KCl	+ 0. 242
1 M Calomel Electrode		Hg/Hg_2Cl_2/1 M KCl	+ 0.280
0.1 M Calomel Electrode		Hg/Hg_2Cl_2/0.1 M KCl	+ 0.334
Copper/ Copper Sulphate	CSE	Cu/sat $CuSO_4$	+ 0.314

Passivation time calculation for WC-10Co-4Cr coating and sintered WC-5.7Co-0.3Cr:

Figure A-1 shows the *It* curves for pH 11 samples of WC-10Co-4Cr coating and sintered WC-5.7Co-0.3Cr. Due to the instantaneous passivation of the coating, six data points were used for the second order exponential decay. Alternatively, for the sintered WC-5.7Co-0.3Cr, due to the relatively slow passivation rate, 120 data points were available before the current values remained constant.

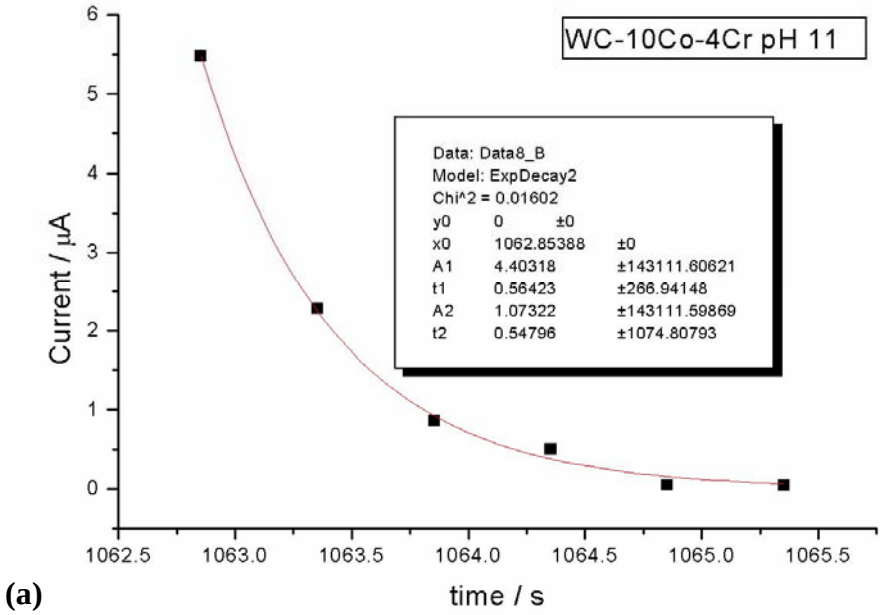

(a)

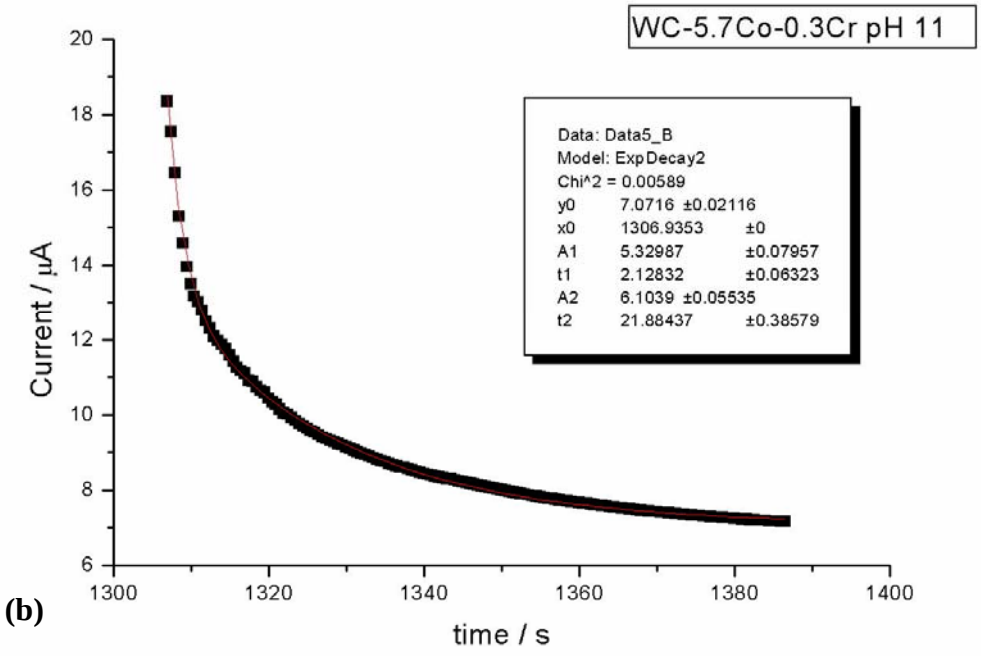

(b)

Figure A-1: Time taken for passivation calculated by fitting a second order exponential decay to the *It* curves at the end of micro-abrasion test for (a) WC-10Co-4Cr coating and (b) sintered WC-5.7Co-0.3Cr.

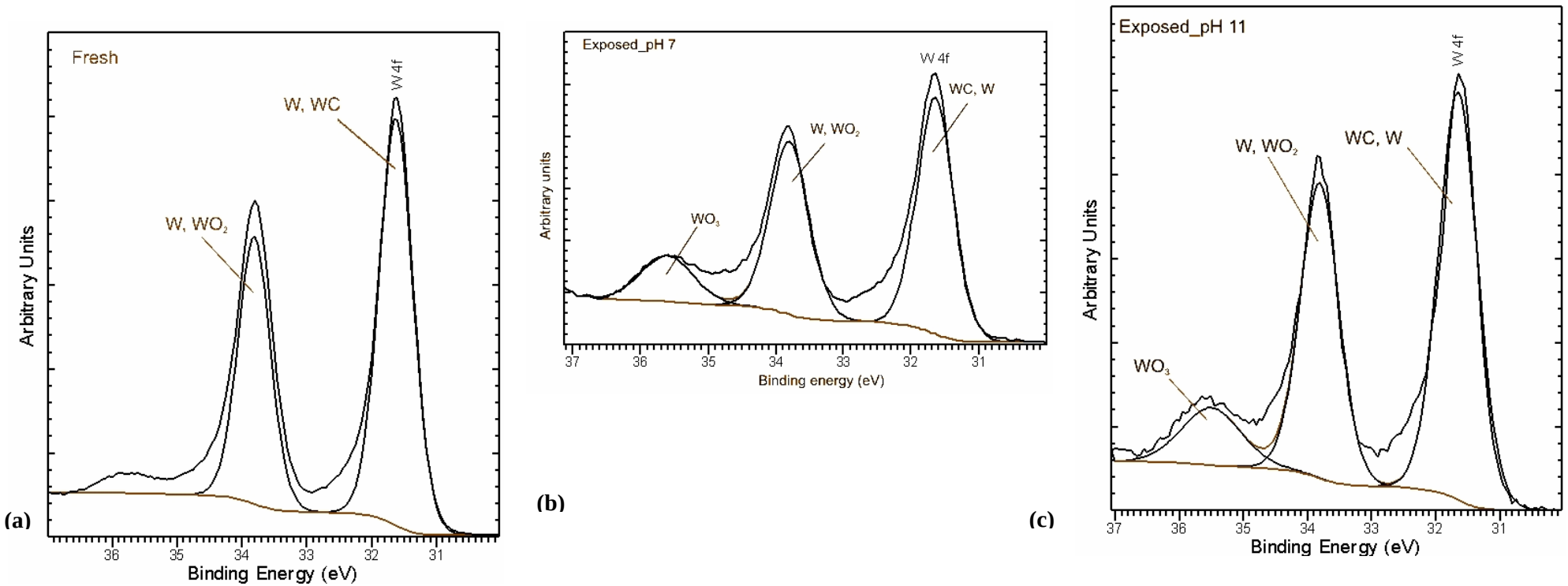

Figure A-2: XPS of W(4f) peak from the surface of WC-10Co-4Cr coating (a) fresh, (b) exposed to pH 7 and (c) exposed to pH 11.

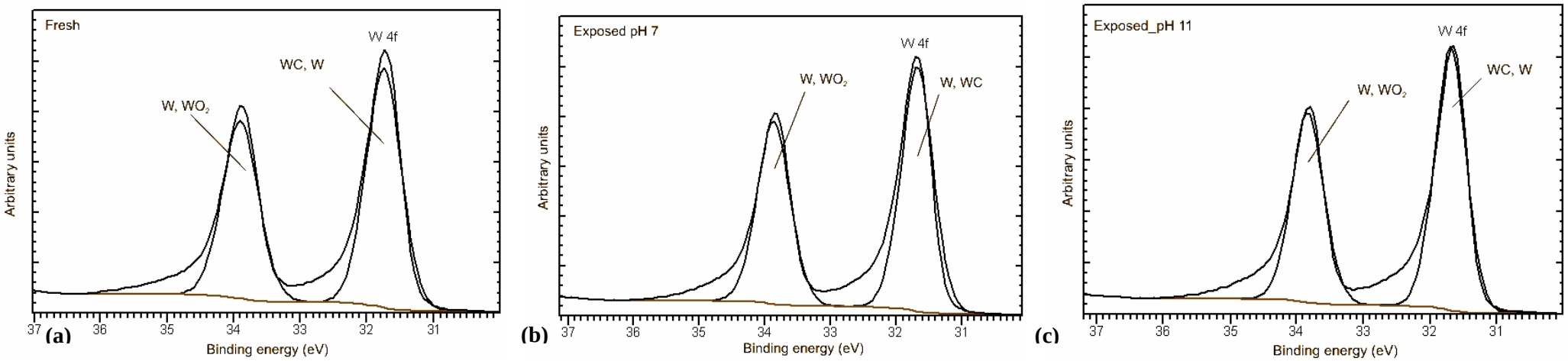

Figure A-3: XPS of W(4f) peak from the surface of sintered WC-5.7Co-0.3Cr (a) fresh, (b) exposed to pH 7 and (c) exposed to pH 11.

REFERENCES

1. I.M. Hutchings, Tribology: Friction and Wear of Engineering Materials 1992 Edward Arnold, London.
2. S. Maw, Industrial Wear Survey: Guide to wear testing requirements, in UK Forum on Friction and Wear Testing. 1997: NPL, Teddington, London.
3. M.J. Neale and M. Gee, Guide to Wear Problems and Testing for Industry. Tribology in Practice, ed. M.J. Neale, T.A. Polak and C.M. Taylor 2000 Professional Engineering Publication, London.
4. D. Dowson, History of Tribology, ed. Longman 1979.
5. Minutes of meeting with Schlumberger Oilfield UK plc.-Private communication. Feb. 2005, Stonehouse Technology Centre, Schlumberger Oilfield UK plc.: Stonehouse.
6. Minutes from 18th-19th April 2005 visit to Stonehouse Technology Centre- Private communication. April 2005.
7. E.O. Cobo, R.A. Suarez Baldo and J.B. Bessone, Corrosion of chromium plated rotor in drilling fluid, Surface Coatings and Technology 122 (1999) 39-49.
8. S. Muttoni, Abrasion Wear of Downhole Oil Well Drilling Materials- 3rd year project, in School of Engineering Sciences. 2005, University of Southampton: Southampton.
9. Z. Yao, J.J. Stiglich and T.S. Sudarshan, Nano-grained Tungsten Carbide-Cobalt (WC/Co), Materials Modification, Inc.
10. W. Dawihl and B. Frisch, Wear properties of tungsten carbide and aluminium oxide sintered materials, Wear 12 (1968) 17-25.
11. C.J. Smithells, Tungsten-A treatise on its metallurgy, properties and applications. 3rd ed 1952 Chapman and Hall Ltd., London.
12. K.T. Kembaiyan and K. Keshavan, Combating severe fluid erosion and corrosion of drill bits using thermal spray coatings, Wear 186-187 (1995) 487-492
13. J. Larsen-Basse, Wear of hard-metals in rock drilling: A survey of the literature, Powder Metallurgy 16 (31)(1973) 1-32.
14. U. Beste, T. Hartzell, H. Engqvist and N. Axen, Surface damage on cemented carbide rock-drill buttons, Wear 249 (2001) 324-329.
15. H.E. Exner, Physical and chemical nature of cemented carbides, Int. Met. Rev. 4 (1979) 149-173.
16. N. Axen and B. Lundberg, Abrasive wear in intermediate mode of multiphase materials, Tribology International 28 (8)(1995) 523-529.

17. H. Saito, A. Iwabuchi and T. Shimizu, Effects of Co content and WC grain size on the wear of WC cemented carbide, Wear 261 (2006) 126-132.
18. J. Larsen-Basse, Effect of Composition, Microstructure and Service Conditions on the Wear of Cemented Carbides, Journal of Metals (November 1983) 35-42.
19. D.G.F. O'Quigley, S. Luyckx and M.N. James, An empirical ranking of a wide range of WC-Co grades in terms of their abrasion resistance measured by the ASTM standard B611-85 test, International Journal of Refractory Metals and Hard Materials 15 (1996) 73-79.
20. D.G.F. O'Quigley, S. Luyckx and M.N. James, New results on the relationship between hardness and fracture toughness of WC-Co hardmetal, Materials Science and Engineering A209 (1996) 228-230.
21. K. Jia, T.E. Fischer and B. Gallois, Microstructure, hardness and toughness of nanostructured and conventional WC-Co composites, Nanostructured Materials. 10 (5)(1998) 875-891.
22. V. T. Golovchan and N.V. Litoshenko, On the contiguity of carbide phase in WC–Co hardmetals International Journal of Refractory Metals and Hard Materials 21 (5-6)(2003) 241-244.
23. J. Gurland, The measurement of grain contiguity in two-phase alloys, Trans. AIME 212 (1958) 452-455.
24. S. Luyckx and A. Love, The dependence of the contiguity of WC on Co content and its independence from WC grain size in WC-Co alloys, International Journal of Refractory Metals and Hard Materials 24 (1-2)(2006) 75-79.
25. H. E. Exner and J. Gurland, A review of parameters influencing some mechanical properties of tungsten carbide-cobalt alloys, Powder Metallurgy 13 (25)(1970) 13-31.
26. T. Sudaprasert, P.H. Shipway and D.G. McCartney, Sliding wear behaviour of HVOF sprayed WC-Co coatings deposited with both gas-fuelled and liquid fuelled systems, Wear 255 (2003) 943-949.
27. R.J.K. Wood, B.G. Mellor and M.L. Binfield, Sand erosion performance of detonation gun applied tungsten carbide/cobalt-chromium coatings, Wear 211 (1997) 70-83.
28. R.C. Tucker, Thermal Spray Coatings, in ASM Handbook for Surface Engineering, C.M. Cotell, J.A. Sprague and J. F.A. Smitd, Editors. 1999 ASM International Ohio, US.
29. C. Verdon, A. Karimi and J. Martin, A study of high velocity oxy-fuel thermally sprayed tungsten carbide based coatings. Part I: Microstructures, Materials Science and Engineering A246 (1998) 11-24.

30. D. Stewart, P. Shipway and D.G. McCartney, Microstructural evolution in thermally sprayed WC-Co coatings: Comparison between nanocomposite and conventional starting powder, Acta Materialia 40 (2000) 1596-1604.
31. M. Vinayo, F. Kassabji, J. Guyonnet and P. Fauchais, Plasma sprayed WC-Co coatings: Influence of spray conditions (atmospheric and low pressure plasma spraying) on the crystal structure, porosity and hardness, Journal of Vacuum Science and Technology A3 (6) (1985) 2483-2489.
32. J.M. Guilemany, J.M.d. Paco, J. Nutting and J.R. Miguel, Characterisation of W_2C phase formed during HVOF spraying of a WC-12Co powder, Metallurgical and Materials Transactions A (1999) 1913-1921.
33. J. Pina, A. Diasb and J. Lebrun, Study by X-ray diffraction and mechanical analysis of the residual stress generation during thermal spraying, Materials Science and Engineering A 347 (1-2)(2003) 21-31.
34. A. Ibrahim and C.C. Berndt, Fatigue and deformation of HVOF sprayed WC–Co coatings and hard chrome plating, Materials Science and Engineering: A 456 (1-2)(2007) 114-119.
35. J. M. Miguel, J.M. Guilemany, B.G. Mellor and Y.M. Xu, Acoustic emission study on WC-Co thermal sprayed coatings, Materials Science and Engineering A352 (2003) 55-63.
36. J. Stokes and L. Looney, Residual stress in HVOF thermally sprayed thick deposits, Surface and Coatings Technology 177-178 (2004) 18-23
37. E. Lopez Cantera and B.G. Mellor, Fracture toughness and crack morphologies in eroded WC-Co-Cr thermally sprayed coatings, Materials Letters 37 (1998) 201-210.
38. D. Tu, S. Chang, C. Chao and C. Lin, Tungsten carbide phase transformation during the plasma spray process, Journal of Vacuum Science and Technology A 3 (6)(1985) 2479-2482.
39. Organisation for Economic Co-operation and Development -Friction Wear and Lubrication Glossary 1969 Paris.
40. J.A. Williams, Engineering Tribology 1994 Oxford University Press, Oxford.
41. J.A. Greenwood and J.B.P. Williamson, Contact of nominally flat rough surfaces, Proc Royal Soc A295 (1966) 300-319.
42. A. Matthews, Nanocomposite coatings for optimised tribological performance, in The Donald Julius Gordon Lecture 2005, IMechE: London.
43. T.R. Oberle, Wear of Metals, Journal of Metals (June 1951) 436-440.
44. J. Larsen-Basse, Role of microstructure and mechanical properties in abrasion, Scripta Metallurgica at Materialia 24 (1990) 821-826.

45. J.F. Archard, Contact and rubbing of flat surfaces, Journal of Applied Physics 24 (8)(1953) 981-988.
46. H. Czichos. Tribology: A Systems Approach to the Science and Technology of Friction. in *Lubrication and Wear*. 1978 Elsevier Amsterdam.
47. D.N. Allsopp, R.I. Trezona and I.M. Hutchings, The effect of ball surface condition in the micro-scale abrasive wear test, Tribology Letters 5 (1998) 259-264.
48. J. Williams and A. Hyncica, Mechanisms of abrasive wear in lubricated contacts Wear 152 (1992) 57-74.
49. K. Adachi and I. Hutchings, Wear-mode mapping for the micro-scale abrasion test, Wear 255 (2003) 23-29.
50. P.H. Shipway, A mechanical model for particle motion in the micro-scale abrasion wear test, Wear 257 (2004) 984-991.
51. J. Gates, Two-body and three-body wear: critical discussion, Wear 215 (1998) 139-146.
52. R.I. Trezona, D.N. Allsopp and I.M. Hutchings, Transition between two-body and three-body abrasive wear: influence of test conditions in the microscale abrasive wear test, Wear 225-229 (1999) 205-214.
53. A.A. Torrance, Modelling abrasive wear, Wear 258 (2005) 281-293.
54. R.I. Trezona and I.M. Hutchings, Three-body abrasive wear testing of soft materials, Wear 233-235 (1999) 209-221.
55. P.H. Shipway, A mechanical model for particle motion in the micro-scale abrasion wear test, Wear 257 (2004) 984-991.
56. G.W. Stachowiak and A. Batchelor, Engineering Tribology. 3rd ed 2002 Elsevier, London.
57. R.C.D. Richardson, Wear of metals by relatively soft abrasives, Wear 11 (1968) 245-275.
58. V. Imbeni, C. Martini, D. Prandstraller, G. Poli, C. Trepanier and T.W. Duerig, Preliminary study of micro-scale abrasive wear of a NiTi shape memory alloy, Wear 254 (2003) 1299-1306.
59. G. B. Stachowiak and G.W. Stachowiak, The effects of particle characteristics on three-body abrasive wear, Wear 249 (2001) 201-207.
60. G.W. Stachowiak, Particle angularity and its relationship to abrasive and erosive wear, Wear 241 (2)(2000).
61. A. Misra and I. Finnie, On the size effect in abrasive and erosive wear, Wear 65 (1981) 359-373.
62. I. Kramer and L. Demer, The effect of surface removal on the plastic behaviour of aluminium single crystal, Trans. AIME 221 (1961) 78-0786.

63. M. Moore and R. Douthwaite, Plastic deformation below worn surface, Metall. Trans. (1976) 1833-1839.
64. G.B. Stachowiak and G.W. Stachowiak, Wear mechanism in ball-cratering test with large abrasive particles, Wear 256 (2004) 600-607.
65. M. Moore. Abrasive Wear. in *ASM Materials Science Seminar*. 1980 ASM Pittsburgh, US.
66. N. Wing, The transformation of soft-abrasive wear into hard-abrasive wear under the effect of frictional heat, Tribology Transactions 32 (1989) 85-90.
67. A.J. Gant and M.G. Gee, Abrasion of WC hardmetals using hard counterfaces, International Journal of Refractory Metals and Hard Materials 24 (2006) 189-198.
68. N. Axen and S. Jacobson, A model for abrasive wear resistance for multi-phase materials, Wear 174 (1994) 187-199.
69. S.G. Bailey and C.M. Perrott, Wear processes exhibited by WC-Co rotary cutters in mining, Wear (29)(1974) 117-128.
70. J. Larsen-Basse, C.M. Perrott and P.M. Robinson, Abrasive wear of tungsten carbide-cobalt composites I. Rotary drilling tests, Materials Science and Engineering 13 (1974) 83-91.
71. P.H. Shipway and L. Howell, Microscale abrasion-corrosion behaviour of WC-Co hardmetals and HVOF sprayed coatings Wear 258 (2005) 303-312.
72. A.J. Gant, M.G. Gee and A.T. May, Micro-abrasion of WC-Co hardmetals in corrosive media Wear 256 (9-10)(2004) 954-962.
73. J. Larsen-Basse, Binder extrusion in sliding wear of WC-Co alloys, Wear 105 (1985) 247-256.
74. R.I. Blombery, C.M. Perrott and P.M. Robinson, Similarities in the mechanisms of wear of tungsten carbide-cobalt tools in rock and metal cutting, Wear 27 (1974) 383-390.
75. R.I. Blombery, C.M. Perrot and P.M. Robinson, Abrasive wear of tungsten carbide-cobalt composites. I. Wear mechanisms, Materials Science and Engineering 13 (1974) 93-100.
76. M. Gee, A. Gant and B. Roebuck, Wear mechanisms in abrasion and erosion of WC/Co and related hardmetals, Wear 263 (2007) 137-148.
77. H. Klaasen and J. Kubarsepp, Abrasive wear performance of carbide composites, Wear 261 (2006) 520-526.
78. M. Gee, C. Phatak and R. Darling, Determination of wear mechanisms by stepwise erosion and stereological analysis, Wear 258 (1-4)(2005) 412-425.
79. A.J. Gant, M.G. Gee and B.R. Roebuck, Rotating wheel abrasion of WC/Co hardmetals, Wear 258 (2005) 178-188.

80. K. Jia and T. Fischer, Abrasion resistance of nanostructured and conventional cemented carbides, Wear 200 (1996) 206-214.
81. K. Jia and T.E. Fischer, Sliding wear of conventional and nanostructured cemented carbides, Wear 203-204 (1997) 310-318.
82. R.B. Bhagat, J.C. Conway Jr, M.F. Amateau and R.A. Brezler III, Tribological performance evaluation of tungsten carbide-based cermets and development of a fracture mechanics wear model, Wear 201 (1996) 233-243.
83. U. Beste, L. Hammerström, H. Engqvist, S. Rimlinger and S. Jacobson, Particle erosion of cemented carbides with low Co content, Wear 250 (1-12)(2001) 809-817
84. K. Anand and H. Conrad, Microstructure and scaling effects in the damage of WC-Co alloys by single particle impacts of hard particles, Journal of Materials Science 23 (1988) 2931-2942.
85. H. Chen, C. Xu, Q. Zhou, I.M. Hutchings, P.H. Shipway and J. Liud, Micro-scale abrasive wear behaviour of HVOF sprayed and laser-remelted conventional and nanostructured WC-Co coatings, Wear 258 (2005) 333-338.
86. V. Ramnathan and N. Jayaraman, Characterisation and wear performance of plasma sprayed WC-Co coatings, Materials Science and Technology 5 (1989) 382-388.
87. H. Liao, B. Normand and C. Coddet, Influence of coating microstructure on the abrasive wear resistance of WC/Co cermet coatings, Surface Coatings Technology 124 (2000) 235-242.
88. M.M. Lima, C. Godoy, J.C. Avelar-Batista and P.J. Modenesi, Toughness evaluation of HVOF WC-Co coatings using non-linear regression analysis, Materials Science and Engineering A357 (2003) 337-345.
89. Yoomin Ahn, N.-G. Cho, S.-H. Lee and D. Lee, Lateral crack in abrasive wear of brittle materials, JSME International Journal Series A, 46 (2)(2003) 140-144.
90. D.K. Shetty, I.G. Wright, P.N. Mincer and A.H. Clauer, Indentation fracture of WC-Co cermets, Journal of Materials Science 20 (1985) 1873-1882.
91. K. Niihara, A fracture mechanics analysis of indentation induced Palmqvist cracks in ceramics, Journal of Materials Science Letters 2 (1983) 221-223.
92. J. Barber, B.G. Mellor and R.J.K. Wood, The development of sub-surface damage during high energy solid particle erosion of a thermally sprayed WC-Co-Cr coating, Wear 259 (2005) 125-134.
93. D.W. Wheeler and R.J.K. Wood, Erosion of hard surface coating for use in offshore gate valves, Wear 258 (1-4)(2005) 526-536
94. D. Stewart, P. Shipway and D.G. McCartney, Abrasive wear behaviour of conventional and nanocomposite HVOF-sprayed WC-Co coatings, Wear 225-229 (1999) 789-798.

95. P.H. Shipway, D.G. McCartney and T. Sudaprasert, Sliding wear behaviour of conventional and nanostructured HVOF sprayed WC-Co coatings, Wear 259 (2005) 820-827.
96. P.J. Blaua and K.G. Budinski, Development and use of ASTM standards for wear testing, Wear 225-229 (1999) 1159-1170.
97. A. Stevenson and I. Hutchings, Development of the dry sand/rubber wheel abrasion test, Wear 195 (1996) 232-240.
98. K.L. Rutherford and I.M. Hutchings, A micro-abrasive wear test with particular application to coated system, Surface Coatings and Technology 79 (1996) 76-80.
99. K. Adachi and I. Hutchings, Sensitivity of wear rates in the micro-abrasion test to test conditions and material hardness, Wear 258 (2005) 318-321.
100. P. Shipway and C. Hodge, Micro-abrasion of glass- the critical role of ridge formation, Wear 237 (2000) 90-97.
101. K.R. Tretheway and J. Chamberlain, Corrosion for Science and Engineering 1995 Longman.
102. M. Pourbaix, Atlas of Electrochemical Equilibria in Aqueous Solutions 1974 NACE-Cebelcor, Houston, USA.
103. H.S. Kalish, Corrosion of Cemented Carbides. 9th ed. Corrosion 13 1987 ASM International, Ohio, USA 846-858.
104. W.J. Tomlinson and C.R. Linzell, Anodic polarisation and corrosion of cemented carbides with cobalt and nickel binders, Journal of Materials Science 23 (1988) 914-918.
105. S. Hochstrasser (-Kurz), Mechanistic study of corrosion reactions on WC-Co hardmetal in aqueous solution- an investigation by electrochemical methods and elemental solution analysis, in Institute of Materials Chemistry and Corrosion. 2006, ETH Zurich: Zurich.
106. S. Hochstrasser(-Kurz), Y. Mueller, C. Latkoczy, S. Virtanen and P. Schmutz, Analytical characterization of the corrosion mechanisms of WC–Co by electrochemical methods and inductively coupled plasma mass spectroscopy, Corrosion Science 49 (4)(2007) 2002-2020.
107. K.M. Andersson and L. Bergstrom, Oxidation and dissolution of tungsten carbide powder in water, International Journal of Refractory Metals & Hard Material 18 (2000) 121-129.
108. S. Imasato, S. Sakaguchi and Y. Hayashi, Corrosion behaviour of WC-Ni-Cr cemented carbide in NaOH solution, Nippon Tungsten Review 32 (2000) 8-16.
109. D. Toma, W. Brandl and G. Marginean, Wear and corrosion behaviour of thermally sprayed cermet coatings, Surface and Coatings Technology 138 (2001) 149-158.

110. T. Rogne, M. Bjordal, T. Solem and E. Bardal, The importance of corrosion on the erosion-corrosion performance of thermal spray ceramic-metallic coatings. Thermal Spray: Practical Solutions for Engineering Problems, ed. C.C. Berndt 1996 ASM International, Ohio, USA.

111. A. Karimi, C. Verdon, J. Martin and R. Schmid, Slurry erosion behaviour of thermally sprayed WC-M coatings, Wear 186-187 (1995) 480-486.

112. G. Barbezat, A. Nicoll and A. Sickinger, Abrasion, Erosion and scuffing resistance of carbide and oxide ceramic thermal sprayed coatings for different applications, Wear 162-164 (1993) 529-537.

113. V.A.D. Souza and A. Neville, Linking electrochemical corrosion behaviour and corrosion mechanisms of thermal spray cermet coatings (WC-CrNi and WC/CrC-CoCr), Materials Science and Engineering A352 (2003) 202-211.

114. J.E. Cho, S.Y. Hwang and K.Y. Kim, Corrosion behaviour of thermal sprayed WC cermet coatings having various metallic binders in strong alkaline environment, Surface and Coatings Technology 200 (2006) 2653-2662.

115. G. Bolelli, R. Giovanardi, L. Lusvarghi and T. Manfredini, Corrosion resistance of HVOF sprayed coatings for hard chrome replacement, Corrosion Science 48 (2006) 3375-3397.

116. J.M. Perry, A. Neville, V. Wilson and T. Hodgkiess, Assessment of the corrosion rates and mechanisms of a WC-Co-Cr HVOF coatings in static and liquid-solid impingement saline environments, Surface and Coatings Technology 137 (2001) 43-51.

117. V.A.D. Souza and A. Neville, Corrosion and synergy in a WC-Co-Cr HVOF thermal spray coating-understanding their role in erosion-corrosion degradation, Wear 259 (2005) 171-180.

118. V.A.D. Souza and A. Neville, Corrosion and erosion damage mechanisms during erosion-corrosion of WC-Co-Cr cermet coatings, Wear 255 (2003) 146-156.

119. M. Takeda, N. Morihiro, E. Ebara and Y. Harada, Corrosion Behaviour of Thermally Sprayed WC Coating in Na_2SO_4 Aqueous Solution, Materials Transactions 33 (11)(2002) 2860-2865.

120. N.G. Thompson and J.H. Payer, DC Electrochemical Test Methods 6 1998 NACE International, Houston, USA.

121. ASTM-G5-82, ed. Standard reference method for making potentiostatic and potentiodynamic anodic polarisation measurements. Annual Book of ASTM Standards, ed. A. Committee. Vol. 03.02. 1982, ASTM. 511-521.

122. A. Legat and V. Dolecek, Corrosion monitoring system based on measurement and analysis of electrochemical noise, Corrosion 51 (4)(1995) 295-300.

123. R.A. Cottis, Interpretation of electrochemical noise data, Corrosion 57 (3)(2000) 265-285.

124. R. J. K. Wood, J.A. Wharton, A.J. Speyer and K.S. Tan, Investigation of erosion–corrosion processes using electrochemical noise measurements, Tribology International 35 (10)(2002) 631-641.

125. P. Jemmely, S. Mischler and D. Landolt, Tribocorrosion behaviour of Fe-17Cr stainless steel in acid and alkaline solutions, Tribology International 32 (1999) 295-303.

126. Y. Puget, K. Trethewey and R.J.K. Wood, Electrochemical noise analysis of polyurethane-coated steel subjected to erosion-corrosion, Wear 233-235 (1999) 552-267.

127. B. Bethune and R.B. Waterhouse, Electrochemical studies of fretting corrosion, Wear 12 (1968) 27-34.

128. S. Mischler, A. Spiegel and D. Landolt, The role of passive oxide films on the degradation of steel in tribocorrosion systems, Wear 225-229 (1999) 1078-1087.

129. D. Landolt, S. Mischler and M. Stemp, Electrochemical methods in tribocorrosion: a critical appraisal, Electrochemica Acta 46 (2001) 3913-3929.

130. J.R. Goldberg and J.L. Gilbert, Electrochemical response of CoCrMo to high speed fracture of its metal oxide using an electrochemical scratch, Journal of Biomedical Materials Research 37 (1997) 421-431.

131. ASTM-G119-93 Standard guide for determining synergism between wear and corrosion, in ASTM Handbook. 1998 529-534.

132. A. Neville and T. Hodgkiess, Characterisation of high-grade alloy behaviour in severe erosion-corrosion conditions, Wear 35 (1999) 669-679.

133. P.E. Sinnett-Jones, J.A. Wharton and R.J.K. Wood, Micro-abrasion-corrosion of a CoCrMo alloy in simulated artificial hip joint environments, Wear 259 (2005) 898-909.

134. M.M. Stack, H. Jawan and M.T. Mathew, On the construction of micro-abrasion maps for a steel/polymer couple in corrosive environments Tribology International 38 (9)(2005) 848-856

135. A.J. Gant, M.G. Gee and A.T. May, The evaluation of tribo-corrosion synergy for WC-Co hardmetals in low stress abrasion Wear 256 (5)(2004) 500-516.

136. S. Mischler, S. Debaud and D. Landolt, Wear-accelerated corrosion of passive metals in tribo-corrosion systems, J. Electrochemical Soc. 145 (3)(1998) 750-758.

137. R. J. K. Wood, Erosion-corrosion, in Comprehensive Structural Integrity. 2007 Elsevier Oxford, UK.

138. A.W. Batchelor and G.W. Stachowiak, Predicting synergism between corrosion and abrasive wear, Wear 123 (1988) 281-291.

139. K.S. Tan, J.A. Wharton and R.J.K. Wood, Solid particle erosion-corrosion behaviour of a novel HVOF nickel aluminium bronze coating for marine applications-correlation between mass loss and electrochemical measurements, Wear 258 (1-4)(2005) 629-640.

140. R.J.K. Wood, T.F. Jones, N.J. Miles and J. Ganeshalingam, Upstream swirl-induction for reduction of erosion damage from slurries in pipeline bends, Wear 250 (2001) 771-779.

141. R. J. K. Wood, Tribo-corrosion of coatings: a review, Journal of Physics D: Applied Physics 40 (2007) 5502-5521.

142. P. Ponthiaux, F. Wenger, D. Drees and J.P. Celis, Electrochemical techniques for studying tribocorrosion processes, Wear 256 (5)(2004) 459-468

143. I. Garcia, D. Drees and J.P. Celis, Corrosion-wear of passivating materials in sliding contacts based on a concept of active wear track area, Wear 249 (2001) 452-460.

144. J. Jiang, M.M. Stack and A. Neville, Modelling the tribo-corrosion interaction in aqueous sliding conditions, Tribology International 35 (2002) 669-679.

145. A.M. Human, I.T. Northrop, S.B. Luyckx and M.N. James, A comparison between cemented carbides containing cobalt and nickel based binders, Journal of Hard Materials 2 (3-4)(1991) 245-255.

146. A. Human and H. Exner, Electrochemical behaviour of tungsten-carbide hardmetals, Materials Science and Engineering A209 (1996) 180-191.

147. A. Human and H. Exner, The relationship between electrochemical behaviour and in-service corrosion of WC based cemented carbides, International Journal of Refractory Metals and Hard Materials 15 (1997) 65-71.

148. P.H. Shipway and S. Wirojanupatump, The role of lubrication and corrosion in abrasion of materials in aqueous environments, Tribology International 35 (2002) 661-667.

149. E.J. Wentzel and C.Allen, The erosion-corrosion resistance of tungsten carbide hard metals with different binder compositions, Wear 181-183 (1995) 63-69.

150. L. Valentinelli, T. Valente, F. Casadei and L. Fedrizzi, Mechanical and tribocorrosion properties of HVOF sprayed WC-Co coatings, Corrosion Engineering, Science and Technology 39 (2004) 301-307.

151. M.M. Stack and T.M.A.E. Badia, On the construction of erosion-corrosion maps for WC/Co-Cr based coatings in aqueous conditions, Wear 261 (2006) 1181-1190.

152. R.S. Lillard, G.S. Kanner and D.P. Butt, The Nature of Oxide Films on Tungsten in Acidic and Alkaline Solutions. 2001, Materials Corrosion and Environmental Effects

Laboratory, Materials Science and Technology Division, Los Alamos National Laboratory: Los Alamos

153. K.L. Rutherford and I.M. Hutchings, Theory and Application of a micro-scale abrasive wear test., Journal of Testing and Evaluation 25 (1997) 250-260
154. Meeting minutes-with Dr. M. Gee and Dr. A. Gant, NPL. 2007.
155. J. Bello and R.J.K. Wood. Abrasion-Corrosion of Stainless Steel. in *OECD*. 2005 Uppsala, Sweden.
156. C. Verdon, A. Karimi and J.-L. Martin, Microstructural and analytical study of thermally sprayed WC-Co coatings in connection with their wear resistance, Materials Science and Engineering A234-236 (1997) 731-734.
157. H.W. Wang and M.M. Stack, The erosive wear of mild steel and stainless steels under controlled corrosion in alkaline slurries containing alumina particles, Journal of Materials Science 35 (2000) 5263-5273.
158. S. Haglund and J. Agren, W content in Co binder during sintering of WC-Co, Acta Metallurgica 46 (8)(1997) 2801-2807.
159. E. Breval, J.P. Cheng, D.K. Agrawal, P. Gigl, M. Dennis, R. Roy and A.J. Papworth, Comparison between microwave and conventional sintering of WC/Co composites, Materials Science and Engineering A 391 (2005) 285-295.
160. W. A. Badawy, F.M. Al-Kharafi and J.R. Al-Ajmi, Electrochemical behaviour of cobalt in aqueous solutions of different pH, Journal of Applied Electrochemistry 30 (2000) 693-704.
161. Charles D. Wagner, A.V. Naumkin, A. Kraut-Vass, J.W. Allison, C.J. Powell and J.R.R. Jr, NIST X-ray Photoelectron Spectroscopy Database. 2006, Measurement Services Division of the National Institute of Standards and Technology (NIST) Technology Services.
162. P. Shipway and J.J. Hogg, Dependence of micro-scale abrasion mechanism of WC-Co hardmetals on abrasive type, Wear 259 (2005) 44-51.
163. A.G. Evans and D.B. Marshall, Wear Mechanisms in Ceramics in Fundamentals of Friction and Wear of Materials, D. Rigney, Editor. 1981 ASM Pittsburgh p.439.
164. I.M. Ogilvy, C.M. Perrott and J.W. Suiter, On the indentation fracture of cemented carbide Part 1-Survey of operating fracture modes, Wear 43 (1977) 239-252.